From Carbazole-containing and π-Expanded Triangular Trinuclear Porphyrinoids

Dissertation zur Erlangung des Grades

"Doktor der Naturwissenschaften"

am Fachbereich Chemie, Pharmazie und Geowissenschaften

der Johannes Gutenberg-Universität Mainz

Dipl.-Ing. Lena Arnold

geboren in Esslingen am Neckar

Mainz im Jahr 2012

Dekan: [redacted]

1. Berichterstatter: [redacted]

2. Berichterstatter: [redacted]

Tag der mündlichen Prüfung: 07.09.2012

Die vorliegende Arbeit wurde in der Zeit von Februar 2009 bis Januar 2012 im Max-Planck-Institut für Polymerforschung in Mainz unter Anleitung von [redacted] durchgeführt.

Meiner Familie.

„Wer fragt, ist ein Narr für eine Minute.

Wer nicht fragt, ist ein Narr sein Leben lang."

-Konfuzius-

[redacted]

Contents

1 INTRODUCTION 1

2 STATE OF THE ART 5

2.1 Porphyrins 5

2.1.1 Syntheses of Porphyrins 8

2.1.2 Modified Porphyrins 10

2.2 N_4-macrocyclic metal complexes as catalysts for ORR 16

2.2.1 History and principle of a fuel cell 16

2.2.2 Rotating Disk Electrode - RDE 21

2.2.3 Rotating Ring Disk Electrode - RRDE 22

3 MOTIVATION AND OBJECTIVES 25

4 MONOCYCLIC PORPHYRINOIDS CONTAINING CARBAZOLE 29

4.1 Building macrocycles *via* Suzuki cross-coupling reaction 32

4.1.1 Synthesis 35

4.1.2 Crystal Structure 39

4.1.3 Electronic Structure 40

4.1.4 Metal Complexation 44

4.1.5 RRDE measurements 55

4.1.6 RDE measurements 58

4.1.7 Surface Deposition 61

4.1.8 Oligomerization of macrocycle 4-18 63

4.1.9 Dimerization of macrocycle 4-18 66

4.1.10 RRDE measurements 70

4.2 $(NH)_4$ – motif porphyrinoid 72

4.2.1 Synthesis 72

4.2.2 Electronic Structure 76

4.2.3 Aromatization 78

4.3 Macrocycle formation based on Click Chemistry 81

4.3.1 Synthesis 85

4.3.2 NMR Analysis 89
4.3.3 Electronic Structure 94
4.3.4 Anion recognition 97

4.4 Summary and Comparison 112

5 TRIANGULAR TRINUCLEAR SYSTEMS 117

5.1 Results and Discussion 123
5.1.1 Synthesis 123
5.1.2 Electronic structure 129
5.1.3 Metal complexation 134
5.1.4 Bulk Properties 139
5.1.5 RRDE measurements 142
5.1.6 Summary 144

6 CONCLUSION AND OUTLOOK 147

7 EXPERIMENTAL PART 153

7.1 General Methods and Analytical Techniques 153

7.2 Synthetic Procedures 157

8 APPENDIX 189

8.1 Crystal Strucutres 189

8.2 Literature 195

Index of Abbreviations

2D-WAXS	two-dimensional wide-angle X-ray scattering
AcOH	acidic acid
Boc	*tert*-butyl formate
d	days
d	doublet (NMR)
CuAAC	copper-catalyzed azide-alkyne cycloaddition
CV	cyclic voltamemetry
DBU	1,8-diazabicyclo[5,4,0]undec-7-en
DCM	dichloromethane
DFT	density functional theroy
DMF	N,N-dimethylformamide
DMSO	dimethylsulfoxid
dtbpy	4,4′-di-*tert*-butylbipyridine
DSC	differential scanning calometry
EtOAc	ethyl acetate
Et_2O	diethylether
EtOH	ethanol
FD	field desortpion
Fc	ferrocene
GPC	gel permeation chromatography
h	hour
dppf	bis(diphenylphosphino)ferrocene
HFIP	hexafluoro-isopropanol
HOMO	highest occupied molecular orbital
HPHATN	hexa(pyrrol-yl)hexaazatrinaphthalene
HRMS	high resolution mass spectrometry
HS	high spin
IR	infrared spectroscopy
KB	ketjen black
LS	low spin
LUMO	lowest unoccupied molecular orbital
m	multiplet (NMR)
MALDI-TOF	matrix-assisted laser desorption/ionization time-of-flight
MeOH	methanol
MS	mass spectrometry
MW	microwave
NBS	N-bromosuccinimide

NMP	N-methylpyrrolidone
NMR	nuclear magnetic resonance
NOE	nuclear Overhauser effect
NOESY	nuclear Overhauser enhancement spectroscopy
PAH	polycyclic aromatic hydrocarbon
ppm	parts per million
$^{i}Pr_2NH$	diisopropylamine
PS	polystyrene
ppm	parts per million
q	quartet (NMR)
RDE	rotating disk electrode
RRDE	rotating ring disk electrode
rt	room temperature
sec	seconds
s	singlet (NMR)
SQUID	superconducting quantum interference device
STM	scanning tunneling microscopy
t	triplet (NMR)
TBTA	tris-[(1-benzyl-1*H*-1,2,3-triazol-4-yl) methyl]amine
TBAF	tetra-iso-butyl ammonium fluoride
TCNQ	7,7,8,8-tetracyanoquinodimethane
TEA	triethylamine
THF	tetrahydrofuran
TGA	thermo-gravimetric analysis
TLC	thin layer chromatography
TMEDA	N,N,N',N'-tetramethylene-diamine
TMS	trimethylsilyl-
TMP	2,2,6,6-tetramethylpiperidine
UV-vis	ultraviolet-visible absorption spectroscopy
XPS	X-ray photoemission spectroscopy

1 Introduction

Ever since the first isolation of a porphyrin from blood – hematoporphyrin (originally named *cruentine*) by J. L. W. Thudichun in 1867,[1-2] this unique *tetra*-pyrrole-macrocycle has captivated researchers from all over the world in its spell. Already in 1955 a conference devoted entirely to porphyrins, founded by a Ciba Foundation Symposium, was convened. Since that time, porphyrins have not lost any of their fascination which is expressed in the multitudinous publications every year on porphyrin chemistry. The foundation of its own journal the *Journal of Porphyrins and Phthalocycanies (JPP)* in 1997 and the formation of *The Society of Porphyrins and Phthalocyanines (SPP)* in 2000 corroborated the great impact of this research topic.

Porphyrins and especially metalloporpyhrins are highly aromatic and stable compounds playing a key role in numerous biological and technical processes like oxygen transport in blood, photosynthesis, catalytic conversions mediated by cytochrome, charge transfer in photovoltaic elements, or chemical sensing.[3] Hereby, special focus lies on the metal centers with four-fold coordination by the *tetra*-pyrrole-macrocycle, as they form the active site for attachment of axial ligands. Of highest biological importance amongst porphyrinoids occurring in nature is surely *heme b*, the red blood pigment (Figure 1-1). The iron center in *heme b* reversibly binds small gas molecules during the respiratory action. Its first isolation was achieved from crystallization of blood by L. Teichmann.[4] Not less in significance are *chlorophyll a*, the green pigment involved in plant photosynthesis and *vitamin* B_{12}, the red pigment essential for numerous biochemically important rearrangement reactions, like cell division or hematosis. In 1914 R. Willstätter[5] succeeded in the isolation of c*hlorophyll a* and was honored only one year later with the Nobel Prize in Chemistry 1915 *"for his researches on plant pigments, especially chlorophyll"*. The Nobel Prize in Chemistry 1930 was awarded to H. Fischer *"for his researches into the constitution of haemin and chlorophyll and especially for his synthesis of haemin"*. R. B. Woodward established the total syntheses of c*hlorophyll a* in 1960[6-

[8] and *vitamin* B_{12} in 1972.[9] The numerous biological functions of porphyrins and metalloporphyrins have stimulated a plethora of investigations and today they certainly represent one of the most extensively studied of all known nitrogen-containing macrocycles. Of special interest herein, are syntheses of artificial porphyrins and porphyrin derivatives which are able to mimic the biological activity.

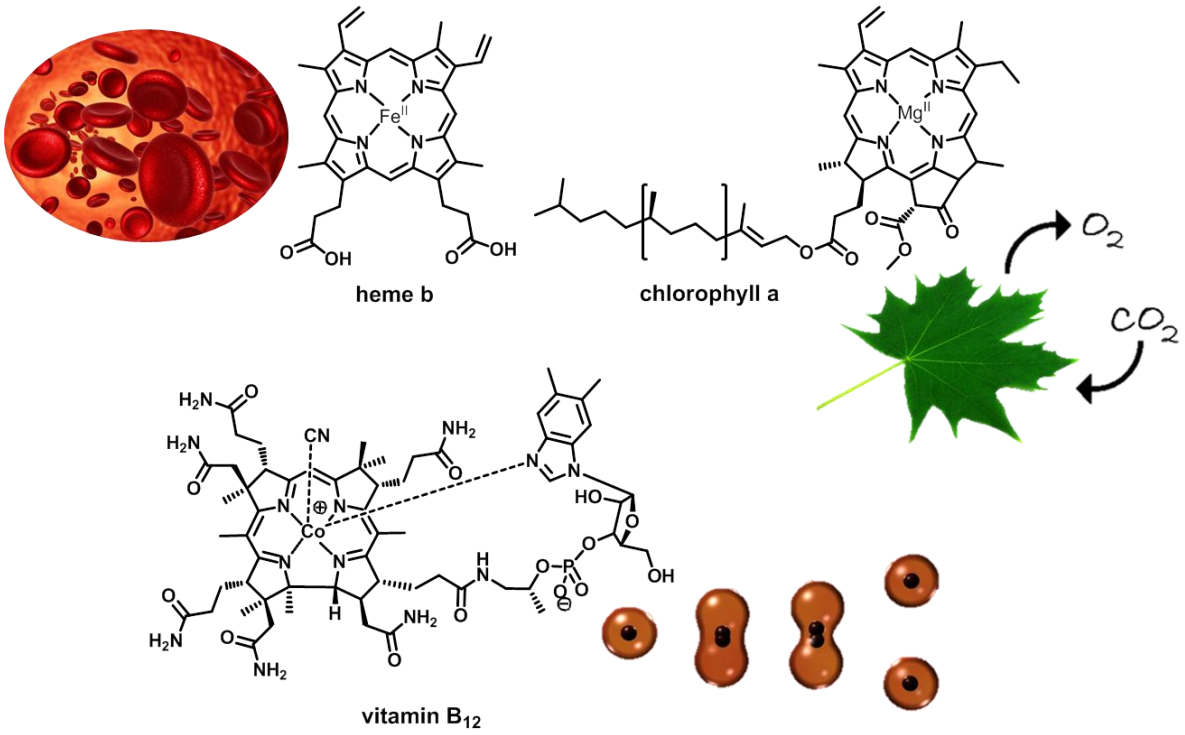

Figure 1-1: Examples of porphyrins in nature: *heme b*, *chlorophyll a* and *vitamin* B_{12}.

The pioneering discovery of isomeric porphyrin, the *porphycene*, by E. Vogel,[10] has revolutionized the porphyrinoid chemistry. A great variety of porphyrins and porphyrin derivatives have become accessible ever since, including calixpyrroles,[11] contracted,[12] expanded,[13-14] heteroatom-exchanged[15-16] and inverted porphyrinoids.[17-18] The elongation of the π–system with fused polycyclic aromatic rings on the periphery of the macrocyclic core results in highly conjugated porphyrins.[19-21] Fully conjugated porphyrins are attractive materials for nonlinear optics[22-23] or as photosensitizers for photodynamic therapy.[24] Edged fused porphyrins can also result in conjugated oligoporphyrins which are promising as molecular wires and molecular switches.[25-28] The replacement of pyrrole units in the porphyrin core with other aromatic rings have revealed unusual physical properties relating to cyclic conjugation, magnetic features, redox potential and

metal-binding behavior.[15-16, 29] In this class hetero[3, 15-16]-, carba[30-31]- and N-confused[17-18] porphyrins with one or more pyrrole units exchanged are the most prominent members. Although, the list of examples is long and could be indefinitely extended, most of these porphyrinoids have been synthesized by the classical acid-catalyzed condensation of pyrroles and aldehydes (or their equivalents).[32-33] Nowadays, modern chemistry including a toolbox full with new synthetic protocols have entered into the laboratories and allow more efficient preparation of novel porphyrinoids with new properties to be explored. Therefore, we and others are keen to design novel porphyrinoids constructed using contemporary synthetic protocols.[34-36]

2 State of the Art

2.1 Porphyrins

Porphyrins have received their denotation deduced from the Greek word for purple, *porphura*. Due to their biological importance in nature and their vivid colors porphyrins have been named the "pigments of life".[3] Porphyrins consist of four pyrrole-type subunits joined together at their α carbon atoms *via* methine bridges (=CH-), resulting in two pyrrole (NH) and two pyrrolenine (=N) units (Figure 2-1). The structure of the cyclic tetrapyrrole was first suggested by W. Küster[37] in 1912 and subsequent investigations proved the *trans* NH-tautomer as the most stable form (Figure 2-1).

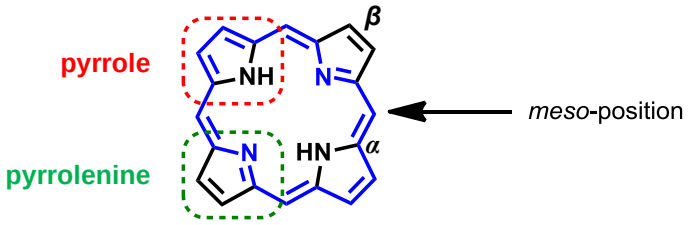

Figure 2-1: The *trans* NH-tautomer of porphyrin and its 18 π-electron aromatic pathway (indicated in blue).

The aromaticity of porphyrins is unique and arises from the diatropic ring current distributed over the cyclic scaffold. Porphyrins obey the Hückel rule[38-39] for aromaticity possessing 4n+2 π-electrons delocalized over the macrocyclic core. However, porphyrins can also be interpreted as multiple-bridged aromatic di-aza[18]annulene systems,[40] due to their similarity to [18]annuelene.[41]

Porphyrins and their derivatives are highly colored, absorbing strongly in the visible region (Figure 2-2a). The most intense absorption band near 400 nm was named after its discoverer J.-L. Soret.[42] Less intense bands in the long-wavelength region between 500-800 nm are

generally called Q-bands. Both, the Soret and the Q-bands arise from the porphyrin core-centered π-π* transition and can be explained by the *four-orbital model*.[43-44] According to this theory, the two degenerated highest occupied molecular orbitals (HOMOs) are of a_{1u} and a_{2u} symmetry, and the two degenerated lowest unoccupied molecular orbitals (LUMOs) are of e_g symmetry (Figure 2-2b). The four orbitals are π and π* orbitals and the two major absorbances arise from the coupling of the two transitions between those orbitals. The weaker absorbance of the Q-bands is the result of the destructive interference of the transition dipoles.[45]

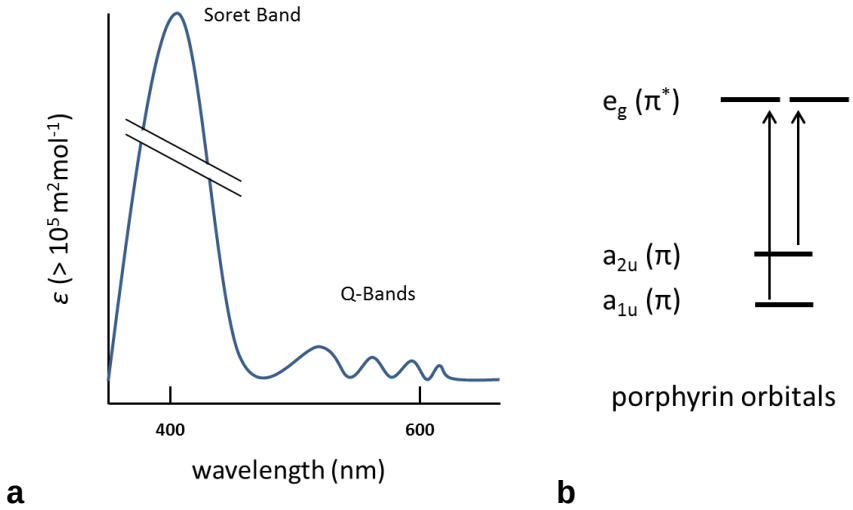

Figure 2-2: **a:** Schematic illustration of a typical UV-vis absorption spectrum of a porphyrin; **b:** Molecular orbital diagram for porphyrin (four-orbital model).

The chemical shifts in the proton NMR spectrum of porphyrins are characteristic and strongly influenced by the aromatic ring current. The signals for the outer protons are shifted to lower fields, whereas the signals of the inner NH-protons are resonating at high field (- 4 ppm) as a consequence of the macrocyclic aromaticity.[3]

Beside the unique optical properties, the most striking feature of porphyrins is undoubtedly the ability to complex almost any transition metal ion in its cavity (Figure 2-3).[46]

Figure 2-3: Metalloporphyrin.

In this regard, porphyrins are rigid chelating ligands which force the transition metal ion into its macrocyclic plane. Upon metalation with metal(II) ions a dianonic species is formed due to deprotonation of the porphyrin ring. The metal center accepts the lone-pair-electrons of the nitrogen atoms, while electrons of the metal ion are donated to the ligand, forming delocalized π-bonds allowing delocalization of the π-electrons.

Based on their UV-vis properties, a distinction is drawn between *regular* metalloporphyrins containing closed-shell metal ion (d^0 or d^{10}) and the *hypso*porphyrins with d^m (m = 6-9) metals where the d_π (d_{xz} and d_{yz}, Figure 2-4) orbitals are filled.[47] For metals with partially occupied d_π orbitals (d^m, m = 1-5) the resulting (d-type) *hyper* spectra are more complex due to extensive mixing of the metal d_π orbitals and the LUMO of the porphyrin.

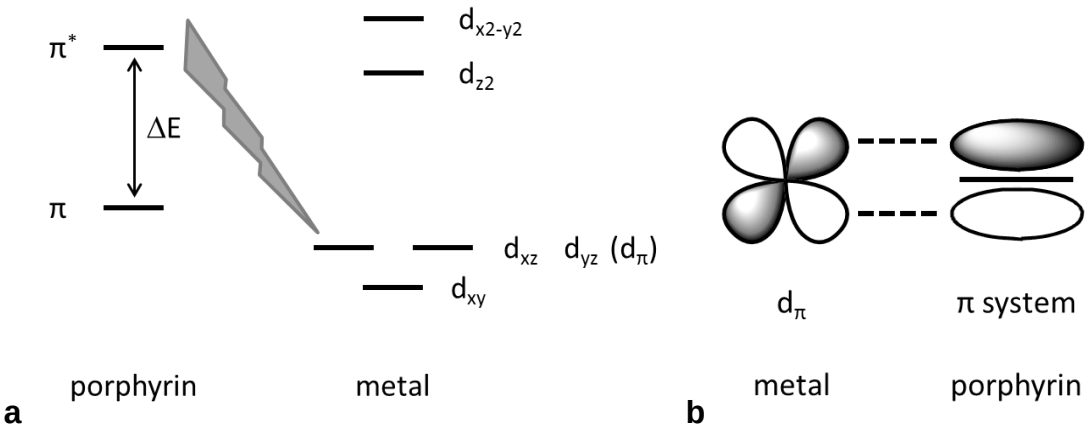

Figure 2-4: **a:** Simplified molecular orbital diagram for metalloporphyrins. Interaction between metal d_π and π* porphyrin orbitals occurs for hypsoporphyrins; **b:** The d_π metal orbital overlap with the π sytem of the porphyrin ring.[47]

In the first category of *regular* porphyrins, the low energy metal orbitals have only little effect on the porphyrin π to π* energy gap, whereas in *hypso*pophyrins a significant metal d_π to porphyrin π* orbital interaction occurs (Figure 2-4a). This is also denoted as metal to ligand backbonding (Figure 2-4b), and results in an increased π to π* energy gap along with an hypsochromic shift in the absoption spectra for metalloporphyrins compared to their ligands.

The vivid colors of the metalloporphyrins are therefore, unlike most transition metal complexes, due to absorption within the porphyrin arising also from porphyrin-centered π-π*-transition. Generally, metalloporphyrins exhibit two Q-bands instead of four for the free ligands, due to the increase of symmetry of the porphyrin core (D_{2h}) upon metalation

(D_{4h}). The orbital mixing also results in the decrease of fluorescence yield (florescence quenching).

Metalloporhyrins can be obtained by refluxing the corresponding porphyrin with a metal salt. Hereby, usually metal(II)acetates and solvents like chloroform, acetic acid[48] or dimetylformamid[49] (DMF) are used. DMF has the advantage that it is a uniformly good solvent for both, the ligand and the metal salt.[49] The HCl produced in the reaction escapes at the reflux temperature of the solvent. The product crystalizes either by cooling or addition of water or methanol. Metal ions which prefer octahedral geometry usually complete the coordination by neutral donor ligands, such as solvent molecules.

2.1.1 Syntheses of Porphyrins

Plenty of synthetic protocols can be found for porphyrins, and therefore only the most common are descried in the following. The most famous synthesis for porphyrins is surely the Rothemund[50-51] reaction. It describes the one-pot condensation of pyrrole (**2-2**) and a simple aldehyde (*e.g.* **2-1**) to form *meso*-tetrasubstituted porphyrins like *meso*-tetraphenylporphyrin **2-3** (commonly abbreviated TPP or H_2TPP, Scheme 2-1). This method however requires high temperatures, long reaction times and results in low yields. Therefore, improvements by Alder and Longo achieved acid-catalyzed reaction conditions avoiding high temperatures and resulting in reasonable yields.[52] When Lewis acids such as BF_3 are used, the reaction is named the Lindsey-type Rothemund reaction.[53]

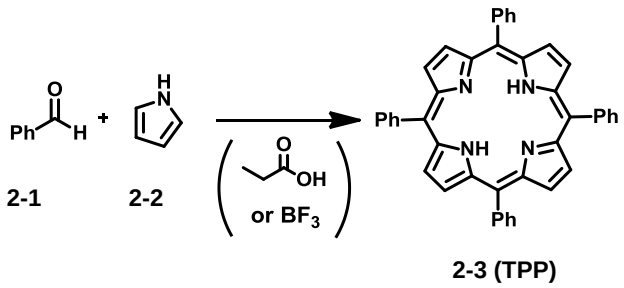

Scheme 2-1: Rothemund reaction without acid and the acid-catalyzed Alder-Longo-Rothemund reaction or Lindsey-type Rothemund reaction, respectively.

For the synthesis of unsymmetrical *meso*-unsubsituted porphyrins, such as **2-6**, the "2+2" MacDonald condensation has been successfully applied (Scheme 2-2).[54] It denotes the condensation of dipyrrylmethanes (**2-4**) and diformyldipyrrylmethanes (**2-5**) in the presence

of an acid catalyst. It is worth mentioning, that this reaction is a key step in the total synthesis of *heme b* and *chlorophyll a*.

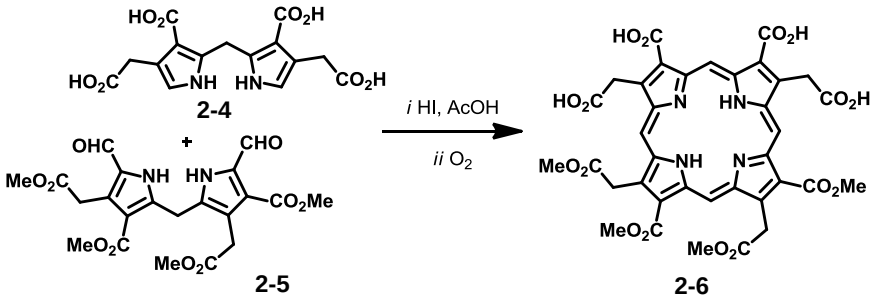

Scheme 2-2: MacDonald "2+2" method.

The most versatile approach for the synthesis of *meso*-unsubsituted porphyrins though, is the "3+1" method as formulated by Broadhurst in 1971.[55] It is a variation of the "2+2" MacDonald approach and describes the condensation of any dialdehyde (**2-7**) with readily available tripyrranes (Scheme 2-3). Although, tripyrrane itself is very unstable it can be generated *in situ* from the corresponding dicarboxylic acid (**2-8**). Dicarboxylic acids easily decarboxylate upon treatment with acids. Albeit the "3 +1" approach has been ignored for over more than two decades it was proven to be the method of choice for the synthesis of a variety of porphyrin analogs.[31]

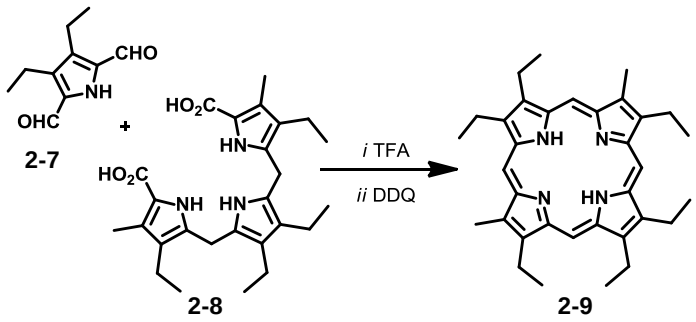

Scheme 2-3: The "3+1" method.

The latter described syntheses for porphyrins are based on the mono-, di- or tripyrrolic precursors. Further syntheses for porphyrins include *e.g.* ring-closure reactions of linear tetrapyrroles or transformations of natural prefabricated porphyrins such as protoporhyrin-dimethyl-ester or hematoporphyrin, both derived from *heme b*.[56]

The chemical reactivity of porphyrins are closely related to those of aromatic hydrocarbons, therefore reductions, oxidations, electrophilic substitutions, cycloadditions, rearrangements or transition metal induced substitutions and dimerizations can also be used to transform porphyrins into new porphyrin derivatives.[3]

2.1.2 Modified Porphyrins

The main motivation to study artificial porphyrins is to control the porphyrin physico-chemical properties.[3, 33] Nowadays, a great variety of core modified porphyrins can be found in the literature, including calixpyrroles,[11] contracted[12] or expanded[57] porphyrins but also hetero[3, 15-16]-, carba[30-31]- and N-confused[17-18] porphyrins. The latter describe porphyrinoids with four heterocyclic rings which are connected in such a way that the porphyrin scaffold (porphyrin-like conjunction) is preserved. Today, chemists are able to exchange one or more pyrrolic units in the porphyrin skeleton, just like puzzle pieces in a jigsaw resulting in a whole zoo of core-modified porphyrins (Figure 2-5).

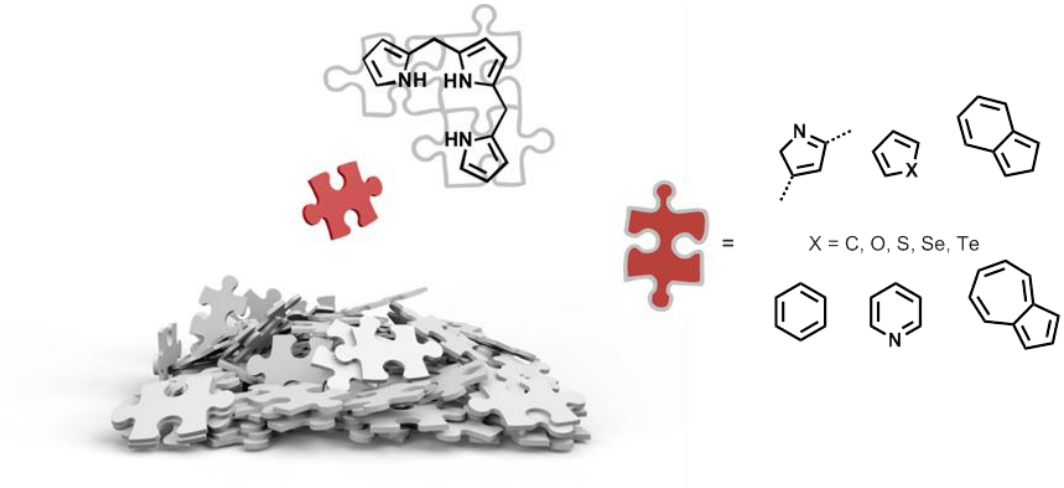

Figure 2-5: Schematic illustration of the porphyrin skeleton as a macrocyclic jigsaw with one piece exchanged. Possible building blocks resulting in hetero[3, 15-16]-, carba[30-31]- and N-confused[17-18] core-modified porphyrins.

The replacement of one or more pyrrole units in the porphyrin core results primarily in the control and tuning of the electronic properties. For example, heteroatom substituted porphyrins (**2-10**) exhibit quite different optical and metal-binding properties compared to regular porphyrins, caused by the introduction of chalcogenide atoms, such as O, S, Se or Te (Figure 2-6). They form stable complexes in unusual oxidation states[58] and large red shifts of the Soret and Q-bands in the visible spectrum are observed.[15] Additionally, the chemical properties are affected, *e.g.* an oxygen causes a pronounced electronic effect in the macrocyclic system due to its electronegativity and a sulfur atom perturbs the planar structure due to its steric bulkiness. *Meso*-unsubstituted heteroporphyrins are accessible through the "3+1" method and have first been reported by Broadhurst.[55, 59] On the contrary, for *meso*-tetraaryl heteroporphyrins the "3+1" method is not suitable and mostly Lindsey conditions are used.[53]

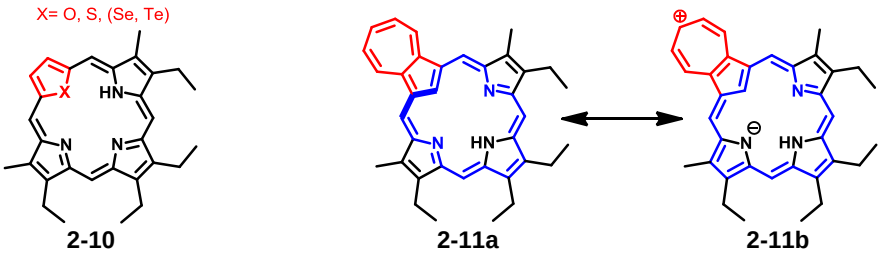

Figure 2-6: Heteroporphyrin **2-10**, cross-conjugated Azuliporphyrin **2-11a** and its dipolar resonance structure **2-11b**.

Azuliporphyrins (**2-11a**), members of the carbaporphyrins, exhibit only borderline aromaticity which is indicated by the absence of defined Soret bands in the UV-vis spectra (Figure 2-6).[60-61] The azuelene unit causes cross-conjugation in the system, which describes the interruption of the strict alternation of single and double bonds by two consecutive single bonds at each cross-conjugated point (Figure 2-6). Anyhow, the proton NMR spectrum gives evidence of the existence of a weak diatropic ring current with the internal CH appearing at $\delta = +1.5$ ppm. This shift was attributed to the combination of the 18π-electron aromaticity and the external tropylium character (Figure 2-6, **2-11b**).[62] *Meso*-unsubsituted azuliporphyrins are accessible by the "3+1" method,[62] whereas *meso*-tetraarylazuliporphyrins are readily available under Lindsey-type Rothemund reaction conditions.[53, 60]

If six-membered rings like benzene or pyridine are incorporated into the porphyrin skeleton, macrocyclic aromaticity can only take place if the six member rings are finessed to give up their resonance stabilization energy.[63-64] Hybrid structures where pyridine rings take the place of a pyrrole unit are called pyriporpyhrin. For the synthesis of pyriporphyrin[65] **2-12** and oxipyriporphyrin[66-68] **2-13** the "3+1" protocol has been successfully applied (Figure 2-7).

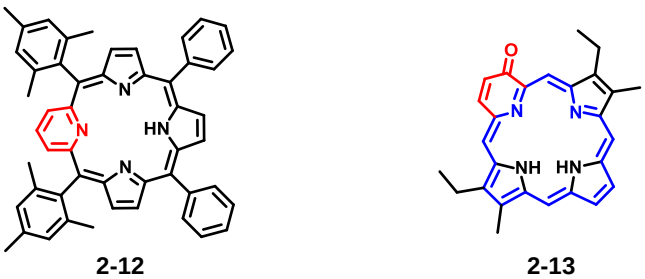

Figure 2-7: Pyriporphyrin[65] **2-12** and oxipyriporphyrin **2-13**.[66-68]

Compared to oxipyriporphyrin **2-13** where porphyrin-like aromaticity could be proven by NMR and UV-vis spectroscopy, the pyriporphyrin **2-12** does not possess a diamagnetic ring

current. The 18π-electron macrocyclic aromaticity can only be achieved by the loss of the resonance stabilization energy of the pyridine ring.[63] Furthermore, pyriporphyrins suffer from instability due to the surrounding *meso*-carbons at the pyridine moiety.[69-70]

The incorporation of benzene-fused pyrroles like carbazoles into the porphyrinic skeleton offers amongst others, the possibility to extend the π-conjugation. Carbazole-based materials have highly emissive and electron-conducting properties and offer good chemical stabilities.[71-72] Furthermore, they show excellent compatibilities with various transformations such as polymerizations and metal-catalyzed cross-coupling reactions.[73] Despite these characteristics, only few examples of carbazole-based porphyrinoids have been reported to date, which usually require different synthetic protocols than those for classical porphyrin syntheses described earlier (cf. chapter 2.1.1).

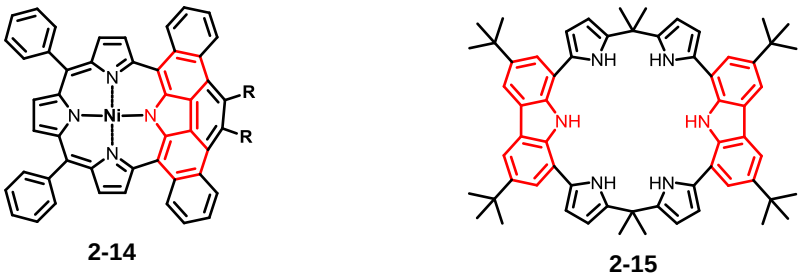

2-14 **2-15**

Figure 2-8: Picenoporphyrin[74-76] **2-14** and calix[4]pyrrole[2]carbazole **2-15**.[77]

Smith *et al.* reported the synthesis of a highly π-extended porphyrin (**2-14**) with fused benzene rings on one side of the tetrapyrrole macrocycle.[74] This was achieved by Bergman[78] aromatization of nickel-containing vicinal dialkynylporphyrin. The resulting compound **2-14** comprises a benzo-fused carbazole and was named "picenoporphyrin" in analoga with its [5]phenancene structure.[79]

Although not being a porphyrin but rather an expanded calixpyrrole, Sessler's calix[4]pyrrole[2]carbazole **2-15** is a nice synthetic example where two of the four acetone derived dimethylmethylene bridging subunits are replaced by carbazoles.[77] A palladium catalyzed Stille-type[80] cross-coupling reaction was used to attach pyrroles to the carbazoles. The pyrrole units were then reacted in an acid catalyzed condensation with acetone to close the macrocycle.

Very recently, Osuka *et al.* reported the carbazole-containing porphyrinoids **2-16** and **2-17** which were constructed by a multiple annulation strategy (Figure 2-9). By this, the authors were able to exchange two pyrrole units by carbazole resulting in porphyrinoid **2-16**. It has to be mentioned that the remaining pyrroles in **2-16** are substituted at the nitrogens and

thus do not serve for further coordination reactions. The authors claim that the deprotection of the pyrrolic nitrogen was unsuccessful.

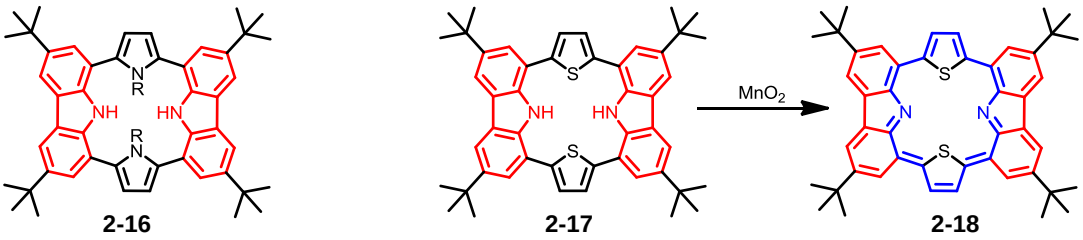

Figure 2-9: Carbazole-containing porphyrinoids **2-16** and **2-17** and core-modified porphyrin **2-18**.[35]

Furthermore, they were able to replace the remaining pyrroles by thiophenes affording compound **2-17**. Both carbazole-containing porphyrinoids, **2-16** and **2-17**, do not possess porphyrin-like aromaticity. Anyhow, thiophene-containing porphyrinoid **2-17** could be oxidized to core-modified porphyrin **2-18** which displays a remarkably intensified and red-shifted absorption spectrum that reaches the near infrared region as a result of its distinct aromaticity and expanded network.

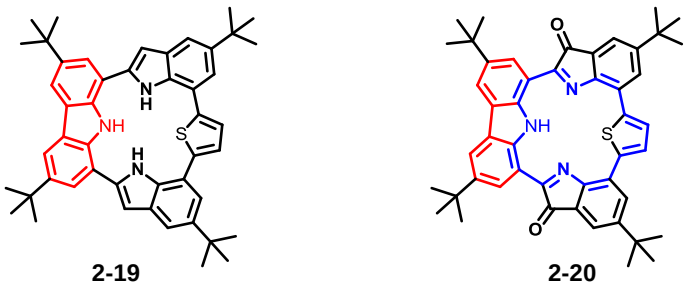

Figure 2-10: Carbazole-indolo-based porphyrinoids **2-19** and **2-20**.[81]

Recently, Yoshioka supplemented the class of benzo-fused porphyrinoids by compounds **2-19** and **2-20** (Figure 2-10), containing both carbazole and indolone moieties.[81] Hereby, metal-mediated syntheses were used for the construction of the macrocyclic core of porphyrinoid **2-19**. The subsequent oxidation afforded then compound **2-20** possessing a diamagnetic ring current. While porphyrinoid **2-19** exhibits absorption primary in the UV-vis region, the spectrum of compound **2-20** is extended to the visible region.

The electronic structure of porphyrins is not only susceptible to core variations but also to peripheral functional modifications, such as the introduction of π-conjugated segments

resulting in π-extended porphyrins.[3] Considerable attention has been given to the fusion of porphyrins and creating expanded π-systems with multi-metal sites.[82-84] For instance, one-dimensional fused oligoporphyrins are expected to be good conducting molecular wires, due to their ability to transfer electronic charge over macroscopically large distances.[26] Besides *meso-meso* ethyne-bridged[85] or *meso-meso* butadiyne-bridged[86] porphyrin arrays, directly fused porphyrins provide especially strong π-conjugation.[87-89] These planar, sheet-like structures are among the most promising scaffolds as advanced materials for applications such as photodynamic therapy,[24] non-linear optics[46] or organic semiconductors.[90]

The synthesis of *meso–meso* linked diporphyrins (**2-23**) can be achieved by the Ag^{I}-promoted oxidation of 5,15-diaryl substituted Zn(II) porphyrins (**2-21**) and the subsequent oxidative fusion reaction with DDQ/$Sc(OTf)_3$ (Figure 2-11).[91]

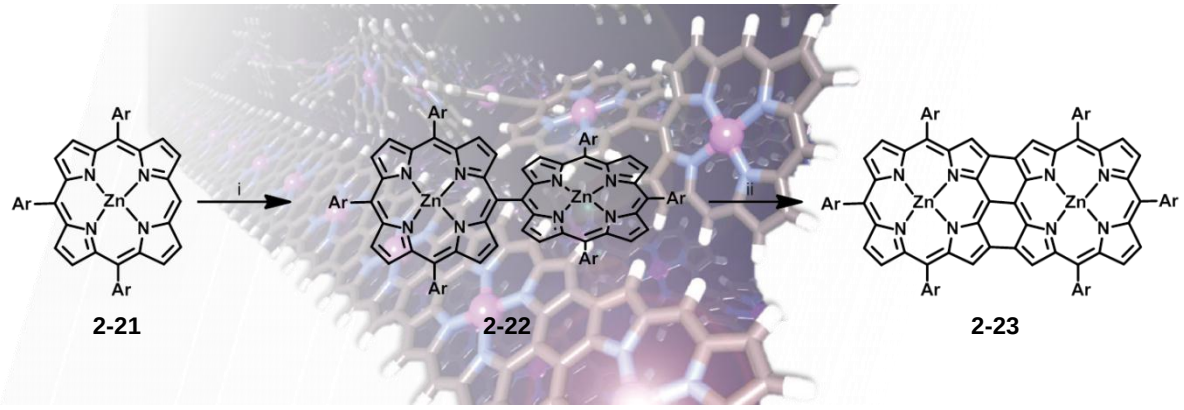

Figure 2-11: Synthesis of *meso-meso* linked diporphyrin **2-23**. Conditions: *i* Ag^{I}; *ii* DDQ/$Sc(OTf)_3$.[92]

By this method a variety of porphyrins with free *meso*- and *β*-positions can be converted into directly linked porphyrin arrays with exceptionally large π-delocalization and strong red-shifted absorption bands.[91, 93-95]

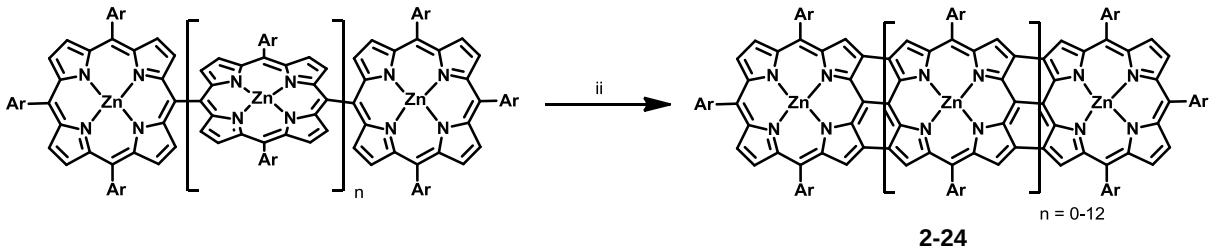

Scheme 2-4: *Meso-meso* linked porphyrin tape **2-24**. Conditions: *ii* DDQ/$Sc(OTf)_3$.[93]

For example, Osuka *et al.* showed that the bathochromic shift increases with the number of porphyrin moiety resulting in very low energy gaps (Scheme 2-4).[96] As an extreme case,

they were able to synthesize porphyrin tapes up to a 12-mer (**2-24**, Scheme 2-4) with an energy gap of only 0.19 eV.

Two-dimensional π-expanded tapelike porphyrin oligomers are challenging due to chemical instability and extremely poor solubility and have rarely been studied. Triple and tetrameric fused porphyrin can be achieved by applying the same synthetic approach described for linear olioporphyrin arrays and were first described by Osuka (Scheme 2-5).[84, 97]

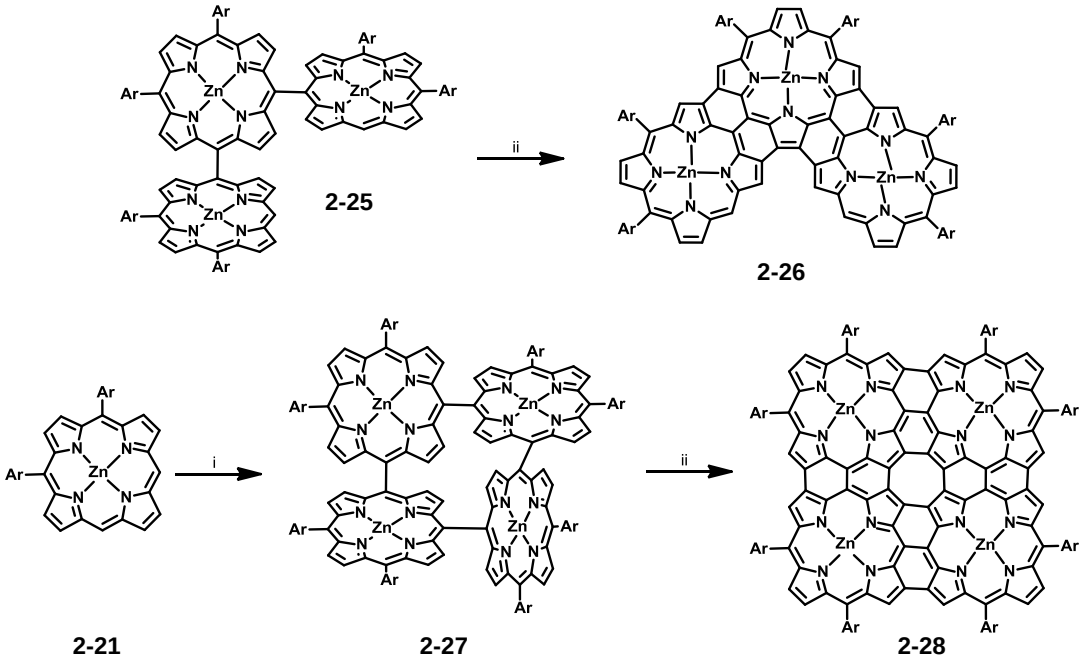

Scheme 2-5: L- and square-shaped porphyrin tapes. Conditions: *i* Ag^{I}; *ii* DDQ/$Sc(OTf)_3$.[84, 97]

Whereas the triple fused L-shaped porphyrin sheet **2-26** exhibits similar electronic and aromatic properties as the related linear trimer porphyrin tape (**2-24** with n = 1), the square-shaped porphyrin sheet **2-28** provides unique features ascribed to its central cyclooctatetraene (COT) segment. The COT is forced to be planar induced by the fused porphyrins and shows a paratropic ring current above the COT core evidenced by the downfield shifts of the guest proton coordinated to the square-shaped sheet.

Besides these extended porphyrin arrays for semiconducting applications, porphyrin complexes have been recognized also to be promising candidates as alternatives to platinum-based cathode catalysts for the oxygen reduction reaction (ORR) in a fuel cell.[98] Due to the significance for this work a brief introduction of fuel cell technology is given in the following chapter along with the various types of novel non-precious metal catalysts for the ORR.

2.2 N_4-macrocyclic metal complexes as catalysts for ORR

2.2.1 History and principle of a fuel cell

Sir William Robert Grove described already in 1839 the principle of a fuel cell,[99] and was therefore named the pioneer of fuel cell technology (Figure 2-12). The Grove cell was an early electric primary cell and consisted of a zinc anode in dilute sulfuric acid and a platinum cathode in concentrated nitric acid, the two separated by a porous ceramic pot (Figure 2-12). Almost no further research was done on this new technology until the NASA used a fuel cell as a self-sustaining energy source for the Gemini Program. The Gemini Program was the second human spaceflight which primarily tested equipment and procedures for the future Apollo missions. Today, fuel cells are among the most promising technologies for the transition to a hydrogen-based economy.

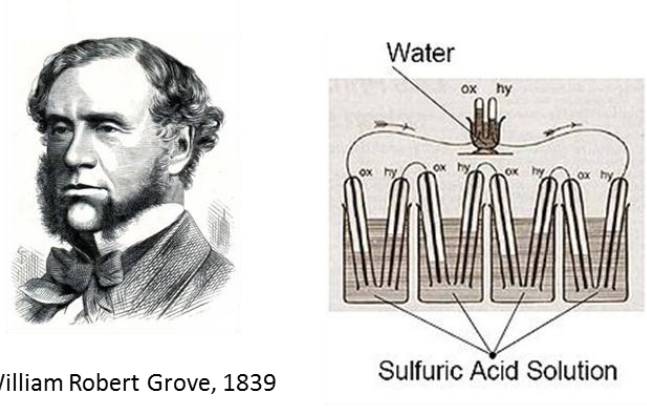

Sir William Robert Grove, 1839

Figure 2-12: The pioneer of fuel cell technology Sir William Robert Grove and its Grove cell.

Fuel cells have already been applied in practice for transportation, portable uses and stationary installations. For example, zero-emission fuel cell vehicles have environmental and economic advantages, since they will have similar range and performance to cars with internal combustion engines, but a significant reduction in carbon dioxide, a greenhouse gas. Fuel cells can also compete with batteries and generators for portable use. Prototypes of fuel cell powered mobile phones and laptops have already been exhibited at the World Expo 2005 in Japan. Fuel cells can also provide electric power for homes and offices. The heat produced by the cell can be circulated just like in applications with conventional heating systems. Some examples have been already applied to power hospitals and industrial plants.

A fuel cell generates electrical power by converting the chemical energy of a fuel into electrical energy by an electrochemical reaction without combustion (Figure 2-13). Fuel

cells typically utilize hydrogen as the fuel and oxygen (from air) as the oxidant. The reaction results in electricity, water and heat.

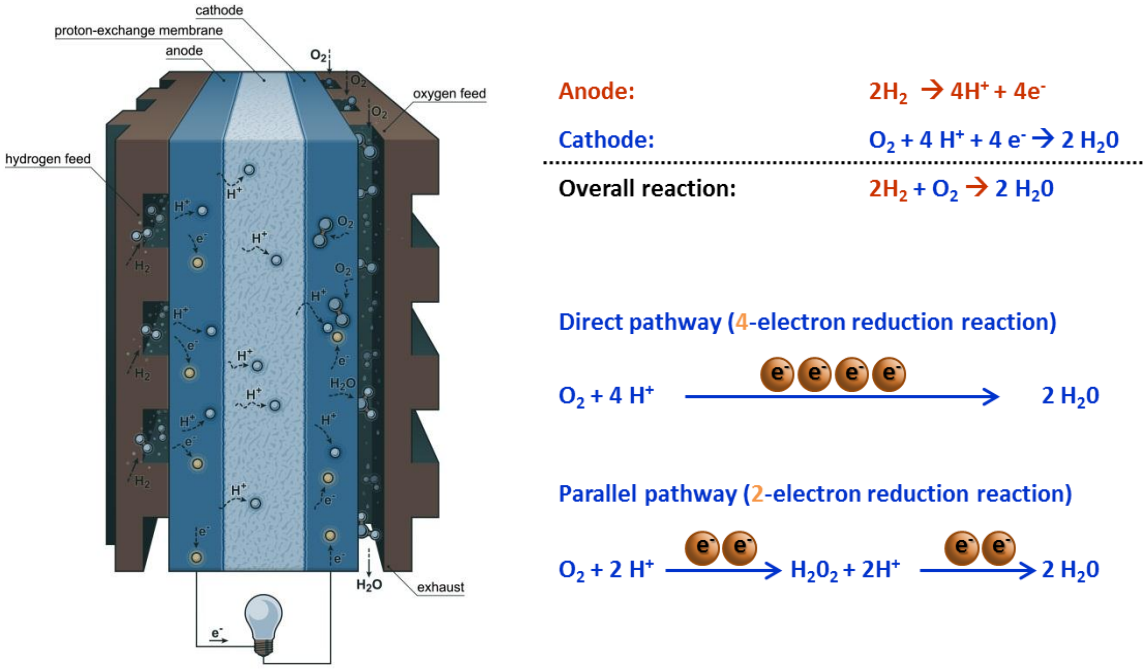

Figure 2-13: **a:** Schematic illustration of a fuel cell and **b:** the overall reduction reaction from oxygen to water and the direct and parallel pathway at the cathode.

The basic cell consists of two electrodes, the anode and the cathode, separated by an electrolyte membrane. Each of the electrodes is coated on one side with a catalyst (most commonly platinum). The contact unit comprising electrolyte, catalyst and electrodes is called membrane electrode assembly (MEA). Hydrogen fuel is fed into the anode while air enters through the cathode. In the presence of the catalyst, the hydrogen molecule splits into two protons and two electrons. The electrons flow through an external circuit creating an electrical current. The protons are transported through the electrolyte membrane and combine at the cathode with the electrons and oxygen from the air to form water and generate heat as a by-product. Overall, oxygen is electrochemically reduced to water, hereby two pathways are possible. Complete reduction (direct four-electron pathway) generates 2 eq of water, whereas the partial reduction (parallel two-electron pathway) yields hydrogen peroxide, a harmful by-product (Figure 2-13b).[100] Hydrogen peroxide can damage the internal components of a fuel cell, therefore oxygen-reduction electrocatalysts are engineered in such a way as to limit the amount of peroxide formed.

There are several different types of fuel cells but all work in the same general manner. The most considered type is the polymeric-electrolyte-membrane fuel cell (PEMFC), which contains platinum catalysts and most commonly Nafion (by DuPont) as an electrolyte membrane. PEMFCs can start up fast and operate at near ambient temperatures. They have been recognized as a potential future power source for zero-emission vehicles.[101-102] Furthermore, the alkaline (AFC) and the phosphoric-acid fuel cells (PAFC) are under active development. Those fuel cells request relatively pure hydrogen, and thus the use of hydrocarbon or alcohols as a fuel requires an additional fuel processor, causing additional costs. High temperature fuel cells like, molten-carbonate fuel cells (MCFC) or solid-oxide fuel cells (SOFC) have the advantages that the CO and H_2 can be electrochemically oxidized at the anode.

Although many improvements in reliability have been made to implement a "hydrogen economy", the scenario is impeded by technical and economic difficulties.[101] One of the main barriers to overcome is the large-scale production of hydrogen. Nowadays, the cheapest technology is the steam reforming of natural gas which produces significant emissions of greenhouse gases.[103] Beyond that, the costs for fuel cells are still high and therefore widespread commercialization is limited.[104] Active research to reduce costs and increase efficiencies for all components in a fuel cell is ongoing. Besides the development of new ion conduction membranes and optimization of bipolar plates and cell frames, especially the heart of a fuel cell, the electrocatalysts is under active development. Major drawbacks in catalyst performance are the cathode catalyst oxidation, carbon monoxide deactivation, catalyst migration, loss of electrode active surface and also corrosion on the carbon support.[105] The currently used platinum (Pt) based catalysts are most promising but one of the major cause for high cost.[106] Although ideally, both fuel cell electrodes should be considered, the substitution of the cathode catalyst with less expensive materials will result in a significantly greater reduction of Pt needed. This is due to the slow oxygen reduction reaction (ORR) at the cathode requiring much more Pt compared to the fast anodic hydrogen oxidation. The cathode suffers from relatively sluggish ORR kinetics and therefore high overpotential which limits the performance of the fuel cell. Therefore, the reduction in the amount of noble-metal without degrading the cell performance for example by alloying Pt with inexpensive metals and the support of nanoparticles of platinum on a carbon materials have been, and continue to be, important research and development activities.[107-109] Recently, non-precious metal catalysts (NPMCs) have attracted enormous interest as an alternative to platinum-based catalysts for ORR.[105] This includes amongst

others nickel, cobalt, iron, copper, chromium and tin. Those metals are usually supported on carbon materials (M-N_x/C) formed by pyrolysis of a variety of metal, nitrogen and carbon precursor.[104] On the other hand, those metals are generally employed in the form of metal complexes such as chalcogenides, transition metal oxides or nitrides and macrocycles (porphyrins and phthalocycanines).[110] Amongst those, metal porphyrins, with cobalt or iron, have been viewed as most promising precursors, due to their similarity to the mammalian fuel cell, *cytochrome c oxidase*, which catalyzes the complete four-electron conversion of oxygen.[98] Other non-precious metal electrocatalysts materials include conductive polymer based complexes as well as enzymatic based electrode materials.[111]

The catalytic activity of cobalt phthalocyanine, a porphyrin related macrocycle, towards the ORR has been discovered by the pioneering work of Jasinski in the early 1960s.[112] The catalytic activity of metal macrocyclic compounds is suggested to arise from the redox potential of M(III)/M(II) of the metals, where M(II) is the active site.[98] The complexes need to be supported on a conducting support, like carbon or graphite materials. The major drawback of these complexes, being its low stability and activity, can be improved by thermal treatment which was discovered by Jahnke *et al.*[113] Pyrolysis is mostly believed to yield MN_4-motifs as the active sites but is still not fully understood.[114-117] N_4-macrocyclic metal complexes are interesting not only due to their lower costs but also due to their high tolerance to methanol, for the case of methanol fuel cell application.

The catalytic activity, though, is sensitive to the structure of the ligand and the nature of the metal center. While simple iron and manganese phthalocycanines (**2-29**) promote the four electron reduction, cobalt and nickel phthalocycanines (**2-30**) reduce oxygen only by a two-reduction pathway (Figure 2-14).[118]

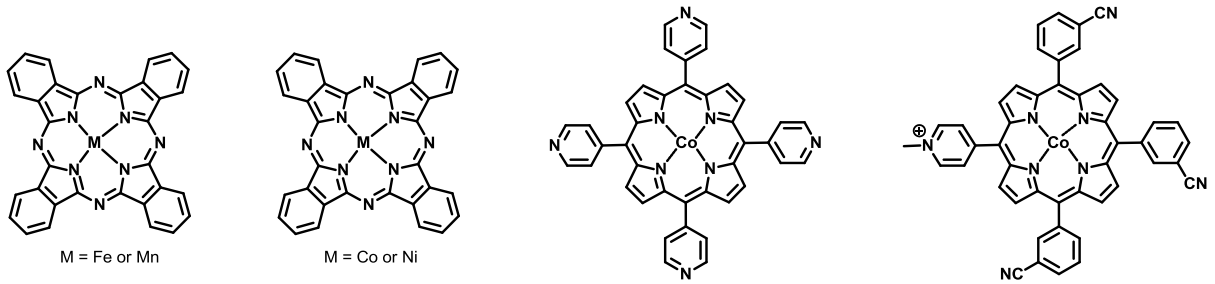

2-29 4-electron pathway

2-30 2-electron pathway

2-31 2-electron pathway

2-32 4-electron pathway

Figure 2-14: Examples of NPMCs for ORR.

Two electron-catalysts such as cobalt porphyrin[119-121] **2-31** can be converted to four-electron catalysts by the introduction of substituents in the periphery to increase the electron back-bonding (**2-32**, Figure 2-14).[122] On the other hand, the manner of interaction between the oxygen and the active site is also an important aspect. The reduction of oxygen involves the rupture of the O-O bond and can possibly happen by the interaction of the metal center of the macrocycle and O_2 with one side (end-on or side-on) or simultaneously with two sides (bridge-*cis* or bridge-*trans*, Figure 2-15). Platinum reduces oxygen almost exclusively *via* the four-electron pathway and a bridge-*cis* type interaction is being suggested since the Pt-Pt separation in certain crystallographic orientations is optimal.[123] As a result, the four-electron reduction is favored by the simultaneous dual-site mechanism.

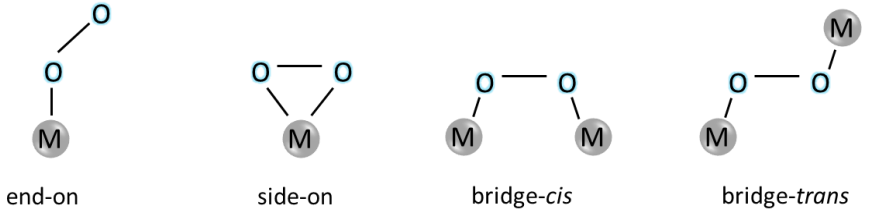

Figure 2-15: Different configuration for molecular oxygen when it interacts with the active sites.

In this regard, cobalt macrocyclic complexes comprising two cobalt centers have been designed with metal-to-metal distance which favors the interaction of dioxygen with both active sites. Chang and Collmann pioneered the development of Pacman porphyrins (such as **2-33** and **2-34**),[124-125] having a face-to-face geometry which allows the binding of O_2 within the "bite" of the cofacial cleft in a bridge-*trans* type (Figure 2-16). The optimal Co-Co distance for Pacman porphyrins to promote the direct four-electron reduction was found to be 4 Å.[126] It is worth mentioning, that those systems promote the four-electron reduction only in acid media.[122]

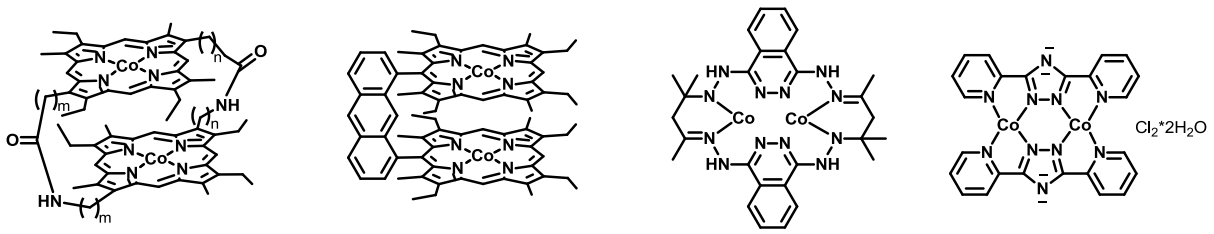

2-33 **2-34** **2-35** **2-36**

Figure 2-16: Examples of dinuclear NPMCs for ORR.

On the other hand, only few planar dinuclear complexes such as **2-35** or **2-36** (Figure 2-16) have been synthesized but reduce oxygen *via* four electrons in alkaline media.[127] Here, the oxygen adopts the same bridge-*cis* type configuration as it is in Pt, nevertheless, those complexes suffer from instability.

Although many efforts involving the design of novel ligands,[112] molecular decoration with functional groups[128] and post-heating treatment[104] have been made, limitations regarding catalytic activity, selectivity, stability and sustainability still exist. The actual activity of the most active non-precious metal catalysts is still well below the United States Department of Energy (DOE) 2015 target.[111] Also the lifetimes are far shorter than targets in DOE 2015.

Important tools employed in the study of the electrocatalytic activity towards ORR are the **r**otating **d**isk **e**lectrode (RDE) and the **r**otating **r**ing **d**isk **e**lectrode (RRDE) techniques and therefore, their basics will be introduced in the following.

2.2.2 Rotating Disk Electrode - RDE

The electrocatalytic ORR can be studied by rotating disk voltammetry (Figure 2-17a). The rather simple three electrode system contains a disk electrode embedded in an insulating material. The disk electrode representing the working electrode is generally made of noble metal or glassy carbon.

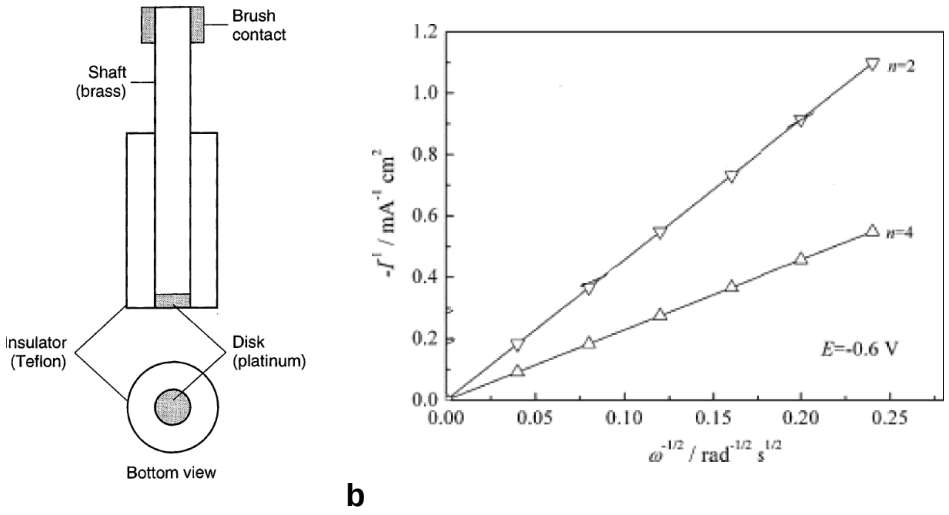

Figure 2-17: **a:** Schematic illustration of RDE;[129] **b:** Koutecky–Levich plots at −0.6 V for the theoretical slopes calculated assuming the 2- and 4-electron processes for the O_2 reduction.[130]

To scan the electrode potential, the water insoluble catalyst is deposited on the disk electrode as a film and then immersed to aqueous electrolyte. The rotation causes a flow of electrolyte to the electrode, bringing the reactants to the catalyst.

The selectivity of the catalysts is often represented as the average number of electrons *n* delivered to an O_2 molecule. The number of electrons transferred can be determined from Koutecky-Levich plots (Figure 2-17b). Here, the inverse disk current (J^{-1}) is plotted *vs.* the inverse square root of the rotational frequency ($\omega^{-1/2}$) resulting in a straight line if the reaction is reversible. The kinetic parameters can then be analyzed on the basis of the Koutecky-Levich equations (2-1 to 2-3):

$$\frac{1}{J} = \frac{1}{J_L} + \frac{1}{J_K} = \frac{1}{B\omega^{1/2}} + \frac{1}{J_K} \qquad (2\text{-}1)$$

$$B = 0.62\, nFC_0(D_0)^{2/3}\upsilon^{-1/6} \qquad (2\text{-}2)$$

$$J_K = n\, FkC_0 \qquad (2\text{-}3)$$

where J is the measured current density, J_k the kinetic current density, J_L the diffusion current density, n the number of electrons transferred, k the rate constant, F the Faraday constant, ω the disk rotation speed, C_0 the bulk O_2 concentration, D_0 the O_2 diffusion coefficient and υ the solution kinematic viscosity. According to this equations the number of electrons transferred n (and the kinetic limiting current density J_k) can be obtained from the slope (and intercept) of the Koutecky-Levich plots. Limitations for the investigation of the reactivity of the products arise, since the products are continuously swept away from the electrode. In contrast, the rotating ring disk electrode (RRDE) is well suited to investigate this further reactivity.

2.2.3 Rotating Ring Disk Electrode - RRDE

The RRDE is a double working electrode in which the disk electrode is surrounded by a concentric second working electrode, the ring electrode (Figure 2-18). In order to prevent a short circuit between disk and ring both electrodes are separated by a thin isolating ring. The rotation causes the electrolyte to be catapulted from the disk electrode to the ring electrode. Products forming on the disk electrode are thereby transported to the ring electrode and can there be identified electrochemically. For example, the ring electrode can

be set to a constant potential acting as an amperometric sensor for peroxide. Zero ring currents would mean no peroxide generation in the reaction. This is important for the characterization of the fundamental properties of electrocatalysts used in fuel cells specially to interpret if the reduction follows the two- or four-electron reduction pathway.

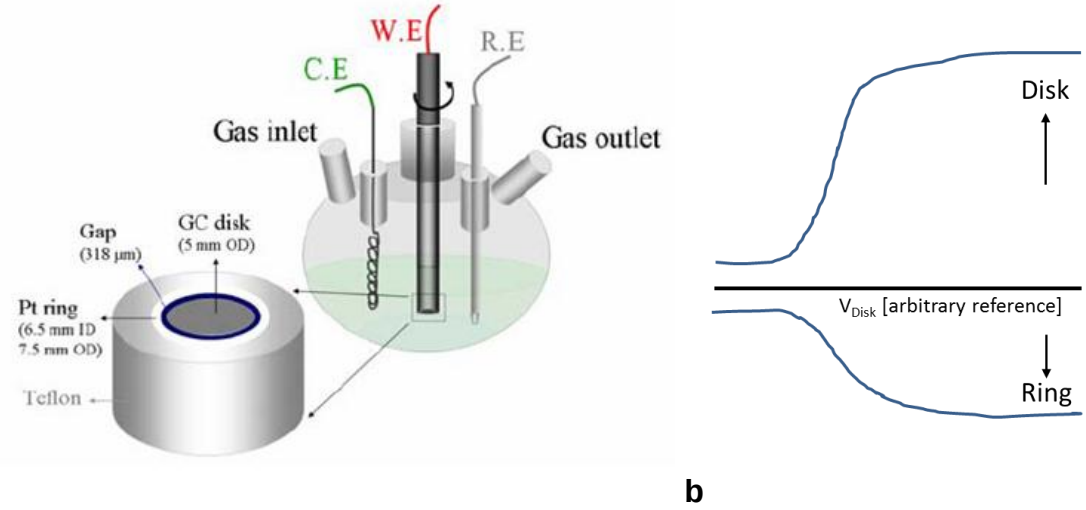

Figure 2-18: Schematic illustration of **a:** a RRDE and **b:** ring-disk voltammograms.

The average number of electron transferred (n) is hereby obtained from the ring-disk current ratio (received from the ring-disk voltammograms, Figure 2-18), if the collection efficiency N of the ring towards H_2O_2 is known:

$$n = \frac{4I_D}{(I_D + \frac{I_R}{N})} \qquad (2\text{-}4)$$

where N is the collection efficiency, I_D the faradic disk current and I_R the faradic ring current. The percentage of peroxide released in the reaction can then be determined by

$$\%H_2O_2 = \frac{100(4-n)}{2} \qquad (2\text{-}5).$$

3 Motivation and Objectives

Although the history of porphyrin chemistry had its beginnings in the late 19th century, this field of research has not lost any of its attractions. Nowadays, still numerous publications are released, predominantly on the modification of the porphyrin core and the thereof resulting properties. Since the late 20th century, aryl chemistry was promoted by a new family of aryl-aryl bond-forming reactions based on transition-metal catalysts.[131-132]
In this regard, the research described in this work aims for the design and synthesis of new porphyrinoids with the aid of contemporary synthetic protocols. Furthermore, the properties of the obtained porphyrinoids are scrutinized in the view of their potential applications such as metal complexing agents, receptors for anion sensing or electrocatalysts for the reduction of oxygen.

The first part of the present work focusses on the modification of the porphyrin core. A porphyrin consists of two pyrrole and pyrrolenine units each, which shall be schematically exchanged by other heterocycles (Figure 3-1a). Hereby, the formation of the macrocycles will be realized by direct aryl-aryl bond coupling of small aromatic building blocks. To replace the pyrrole units, carbazole is particularly qualified since it provides the pyrrolic NH motif together with the ability to create a similar ring size to that of a porphyrin, when using 1,8-disubstituted derivatives. The benzene annulation additionally enhances not only the stability but also the acidity[133-134] of the NH-moiety, which will be beneficial for the use of the resulting macrocycle *e.g.* as metal complexing agent or anion receptor.
On the contrary, the pyrrolenine units will be exchanged by various heterocycles, in particular pyridine, pyrrole or triazole, for reasons which will be explained in detail in the following (Figure 3-1b).

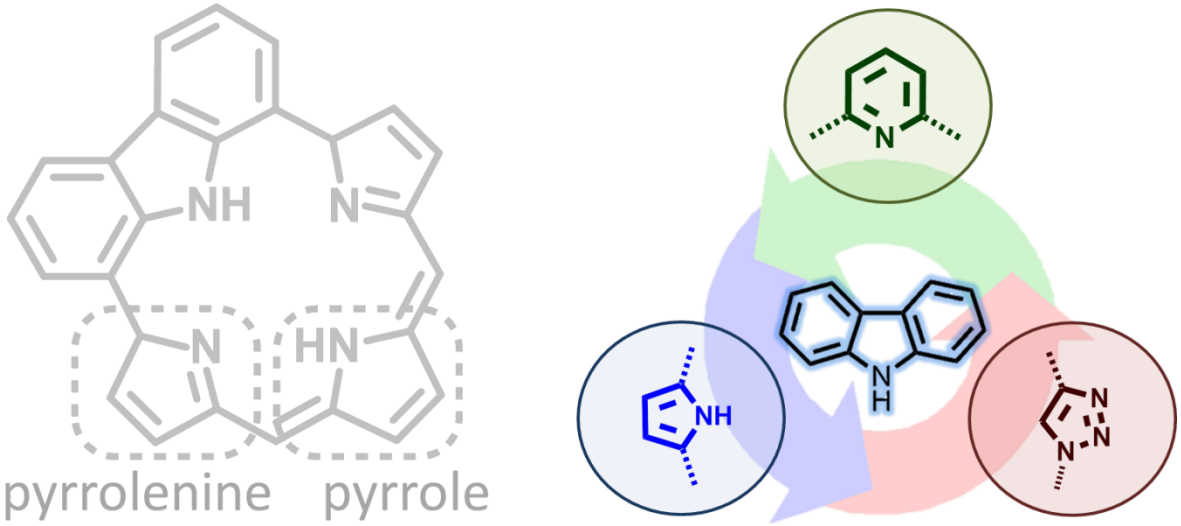

Figure 3-1: **a:** The structure of porphyrin with the schematic illustration of the replacement of one pyrrole unit by carbazole; **b:** building blocks used for the planned modifications of the porphyrin core.

- The obvious conception to firstly mimic the *trans*-NH-tautomer of porphyrins requires a heterocycle offering an imine-type nitrogen, similar to the pyrrolenine moieties. In respect to this nitrogen pattern, the first complement to the carbazole will be pyridine (Figure 3-1b, green). By combining these two aromatic building blocks a porphyrin-like macrocycle without unstable methine-bridges will be formed. The resulting properties will give valuable insights into this new class of core-modified porphyrins when compared to regular ones. To achieve the demanding aim, the use of a Suzuki-Miyaura[135] coupling will be considered.
- As a second target, the $(NH)_4$ cavity of related calixpyrrole[136] shall be imitated. Calixpyrroles are well known for their unusual metal binding[137] and their excellent anion recognition ability.[138] This will be achieved by the replacement of the pyrrolenine units with pyrroles but retain the carbazoles (Figure 3-1b, blue). If the pyrroles are connected to the carbazoles *via* aryl-aryl bonds, they are not able to adopt the pyrrolenine conformation and the $(NH)_4$ pattern will remain. Additionally, the new $(NH)_4$ macrocycle omits sp^3 hybridized carbon atoms in contrast to calixpyrroles.
- Finally, additionally to the NH bond donor units of the carbazole, CH bond donor moieties shall be introduced into the porphyrinic core. Compared to the well-known halide binding properties of NH[138-140] bond donors, the successful use of CH[141-142] bond donor motifs for halide binding in preorganized receptors has only been proven recently. The CH motif will be achieved by the creation of triazoles (Figure 3-1b, red) at

the place of the pyrrolenine units, by the use of a Huisgen's[143] copper catalyzed 1,3-dipolar cycloaddition (CuAAC). On the contrary to the introduction of pyridine and pyrrole, here two carbazole derivatives will be "clicked" together to generate the triazoles and the macrocyclic core. The emerging porphyrinoid will be the first example of a macrocycle comprising NH bond (carbazoles) and CH bond donor units (triazoles) for halide binding.

Within the scope of this work, the syntheses, the study of the properties along with possible applications such as metal complexing agent or anion receptor, will be covered. The herein developed synthetic designs shall guide future development of new porphyrinoids based on contemporary synthetic protocols.

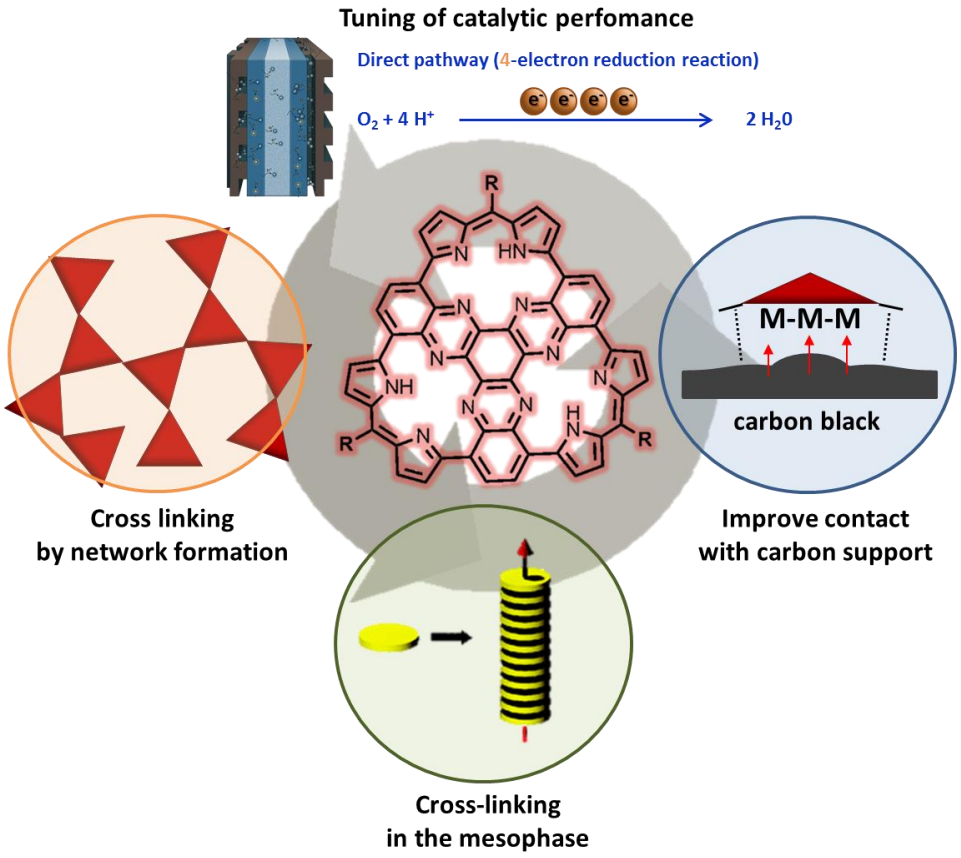

Figure 3-2: Schematic illustration of the considered strategies to improve catalytic activity of the triangular trinuclear compound.

The second part of the present work aims for the extension of the porphyrin π-system, rather than its core-modification. This research is inspired by the emerging interest in the field of non-precious metal catalysts for the reduction of oxygen (ORR) in fuel cells. Hereby, the development of N_4-macrocyclic metal complexes is currently directed to the design of

metal complexes providing multiple active sites to ensure the promotion of the desired direct 4-electron reduction of oxygen to water (cf. chapter 2.2). In this regard, the *Müllen* group has developed an unprecedented triangular trinuclear complex which showed good preliminary results in an electrocatalytic evaluation towards ORR (Figure 3-2).[144] Based on these results, the present work aims for the improvement of the performance by the modification of the triangular molecule in the sense of selective substituent adjustment. The concept towards the tuning of the catalytic activity presented herein is based on the following considerations (Figure 3-2):

- Increasing the density of active sites by cross-linking of the molecules through heat treatment in the mesophase. Consequently, long alkyl side chains which enable mesophase formations shall be introduced at the trinuclear core. 2D-WAXS techniques will be used to investigate the supramolecular organization dependent on the substituents, to gain insights into structure-performance relationships in order to improve the catalytic activity.
- Secondly, the accumulation of the active sites by covalent connection of the triangles will be taken into consideration. For this reason, substituents which are able to undergo further synthetic transformations will be attached in the periphery and will lead to non-directed network formation.
- Finally, an enhancement of the contact between the carbon support and the catalyst is expected to further tune the catalytic performance. In this regard, the introduction of substituents which will beneficially affect the interaction with the carbon support by adsorption will be considered.[145]

Within the frame of work the synthetic issues, the electronic properties as well as the self-assembly behavior of the different derivatives will be studied. Preliminary results of the catalytic evaluation will be given as well. The findings presented herein will be helpful to gain a more thorough understanding of the potential of such materials and to elucidate the relationship between the catalyst's performance and molecular and/or supramolecular properties.

4 Monocyclic Porphyrinoids containing Carbazole

In this part of the present work the goal was to design porphyrinoidic macrocycles *via* aryl-aryl bond formation with a similar ring size to that of a porphyrin. Therefore, the palladium-catalyzed Suzuki-type[135] cross-coupling and the copper(I)-catalyzed azide-alkyne cycloaddition (CuAAC)[146] were considered. The design concept is based on the modification of the porphyrin skeleton by replacing the pyrrole units by carbazole and the pyrrolenine units by heterocycles such as pyrrole, pyridine or triazole (Figure 4-1).

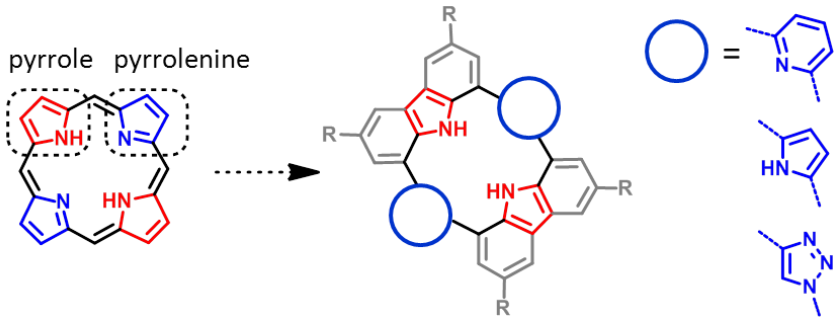

Figure 4-1: Modifications of porphyrin macrocycle by replacing pyrrole and pyrrolenine units by carbazole and pyridine, pyrrole or triazole, respectively.

Carbazole was chosen due to its close relation to pyrrole since it is formally deduced from it by attaching two benzenes and hence also denoted as dibenzopyrrole. Carbazole is an electron rich, rigid and fully aromatic heterocycle with a good chemical and environmental stability. Upon conjugation with benzene rings not only the stability is enhanced but also the acidity of the proton at the nitrogen (pK_a (pyrrole) = 23.0, pK_a (carbazole) = 19.9 in DMSO).[133-134] The more acidic the NH, the better is its hydrogen bond-donating and deprotonation ability, which can be useful in further application *e.g.* as metal complexing agent or as receptor for anions.

Carbazole is isolated from the anthracene fraction of coal tar,[147-148] and thus a cheap starting material (33.3 € per 100g ; CAS: 86-74-8, Sigma-Aldrich).[149] Furthermore, it is able to bind metals in its deprotonated form,[150] which enables the insertion of metals into

the cavity of the macrocylce for further applications *e.g.* in catalysis. To achieve a ring size similar to that of a porphyrin, 1,8-difunctionalized carbazole derivatives are required. These derivatives offer an almost perfect angle to maintain a porphyrinic skeleton (Figure 4-2b). On the contrary, the larger angle between positions 2 and 7 is better suitable for greater macrocycles[151] or conjugated polymers.[72-73]

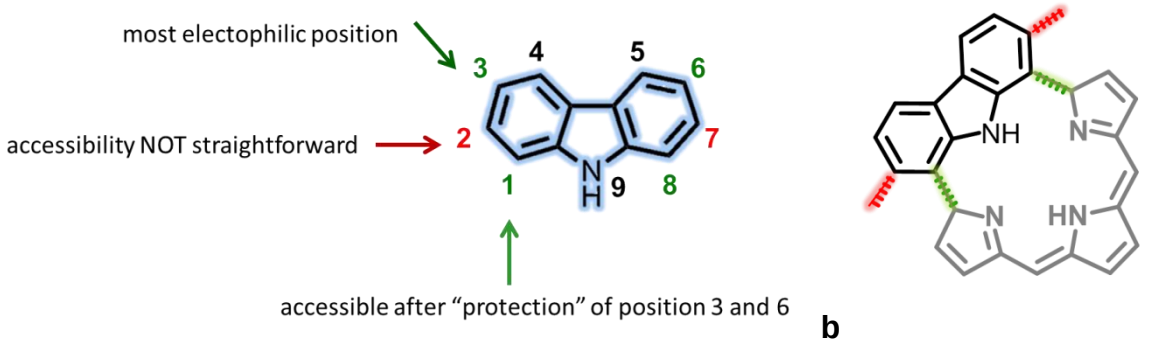

Figure 4-2: **a:** Carbazole structure and numbering; **b:** similar ring size to that of a porphyrin is only possible with 1,8-disubsituted carbazole derivative.

When developing a synthetic strategy for a new molecule with potential applications, the synthesis should be as easy, inexpensive and efficient as possible. In this sense, 1,8-disubtituted carbazole derivatives are easily accessible by the halogenation of 3,6-disubsituted carbazoles.[152] Nevertheless, positions 3 and 6 need to be blocked because they are the most susceptible to an electrophilic attack (Figure 4-2).[72] Alkyl groups are suitable protection groups, since they can be introduced at the 3,6-positions on the already formed carbazole by standard Friedel-Crafts alkylation.[153-154] Protocols for electrophilic aromatic substitutions to introduce bromine or idodine at the 1,8-positions are well described in the literature (Scheme 4-1).[152, 155]

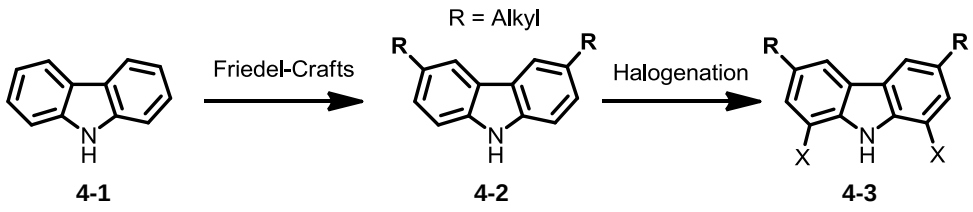

Scheme 4-1: Straightforward two-step synthesis towards 1,8-dihalogenated-3,6-dialkylated-carbazoles **4-3**.

On the contrary, the more popular 2,7-disubsituted relatives are usually prepared by strategies involving biphenyl precursors and Cadogan[156-158] ring closure reaction (Scheme 4-2).[159] Starting from the bare carbazole, positions 2 and 7 cannot directly be

functionalized by standard electrophilic aromatic substitutions since they are in *meta* position to the amino group and thus inactive. 2,7-Disubsituted carbazoles gained considerable recognition in the field of conjugated polymers over the last decades, since they are promising candidates in organic electronic devices.[72]

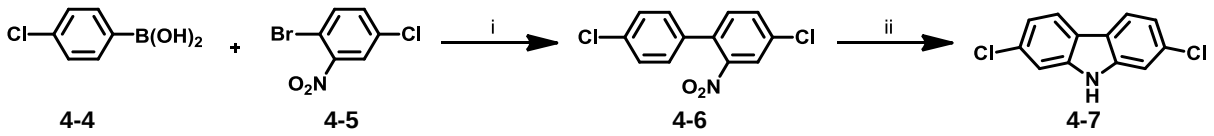

4-4 4-5 4-6 4-7

Scheme 4-2: Synthesis of 2,7-dichloro carbazole **4-7** including Cadogan ring closure reaction. Conditions: *i* $Pd(PPh_3)_4$, K_2CO_3, benzene, reflux, 2h; *ii* $P(OEt)_3$, reflux 5h.

Consequently, 1,8-disubsituted carbazole derivatives not only provide the perfect angle for the targeted ring size similar to a porphyrin but also fulfill the requirement of a straightforward and inexpensive synthesis.

For the present case, *tert*-butyl groups were chosen as protecting substituents (positions 3 and 6) due to their stability in the following synthetic transformations and their bulkiness preventing aggregation of the formed macrocycle. Furthermore, they help to render the conformationally rigid macrocycle soluble in common organic solvents under ambient conditions and provide the feasibility to form crystals for possible X-ray studies.

To mimic the most favored *trans* NH- tautomer of porphyrins, firstly, pyridine was chosen to represent the imine-type nitrogen. Later, pyrrole and triazole were introduced instead of pyridine (see chapter 4.2 and 4.3). Although pyridine is an electron deficient moiety, it can act as a good Lewis base due to the availability of the nitrogen lone pair electrons. Suzuki-Miyaura[135] cross-coupling reaction was used for the macrocyclization, therefore a brief introduction to this method is described in the following.

4.1 Building macrocycles *via* Suzuki cross-coupling reaction

Since the early 1970s,[160-161] carbon-carbon bond formation methods have received significant attention.[162-163] The most important among them are unambiguously transition metal catalyzed cross-coupling reactions. These transformations have become important key steps in the synthesis of natural products, biologically active molecules, drugs and agrochemicals.[131, 164] Moreover, they facilitate the construction of building blocks in supramolecular chemistry, organic materials and polymers.[165-166] In this respect, the Suzuki-Miyaura coupling has become one of the most popular cross-coupling reactions. This is not astonishing, since the Suzuki-Miyaura reaction proceeds under mild reaction conditions and a variety of boronic acids or esters are nowadays commercially available. Besides this, they are environmentally safer than other organometallic reagents, and boron-containing sideproducts are easy to handle. The reaction tolerates an array of functional groups. The original Suzuki reaction was first published by Akira Suzuki[167-168] in 1979 and reported the coupling of alkenyl boronates with alkenyl bromides. This was further developed to the reaction between phenylboronic acid with haloarenes under the conditions which are known today as the Suzuki-Miyaura reaction (Scheme 4-3).[135] The tremendous impact of this cross-coupling reaction on organic chemistry was honored by the Nobel Prize in Chemistry in 2010. Akira Suzuki received jointly with Richard F. Heck and Ei-ichi Negishi the price for "*palladium-catalyzed cross couplings in organic synthesis*".[169]

Generally, the Suzuki-Miyaura reaction is the intermolecular cross-coupling between an organoboron compound and an organic electrophile, catalyzed by a palladium complex in the presence of a base (Scheme 4-3). The electrophile can be an aryl, vinyl or alkyl halide/pseudohalide and the nucleophile a boronic-acid or -ester. The mechanism of the Suzuki-Miyaura cross-coupling reaction is comprised of 3 major steps: the oxidative addition (I), the transmetallation (IV) to form an organoboron intermediate and finally the reductive elimination (V) and regeneration of the catalyst (Scheme 4-3). The base is needed to form the active catalyst species (II) and also to activate the organoboron to provide the wherewithal tetravalent boratom (III). Many examples of shape-persistent macrocycles using the Suzuki-Miyaura coupling have been reported.[170] The most successful approaches are the intramolecular ring closure of an AB-disubstituted oligomer or the one-pot intermolecular coupling of A2 and B2 building blocks (Figure 4-3).

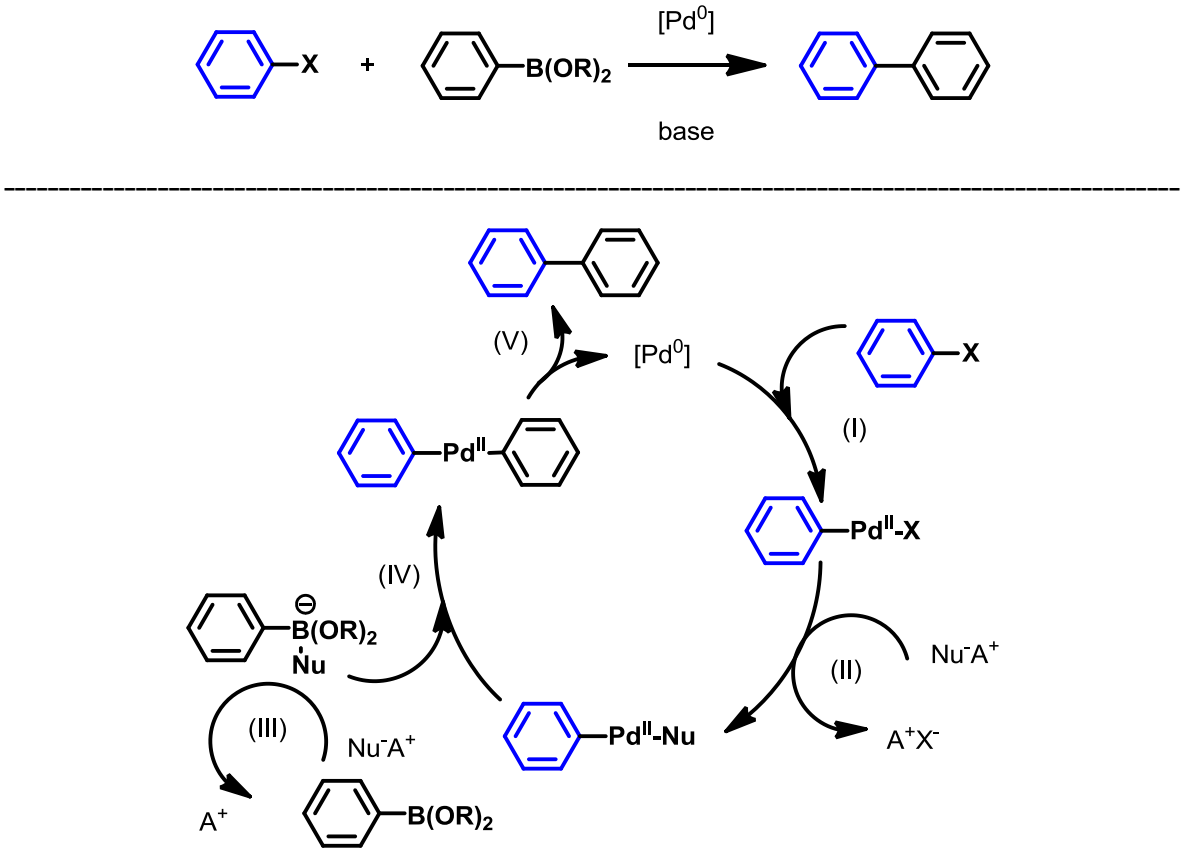

Scheme 4-3: Schematic illustration of the Suzuki-Miyaura reaction and its mechanism: oxidative addition (I); transmetallation (IV); reductive elimination (V).

Schlüter *et al.* pioneered the synthesis of phenylene-based shape persistent macrocycles such as compound **4-8**[171] and even larger cycles by using the AB-oligomer method (Figure 4-3). The one-pot approach has been successfully applied to build a variety of macrocycles like **4-9**,[172] **4-10**,[173] **4-11**,[174] or **4-12**[175] (Figure 4-3). Macrocycle **4-9**, which can be addressed as two phenothiazines embedded into a cyclophane topology, could be obtained in 13% *via* the Suzuki-Miyaura reaction.[172] Carbazole-containing macrocycle **4-10** was synthesized by the coupling of 3,6-dibromocarbazole (monomer A2) and diboronic pinacol ester (monomer B2) in yields between 16-67% using the catalyst-transfer Suzuki-Miyaura cross-coupling (CTSMCC).[173, 176] Shape-persistent cycle **4-11** comprising two opposing terpyridine units was constructed from two symmetrical half-cycles, one bearing the organoboron functionalities (A2) and the other the iodines (B2).[174] Phenantroline-containing cycle **4-12** was obtained rather accidently during the attempts to synthesize a high-molecular weight polymer. The remarkable selectivity of the

cyclotrimerization was explained by the favorable 60° angle of the chain direction due to the 2,9-substituted units.[175]

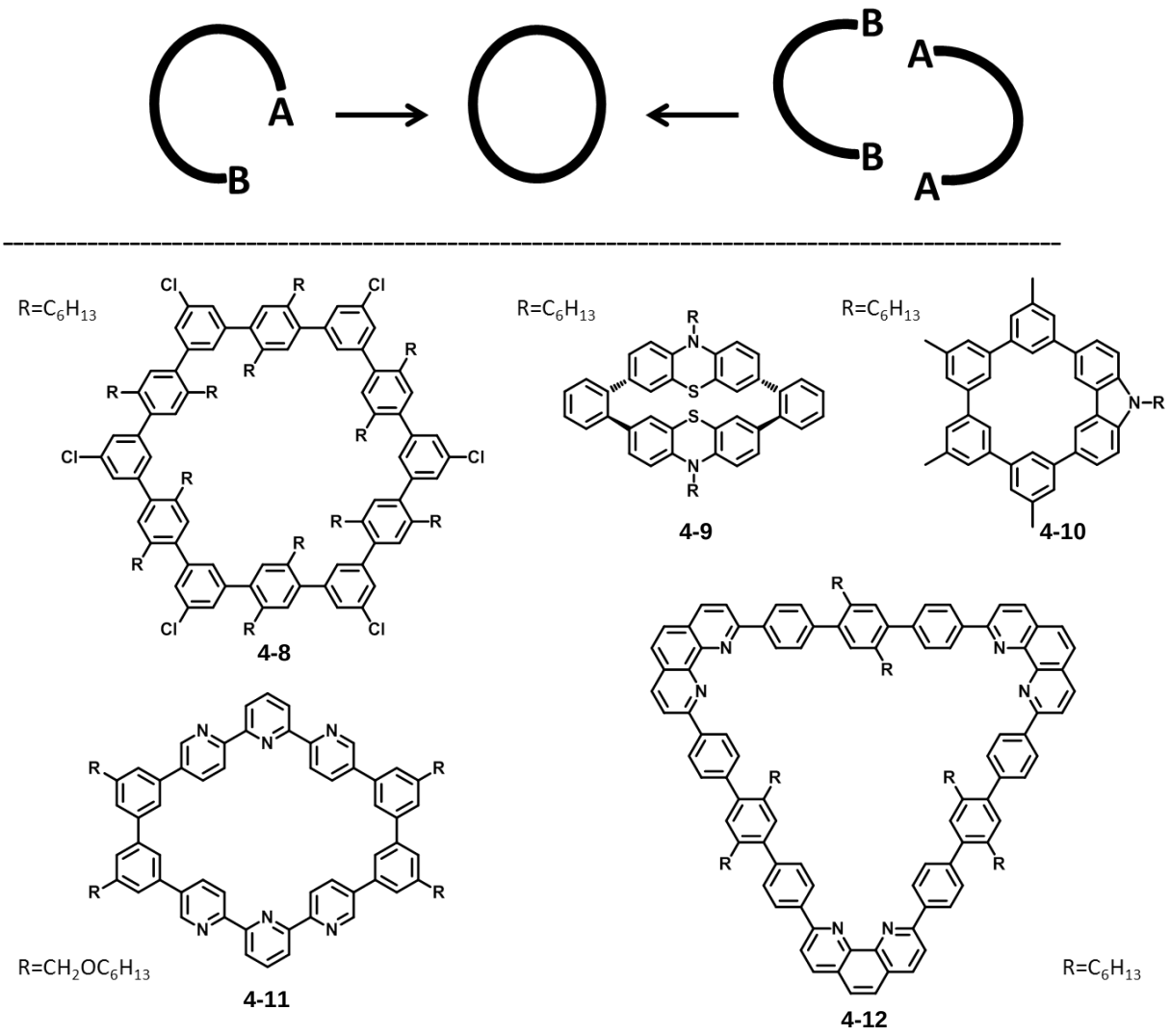

Figure 4-3: Examples of macrocycle formation using the Suzuki-Miyaura cross-coupling reaction.

For the synthesis of the herein described carbazole-pyridine-containing macrocycle **4–18** the intermolecular one-pot approach was chosen and will be described in detail in the following chapter.

4.1.1 Synthesis

Macrocycle **4-18** was synthesized *via* a fourfold palladium-catalyzed Suzuki-Miyaura cross-coupling reaction between 1,8-disubstituted carbazole derivative **4-16** (A2) and commercially available 2,6-dibromopyridine (**4-17**, B2). The *tert*-butyl groups were introduced at the bare carbazole (**4-1**) in positions 3 and 6 using literature known Friedel-Crafts reaction conditions (Scheme 4-4).[153] Once the 3 and 6 positions were substituted, the bromination at the carbazole was directed to positions 1 and 8 using Br_2 in AcOH as described in the literature.[152] Contrary to the previously reported unsuccessful attempts to introduce boronic acid groups at the 1,8-positions of the carbazole moiety,[177] we were able to synthesize diboronic-ester **4-16** in 50% yield. This was achieved by an *in situ* protection of the carbazole NHs of compound **4-14** with CO_2 followed by the introduction of the boronic-ester groups using 2-isopropoxy-4,4,5,5-tetramethyl-1,3,2-dioxaborolane (**4-15**).[178]

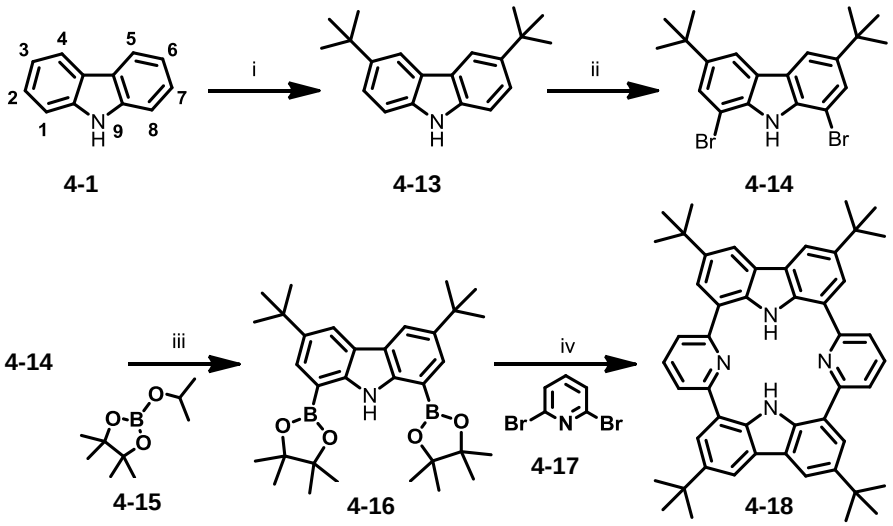

Scheme 4-4: Synthesis of macrocycle **4-18**. Conditions: *i* $ZnCl_2$, *t*-BuCl, nitromethane, rt, 69%; *ii* Br_2, AcOH, 90°C, quant. *iii* 1. *n*-BuLi, THF, 0°C, 2. CO_2, rt, 3. *t*-BuLi, THF, -78°C, 4. **4-15**, 50%; *iv* $Pd(PPh_3)_4$, 2M K_2CO_3, EtOH, toluene, 85°C, 15%.

The structure of novel 1,3,2-dioxaborolan-2-yl-9*H*-carbazole derivative **4-16** was evidenced by FD-MS spectrometry, NMR and X-ray spectroscopy. Due to the fast quadrupole relaxation of boron, the quaternary carbon atom next to the boron atom could not be observed in the ^{13}C NMR spectrum of compound **4-16**. It is known that carbon atoms in direct vicinity to a boron atom resonate broad structureless signals induced by the

quadrupole nucleus boron.[179] Nonetheless, the crystal structure revealed not only the structure but also the packing of compound **4-16** (Figure 4-4).

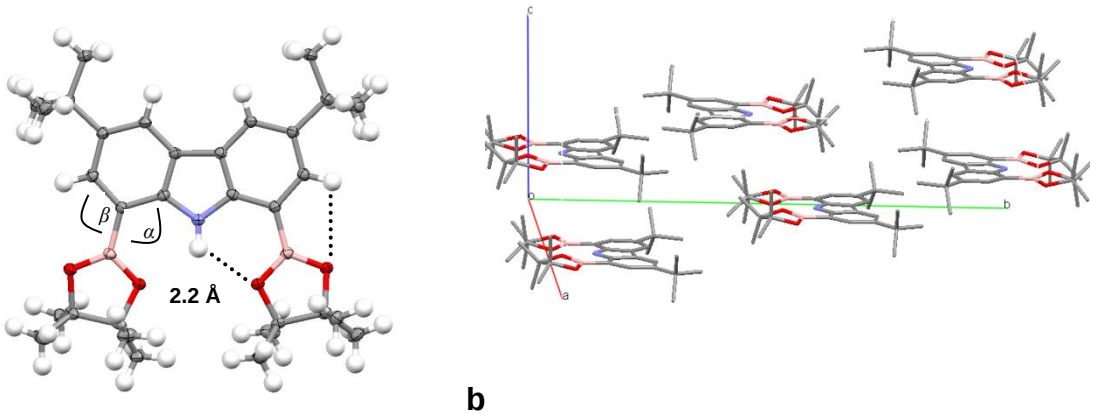

a **b**

Figure 4-4: Crystal structure of 1,3,2-dioxaborolan-2-yl-9*H*-carbazole derivative **4-16** **a**: single molecule (the ellipsoids correspond to 50% propability); **b**: unit cell (hydrogen atoms are omitted for clarity).

Suitable crystals for X-ray analysis were grown by slow evaporation from hexane. The crystal structure nicely showed the boronic-ester groups with the bulky methyl substituents attached. They are aligned parallel to the carbazole's plane which is due to the intramolecular hydrogen bonding between the NH···O and CH···O (Figure 4-4a). The distance between the NH, acting as the hydrogen bond donor and the oxygen is 2.2 Å, which is in the range of a strong hydrogen bond.[180] The weaker hydrogen bond between the carbazole's CH and oxygen (2.8 Å) helps to hold the boronic ester groups in plane. The stronger NH···O bond is also reflected in the smaller angle α = 120.5° compared to β = 123.7°. The unit cell of compound **4-16** is depicted in Figure 4-4b and shows no π-stacking between the aromatic moieties, which is most probably hindered by the bulkiness of the boronic-ester and *tert*-butyl groups. The π-systems are aligned in a parallel but staircase fashion which is facilitated by the intermolecular hydrogen bonding between the boronic-ester groups (CH···O = 2.6 Å, Figure 4-5a). They arranged in a way that alternately the molecule is up and down caused by the earlier described intermolecular hydrogen bonds (Figure 4-5b).

1,3,2-Dioxaborolan-2-yl-9*H*-carbazole derivative **4-16** was then used for the macrocyclization towards macrocycle **4-18** and succeeded in a one-pot palladium-catalyzed Suzuki-Miyaura coupling reaction in 15% yield.[181] To avoid the competitive linear polymer formation, the reaction was carried out in high dilution (10^{-4} M) following the Ruggli-Ziegler dilution principle.[171, 182] Though the yield was rather low it could clearly compete

with yields in porphyrin syntheses (commonly < 10%),[183] and other palladium catalyzed macrocyclization reactions.[172] Macrocycle **4-18** is well soluble in common organic solvents like THF, DCM, DMF and $CHCl_3$ but rather poorly soluble in unpolar solvents like hexane.

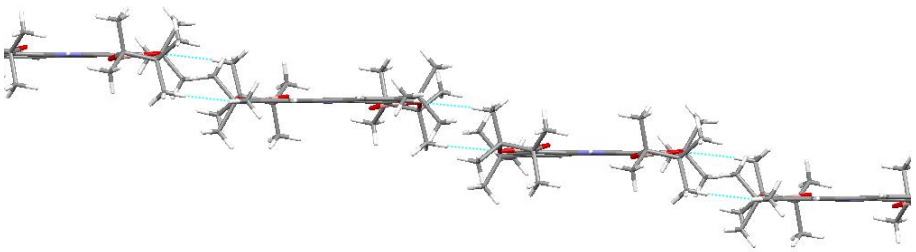

a

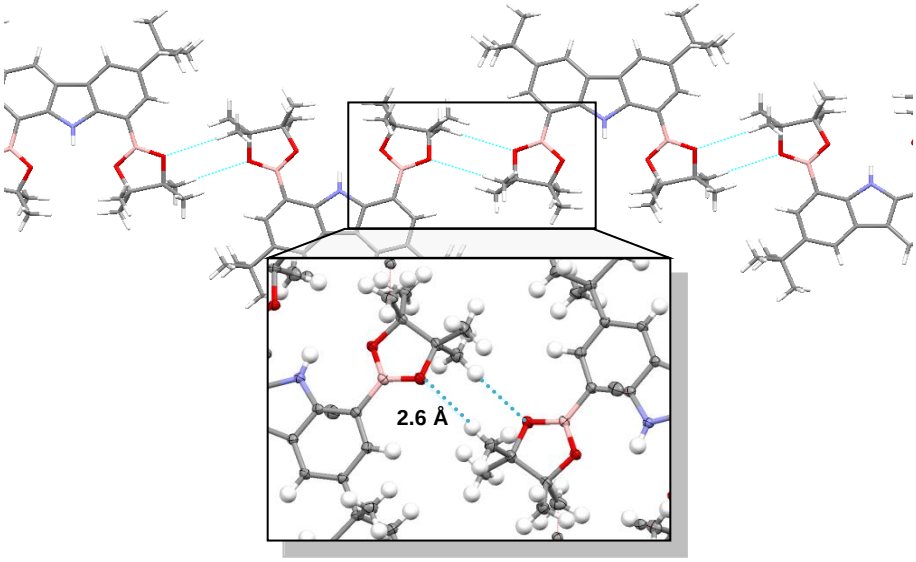

b

Figure 4-5: Intermolecular hydrogen bonding in the packing of compound **4-16**. **a:** side view; **b:** top view with close-up (hanging short contacts are omitted).

The ^{1}H NMR spectrum of macrocycle **4-18** did not show any evidence for a macrocyclic ring current with the signals for the carbazole NH protons resonating at 9.66 ppm (CD_2Cl_2, 300 MHz, 298 K, Figure 4-6). Anyhow, the NH signals were shifted downfield compared to 1,8-dibromo carbazole **4-14** (8.26 ppm),[152] which can be attributed to the presence of hydrogen bonding. Compared to porphyrins, where the ^{1}H NMR signals for the internal NHs are shifted upfield to approximately -4 ppm, in macrocycle **4-18** no specific diamagnetic ring current was observed, which is due to the lack of annulene conjugation in the non-planar ring.[3]

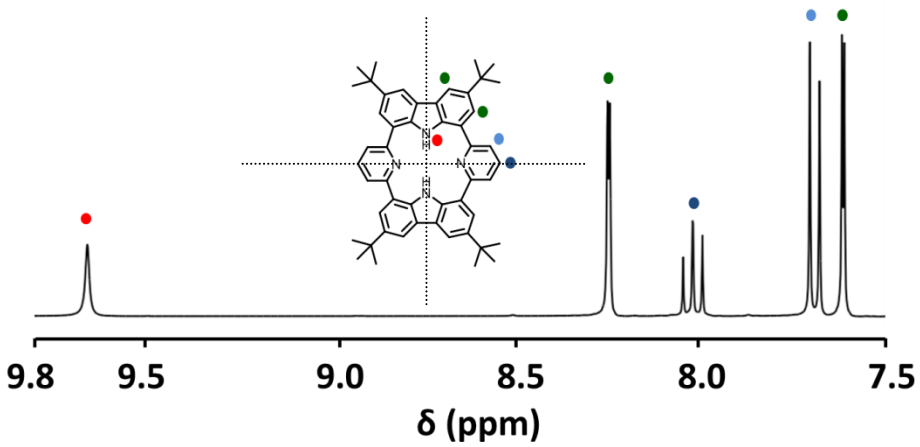

Figure 4-6: Aromatic region of the ^{1}H NMR spectrum of macrocycle **4-18** in $C_2D_2Cl_2$, 298 K, 300 MHz.

To verify the closed ring structure of macrocycle **4-18** a NOESY (Nuclear Overhauser effect spectroscopy) spectrum was recorded. In a NOESY spectrum the cross peaks connect resonances from nuclei which are spatially close to each other (within about 4 Å). Therefore cross peaks were expected for H-2 and H-3 (Figure 4-7).

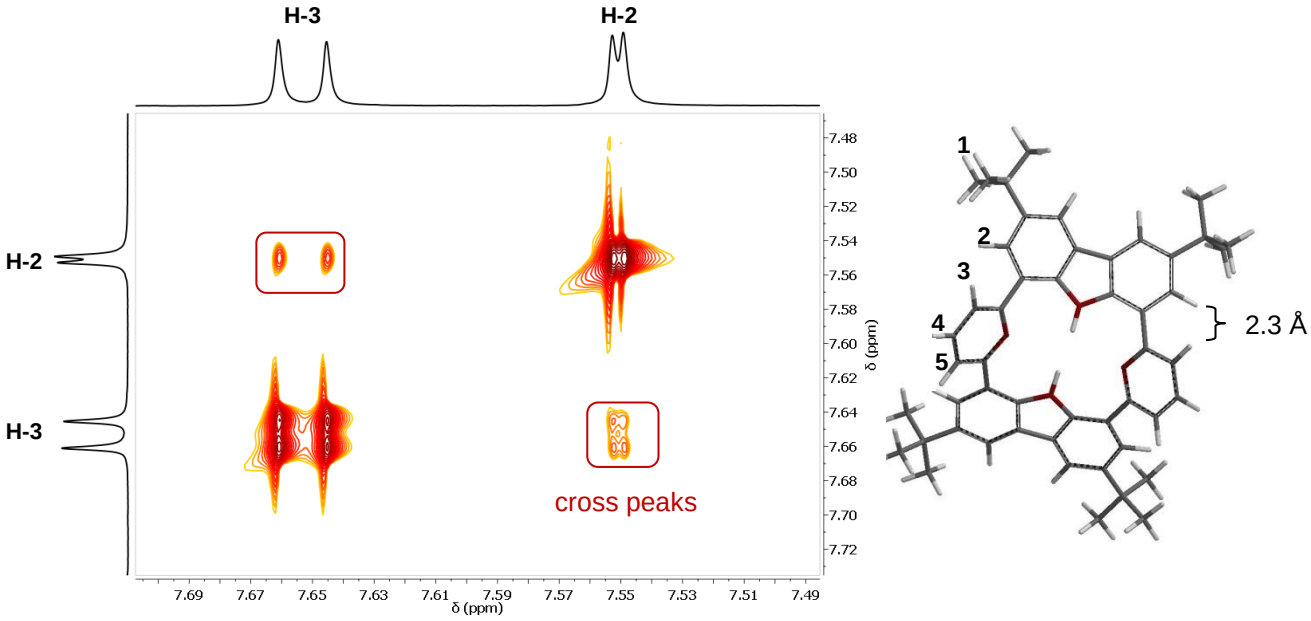

Figure 4-7: NOESY NMR spectrum of macrocycle **4-18** in CD_2Cl_4, 298 K, 500 MHz and molecular modeling of its geometric structure (DFT, B3LYP/6-31G*).

Indeed, the cross peaks for H-2 and H-3 could be observed in the NOESY spectrum (CD_2Cl_4, 298 K, 500 MHz) which proved that those nuclei undergo cross-relaxation due to their NOE (Nuclear Overhauser effect) and reside in a closed ring. This is in agreement with molecular

modeling[184] according to which the distance between H-2 and H-3 was determined to be 2.3 Å (Figure 6).

4.1.2 Crystal Structure

The structure of macrocycle **4-18** was further elucidated by X-ray crystallography (Figure 4-8). Crystals were grown from THF by slow evaporation. Unfortunately, the crystals turned out to be very unstable under ambient conditions by the rapid loss of solvate molecules and degraded within 10 to 30 seconds. Therefore crystals were isolated from the mother liquor in cooled Silicon oil (Riedel-de-Häen Perfluoroether 216) and mounted in sealed glass capillaries. The crystal structure revealed that the molecule is nonplanar with C_{2v} symmetry, the pyridine moieties being twisted "up" and the carbazoles twisted "down", resulting in a saddle-like conformation (Figure 4-8).

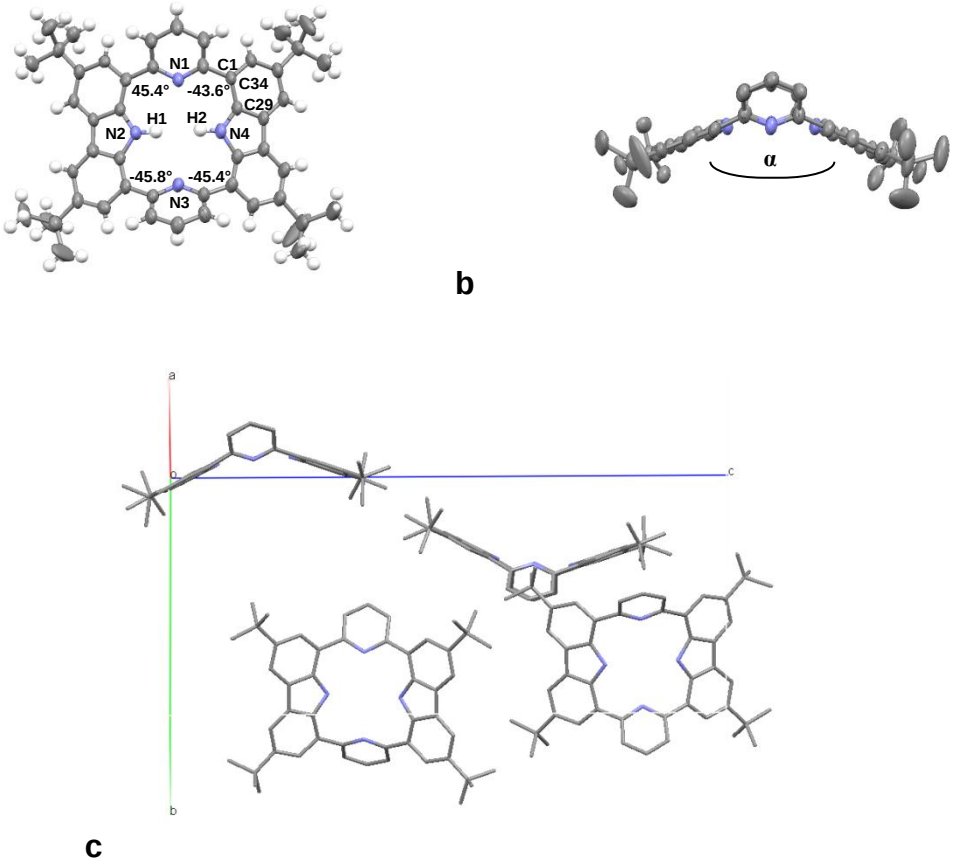

Figure 4-8: Crystal structure of macrocycle **4-18** with **a:** top view and **b:** side view. The side view is showing the saddle-like conformation. THF solvate molecules are omitted for clarity; the ellipsoids correspond to 50% probability; dihedral angles are shown in the molecules *e.g.* Φ(N(1)-C(1)-C(34)-C(29))= -43.6°. **c:** unit cell (for b/c the hydrogen atoms are omitted).

The carbazole moieties span an angle of α = 162.6° and the average dihedral angle between the carbazole plane and the pyridine plane is Φ = 45.1°. The cavity of macrocycle **4-18** is rectangular (N(2)-N(4) 3.90 Å; N(1)-N(3) 4.86 Å) with the shortest distance between the carbazole nitrogens, resulting in a slightly smaller ring size than in the case of porphyrins (4.2 Å). The unit cell consists of four macrocyclic π-systems which arrange in two wiggly lines which are almost perpendicular to each other. The wave-like alignment arises from the alternately up and down "saddles" (Figure 4-8c).

4.1.3 Electronic Structure

The absorption and emission spectra of macrocycle **4-18** were recorded in THF at rt (c = $5*10^{-5}$ M) and are depicted in Figure 4-9. The absorption spectrum of macrocycle **4-18** showed two local maxima at 311 nm and 373 nm. For unsubstituted 3,6-di(*tert*-butyl)carbazole (**4-13**) and 3,6-di-*tert*-butyl-1,8-di(pyridin-2-yl)-9*H*-carbazole (**4-14**) a band at about 230 nm is observed and originates from carbazole-centered transitions.[152, 185] For macrocycle **4-18** this band was bathochromically shifted to 311 nm. The optical energy gap was estimated from the absorption edge to be ΔE_{opt} = 3.19 eV.

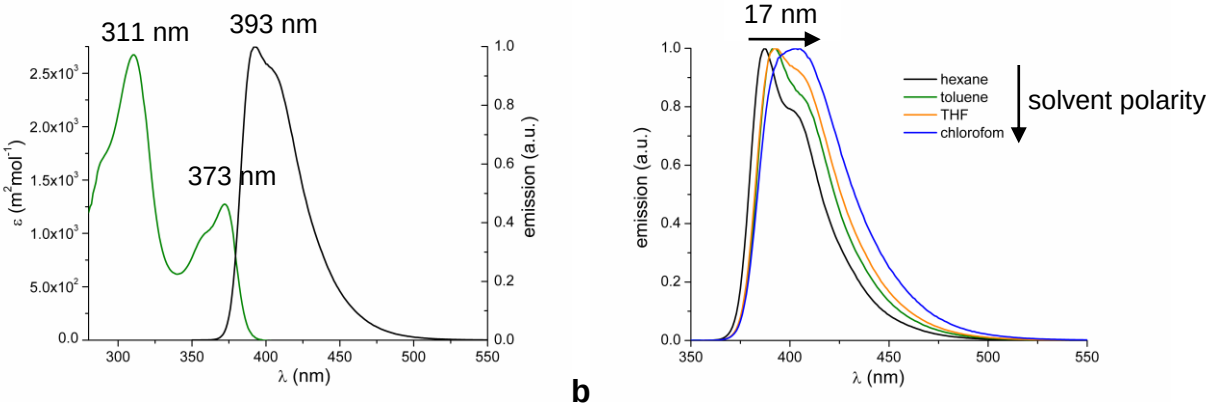

Figure 4-9: **a:** Electronic absorption and emission spectra of macrocycle **4-18** (c = $5*10^{-5}$ M in THF); **b:** Solvent dependent emission spectra of macrocycle **4-18** (c = $5*10^{-5}$ M, λ_{ex} = 311 nm).

Compound **4-18** exhibits blue emission with a maximum at 393 nm. The quantum yield was estimated to be Φ_f = 0.46 by calibration with coumarin 1 using the Comparative Method (λ_{ex} = 349 nm in THF).[186] Solvent dependent emission measurements showed that by

increasing the polarity of the solvent the emission maxima was bathochomically shifted (Figure 4-9b), indicating an intrinsic polar character of the emitting state.

Usually, the formation of mono- and dications of the porphyrinic species are investigated by the protonation of the examined compound with an acid.[30, 187] Generally, TFA is used and therefore, the electronic absorption spectra of macrocycle **4-18** were taken in DCM and in DCM with 1% TFA (Figure 4-10). By the addition of TFA to the solution of **4-18** in DCM a vivid color change from colorless to shiny yellow occurred (Figure 4-10b). Along with the color change, the second absorption maximum was bathochromically shifted from 373 nm to 417 nm. The red-shift could be attributed to the formation of the dicationic species **4-18-H$_2$** by protonation.[69]

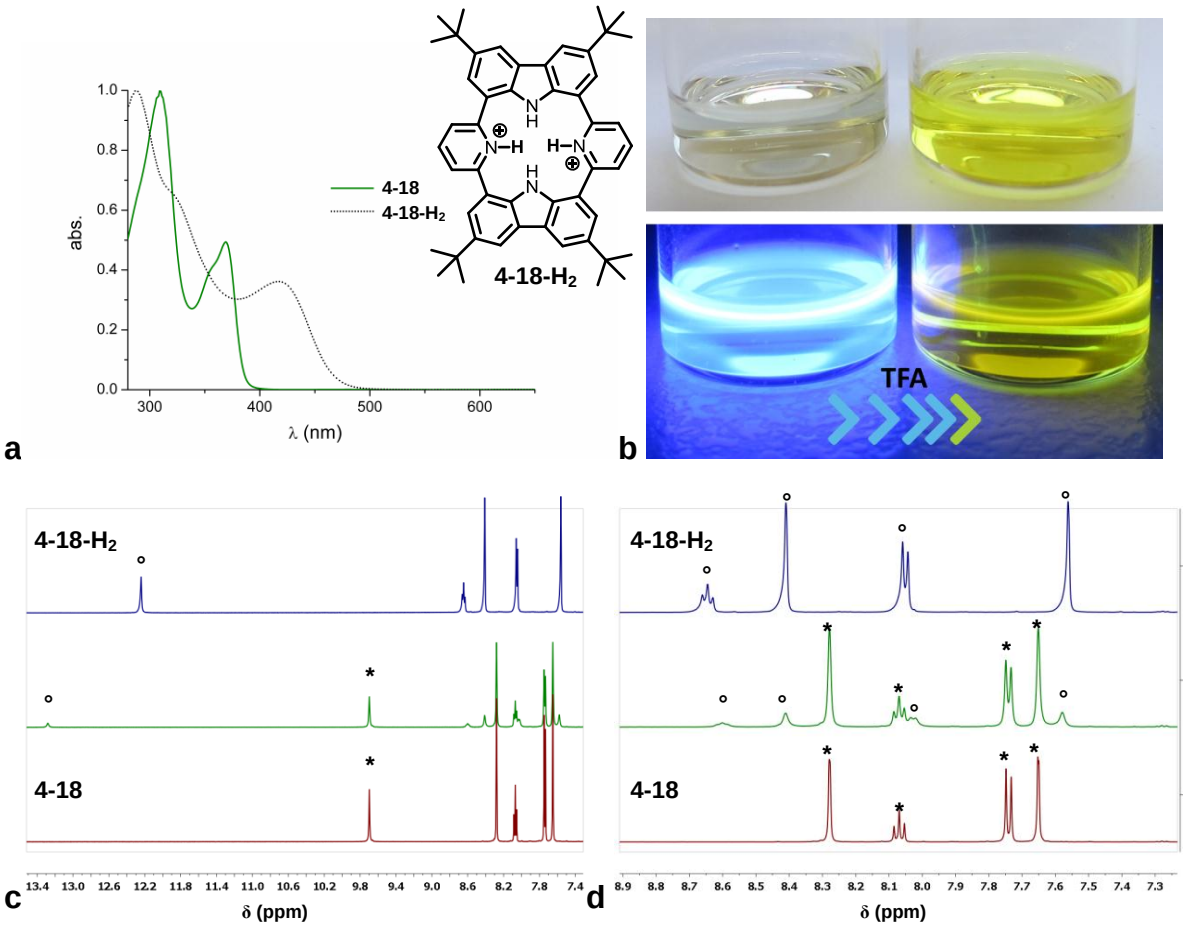

Figure 4-10: **a:** Electronic absorption spectra of macrocycle **4-18** (in DCM, green) and its dication **4-18-H$_2$** (in DCM + 1% TFA, dotted line); **b:** color change upon addition of TFA in ambient light and λ = 366 nm; **c and d:** aromatic region of ^{1}H NMR spectra of macrocycle **4-18** (c = 10^{-3} M, CD_2Cl_2, 298 K, red,*), its dication **4-18-H$_2$** (CD_2Cl_2 + 2 µl TFA-d_1, 298 K, blue,°) and the intermediate state (CD_2Cl_2 + 1 µl TFA-d_1, 298 K, green)

The proton NMR of dication **4-18-H$_2$** showed mostly downfield shifts which are consistent with protonated species (Figure 4-10c,d).[187] Also the resonance for the interior carbazole's NH was shifted to lower fields (δ_{NH} = 12.24 ppm, 298 K) which may be caused by a

conformational change in the macrocycle (Scheme 4-9a, blue line). By the treatment of macrocycle **4-18** with only a small portion of TFA, both species could be observed in coexistence (Scheme 4-9c/d green line). The ^{1}H NMR spectrum nicely displayed the appearance of the new signals and the disappearance of the original ones (Figure 4-10), meanwhile the two species are coexistent. The coexistence supports the assumption that the dicationic species **4-18-H$_2$** is stable once being formed not exchanging with **4-18**. Nevertheless, no signal for the proton at the pyridine unit could be monitored. Most probably the pyridine's proton exchanges with the protons of the TFA resulting in broad resonances, since the proton exchange is fast on the NMR timescale. In contrary, at lower temperatures the exchange of acidic protons is much slower and their signals get sharper. Therefore, ^{1}H NMR spectra were recorded at different temperatures between 298-203 K. In fact at 233 K the signal for the protons at the pyridines became visible and at 203 K it was sharp and clearly observable (Figure 4-11). The integration of the signals was 4:4:4:2:2:2 and therefore in agreement with the suggested protonated structure **4-18-H$_2$** (Figure 4-10a). The proton at the pyridine resonated at 16.2 ppm (203K, 500 MHz in DCM + 0.2% TFA-d$_1$) which is in consensus with values reported for hydrogen bonded protons at pyridine in the literature.[188]

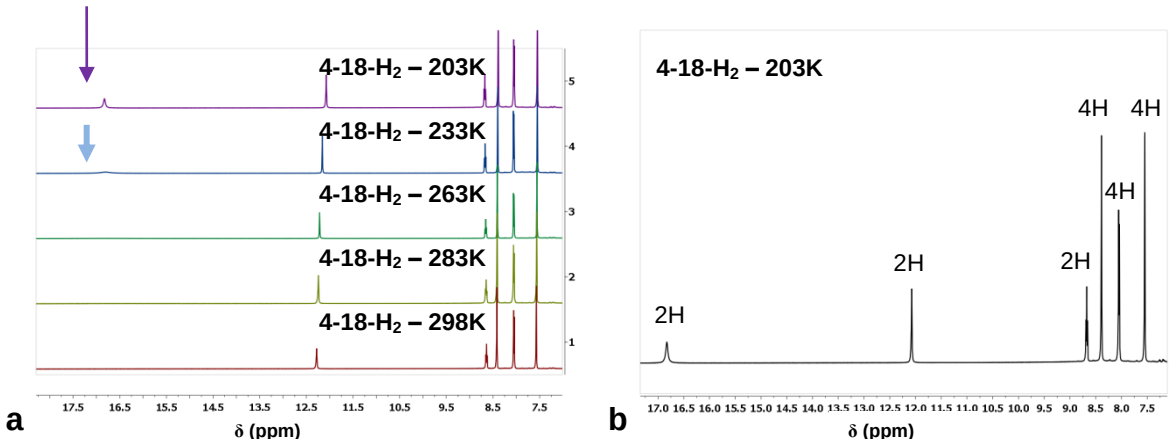

Figure 4-11: ^{1}H NMR spectra of **4-18-H$_2$** in DCM + 0.2% TFA-d$_1$ **a:** at different temperatures and **b:** at 203 K.

To further investigate the electronic properties of macrocycle **4-18** cyclic voltammetry was employed.[189] Compound **4-18** was dissolved (10^{-3} M) in a solution of anhydrous DMF together with *n*-Bu$_4$NPF$_6$ (10^{-1} M), which served as the electrolyte. Ferrocene (Fc/Fc$^+$) was added as an internal reference.[190] The cyclic voltammogram of macrocycle **4-18** was recorded at a scan rate of 100 mVs^{-1} and showed two irreversible oxidation waves (Figure 4-12). Generally, carbazole is oxidized by the removal of one electron to form a cation

radical.[191-192] This radical can then react by deprotonation-coupling to generate N,N'- or 3,3'-bicarbazyls. Only the 3,3'-bicarbazyls are known to be further oxidized in two reversible one electron steps. When N,N'-bicarbazyls are formed further oxidation occurs in an irreversible multi-electron process. When positions 3 and 6 are blocked only N,N'-couplings and in some rare cases 1,1'-couplings can occur.[191] Since for porphyrinoid **4-18** position 3,6 and 1,8 are substituted only intermolecular N,N'-bicarbazyls can be formed which explains its undefined irreversible cyclic voltammetric behavior (Figure 4-12). The appearance of two oxidation waves could be explained by the successively oxidation of the two carbazole moieties to their cation radicals. The HOMO level was estimated from the first oxidation onset potential (Figure 4-12, red arrow) to be E^{HOMO} = -5.43 eV with regard to the internal reference (Fc/Fc^+). E^{LUMO} was empirically calculated to be E^{LUMO} = -2.24 eV, by taking the optical energy gap into account.

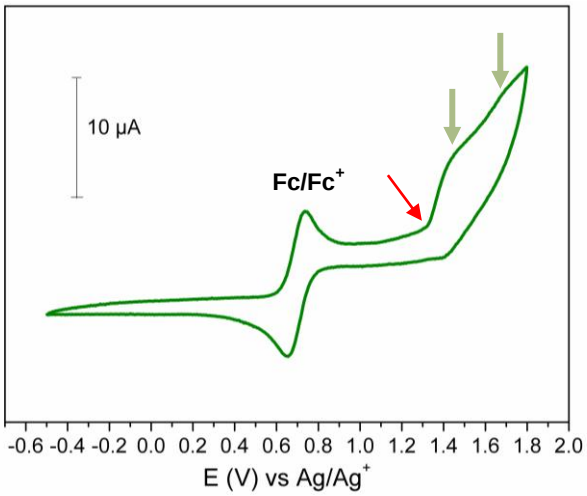

Figure 4-12: Cyclic voltammogram of macrocycle **4-18**; 10^{-3} M sample solution in DMF, 10^{-1} M solution of *n*-Bu_4NPF_6 as electrolyte; working and counter electrode: Pt, reference electrode: Ag; ferrocene reference (Fc/Fc^+), scan rate 100 mVs^{-1}.

For comparison, the geometry and electronic structure were calculated using density functional theory calculation (DFT, B3LYP/6-31G*,[184] Figure 4-13). These calculations revealed that the LUMO and LUMO+1 were degenerated, with the LUMO orbitals located on one and the LUMO+1 orbitals on the other carbazole moiety. In contrast, the electronic density of the HOMO was distributed over both carbazole moieties. The HOMO and LUMO levels were caclulated to be E^{HOMO} = -5.14 and E^{LUMO} = -1.17 eV. The resulting energy gap (3.97 eV) and the energy levels were in good agreement with the values derived from the UV-vis absorption and CV measurements.

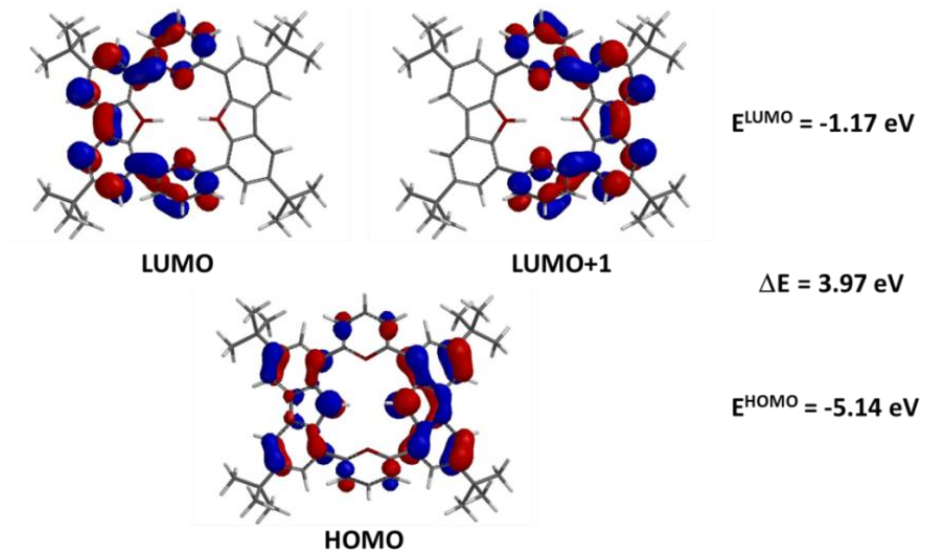

Figure 4-13: Calculated HOMO, LUMO and LUMO+1 orbital energies of macrocycle **4-18** at B3LYP/6-31G* level of theory.[184]

4.1.4 Metal Complexation

The ability of macrocycle **4-18** to act as a metal ligand was investigated by the insertion into the ring cavity of different metal(II)-ions, namely, Ni(II), Cu(II), Fe(II) and Co(II) ions. Related tetrapyrrole macrocycles, such as porphyrins and phthalocyanines are excellent metal-complexing ligands with the possibility to bind almost every transition metal.[193] Although, as described before, the cavity of compound **4-18** is rectangular and slightly smaller compared to the one of a porphyrin (4.2 Å), it is theoretically still large enough to bind 3d transition metal ions with effective ionic radii between 0.5-0.9 Å.[194]

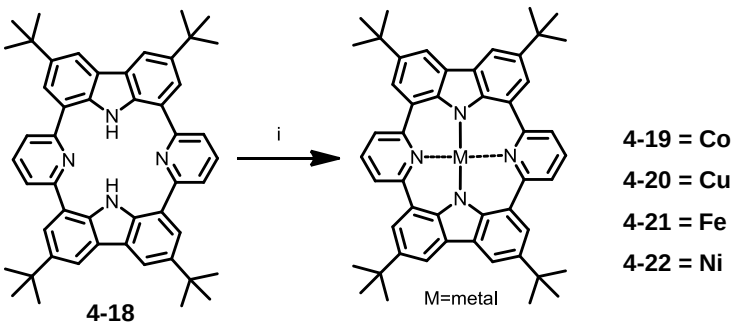

Scheme 4-5: Complexation of macrocycle **4-18** with different metal(II) ions. Conditions: *i* $M(OAc)_2$, DMF, microwave, 300 W, 170°C.

The metal complexes were obtained by refluxing macrocycle **4-18** with the corresponding metal(II)acetate in DMF under microwave irradiation (Scheme 4-5). After the reaction was completed the metal complexes were precipitated into cold H_2O, filtered and dried in high vacuum. The insertion of all metal(II)ions was proven by Maldi-Tof mass spectrometry (Figure 4-14).

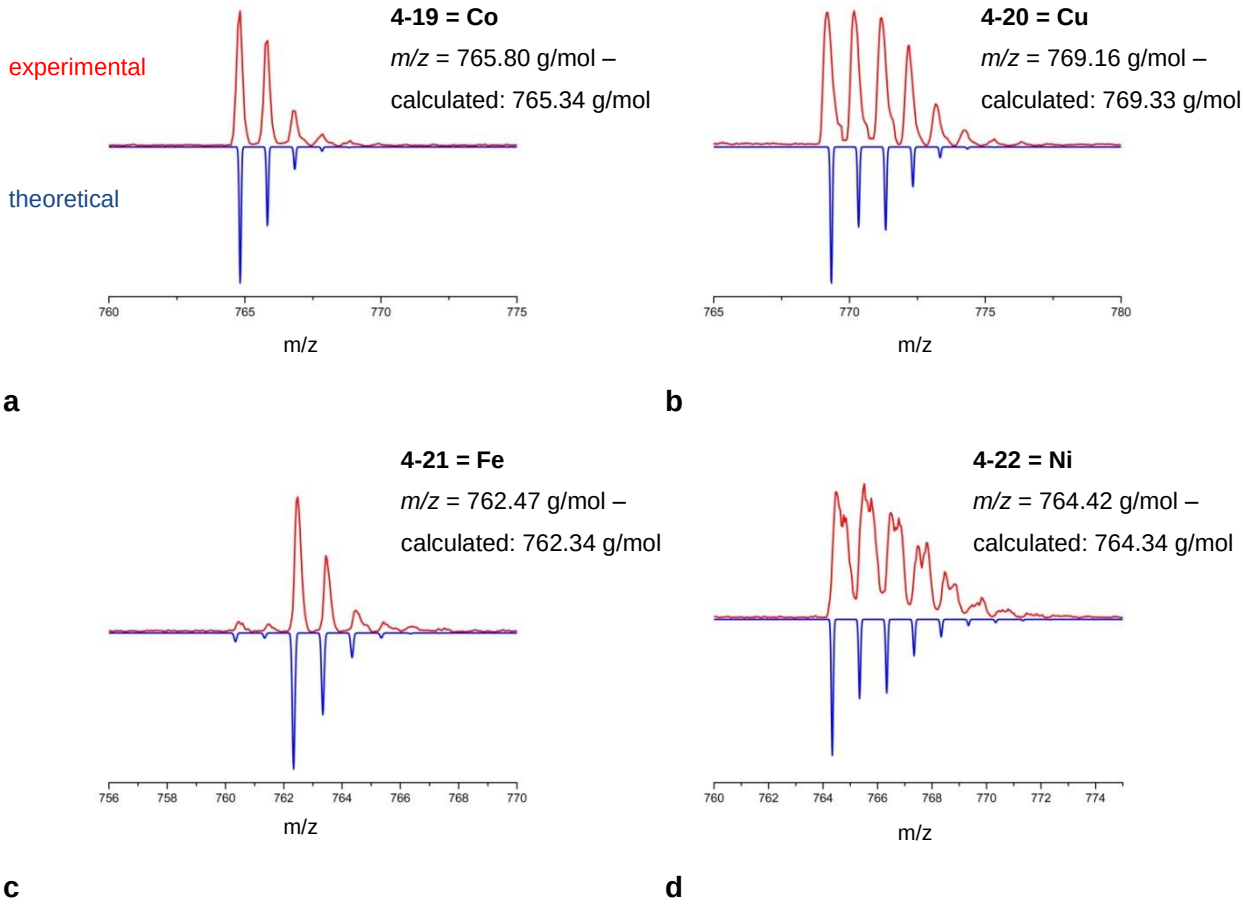

Figure 4-14: Maldi-Tof mass spectra for metal complexes **4-19-4-22**. Experimental data depicted in red and theoretical isotropic distribution depicted in blue.

The peaks found (red) were benchmarked against their theoretical isotropic distribution (blue) and were found to be in very good agreement. Unfortunately, it was beyond the scope of this work to further investigate the coordination ability of **4-18** to other metal ions.

FT-IR spectroscopy confirmed the metal insertion by the absence of NH stretching vibrations at 3487 cm^{-1} for the complexes which was distinct for ligand **4-18** (Figure 4-17).

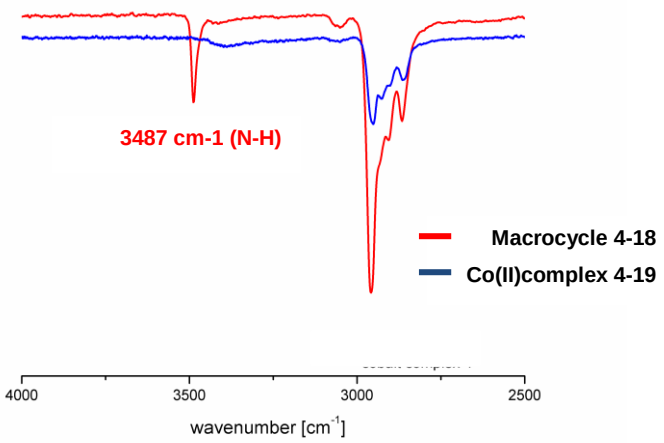

Figure 4-15: FT-IR spectra of macrocycle **4-18** and its cobalt complex **4-19**.

^{1}H NMR spectroscopy was used to monitor the insertion of the cobalt atom into the macrocycle (Figure 4-16). Although, Co^{2+} is paramagnetic due to the unpaired electrons (Figure 4-23) which makes NMR spectroscopy complicated, the interaction of macrocycle **4-18** with the cobalt(II) ion could be followed. Typically the recording of ^{1}H-NMR of paramagnetic complexes is precluded on account of slow electronic relaxation and subsequent broad, irresolvable signals.[195] For this study, a NMR tube with a solution of macrocycle **4-18** in DMF-d_7 and an excess of $Co(OAc)_2$ was heated to 403 K. The formation of the cobalt complex **4-19** could be observed by the disapearance of the signals for **4-18** and the appearance of new resonances (Figure 4-16). The signals for the cobalt complex **4-19** were broad and highly shifted compared to macrocycle **4-18**, which was caused by contact and pseudocontact contributions and is typical for paramagnetic species.[195] Most peaks were shifted downfield with the highest shifted signal appearing at 45.41 ppm (H4) and one signal was shifted upfield to -8.49 ppm (H5). The high downfield shift was attributed to a σ-contact shift mechanism in Co(II)-pyridyl complexes.[196] Upfield-shifts could be explained by a π-contact shift contribution at this position.[197-198] The broad signals appearing at approx. 26 ppm could be assigned to the acidic proton of the acetic acid formed during the reaction. The time-scale on which the insertion happened was recorded to be less than one hour. Unfortunately, the protons H-2 and H-3 could not be distinguished. NOESY NMR measurements, which usually can help to resolve such problems, were not possible due to very short T2 times.

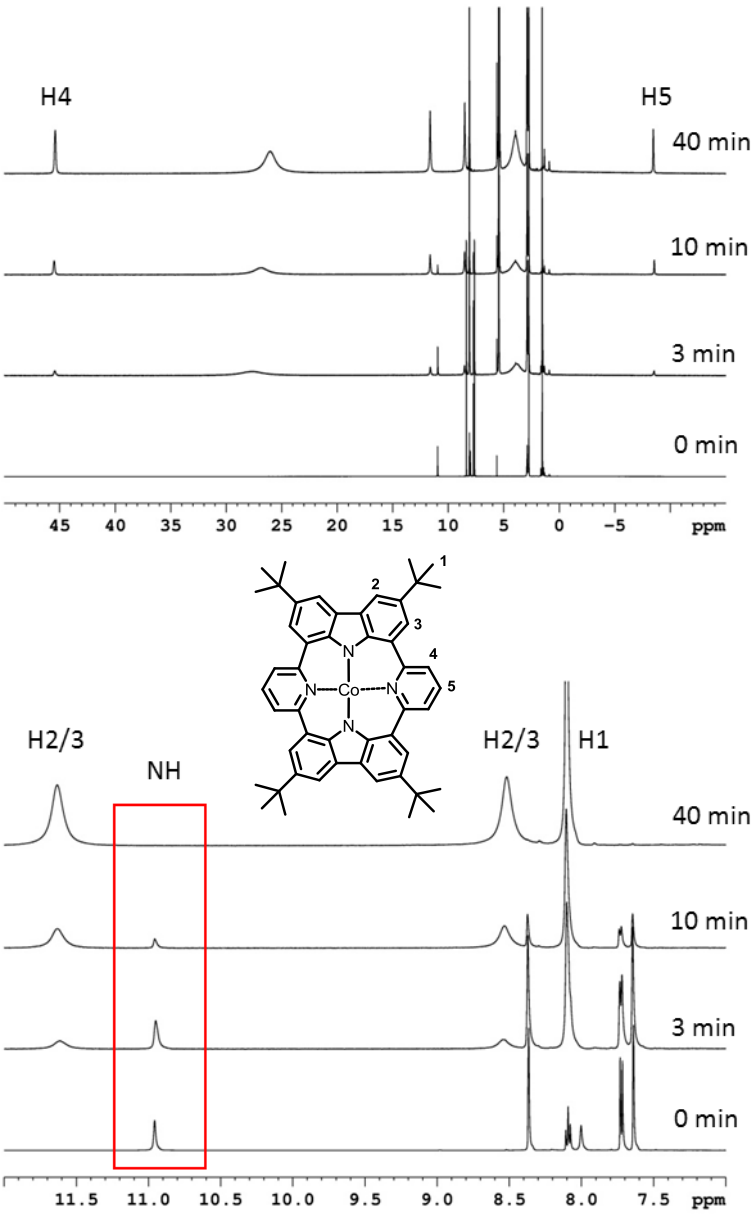

Figure 4-16: ^{1}H NMR study of the cobalt insertion into the macrocycle **4-18 a:** full range spectra; **b:** aromatic region. For labelling see inlay. Spectra recorded in DMF-d_7 at 500 MHz and 403 K with acquisition time of 1.1 s, sweep width 119 ppm and a delay of 2 s.

The electronic absorption spectra of all complexes were measured in DCM at a concentration of c = 10^{-4} M (Figure 4-17). For comparison the UV-vis absorption of the free-ligand **4-18** is shown as well (red line). For all metal complexes the carbazole centered transition maximum was weakly red-shifted compared to the free ligand **4-18** (λ = 313 nm (**4-18**), λ = 330 (**4-19**), 326 (**4-20**), 321 (**4-21**), 326 (**4-22**) nm). In contrast, for porphyrins the Soret band is generally hypsochromically shifted upon insertion of Cu(II), Ni(II) and

Co(II) and little effected for Fe(II).[199] It is typical for metalloporpyhrins that the number of Q-bands is reduced compared to the free porphyrin which is caused by the increase of symmetry upon metallation. In the present case, the band in the visible region of **4-18** was bathochromically shifted as a result of the metal insertion for **4-19** (424 nm), **4-20** (442 nm) and **4-22** (437 nm).

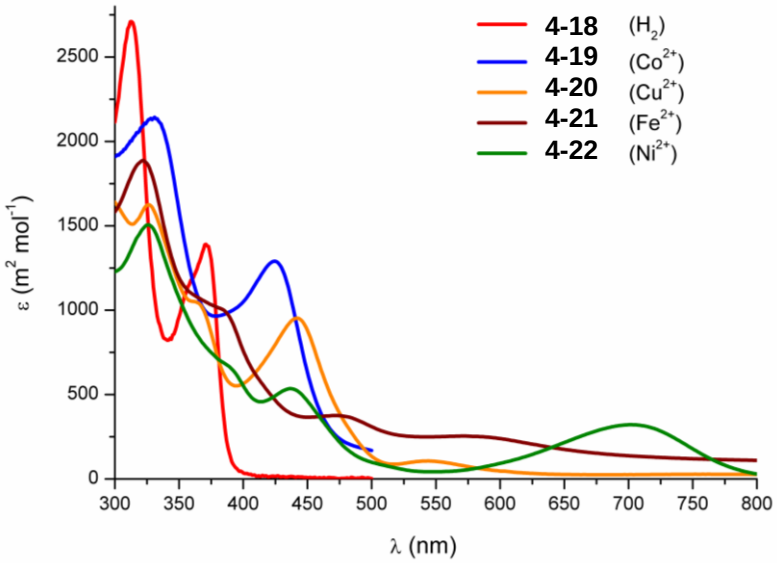

Figure 4-17: UV-vis spectra of macrocycle **4-18** and its metal complexes **4-19** to **4-22** ($c = 10^{-4}$ M in DCM).

The absorption for the iron complex **4-21** was rather broad and structureless over the whole spectrum. An absorption maximum in the red-region at $\lambda = 702$ nm was exclusively observed for the Ni(II)complex **4-22**. Similar absorption bands have been found for metal-porphyrins if dimers are formed.[200] This is consistent with the results from SQUID (Superconducting Quantum Interference Device) measurements which will be explained in the following.

The blue emission of the free ligand **4-18** was quenched upon complexation with metal(II)ions and caused by the interaction of the metal and the aromatic system of the ligand. This phenomenon is also common for the same metals in metalloporphyrins.[199]

Cyclic voltammetry was conducted on the metal complexes **4-19**, **4-20** and **4-22** and are depicted in Figure 4-18. They were all performed under identical conditions as described for ligand **4-18** on the potential range of +1.6 V to -1.6 V with the half wave potentials referenced against SCE ($E^{1/2}(Fc/Fc^+) = 0.43$ V).[201] Porphyrins and their metal complexes generally feature two reversible one-electron oxidations as well as two one-electron

reductions which are all centered on the tetrapyrrolic ring.[202] For some metals, like Co(II) or Fe(III) the metal centered oxidation or reduction can also be observed.[203]

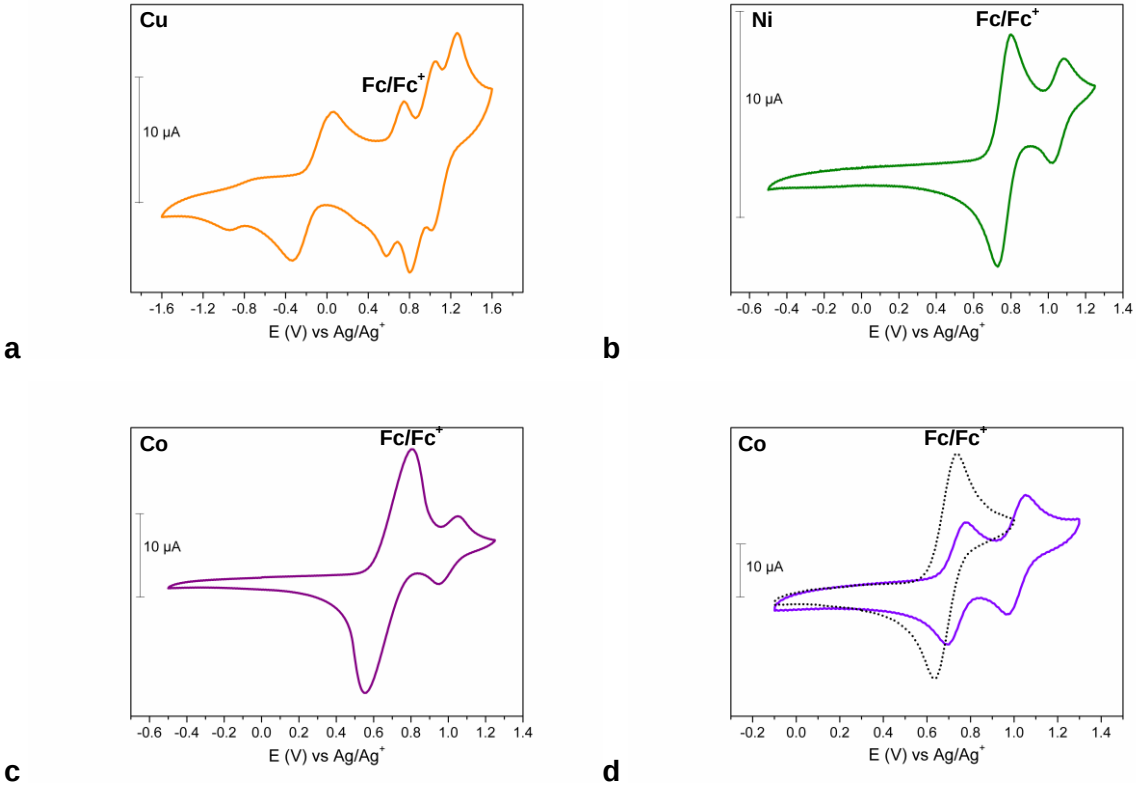

Figure 4-18: Cyclic voltammogram of metal complexes **a: 4-20**; **b: 4-22**; **c** and **d: 4-19**; 10^{-3} M sample solution in DMF, 10^{-1} M solution of *n*-Bu_4NPF_6 as electrolyte; working and counter electrode: Pt, reference electrode: Ag; ferrocene reference (Fc/Fc^+), scan rate 100mVs^{-1}.

The cyclic voltammogram of copper complex **4-20** showed almost textbook-like two reversible oxidation, one reversible reduction and one quasi-reversible reduction waves at $E^{1/2}(1)$ = -1.02 V, $E^{1/2}(2)$ = -0.35 V, $E^{1/2}(3)$ = 0.70 V and $E^{1/2}(4)$ = 0.92 V. Related CuTPP (copper *meso*-tetraphenylporphyrin) exhibits also two well-resolved reversible stepwise one-electron oxidation and reduction processes which proceed all ring-centered generating π-radical cations and anions, dications and dianions, respectively .[200, 204-205] Therefore, the found redox processes in copper complex **4-20** are suggested to occur in the same manner. For the nickel complex **4-22** only one well-resolved oxidation wave at $E^{1/2}(1)$ = 0.73 V was observed, which is probably also occurring ring-centered at the ligand to generate a dication. No reduction processes were observed for **4-22** under the applied conditions. The voltammogram of the cobalt complex **4-19** resulted in a displaced curved due to overlapping with the redox potential of internal standard (Fc/Fc^+, Figure 4-18c). Therefore, a spectrum without internal standard was recorded to impede this problem (Figure 4-18d). Cobalt

complex **4-19** showed two nicely reversible oxidation waves at $E^{1/2}(1)$ = 0.50 V and $E^{1/2}(2)$ = 0.77 V. Similar to CoTPP it is suggested that the first oxidation wave occurred at the cobalt center ($Co^{2+}+L \rightarrow Co^{3+}+L$) and the second one-electron oxidation at the ligand ($Co^{3+}+L \rightarrow Co^{3+}+L^{+}$).[200, 205-207] Furthermore, in the case of **4-19**, no reduction process was observed in the measured potential range.

In conclusion, although the macrocyclic structure of porphyrinoid **4-18** differed from regular porphyrins, similar electronic properties could be found for the complexes **4-19**, **4-20** and **4-22** when compared to metalloporphyrins.

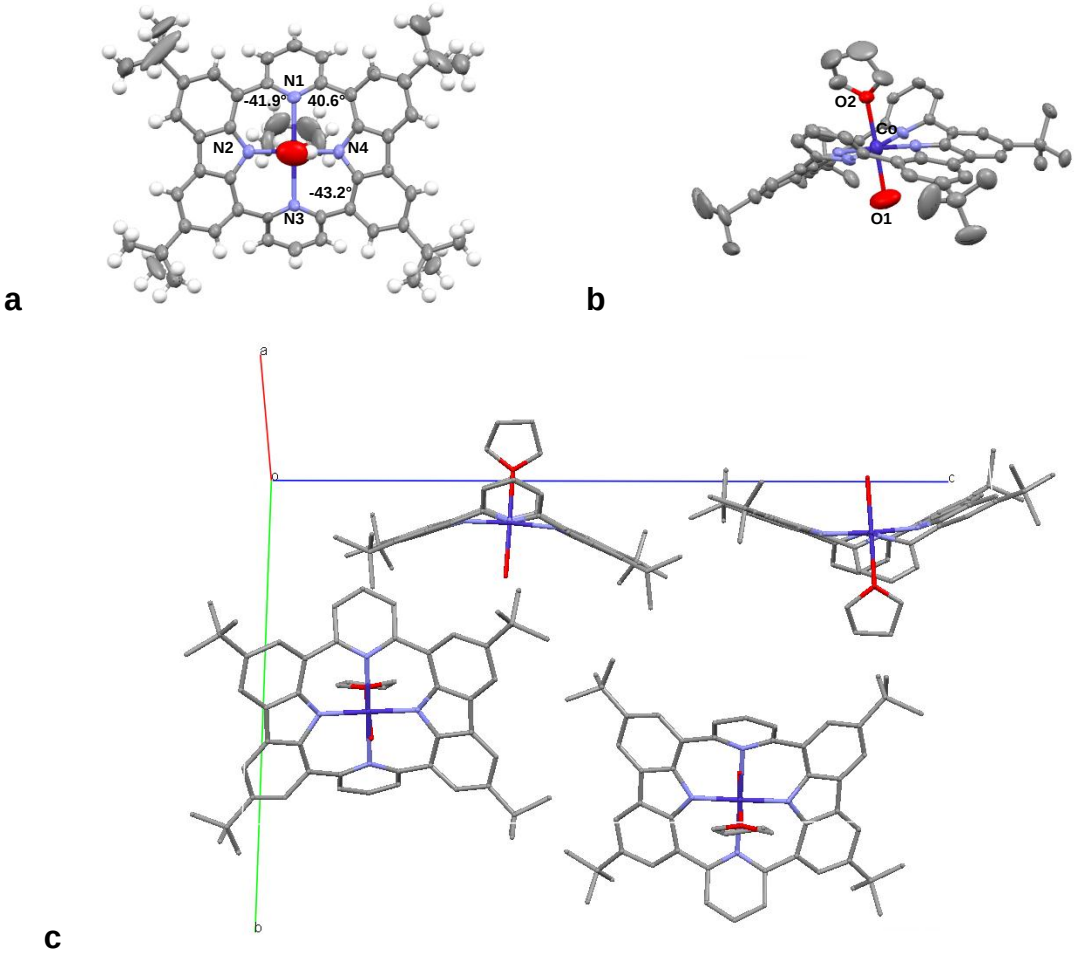

Figure 4-19: Crystal structure of cobalt complex **4-19** with **a:** top view and **b:** side view. The side view is showing the saddle-like conformation. THF solvate molecules are omitted for clarity; the ellipsoids correspond to 50% probability; **c:** unit cell (for b/c the hydrogen atoms are omitted).

Fortunately, suitable crystals for X-ray structure determination of cobalt complex **4-19** could be obtained by slow evaporation of THF (Figure 4-19). Similarly to the case of its ligand **4-18**, the needles had to be treated with care due to low stability in ambient

conditions. Therefore, the solvent was not allowed to evaporate to dryness during the crystallization process and crystals were isolated from this solution. The X-ray analysis revealed that neither the saddle-like conformation nor the distances between the nitrogens (N(2)-N(4) 3.88 Å; N(1)-N(3) 4.67 Å) changed upon complexation. This was reflected in the negligible change of $\alpha = 162.0°$ and the average dihedral angle ($\Phi = 42.2°$, Figure 4-19). In addition to the four nitrogen atoms, two solvent molecules are axially coordinated by oxygen atoms to the cobalt(II)-ion. A THF molecule is coordinated from above the saddle and a water molecule from below. The coordination polyhedron around the cobalt(II)-ion can be described as distorted octahedral. The cobalt-carbazole nitrogen bond distances (Co-N(2) 1.95 Å; Co-N(4) 1.93 Å) are significantly shorter than those of cobalt-pyridine nitrogens (Co-N(1) 2.32 Å; Co N(3) 2.35 Å) or the cobalt-oxygens (Co-O(1) 2.27 Å; Co-O(2) 2.22 Å). This indicates some degree of π-donation from the sp^2-hybridized carbazole nitrogen to the metal center.[178] Carbazole usually undergoes ionisation and behaves as an amido-N donor in organometallic chemistry, and the Co-N(2,4) distances are well within the range of Co-N_{amido} distances noted for similar complexes (1.91-1.93 Å).[150, 208] Like the free ligand **4-18**, the unit cell of **4-19** consists of four molecules which arrange in the same wave-like alignment (Figure 4-19c).

The magnetic properties of the metal complexes have been investigated using SQUID (Superconducting Quantum Interference Device) measurements. A SQUID magnetometer is a very sensitive sensor to measure extremely weak magnetic field. Its principle is based on quantum effects in a superconducting loop (Figure 4-20).

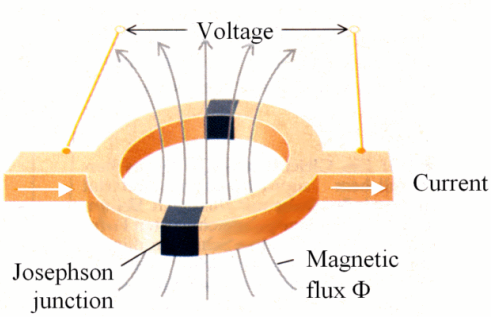

Figure 4-20: Principle of a Superconducting Quantum Interference Device (SQUID).[209]

The applied device is called a Josephson junction named after its inventor the British physicist B. D. Josephson. The Josephson Effect occurs when an electric current (Cooper pairs) flows between two superconductors separated by a thin nonsuperconducting layer

through quantum tunnelling. If the magnetic flux through the loop changes a current around the loop is induced (Figure 4-20). This affects the current flowing through the loop, because the net current through each junction is no longer the same. The resulting potential difference across the loop can then be measured.

In general, the obtained parameter in a SQUID measurement is the magnetic susceptibility χ. For weak magnetic fields, the magnetic susceptibility is a proportionality constant that indicates the degree of magnetization of a material in response to an applied magnetic field.

For the investigation of the magnetic properties of the metal complexes the powdered samples were studied by variable temperature susceptibility measurements in the range of 2-300 K in an applied field of 1 Tesla. The collected data are shown as $\chi_M T$ *vs.* T. Theoretical values for $\chi_M T$ have been calculated according formula (4-1):

$$\chi_M T = \frac{N\mu_B^2}{3k} g^2 S(S+1) \qquad (4\text{-}1)$$

where N is the Avogadro constant (6.0221415*10^{23} mol^{-1}), μ_B the Bohr magneton (4.66864374*10^{-5} $cm^{-1}G^{-1}$), k the Boltzmann constant (0.69503877 $cm^{-1}K^{-1}$) and g the g-factor (2.0023).[210-211]

The theoretical calculations were based on the assumption that the metal ions reside an oxidation state of M(II) along with a (distorted) octahedral coordination polyhedron. Hereby, the metal coordinates to the chelating tetradentate ligand (**4-18**) and additionally has the possibility to complex two axial ligands, such as solvent molecules (Figure 4-21).

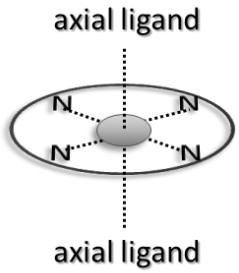

Figure 4-21: Schematic illustration of octahedral coordination polyhedron for metal (II) ion.

The data received from SQUID measurements unambiguously confirmed the emanate oxidation states for all metal(II) ions, namely Co(II), Cu(II), Ni(II) and Fe(II) (Figure 4-22).

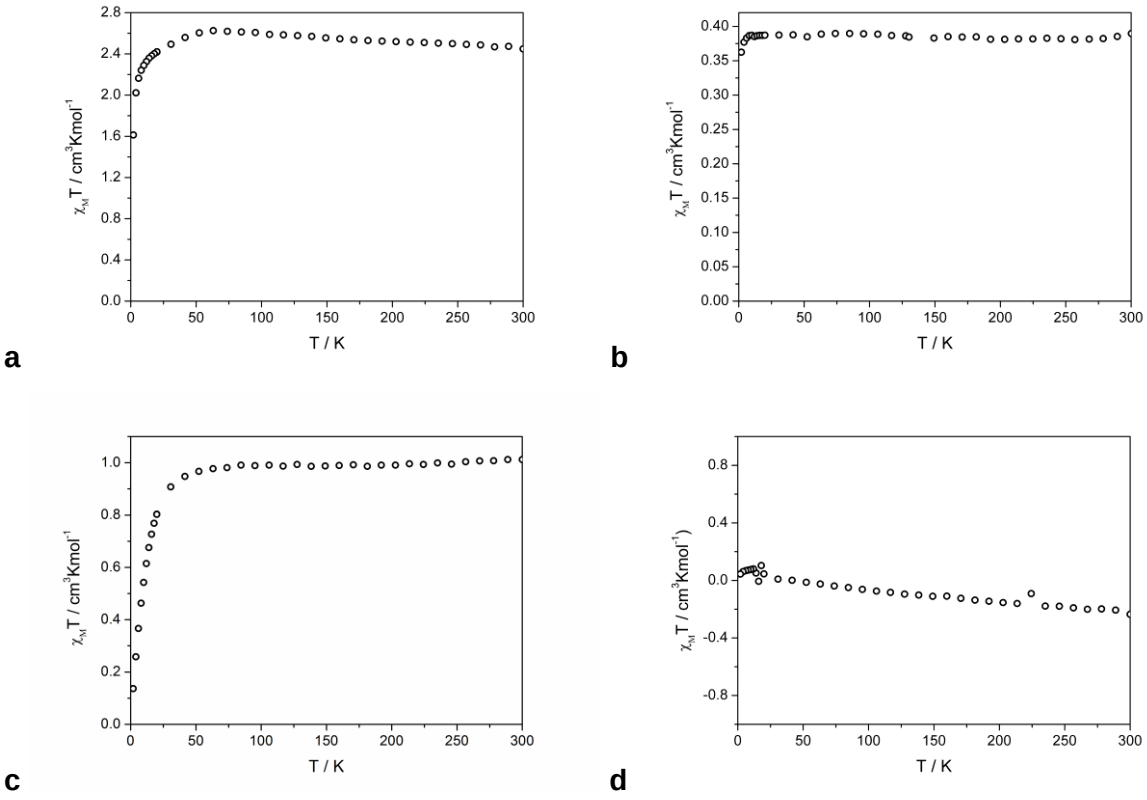

Figure 4-22: Temperature dependence in $\chi_M T$ versus T of **a:** cobalt(II)complex **4-19**, **b:** copper(II)complex **4-20**; **c:** nickel(II)complex **4-22** and **d:** iron(II)complex **4-21**.

The observed $\chi_M T$ value for the paramagnetic cobalt complex **4-19** at 300 K was 2.448 cm^{3}Kmol^{-1} (Figure 4-22a). This was higher than the expected value of 1.875 cm^{3}Kmol^{-1} for an uncoupled spin with S = 3/2. The higher experimental value can be explained by the strong and well known orbital contributions of Co(II).[212] As a result, the cobalt atom is existent as a Co(II) high spin configuration with three unpaired electrons (Figure 4-23). Interestingly, this is different from the usually low-spin configurations in simple cobalt(II) porphyrins such as CoTPP.[213-214]

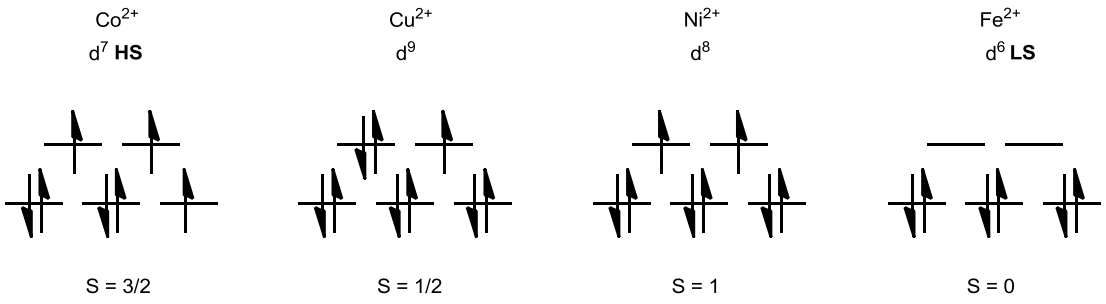

Figure 4-23: Electron configuration of the metal(II) cations in an octahedral ligand field; (for cobalt only the high spin (HS) and for iron only the low spin (LS) configurations are shown).

The d^9 electron configuration of copper(II) complex **4-20** results in one unpaired electron with S = ½ (Figure 4-23). The expected $\chi_M T$ value for S = ½ according formula (4-1) is 0.375 cm^3Kmol^{-1}. The experimental value for **4-20** at 300 K was 0.389 cm^3Kmol^{-1} (Figure 4-22b) and is in good agreement with the theoretical one, confirming the paramagnetic copper(II) oxidation state which was constant over the hole temperature range.
The data received for nickel(II) complex **4-22** at rt was 1.012 cm^3Kmol^{-1} and is consistent with the theoretical paramagnetic value of $\chi_M T$ = 1 cm^3Kmol^{-1} for S = 1. In contrast, the nickel in NiTPP is diamagnetic due to the quadratic planar coordination to the porphyrin.[213] By lowering the temperature, first a slow decrease of $\chi_M T$ till 50 K was observed which was followed by a rapid decay reaching a $\chi_M T$ value of 0.137 cm^3Kmol^{-1} at 2 K (Figure 4-22c). This indicates a weak antiferromagnetic coupling between the nickel atoms and therefore, the formation of dimers or oligomeric species are considered. This has also been observed in the earlier described electronic absorption measurement.
For the iron complex **4-21** no paramagnetic signal could be observed which confirmed the existence of a diamagnetic iron(II) low spin complex (Figure 4-23 and Figure 4-22).

Additionally to the magnetic investigations using SQUID magnetometry, the cobalt(II) complex **4-19** was investigated by electron spin resonance (ESR) and X-ray photoelectron (XPS) spectroscopy. Unfortunately, no ESR data of complex **4-19** could be obtained neither at 298 K nor at 8 K, which may be due to the high-spin Co(II) species,[215] confirmed by SQUID measurements. The XPS data were recorded at Sumitomo Chemical Co., Tsukuba, Japan (Figure 4-24).

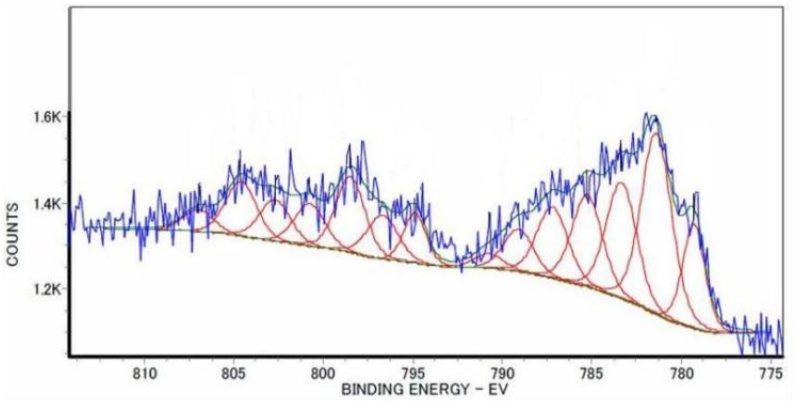

Figure 4-24: XPS Co2p narrow scan for cobalt complex **4-19**.

XPS is an analysis technique used to obtain chemical information about the surfaces of solid materials. The sample is exposed to a low-energy, monochromatic X-ray source which causes the ejection of core-level electrons from the sample atoms. The energy of a photoemitted core electron is a function of its binding energy and is characteristic of the element from which it was emitted.

The observed Co $2p_{3/2}$ peak at 779.4 eV and the multiple structure of the signal are in agreement with literature data for Co(II) compounds and with theoretical calculations on the free Co^{2+} ion considering spin-orbit and electrostatic electron-electron interactions.[216-217] As described in the literature a spin-orbit splitting $\Delta E = E_{b2p1/2} - E_{b2p3/2}$ higher than 15 eV (E_b are the binding energies for the Co2p and Co3p lines) corresponds to high-spin Co(II) complexes.[218] In the case of complex **4-19** ΔE was equal to 15.6 eV, thus the neutral cobalt complex appears to be a high-spin Co(II) species, which is in agreement with the results received from SQUID measurements.

4.1.5 RRDE measurements

As described in chapter 2.2.1 non-precious metal catalysts (NPMCs) are promising candidates as alternatives to platinum-based cathode catalysts for the reduction of oxygen (ORR) in fuel cell.[105] Amongst those, metal porphyrins, with cobalt or iron, have proven to be most prospective.[110] Therefore, the electrochemical activity of cobalt complex **4-19** in the reduction of oxygen was investigated in collaboration with Sumitomo Chemical Co. in Tsukuba, Japan. Experiments were conducted by Dr. Nobuyoshi Koshino under the supervision of Prof. Dr. Hideyuki Higashimura. Electrochemical experiments were performed using rotating ring disk electrode (RRDE) techniques. A standard three-electrode-electrochemical cell including a platinum ring as counter electrode, (d_{inner} = 7 mm and d_{outer} = 9 mm, 1.4 V *vs.* RHE), a glassy carbon working electrode (disk electrode, d = 6 mm) and an Ag/AgCl (sat. KCl) reference electrode were used. Catalyst inks have been prepared by suspending 5 mg of catalyst and 40 mg carbon black (Ketjen Black KB600) in 15 ml MeOH and subsequent ultrasonic treatment. The inks were then dried and/or pyrolyzed for 2 h at the corresponding temperature. The RRDE measurements were performed in O_2 saturated 0.5 M H_2SO_4 solution at a potential scan rate of 5 mVs^{-1} and a rotation speed of 900 rmp. Cobalt complex **4-19** has been evaluated non-pyrolyzed and pyrolyzed at 600 and 800°C.

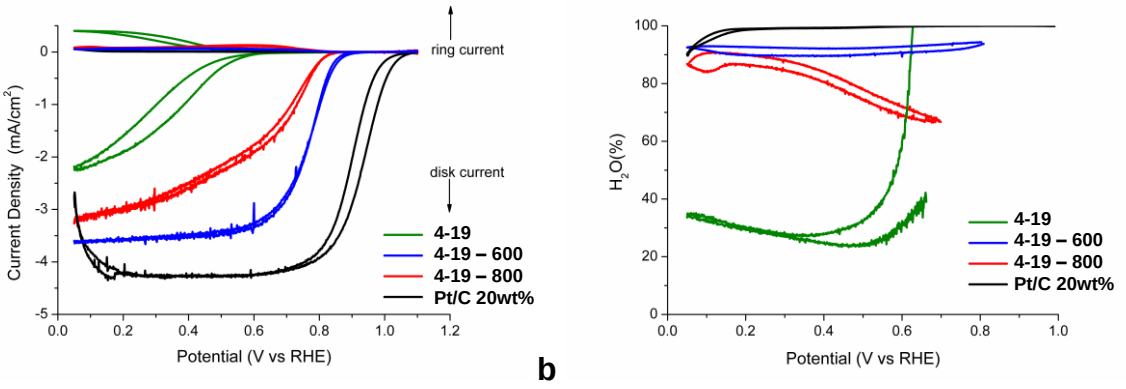

a b

Figure 4-25: **a:** Ring and disk current at rt for the determination of collection efficiency on a RRDE; three-electrode-system with a platinum ring as counter electrode (d_{inner} = 7 mm and d_{outer} = 9 mm, 1.4 V *vs.* RHE), glassy carbon working electrode (disk electrode, d = 6 mm), Ag/AgCl (sat. KCl) reference electrode and 0.5 M H_2SO_4 as electrolyte; potential scan rate 5 mVs^{-1}, rotation speed 900 rmp. **b:** H_2O production efficiency.

The corresponding ring and disk currents are shown in Figure 4-25 and summarized in Table 4-1 for all samples at 0.6 V. For comparison, the received data was benchmarked against commercial Pt/C (20wt% platinum on KB600). Unfortunately, the non-pyrolyzed sample showed no detectable activity for oxygen reduction, whereas if pyrolyzed the activity significantly increased (Table 4-1). The enhancement in activity after heat treatment is also known for metallo-porphyrins and phthalocyanines.[112] Conspicuously, the sample heat treated at 600°C showed the highest activity with a number n = 3.78 of electron transferred, while at higher temperature the activity decreased again. This observation can be understood if the thermal properties of complex **4-19** are considered.

Table 4-1: Summary of the activity and selectivity results received by RRDE measurements.

Compound	Current density @0.6V [mA/cm²]	%H_2O[a]	n[b]
Pt wt20%	4.26	99.7	3.99
4-19	0.05	n.a.[c]	n.a.[c]
4-19-600	2.88	89.3	3.78
4-19-800	1.90	68.8	3.38

[a] efficiency of 4 electron transfer @0.6 V; [b] number of electrons passed @0.6 V (n = %H2O/50+2); [c] n.a.: not available, disk current too small, no O2 reduction @0.6V.

The thermogravimetric analysis showed that the complex was stable up to T_{d1} = 480°C (Figure 4-26, T_d corresponds to 5% weight loss), at which point the decomposition of the attached alkyl substituents starts to set in.

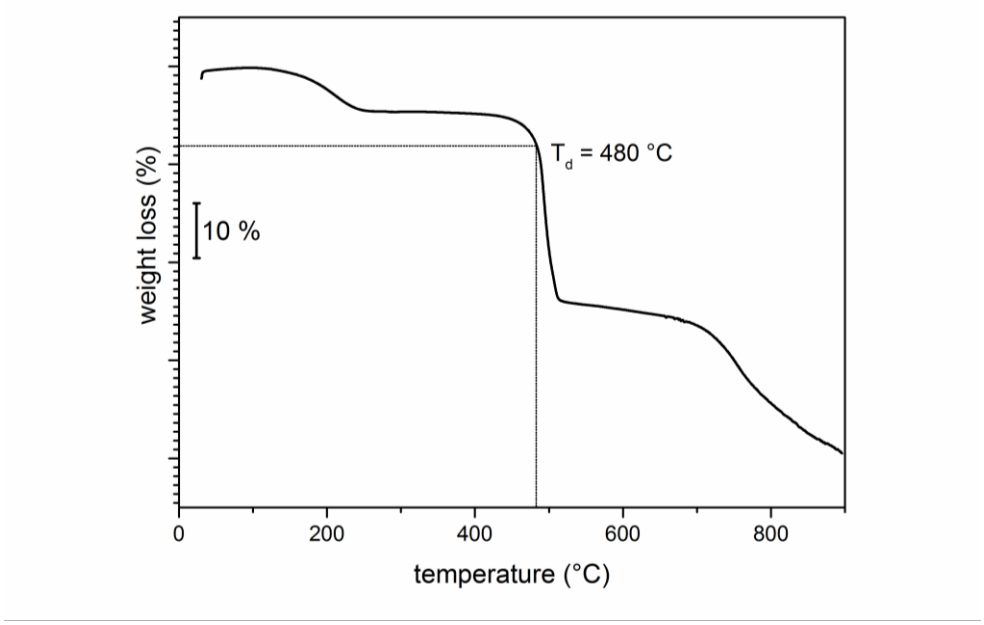

Figure 4-26: TGA of cobalt(II) complex **4-19** under N_2 atmosphere. 25-900°C, scan rate 10 $Kmin^{-1}$.

The second weight loss at T_{d2} = 750°C was caused by the rupture of the macrocyclic core. Consequently, after heat treatment at 800°C the active site are most likely to be individual CoN_4 units. On the contrary, if complex **4-19** was pyrolyzed at 600°C the active sites resided in the intact macrocyclic core, which proved to be advantageous for the catalytic performance. As a result, the active CoN_4 sites showed better electrochemical activity and selectivity if they were embedded in a stable macrocyclic environment. Although not as good as Pt/C (measured under the same conditions) the sample pyrolyzed at 600°C showed very promising preliminary results with a high number of electrons transferred (n = 3.78) and good selectivity towards water production (%H_2O = 89.2%, Table 4-1). These results are superior to values reported in the literature for related Co(II)TPP (n = 2.8, pyrolyzed at 600°C) and Co(II)phthalocyanines (n = 3.0, pyrolyzed at 600°C).[219] Furthermore, the catalytic performance of cobalt complex **4-19** competes well with those reported in literature for other non-precious metal catalysts for ORR.[110-111] Nevertheless, the performance of cobalt(II) complex **4-19** can surely be tuned by the optimization of the processing methods such as catalyst preparation or variation of the carbon support.

From a synthetic point of view, the connection of the single macrocycles could help to improve the overall electron-supply, since the catalytic sites could borrow electrons from their neighbors and facilitate a four electron transfer (Figure 4-27). Also, it has been shown, that the four-electron reduction of oxygen to water is favored by the simultaneous rupture of the oxygen molecule.[98] This can be provided by dimer or oligomer formation of

macrocyclic complex **4-19**. It was suggested that by covalent connection of the active sites heat treatment can be avoided.

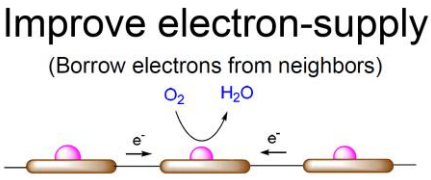

Figure 4-27: Schematic illustration of oligomerization of the cobalt complex to improve electrocatalytic performance.

For this reason, the next target to further improve the catalytic activity was the design of an appropriate monomeric macrocycle and to oligomerize and accordingly dimerize it. This challenge could be resolved by the introduction of chlorine substituents at the pyridine moiety of macrocycle **4-18** and will be explained in detail in the following chapters 4.1.8 and 4.1.9. The results of the electrochemical activity measurements are summarized in chapter 4.1.10.

4.1.6 RDE measurements

Additionally to the RRDE measurements evaluated in acidic conditions, rotation disk electrode (RDE) techniques were performed. In this case, the electrochemical activity of cobalt complex **4-19** towards the reduction of oxygen was determined in alkaline solution. These measurements were carried out under supervision of Dr. Ruili Liu at the Max Planck Institute for Polymer Research. Electrochemical RDE measurements were performed on the non-pyrolyzed and pyrolyzed (470, 600 and 800°C) samples, the resulting samples were denoted **4-19-470**, **4-19-600** and **4-19-800**, respectively. The samples were supported on carbon black (20wt%, Vulcan XC-72R) and measured in an O_2-saturated 0.1 M alkaline solution of KOH. For all substances the same amount of sample by mass (25.5 µg/cm^2) was loaded onto a glassy-carbon RDE.

The cyclic voltammograms for all samples at a scan rate of 100 mVs^{-1} are depicted in Figure 4-28a. For comparison the featureless voltrammogram of **4-19-470** in saturated Ar solution is benchmarked (Figure 4-28a, black line). In contrast, when the electrolyte solutions were saturated with O_2, well-defined cathodic peaks in the range of -0.49 to -0.26 V could be observed, suggesting pronounced electrochemical activity. The least distinct cathodic peak

(-0.49 V) was found for unpyrolyzed sample **4-19** and the most promising for **4-19-600** (-0.26V), which is in agreement with the results of the previous described RRDE measurements.

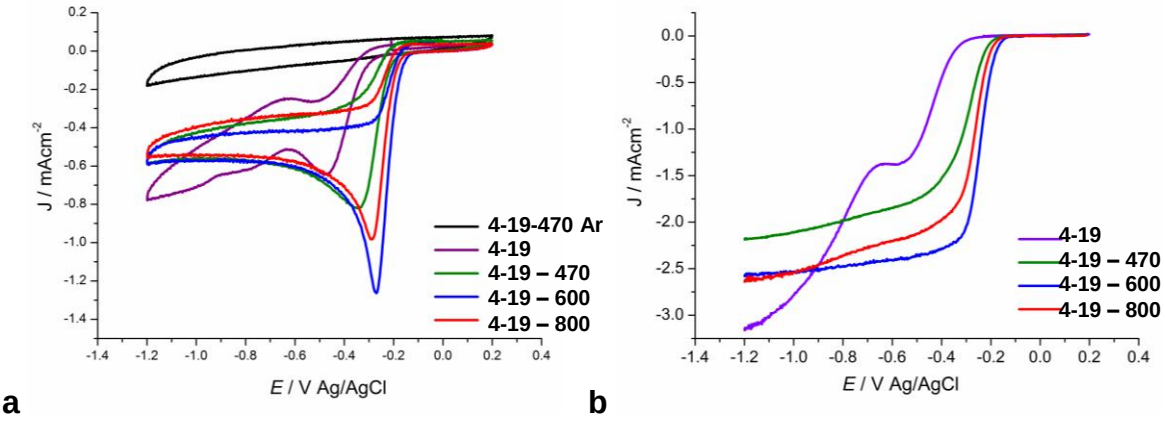

Figure 4-28: **a:** Cyclic voltammograms for **4-19**, **4-19-470** (in saturated Ar and O_2 solution), **4-19-600** and **4-19-800** on glassy carbon RDE electrode in an O_2-saturaled 0.1 M solution of KOH; **b:** RDE voltammograms recorded at a scan rate of 10 mVs^{-1} and 1600 rpm.

The rotating-disk voltammetric profiles showed that the current density was enhanced by an increase in the rotating rate (from 225-4400 rpm; not shown here). For comparison the profiles at 1600 rpm were plotted and onset potentials for all samples in the range of -0.17 to -0.22 V were obtained (Figure 4-28b). Again, the non-pyrolyzed sample showed almost no catalytic activity whereas the sample heat treated at 600°C featured highest activity with an onset potential at -0.17 V. The corresponding Koutecky-Levich plots at various electrode potentials showed good linearity, and exemplary the plot for **4-19-470** is shown (Figure 4-29a).

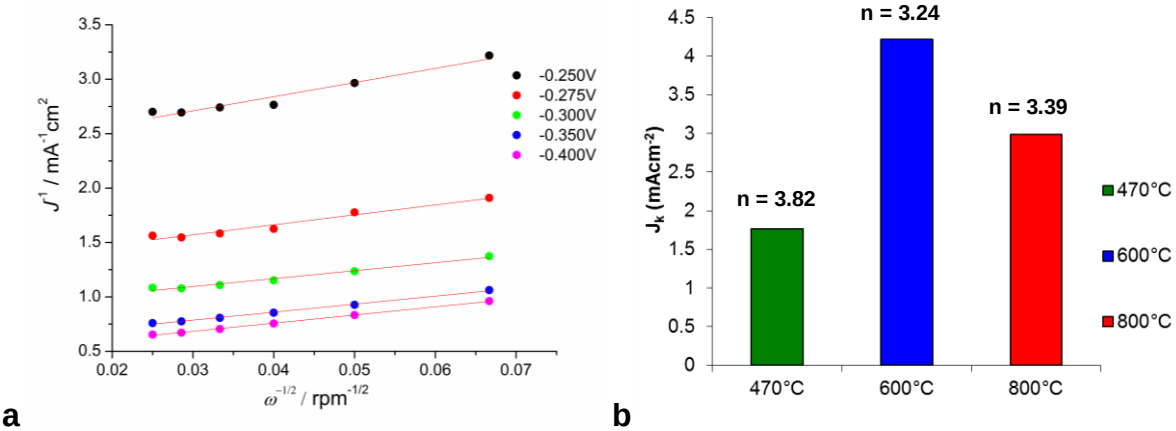

Figure 4-29: **a:** Koutecky-Levich plots at different electrode potential for **4-19-470** and **b:** electrochemical activities given as kinetic limiting denisites J_k (for commercial Pt-C electrode n = 3.91, J_k = 4.44 $mAcm^{-2}$).

The slopes remain constant over the potential range of 0.25 to 0.40 V suggesting similar electron transfer numbers for the ORR at different electrode potentials. Generally, first-order kinetics show linearity and parallelism of the plots. The kinetic parameters can be analyzed on the basis of the Koutecky-Levich equations (cf. chapter 2.2.2). According to these equations the number of electrons n transferred and the kinetic limiting current density J_k can be obtained from the slope and intercept, respectively (C_o = 1.2*10^{-3} molL^{-1}, D_o = 1.9*10^{-5} cms^{-1}, ν = 0.1 m^{2}s^{-1}).

The determined values for the pyrolyzed samples are summarized in Table 4-2, with the highest number of electron transferred (n = 3.82) for **4-19-470** suggesting a four-electron transfer in oxygen reduction. Unfortunately, the onset potential and J_k for this sample showed lower values as for the sample pyrolyzed at 600°C. The onset potential for **4-19-600** was determined to be -0.17 V. The calculated J_k value of 4.22 mAcm^{-2} at -0.35 V for **4-19-600** was almost as high as that of commercially available Pt-C (4.44 mAcm^{-2} at -0.35V).[220]

Table 4-2: Results for the RDE measurements in basic conditions (0.1 M KOH).

Compound	J_K[a] [mAcm^{-2}]	k[a]	n[a]	onset potential [V]	cathode peak [V]
4-19-470	1.7661	4.00*10^{-3}	3.82	-0.22	-0.34
4-19-600	4.22172	11.25*10^{-3}	3.24	-0.17	-0.26
4-19-800	2.98339	7.60*10^{-3}	3.39	-0.19	-0.29

Summarizing, the electrochemical catalytical activity of cobalt complex **4-19** towards the ORR was also evaluated and proven in alkaline conditions. Similar trends as for the results in acidic conditions could be observed. In particular, heat treatment improved significantly the activity but milder pyrolysis turned out to be more beneficial. As mentioned before, this could be explained if the thermal properties of **4-19** were taken into account (Figure 4-26). The reduced results for **4-19-800** were due to the incipient decomposition of the macrocyclic core if heat treated at 800°C. If pyrolyzed at 600°C the core was still existent. TGA measurements showed that complex **4-19** is stable till 480°C, and therefore, the intact complex is responsible for promising results for **4-19-470**. It is suggested, that the alky groups help to crosslink the individual macrocycles resulting in the accumulation of the active sites, which is believed to be beneficial in catalytic performance. Related discotic polycyclic aromatic hydrocarbon are known to cross-link after heat treatment in the

mesophase.[221] This strengthens the suggestion to synthesize oligomeric species and connect the individual active sites for further improvement in performance (see chapter 4.1.8).

4.1.7 Surface Deposition

Visualization of molecules by scanning tunneling microscopy (STM)[222] permits information about the mode of 2D network formation and the interfacial assembly. Sometimes, it is even feasible to monitor the progress of a chemical reaction or catalytic processes by this technique.[223-225] Therefore, the visualization of cobalt complex **4-19** by STM might offer the possibility to follow the reduction of oxygen at the metal center. Besides the deposition of molecules on surface by the LANGMUIR BLODGETT technique[226-227] or sublimation,[228-229] the deposition from solution by self-assembling monolayers is possible.[230-232] Usually, the formation of self-assembled monolayers is induced by the spontaneous physisorption of the molecules on a suitable substrate.[233-234] Linear, long alkyl-chains attached at the periphery of the molecule have been shown to be the driving force for the formation of monolayers.[235] In other words, the *tert*-butyl groups attached at ligand **4-18** are poorly suitable for the deposition on a substrate, and long alkyl-chains had to be introduced to allow the formation of self-assembling monolayers.

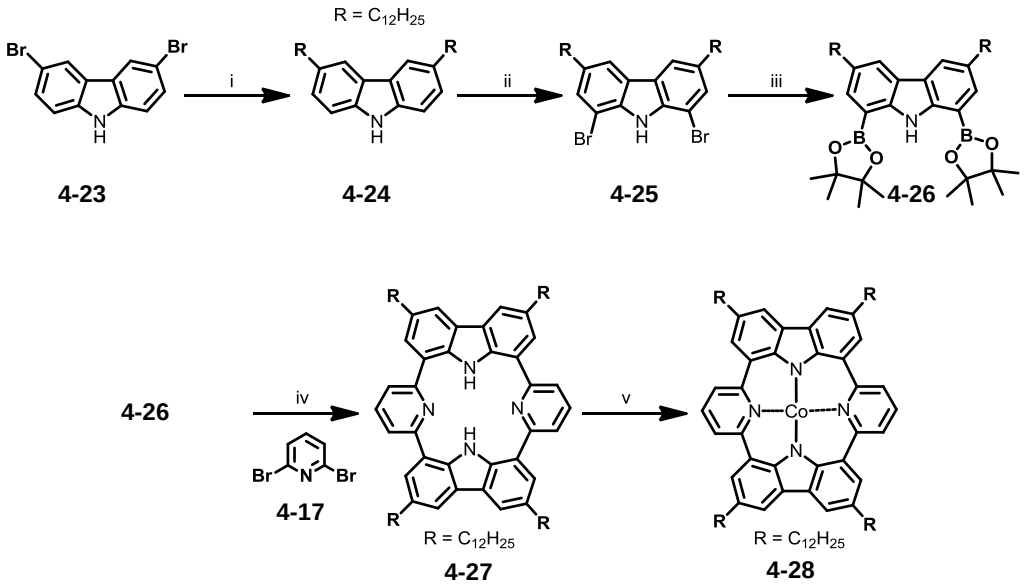

Scheme 4-6: Synthesis of long alkyl-chain substituted macrocycle **4-27** and its cobalt complex **4-28**. Conditions: *i* docecylmagnesium bromine (1M in Et_2O), $Pd(dppf)Cl_2$, THF, 75°C, 56%; *ii* NBS, AcOH, DCM, rt, 90%. *iii* 1. *n*-BuLi, THF, 0°C, 2. CO_2, rt, 3. *t*-BuLi, THF, -78°C, 4. **4-15**, 50%; *iv* $Pd(PPh_3)_4$, 2M KCO_3, EtOH, toluene, 85°C, 15%.*v* $M(OAc)_2$, DMF, microwave, 300 W, 170°C.

3,6-Dialkylated carbazole derivatives are commonly prepared by the reduction of the corresponding carbonyl derivatives, which can be obtained by Friedel-Crafts acylation protocols.[236] To avoid the two step synthesis, palladium-catalyzed Kumada-coupling reaction between commercially available 3,6-dibromo carbazole (**4-23**) and dodecylmagnesium bromide was applied (Scheme 4-6).

Both compounds, the free ligand **4-27** and the cobalt complex **4-28**, were investigated by solution STM in collaboration with the group of Prof. J. Rabe at the Humboldt-Universität zu Berlin. The experiments were conducted by Jose David Cojal by dissolving the compounds in *n*-phenyloctane at a concentration of 10^{-6} M. The solutions were then applied onto a basal plane of a freshly cleaved surface of HOPG (**h**ighly **o**rdered **p**yrolytic **g**raphite). The STM image of compound **4-27** (Figure 4-30) was recorded at the solution/HOPG interface with a bias voltage of -800 mV and a tunneling current of 100 pA. In the STM image, the electron rich π-systems appear as bright features whereas the regions with lower energy density, in this case the alkyl-chains, in darker contrast. The macrocyclic core created bright features suggesting that the electrons were well delocalized around it.

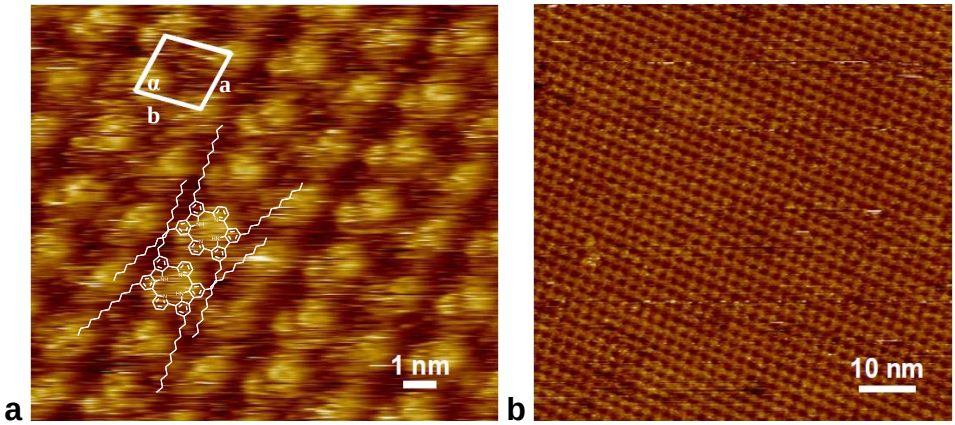

Figure 4-30: STM image of saturated *n*-phenyloctane solution of **4-27** on HOPG. **a:** Unit cell is indicated; lattice constants: a = 2.08±0.07nm, b = 2.22±0.05 nm, α = 75.4±1.1°, A = 4.47±0.07 nm^2; U_S = -800 mV, I_t = 100 pA).

By the deposition of macrocycle **4-27** from *n*-phenyloctane on HOPG a highly ordered monolayer was formed (Figure 4-30). The substance formed uniform patterns with a unit cell spanned by 4 molecules (characteristic parameters of a = 2.08±0.07 nm, b = 2.22±0.05 nm and α = 75.4±1.1°). The molecules were aligned in linear lamellar arrays with the interdigitated alkyl-chains keeping the core of the macrocycle at a fixed distance. The homogenous assembly showed almost no defects or impurities over large areas. Similar behavior has also been observed for related *meso*-tetraalkylporphyrins on HOPG.[237]

Unfortunately, the investigation of the cobalt-complex **4-28** by STM was not successful. This could be explained by agglomeration of the molecules due to the presence of the cobalt. Another explanation could be that simply the forces *e.g.* electrostatic or van der Waals, driving the physisorption are not strong enough to create the self-assembly monolayer.

4.1.8 Oligomerization of macrocycle 4-18

As described earlier, the four-electron reduction of oxygen to water is favored by the simultaneous rupture of the oxygen molecule (cf. chapter 2.2). Therefore, the electrochemical performance of the cobalt(II) complex **4-19** could be improved if the active site are connected to each other. Additionally, we believe that by the covalent connection of the active sites the need of heat treatment can be avoided. Thus, the chemical approach includes an oligomerization of the macrocyclic monomer (cf. chapters 4.1.5 and 4.1.6). For the oligomerization of macrocycle **4-18**, Yamamoto[238] reaction conditions were considered. Therefore, the macrocyclic core had to be functionalized with a halide at the pyridine ring in *para* position to the nitrogen (position 5, Scheme 4-7).

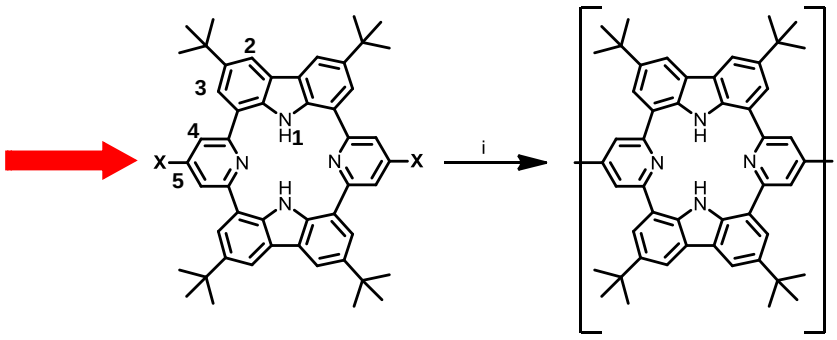

Scheme 4-7: Oligomerization of macrocycle **4-18** using Yamamoto (*i*) reaction conditions.

For this reason, firstly direct halogenations on the already formed macrocycle **4-18** by the treatment with bromine or NBS have been examined. Unfortunately, all trials failed and a different synthetic strategy was developed, consisting of the introduction of functional groups at the pyridine unit before the ring-closure. The functionalization of pyridines usually requires the preparation of pyridine N-oxides[239] as intermediates, which have to be handled with great caution. On the other hand direct lithiation of 2,6-dihalogenated pyridines generally dirigates *meta* to the nitrogen.[240] Knochel *et al.* showed that the use of highly active TMPMgCl·LiCl (TMP = 2,2,6,6-tetramethylpiperidine) furnishes magnesiated

pyridines selectivity in *para* postion to the nitrogen.[241] Further reactions with electrophiles *e.g.* I_2 or DMF provide then the expected products.

In the present case, iodine was not suitable since it would hinder the subsequent macrocyclization due to the major reactivity of iodine over bromine (at the pyridine) in Suzuki-Miyaura cross-coupling reactions.[135] Thus, chlorine was the perfect halogen because it prevented the mentioned selectivity problems and supplementary served as a well reactive halogen in Yamamoto reactions.[238]

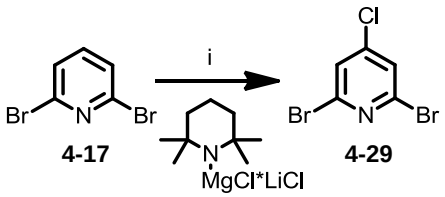

Scheme 4-8: Synthesis 4-chloropyridine **4-29**. Conditions: *i* TMPMgCl·LiCl, THF, C_2Cl_6, -30°C, 44%.

2,6-Dibromo-4-chloropyridine (**4-29**) was synthesized by treating 2,6-dibromopyridine (**4-17**) with a 1M solution of TMPMgCl·LiCl at -30°C followed by the addition of hexachloroethane (C_2Cl_6). 4-Chloropyridine **4-29** was obtained in 44% yield as a colorless solid (Scheme 4-8). The subsequent cyclization reaction of compound **4-29** and 1,3,2-dioxaborolan-2-yl-9*H*-carbazole derivative **4-16** was performed under standard Suzuki-Miyaura conditions, as also described for macrocycle **4-18** (Scheme 4-9, cf. 4.1.1). The ring-closure proceeded in 13% yield to give macrocycle **4-30** as a colorless solid.

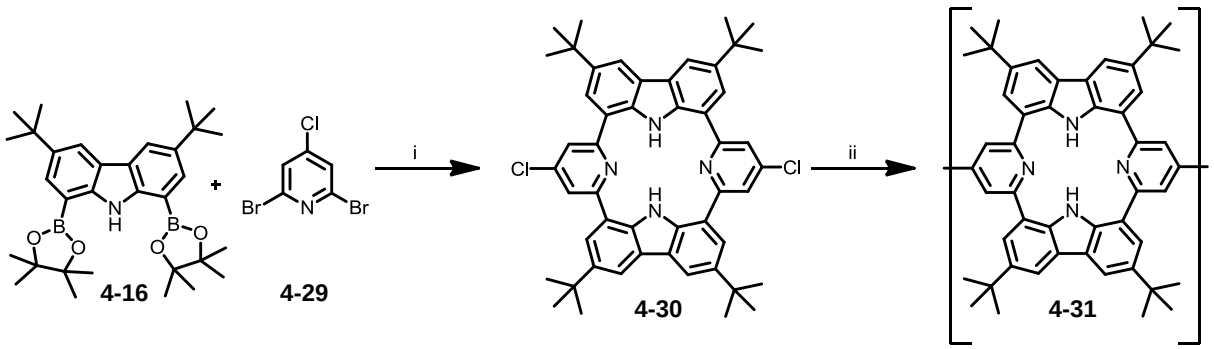

Scheme 4-9: Synthesis of macrocycle **4-30** and its oligomerization. Conditions: *i* $Pd(PPh_3)_4$, 2M K_2CO_3, EtOH, toluene, 85°C, 13%; *ii* $Ni(COD)_2$, COD, 2,2-bispyridine, toluene, DMF, 60°C.

The structure of macrocycle **4-30** was verified by NMR spectroscopy, Maldi-Tof and HRESI MS spectrometry. Its ^{1}H NMR spectrum showed similar signals to macrocycle **4-18**,

with the triplet for proton in *para* position to the pyridine nitrogen missing due proving the substitution with chlorine.

For the purpose of linear oligomer formation and to avoid the competitive generation of large macrocyclic compounds, the reaction was carried out in concentrated solution. The oligomerization was performed under Yamamoto conditions[238] by adding compound **4-30** to a solution of $Ni(COD)_2$, COD, 2,2-bipyridine in DMF/toluene at 60°C. The reaction mixture was stirred for 3 days at this temperature and then precipitated into a methanol/HCl solution. The precipitate was filtered off and reprecipitated two times. GPC results showed a mixture of oligomeric products (M_n = 3749 g/mol, M_w = 20993 g/mol, PDI = 5.60, referenced against PS in THF, UV detector). For comparison, the monomer macrocycle **4-30** was also subjected to a GPC measurement and showed M_n = 430 g/mol M_w = 536 g/mol, PDI = 1.24 (referenced against PS in THF, UV detector). If the number average molecular weight M_n are compared, the oligomeric species correspond to approx. 8-9 repeating units. Nevertheless, comparing the values of the single maximum of the macrocycle **4-30** with local maxima of **4-31**, the oligomer exists as a mixture of oligomeric species with repeating units (ru) varying between 4 to 60 ru (Figure 4-31).

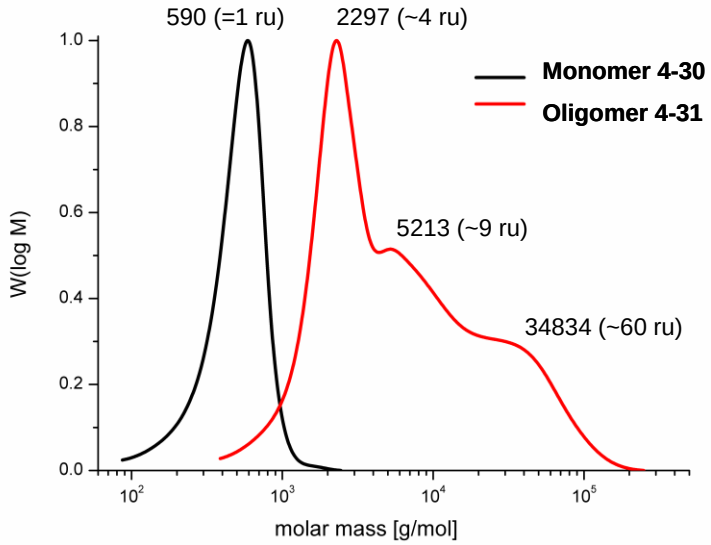

Figure 4-31: Molecular mass distrubtion of oligmeric species **4-31** (red) benchmarked against monomer **4-30** (black). GPC measurements were performed in THF at rt against PS standard with UV detection.

The oligomeric mixture was not fractionized but the composition served sufficiently for the investigation of the oligomeric effect on the electrochemical activity towards the ORR. Therefore, **4-31** was treated with $Co(OAc)_2$ in DMF to insert Co(II) into the macrocyclic

cavities to yield oligomeric cobalt complex **4-32**. The insertion was proven by Maldi-Tof spectrometry.

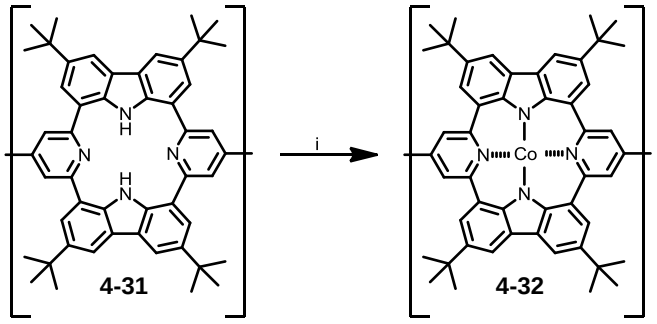

Scheme 4-10: Complexation of oligomer **4-31** with cobalt. Conditions. *i* $Co(OAc)_2$, DMF, microwave, 300 W, 170 °C.

The absorption and emission spectra of oligomer **4-31** will be discussed in the next chapter (4.1.9) along with that of the dimer **4-34**.

4.1.9 Dimerization of macrocycle 4-18

Having established the introduction of chlorine at the pyridine unit, the design of a defined dimer of macrocycle **4-18** was manifest. The synthesis started with the statistically macrocyclization reaction between compounds **4-16**, **4-17** and **4-29** (Scheme 4-11).

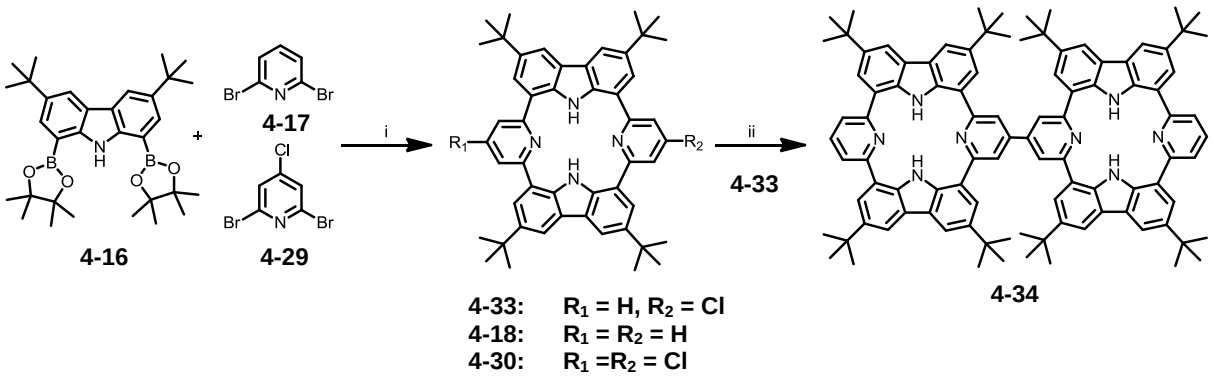

Scheme 4-11: Synthesis of dimer **4-34**. Conditions: *i* $Pd(PPh_3)_4$, 2M K_2CO_3, EtOH, toluene, 85°C, 7%; *ii* **4-33**, $Ni(COD)_2$, COD, 2,2-bispyridine, toluene, DMF, 60°C.

The statistical reaction afforded not only the desired monosubstituted macrocycle **4-33** but also, disubstituted compound **4-30** and the bare ring **4-18**. Nonetheless, the resulting three cycles could be separated by column chromatography. However, the yield of macrocycle

4-33 was reduced to 7%. The formation of macrocycle **4-33** was proven by NMR spectroscopy and HRESI MS spectrometry. The ^{1}H NMR spectrum of unsymmetrical compound **4-33** was more complicated compared to macrocycle **4-18**, due to the loss of symmetry caused by the presence of only one chlorine substituent (Figure 4-32). Therefore, one set of signals for each "side" of the molecule was observed in both, the ^{1}H NMR and the ^{13}C NMR spectrum. Due to the deshielding effect of the chlorine substituent, the protons which are influenced by the electronegative chlorine were shifted to lower fields. Unfortunately, the doublet for the proton *meta* to the pyridine's nitrogen (●) was superimposed by the singlet arising from the proton next to the chlorine (●). Even the *tert*-butyl groups were no longer identical and resonated in two individual signals (Figure 4-32 inlay, ●●).

The dimerization was performed under the same conditions as described for the oligomerization of **4-30** (cf. chapter 4.1.8). Macrocycle **4-33** was added to a solution of Ni(COD)$_2$, COD, 2,2-bipyridine in DMF/toluene at 60°C. Dimer **4-34** could be purified by column chromatography and was isolated in 30% yield as a yellow solid.

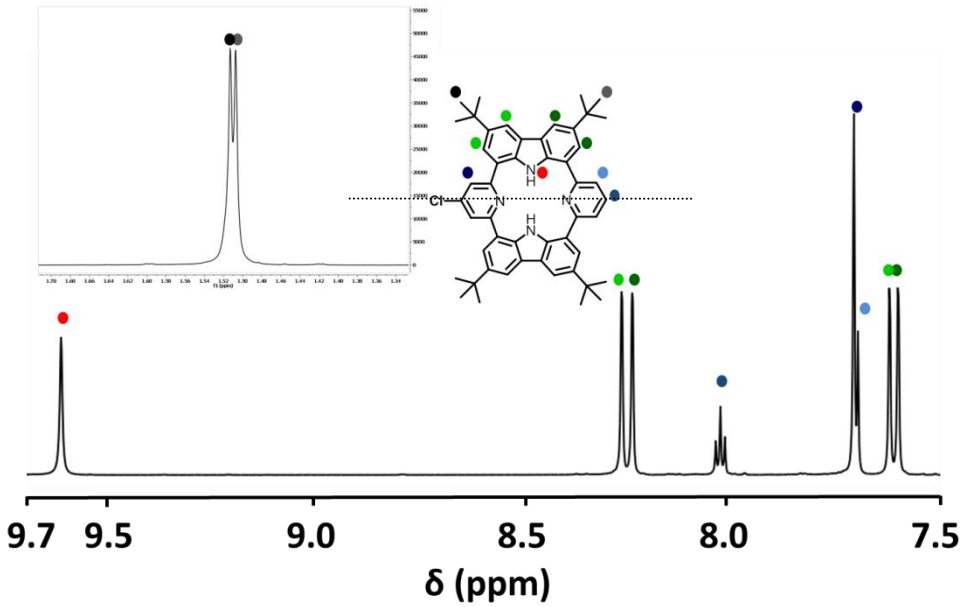

Figure 4-32: Aromatic region of the ^{1}H NMR spectrum of macrocycle **4-33** in CD_2Cl_2, 298 K, 700 MHz. Inlay: aliphatic region showing the *tert*-butyl groups.

Similar to its unsymmetrical starting material **4-33**, dimer **4-30** exhibited two sets of aromatic signals and only one signal for the proton at the nitrogen of the carbazole in the ^{1}H NMR spectrum (Figure 4-33). Compared to monochlorinated compound **4-33**, the singlet signal for the proton *meta* to the pyridine's nitrogen (●, from 7.70 to 8.14 ppm) was

shifted to lower fields in dimer **4-30**. This can be attributed to the lower deshielding effect of the substituent at this position, which is in this case the macrocycle itself. The strucutre of dimer **4-34** was further evidence by HRESI MS spectrometry.

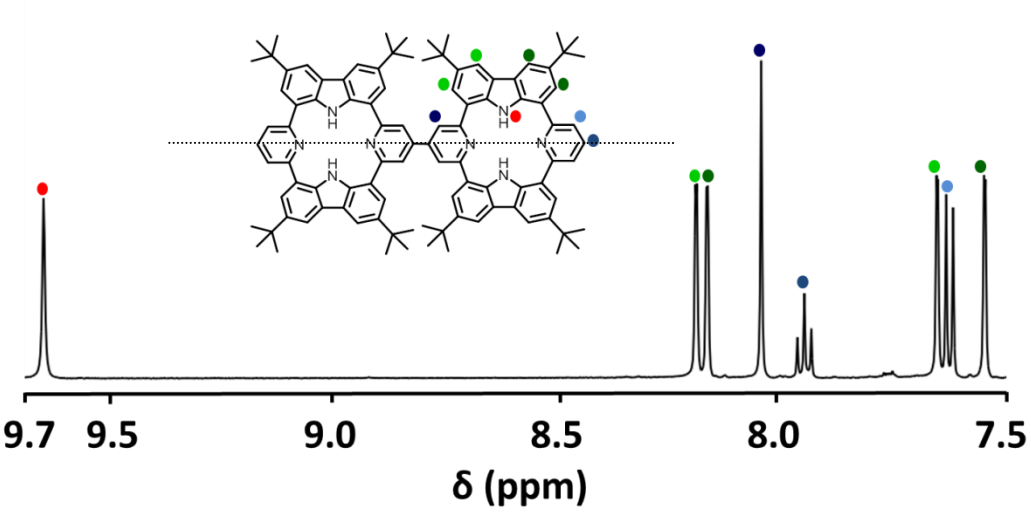

Figure 4-33: Aromatic region of the ^{1}H NMR spectrum of dimer **4-34** in CD_2Cl_2, 298 K, 500 MHz.

GPC analysis approximately reflected the relative repeating units (ru) of dimer **4-34** (2 ru) compared to monomer **4-18** (1 ru) and oligomeric species **4-31** (> 4 ru).

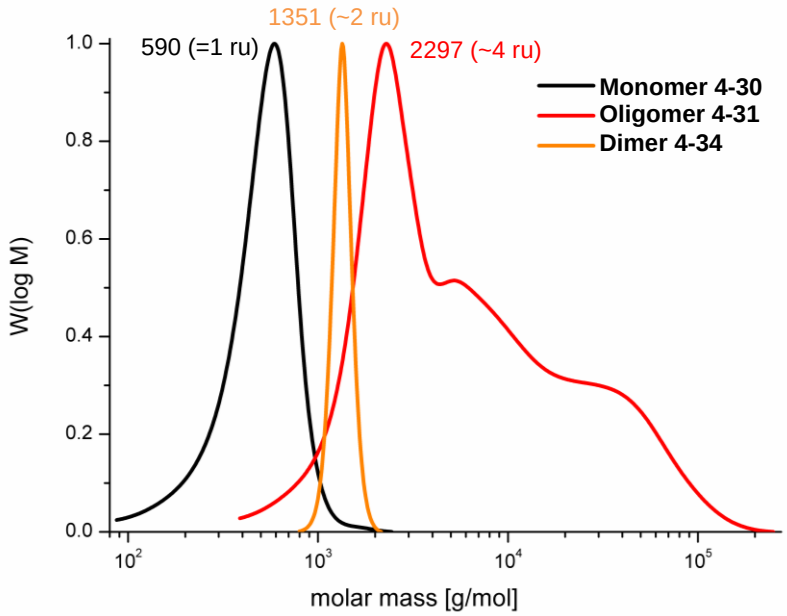

Figure 4-34: Molecular mass distrubtion of dimer **4-34** (orange) and oligmeric species **4-31** (red) benchmarked against monomer **4-30** (black). GPC measurements were performed in THF at rt against PS standard with UV detection.

Electronic absorption and emission spectra were recorded in DCM (c = $5*10^{-5}$ M) for all macrocycles **4-18**, **4-33**, **4-30**, dimer **4-34** and oligomer **4-31** (Figure 4-35). The absorption spectra for all compounds showed absorption maxima in the same region. This wass not surprising, as monocyclic compounds **4-18**, **4-33** and **4-30** are analogues and differ only by the presence of the chlorine substituents. Interestingly, dimer **4-34** and oligomer **4-31** behaved also similar to the monocyclic derivatives and absorbed in the same region, which could be explained by the lack of conjugation between the individual repeating units. The free rotation of the single bond between the units resultec in an inefficient extension of the π-conjugation in the ground state. Similar behavior has been observed for other non-conjugated oligoarylenes[242] suggesting electronically decoupled monomeric units.[243-245]

The emission maxima for chlorinated compounds **4-33** (λ_{em} = 412 nm) and **4-30** (λ_{em} = 414 nm) were redshifted due to presence of the chlorine substituents compared to macrocycle **4-18** (λ_{em} = 404 nm). Surprisingly, the emission maxima of dimer **4-34** and oligomer **4-31** (λ_{em} = 472 nm and 492 nm, respectively) were highly bathochromically shifted compared to the monocyclic compounds. As this was not the case in the absorption, this might be due to a partial flattening of neighboring cycles in the excited state enhancing the conjugation between the repeating units.

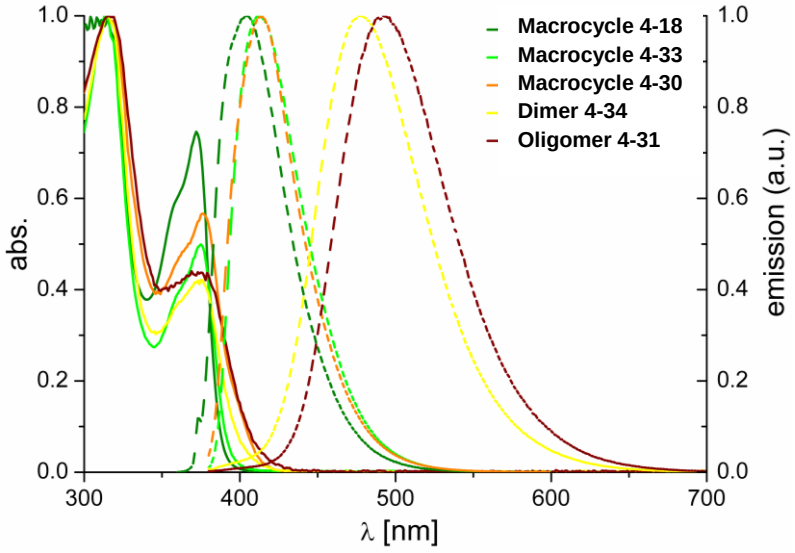

Figure 4-35: Electronic absorption and emission spectra of macrocycles **4-18**, **4-33**, **4-30**, dimer **4-34** and oligomer **4-31**; (c = $5*10^{-5}$ M in DCM).

Quantum Yields (QY) were estimated for all compounds using the Comparative Method (Table 4-3).[186] The QY for the monocyclic systems **4-18, 4-30** and **4-33** were all very alike

in the range of 0.42-0.46, although generally in the presence of heavy atom substituents such as chlorine, fluorescence quenching is expected.[246] On the contrary, the QY for dimer **4-34** and oligomer **4-31** were drastically reduced to a minimum of $\Phi_f = 0.11$. This can be attributed to the favored free rotation around the single bond which combines the individual macrocycles. Twisting of the monomeric units are known to hinder high luminescence efficiency in polymers.[247]

Table 4-3: Summary of the electronic absorption and emission data in DCM (c = 5*10^{-5}M).

compound	λ_{abs} [nm]	λ_{em} [nm]	Φ_f [a]
4-18	313, 372	404	0.46
4-33	313, 377	412	0.43
4-30	315, 375	414	0.42
4-34	315, 375	472	0.14
4-31	317, 376	492	0.11

[a] Φf were estimated using the Comparative Method.[186] Samples in THF are referenced against Coumarin 1 in EtOH, λex = 346 nm.

4.1.10 RRDE measurements

As described earlier, the purpose to synthesize the oligomeric complex **4-32** was to improve the catalytic activity of monocyclic complex **4-19** and to avoid heat treatment. Since complex **4-19** did not show activity in acidic conditions without heat treatment (cf. chapter 4.1.5) the influence of the oligomerization (monomeric cobalt(II) complex **4-19** *vs.* oligomer **4-32**) was evaluated in basic conditions where measurable quantites of current density was obtained (0.1 M KOH, Figure 4-36).

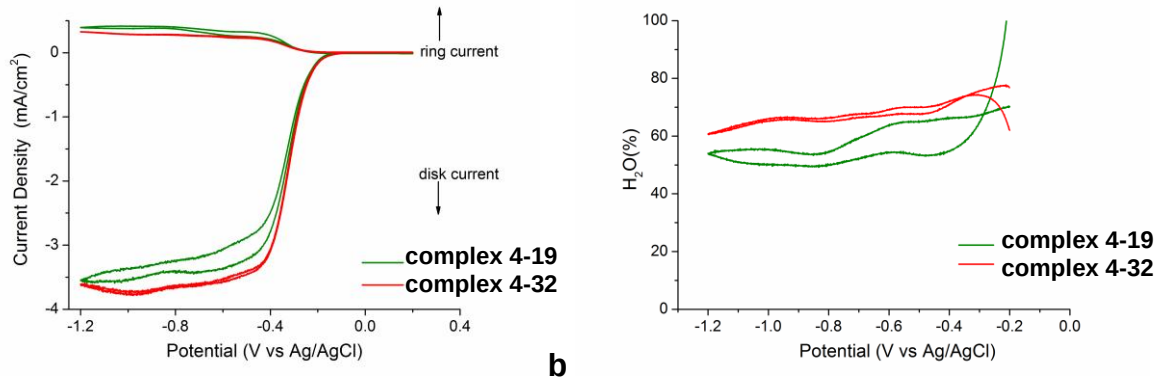

Figure 4-36: **a:** Ring and disk current at rt of cobalt complex **4-19** (black) and oligomeric complex **4-32** (red) in alkaline conditions (0.1 M KOH, 1600 rmp); **b:** efficiency of H_2O production.

The experiments were conducted in collaboration with Sumitomo Chemical Co using RRDE measurements without prior thermal treatment of the samples. The electrochemical evaluation unfortunately showed that the ORR activity of **4-32** was only slightly improved compared to single complex **4-19**. As depicted in Figure 4-36, the disk current for the oligomeric species **4-32** (red line) featured only a marginally superior current density over the measured range compared to the monomer **4-19** (green line). The negligible improvement was also reflected in the almost identical efficient H_2O production of around 60% in the applied potential region.

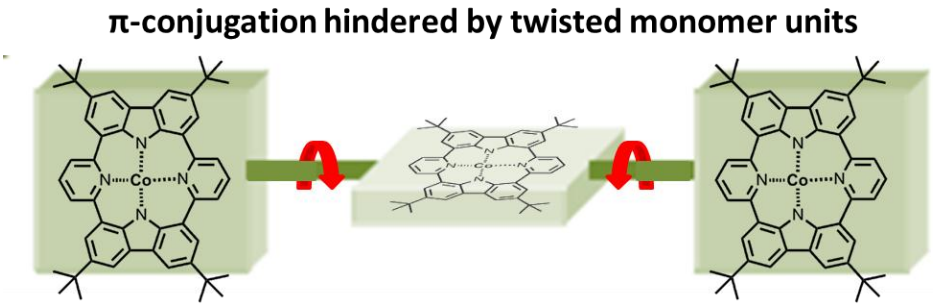

Figure 4-37: Schematic illustration of the π–conjugation in planar and non-planar polymers.

The small effect on the electrochemical performance can be explained by the non-planarity of the oligomeric species and the free rotation around the single bonds (Figure 4-37). Due to the twisting, the oxygen is not able to simultaneously interact with two cobalt centers in the dual-site mode (bridged-*cis* configuration), and therefore the four-electron reduction cannot be promoted. Further, the single bonds connecting the monomeric units do not allow π-conjugation between the individual macrocycles and thus hinder improved electron supply.

Due to the already small improvement in activity observed for the oligomeric complex **4-32**, the dimer **4-34** was not taken into consideration for an electrocatalytic evaluation. Therefore, no further studies on these systems were done and a novel planar well π-conjugated multi-metal complex was developed which will be explained in detail in the second part of the present work (see chapter 5).

4.2 $(NH)_4$ – motif porphyrinoid

For symmetrically substituted porphyrins, the degenerate *trans*-NH-tautomers are most favored, resulting in two pyrrolic and two imine-type nitrogens. The motif of four pyrrolic (NH) groups combined in one macrocyclic core can be found in *e.g.* calix[4]pyrroles.[136] Calix[4]pyrroles are *meso*-octasubsituted porphyrinogens with the pyrrole rings linked by sp^3 hybridized carbon atoms and hence are not susceptible to oxidation which would result in the porphyrin state. They do not possess a diamagnetic ring current in the macrocyclic core as it is in the case of porphyrins. The pyrrolic NH group has been proven to be useful as hydrogen-bond donor in anion recognition chemistry, especially for calixpyrroles.[248-251] Moreover, due to the $(NH)_4$ cavity calix[4]pyrroles offer the opportunity to bind metals in unusual oxidation states.[137, 252-254]

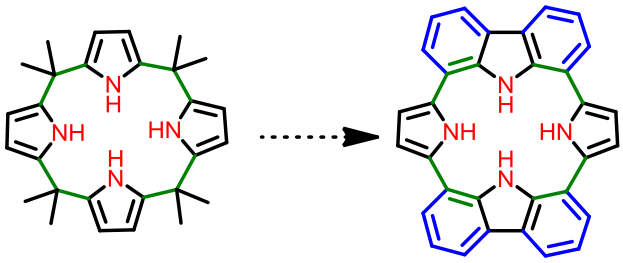

Figure 4-38: From non aromatic calix[4]pyrrole to aromatic $(NH)_4$ macrocycle.

By the replacement of two pyrrolic units in a calixpyrrole by carbazoles, the valuable $(NH)_4$ motif is maintained while the sp^3 carbon atoms are replaced by stable sp^2 carbon atoms from the fused benzene rings. In this form the molecule does not exhibit porphyrin-like aromaticity but four individual aromatic heterocycles are combined together resulting in an overall aromatic character. The fusion of benzenes results in an oxidizable macrocycle which can adopt the porphyrin state, as will be described later (see chapter 4.2.3).

4.2.1 Synthesis

Macrocycle **4-38** was synthesized, similar to pyridine-containing macrocycle **4-18**, *via* a fourfold Suzuki-Miyaura coupling reaction in a diluted system (10^{-4} M, Scheme 4-12). Carbazole is acting as the electrophile, unlike in the synthesis of macrocycle **4-18**. Since

pyrrole tends to easily polymerize at the α-α' positions,[255] the introduction of boronic ester groups at this positions avoided the formation of side products. Furthermore, the substitution benefits the handling, because compound **4-37** is a crystalline powder and can be readily crystallized compared to liquid pyrrole. This is also beneficial for the purification of the compound since high purity starting materials are required for the Suzuki cross-coupling reaction as a consequence of the Carothers' law.[256]

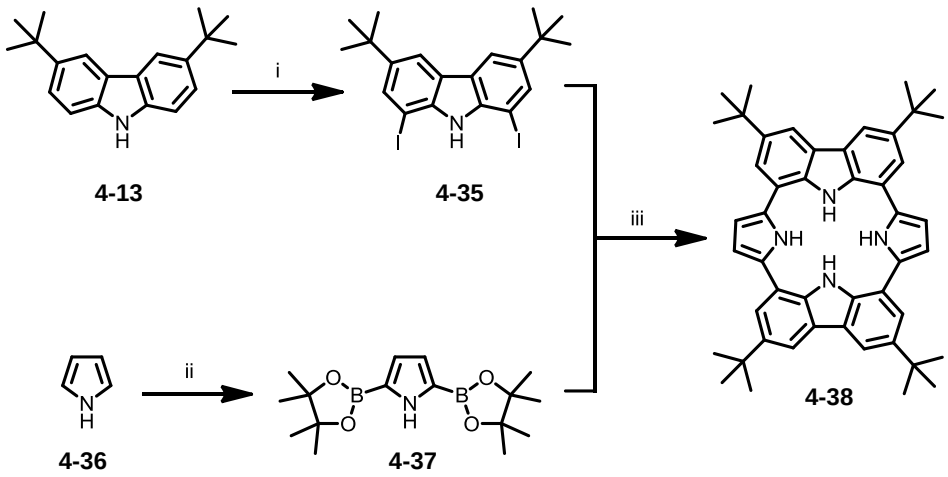

Scheme 4-12: Synthesis of macrocycle **4-38**. Conditions: *i* H_2O, H_2SO_4, HIO_4*$2H_2O$, I_2, AcOH, 80°C, 50%; *ii* $[IrCl(COD)]_2$, dtbpy, bisbinacolatodiboronate, octane, 80°C, 60%; *iii* $Pd(PPh_3)_4$, 2 M K_2CO_3, EtOH, toluene, 85°C, 10%.

As described earlier, the introduction of halogens at the carbazole at positions 1 and 8 is well established. Here, iodine was chosen over bromine to ensure high reaction rates during the oxidative addition of the catalytic cycle. 3,6-Di-*tert*-butyl-1,8-diiodo-9*H*-carbazole (**4-35**) was synthesized following the literature procedure[155] in 50% yield starting from alkylated carbazole **4-13**. Pyrrole (**4-36**) can be functionalized with boronic ester groups at position 2 and 5 using an iridium catalyzed borylation reaction.[257] Compound **4-37** could be isolated in 60% yield as colorless crystals. Both building blocks, compounds **4-37** and **4-35**, could be obtained in high purity by repeated recrystallizations. The fourfold Suzuki-Miyaura cross-coupling reaction proceeded in 10% yield. Macrocycle **4-38** was obtained as a greenish solid which proved to be difficult to handle during the purification process, due to its low stability towards heat and acidic silica gel. The high instability can be attributed to its extreme electron richness, originating from the electron-rich character of its building blocks pyrrole and carbazole.[258-259] Column chromatography was possible, but suffered from decomposition of the compound on the acidic silica (also when basificated) leading to only a low amount of pure macrocycle. Due to the sensitivity towards heat, recrystallization proved

to be extremely difficult as well. In order to investigate the sensitivity of compound **4-38** towards heat, temperature dependent UV-vis spectroscopy was performed (Figure 4-39). Therefore, macrocycle **4-38** was dissolved in THF (c = $5*10^{-5}$ M) and a spectrum every 10 K was registered starting from 283 K up to 353 K. At already 313 K (Figure 4-39, blue line) a significant change in the absorption could be observed which indicated decomposition of macrocycle **4-38** at this temperature.

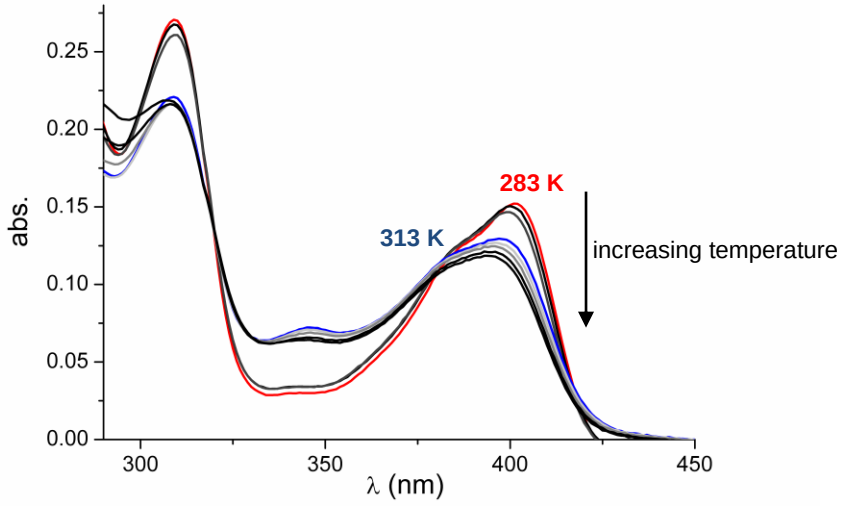

Figure 4-39: Temperature dependent UV-vis spectra of macrocycle **4-38** in THF (c = $5*10^{-5}$ M).

If handled with care, enough pure material of macrocycle **4-38** could be achieved and its structure could be characterized by NMR spectroscopy, Maldi-Tof and HRESI MS spectrometry.

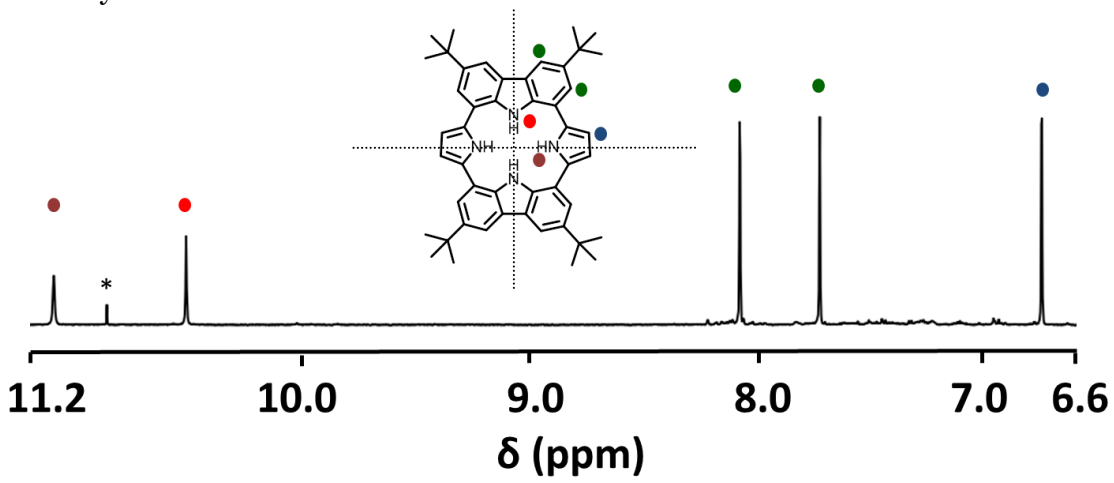

Figure 4-40: Aromatic region of the ^{1}H NMR spectrum of macrocycle **4-38** in THF-d_8, 298 K, 700 MHz (*from solvent).

Macrocycle **4-38** provided the same C_{2v} symmetry as compound **4-18** and therefore featured clear signals which were easy to assign (Figure 4-40). The protons at the carbazole and pyrrole resonated in the typical aromatic region, coming to support no evidence for a macrocyclic aromaticity as it is found for porphyrins. The signal for the *β*-proton at the pyrrole was shifted to lower field (6.73 ppm) compared to the carbazole protons, due to its more electron-rich character. Also the NH signals resided at 10.53 and 11.13 ppm and did not indicate the existence of a diamagnetic ring current. $^{1}H^{15}N$ correlations for the protons attached to the nitrogens were measured with HSQC (heteronuclear single quantum coherence) techniques. HSQC is a two-dimensional method and detects the correlation of two different nuclei. The nuclei usually couple scalar over only one bond and the resulting spectra are therefore facile to interpret. The $^{1}H^{15}N$ HSQC spectrum of macrocycle **4-38** nicely revealed the correlations of the different protons attached to the nitrogens of the carbazole and pyrrole, respectively (Figure 4-41). The proton attached to pyrrole resonated at -231.35 ppm and the chemical shift for the carbazole NH was -271.68 ppm (relative to nitromethane), which is in good agreement with values from the literature.[260-261] Unsubstituted carbazolic nitrogens resonate at higher fields compared to the nitrogen in pyrroles due to their higher electron density and, therefore, higher magnetic shielding.

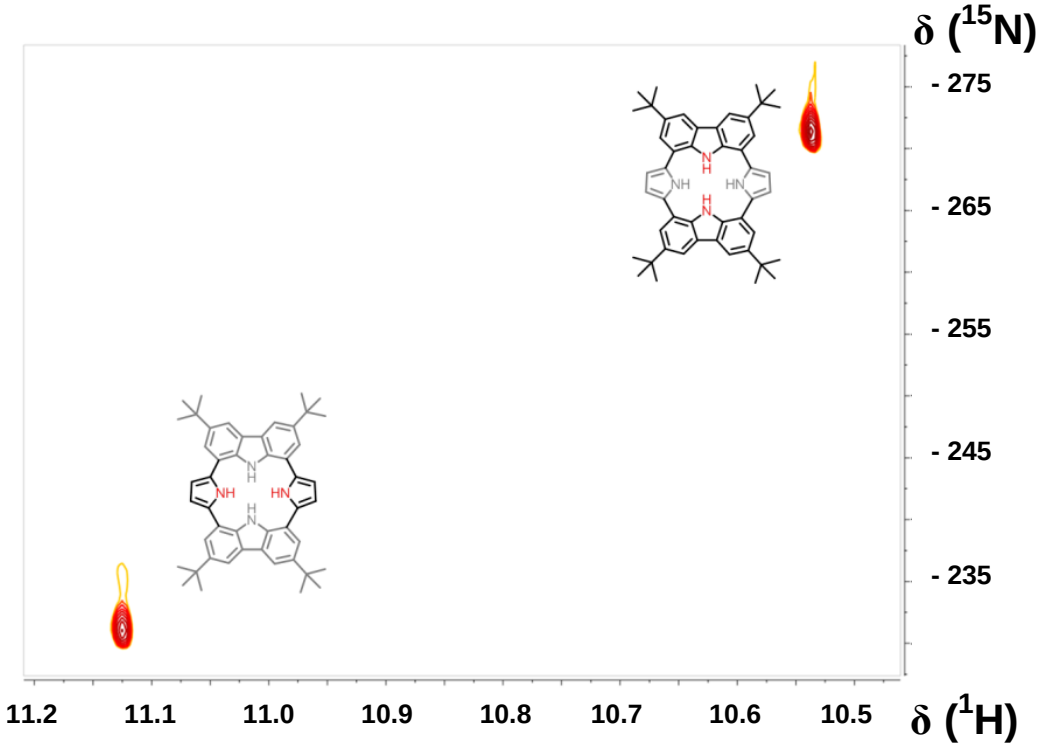

Figure 4-41: $^{1}H^{15}N$ HSQC 2D NMR spectrum of macrocycle **4-38** in THF-d_8, 298 K, 700 MHz, chemical shifts are referenced to nitromethane nitrogen at 0 ppm.

4.2.2 Electronic Structure

The absorption and emission spectra of macrocycle **4-38** were recorded in THF at rt and are depicted in Figure 4-42. The absorption spectrum showed two local maxima at λ_{max} = 307 and 400 nm. The carbazole-centered transition[152, 185] at λ = 307 nm was only little hypsochomically shifted compared to macrocycle **4-18** (cf. chapter 4.1.3). On the other hand the maximum at higher wavelength, was bathochromically shifted with 27 nm and could be interpreted as a stronger donor-acceptor interaction between the carbazole and pyrrole in **4-38** relative to carbazole and pyridine in **4-18**. The optical energy gap was estimated from the absorption edge to be E_{opt} = 2.94 eV.

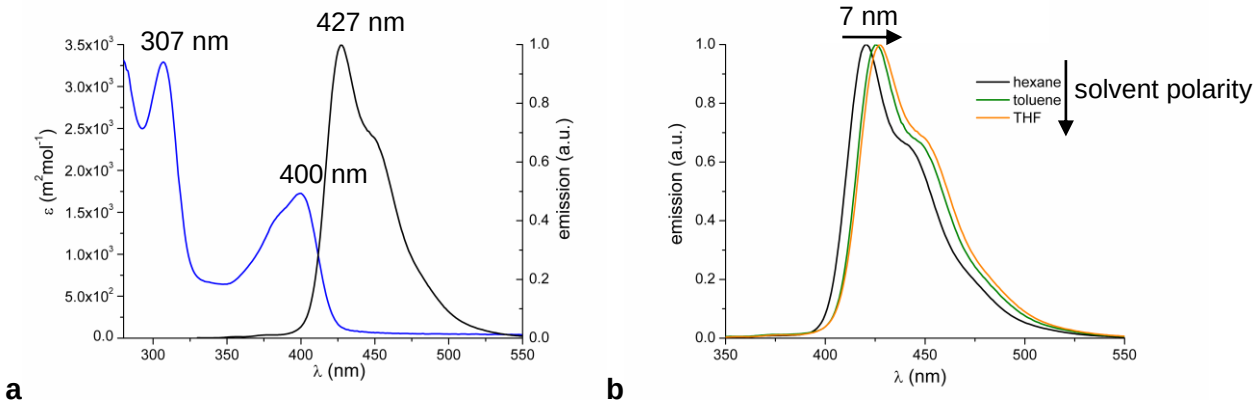

Figure 4-42: **a:** Electronic absorption and emission spectra of macrocycle **4-38** (c = 5*10^{-5} M in THF), **b:** Solvent dependent emission spectra of macrocycle **4-38** (c = 5*10^{-5} M, λ_{ex} = 307 nm).

The blue emission of macrocycle **4-38** (λ_{em} = 427 nm) was relatively strong with a quantum yield Φ_f = 0.68. The quantum yield was estimated against coumarin 1 at rt in THF (λ_{ex} = 349 nm) using the Comparative Method.[186] The emission spectrum of compound **4-38** recorded in solvents with different polarities revealed a bathochromic shift of the emission with increasing the polarity (Figure 4-42b). This can be attributed to an intramolecular charge transfer (ICT) from the donor to the acceptor moiety in the excited state.[246]

The redox properties of macrocycle **4-38** were investigated using cyclic voltammetry under the same conditions as described for compound **4-18** (cf. chapter 4.1.3). Macrocycle **4-38** showed similar behavior as compound **4-18** with two irreversible oxidation waves corresponding to the successively oxidized carbazole units to their cation radicals (Figure 4-43). The two-step oxidation also suggests an electrostatic repulsion between the

carbazoles through the pyrrole units. The first oxidation onset potential (Figure 4-43, red arrow) was used to estimate the HOMO level (E^{HOMO} = -5.07 eV) with respect to ferrocene as a standard. Empirical calculation including the optical energy gap resulted in E^{LUMO} = -2.13 eV.

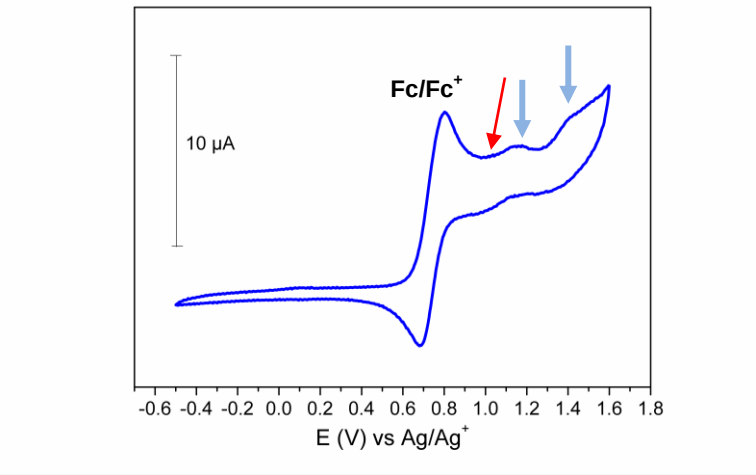

Figure 4-43: Cyclic voltammogram of macrocycle **4-18**; 10^{-3} M sample solution in DMF, 10^{-1} M solution of *n*-Bu_4NPF_6 as electrolyte; working and counter electrode: Pt, reference electrode: Ag; ferrocene reference (Fc/Fc^+), scan rate 50 mVs^{-1}.

Further insight into the electronic structure was gained by quantum mechanical calculations. The orbital surfaces of HOMO and LUMO were distributed uniformly over the whole molecule. The calculated HOMO and LUMO levels were E^{HOMO} = -4.74 eV and E^{LUMO} = -1.18 eV. The calculated energy gap (3.56 eV) and the energy levels are in good agreement with the values derived from the UV-vis absorption and CV measurements.

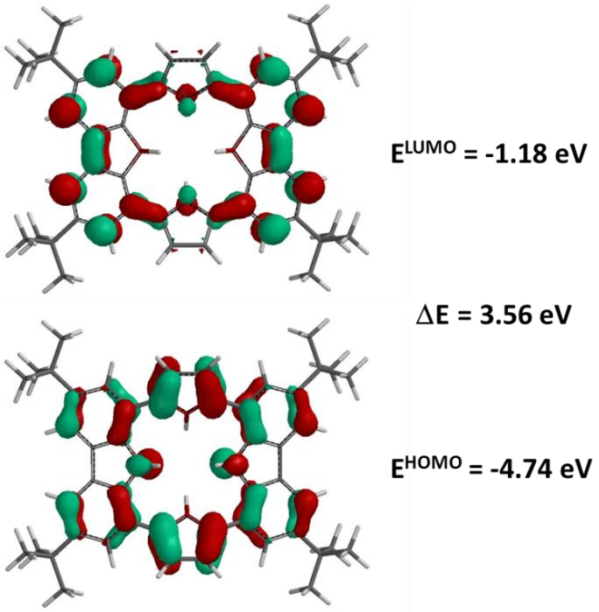

Figure 4-44: Calculated HOMO and LUMO orbital energies of macrocycle **4-38** (DFT, B3LYP/6-31G*).[184]

Unfortunately, no suitable crystal for X-ray analysis of macrocycle **4-38** could be obtained. Nonetheless, the calculated electronic structure revealed a similar saddle-like conformation as found for the structurally close related macrocycle **4-18** (cf. chapter 4.3.4). The non-planar geometry of the macrocycle is in agreement with the results derived from UV-vis and NMR spectrometry, evidencing a non porphyrin-like aromaticity.

4.2.3 Aromatization

The pyrrole-containing macrocycle **4-38** offers the opportunity to create macrocyclic conjugation upon oxidation (Scheme 4-13). On the other hand, earlier described compound **4-18** and upcoming **4-48** do not provide this feasibility since their containing pyridine and triazole moieties do not support the formation of a diamagnetic ring current over the ring-shaped molecules. Macrocycle **4-38** is a $(NH)_4$-macrocycle which can undergo dehydrogenation enabling a porphyrin-like state. Two different annulenes are possible after the oxidation, namely, an [18π] annulene (**4-38-arom1**), with the two pyrrolic protons remaining, or an [16π] annulene (**4-38-arom2**), without any protons in the macrocyclic cavity (Scheme 4-13).

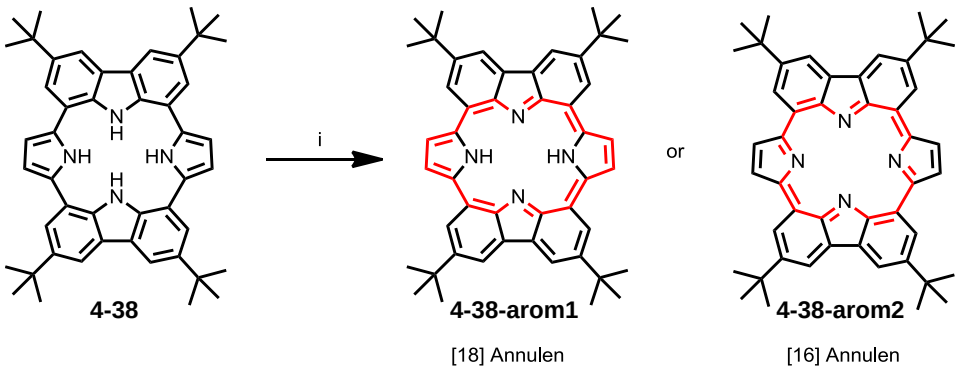

Scheme 4-13: Oxidation of macrocycle **4-38** and its possible oxidized structure. Conditions: *i* activated MnO_2, DCM, rt.

In porphyrin syntheses usually DDQ (2,3-dichloro-5,6-dicyano-1,4-benzoquinone) or *p*-chloranil are used as oxidants to obtain the final porphyrin species.[3] Those quinonoid oxidants are quite expensive and have to be separated from the final product by lengthy chromatographic purification procedures. Recently, Pineiro *et al.* showed that activated MnO_2 is an advantageous dehydrogenation agent since it is inexpensive and simple filtration is the only separation step needed.[262] To monitor the stepwise oxidation of

macrocycle **4-38** *via* UV-vis spectroscopy, it was solved in DCM and an initial spectrum was registered. Then activated MnO_2 was added in excess to the solution without stirring and every 6-8 min a spectrum was recorded. Note that the oxidation proceeded only by diffusion of the oxidizing agent into the solution. The formation of an aromatic porphyrin species could be observed by the appearance of three extremely bathochromically shifted bands (Figure 4-45a/b). The original absorption maxima of compound **4-38** vanished and the new bands appeared at 846, 945 and 1076 nm. The dehydrogenation was completed after approx. 40 min.

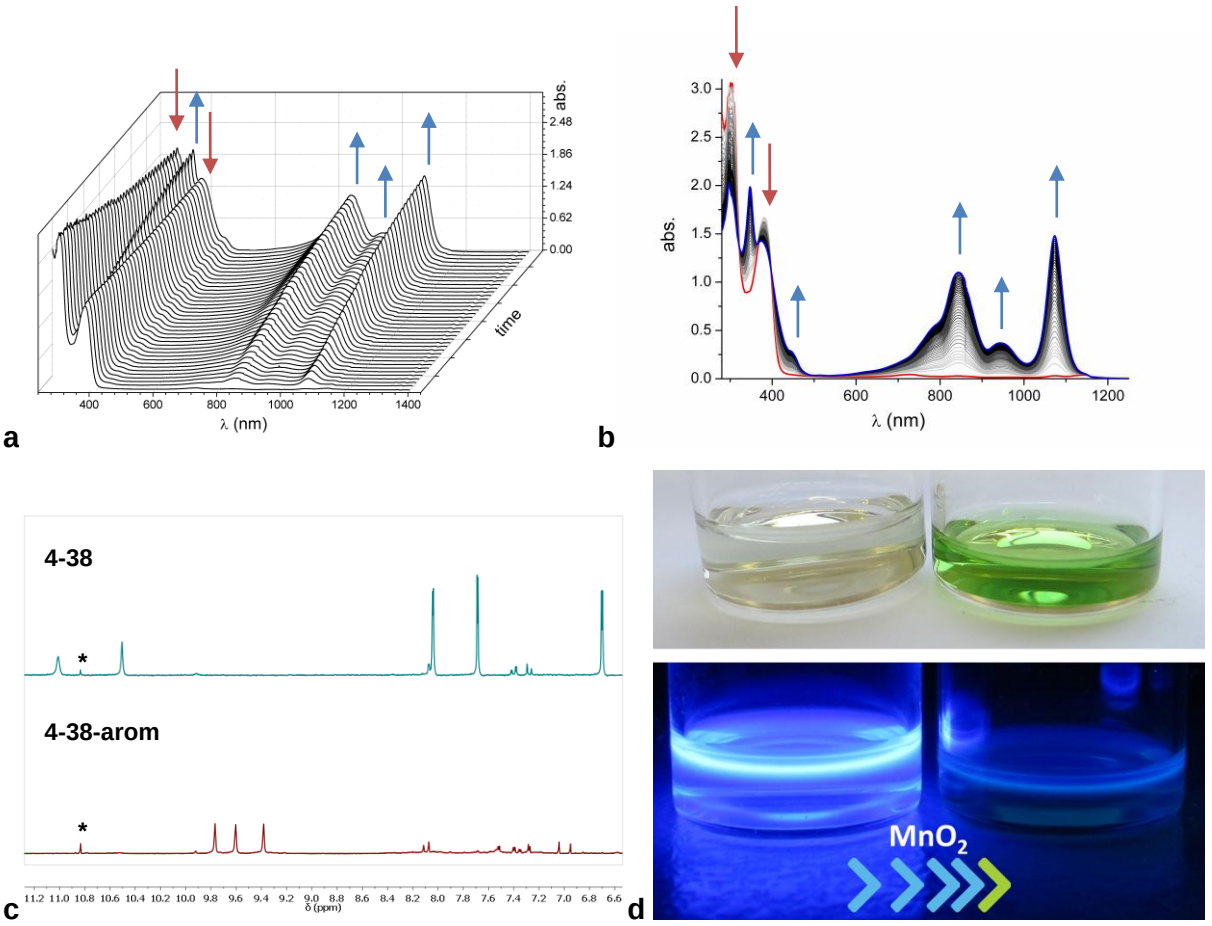

Figure 4-45: **a, b:** Electronic absorption spectra of macrocycle **4-38** in DCM upon stepwise oxidation with MnO_2; **c:** aromatic region of the ^1H NMR spectra of macrocycle **4-38** (blue) and its oxidized species **4-38-arom** (in THF-d_8,*from solvent) ; **d:** color change upon oxidation in ambient light and λ = 366 nm.

Similiar bands have been described by Osuka *et al.* to be Q-like bands of an aromatic 18π-porphyrin system.[35] The therein described porphyrinoid contains two *tert*-butyl substituted carbazole units and two thiophenes, instead of the pyrrole unit in macrocycle **4-38**. Due to the strong similarity, the species being formed by the oxidation of macrocycle **4-38** was considered to be the [18π] annulene **4-38-arom1**. Additionally, the

vivid color change from colorless to green, has also been observed by Osuka, which underlines the likeness of these two porphyrins (Figure 4-45d). Also consistent for both species are the observed downfield shifts for the signals of the peripheral protons in the ^{1}H NMR proton spectrum. The signals for **4-38-arom1** resonate at $\delta = 9.38$, 9.60 and 9.77 ppm. Unfortunately, the signal for the remaining protons at the pyrroles could not be observed.

In the view of the poor stability of macrocycle **4-38**, the steadiness of the dehydrogenated porphyrin species **4-38-arom1** was investigated as well. Therefore, compound **4-38** was dissolved in DCM and an excess of MnO_2 was added while the solution was stirred. Every 20 min a spectrum was taken and agitation was continued. The recorded spectra are depicted in Figure 4-46 and show, that after only 20 min the oxidation was completed (with agitation). Shortly after, decomposition of **4-38-arom1** started to set in and within only 120 min the compound was fully decomposed, which could be followed by the complete disappearance of the absorption bands. Thus, not only the porphyrinoid **4-38** is sensitive due to its electron rich character, but also the dehydrogenated aromatic porphyrin **4-38-arom1**.

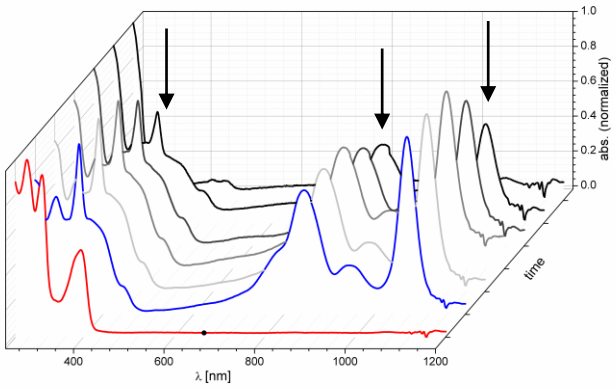

Figure 4-46: Electronic absorption spectra of macrocycle **4-38** (red), its oxidized species **4-38-arom1** (blue) in DCM and the stepwise decomposition of this.

Summarizing, pyrrole-containing macrocycle **4-38** is an electron-rich and therefore unstable molecule. Nevertheless, it could be isolated in its pure form to perform a complete study of its electronic properties. Owing to the presence of the pyrrole unit, porphyrinoid **4-38** offers the possibility of oxidization resulting in its aromatic porphyrin state.

Unfortunately, due to the low-yield synthesis and the instability of **4-38**, only small amounts of macrocycle **4-38** could be obtained. Therefore, no further investigation regarding metal-complexation could be performed. Nevertheless, its host-guest chemistry could be investigated and will be described in detail in chapter 4.3.4.

4.3 Macrocycle formation based on Click Chemistry

The aim to introduce triazole moieties into the porphyrinoidic core was driven by the idea to combine NH and CH hydrogen bond donor units for halide binding in one macrocycle. Therefore, different from the latter described macrocycles **4-18** and **4-38**, the design of triazole-containing macrocycle **4-48** included the copper(I)-catalyzed azide-alkyne cycloaddition (CuAAC) which belongs to the group of Click Chemistry reactions.

Ever since Sharpless[263] and co-workers introduced the concept of "Click" Chemistry in 2001, it became a powerful tool in organic chemistry and material science. Click Chemistry is not a specific reaction but rather a chemical philosophy which mimics nature by creating new substances reliably by joining small units *via* heteroatom links. Reactions which are included into the Click Chemistry approach have to fulfill certain criteria. The reactions have to be modular, wide in scope, high yielding, stereospecific and produce inoffensive side products. They should be based on simple reaction conditions, like being insensitive to oxygen and water, with the use of readily available starting materials and reagents. Solvents, if needed, should be non-hazardous and products should be easily purified avoiding column chromatography.[263] Chemical transformations like 1,3-dipole cycloadditions, nucleophilic substitution reaction, carbonyl chemistry of the "non-aldol" type and additions to carbon-carbon multiple bonds are reactions which meet Click Chemistry standards. Nevertheless, the most popular Click Chemistry reaction is doubtlessly Huisgen's[143] copper catalyzed 1,3-dipolar cycloaddition of azides and terminal alkynes (Figure 4-47).[264-265] Sharpless entitled this powerful reaction even as the "cream of the crop" under the Click reactions.[263] Its only drawback is the use of an azide and the consequential safety concerns. However, azides possess remarkable stability towards water and oxygen, tolerate almost every reaction condition and show hardly any side reactions, what makes them the most convenient reactant. The Huisgen cycloaddition formally is the thermally allowed reaction between a 1,3-dipole and a dipolarophile which form a 5-membered heterocycle.[264] It belongs to the class of pericyclic [4+2] cycloaddtition similar to the Diels Alder (DA) reaction. Its mechanism is concerted and controlled by frontier molecular orbital (FMO) interactions following the Woodward-Hoffmann[266] rules (Figure 4-47). The Woodward-Hoffmann rules state, that "*a thermal pericyclic cycloaddition is allowed if the total number of electrons involved can be expressed in the form (4n+2), where n is an integer. If the total number of electrons can be expressed in the form 4n it is forbidden.*"[267] In the case of the Huisgen

1,3-dipolar cycloaddition the number of electrons involved is 6 which can be expressed as (4n+2) with n = 1, and therefore is allowed by the Woodward-Hoffmann rules. As its denotation implies, 1,3-dipoles are both electrophilic and nucleophilic and therefore can use either their HOMOs or their LUMOs depending on whether the dipolarophile is electron-deficient or electron-rich. The possible FMO interactions are depicted in Figure 4-47.

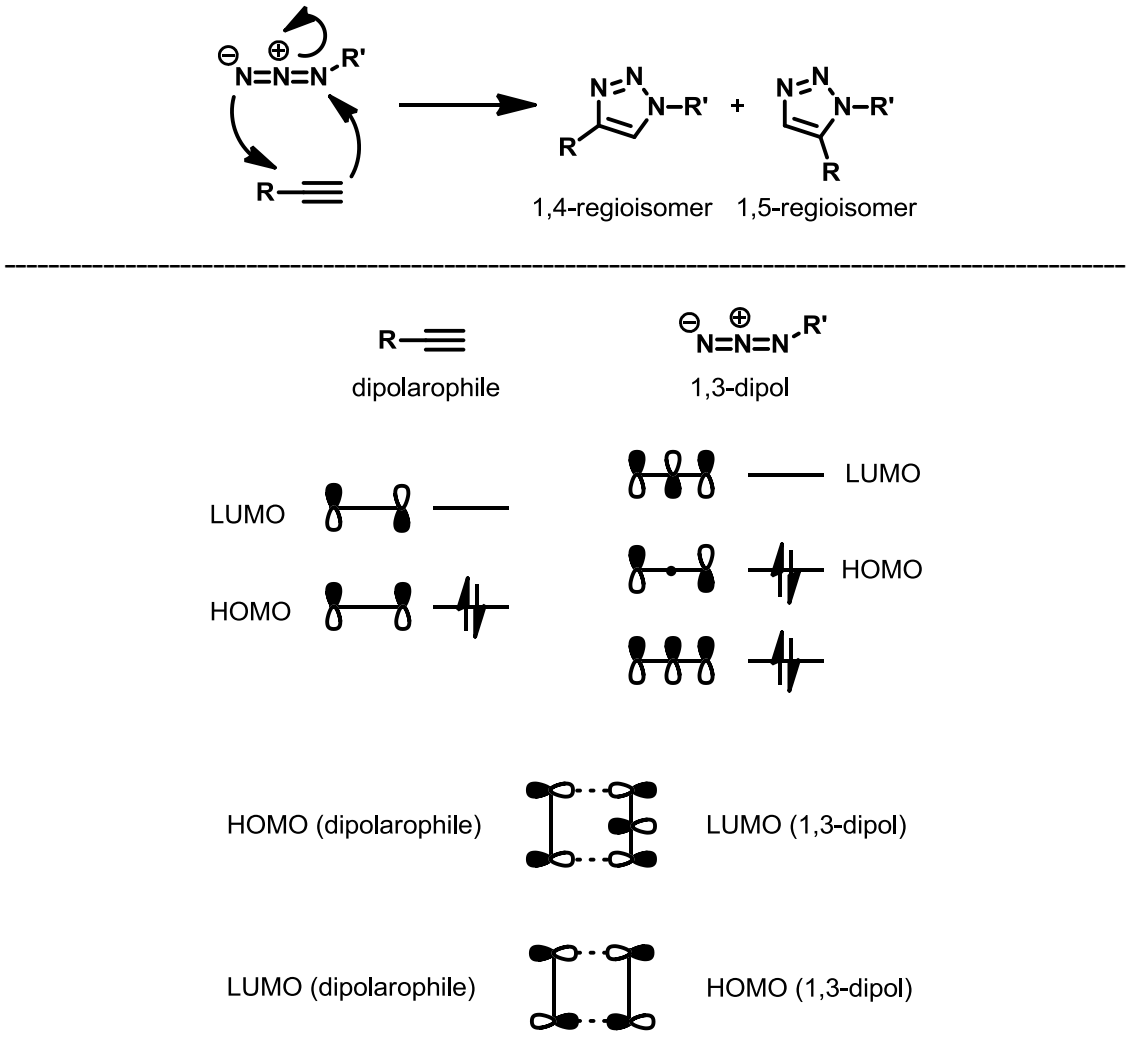

Figure 4-47: Schematic illustration of the Huisgen 1,3-dipolar cycloaddition of azides and terminal alkynes (up) and the corresponding frontier orbital (FMO) interactions (down).

Since alkynes are rather poor 1,3-dipol acceptors, reactions with azides proceed usually slow. In the presence of copper(I) as a catalyst though, cycloadditions are fast and efficient.[146, 268] While in the case of uncatalyzed cycloaddition regioisomers are possible, when copper is used as a catalyst the reaction occurs regiospecific providing exclusively 1,4-disubsituted 1,2,3-triazoles. However, as soon as a catalyst is involved formally the reaction is no longer

a 1,3-dipolar cycloaddition and thus should not be termed as Huisgen's cycloaddition, but copper(I)-catalyzed azide-alkyne cycloaddition (CuAAC). Sharpless *et al.* found that Cu(II) salts (*e.g.* copper(II) sulfate), which can be reduced *in situ* to Cu(I) by ascorbic acid or sodium ascorbate, are more convenient catalysts compared to the use of direct Cu(I) sources such as cuprous bromide or iodide.[146] Since Cu(I) can be unstable, stabilizing ligands like tris-(benzyltriazolylmethyl)amine (TBTA) are often used. The CuAAC tolerates a variety of solvents, functional groups and pH values and the facile procedure often allows a simple filtration of the product from the reaction solution as the only purification step.

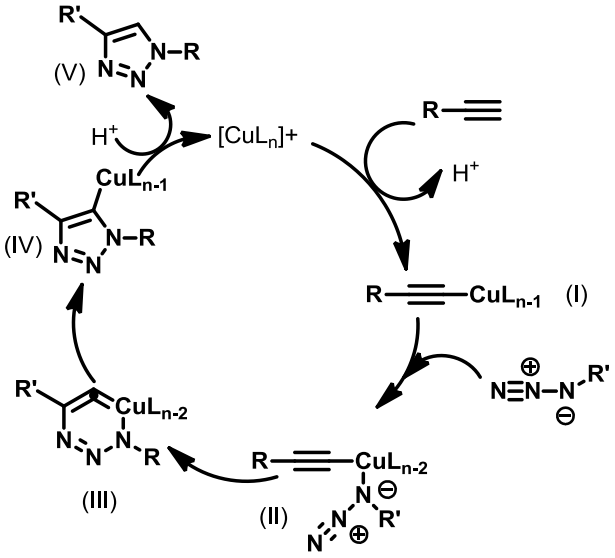

Figure 4-48: Mechanism of the CuAAC.[269]

The mechanism of CuAAC was first proposed to be stepwise and not concerted in 2002 by Sharpless and was later corroborated by computational studies in 2005.[146, 269] Nevertheless, the exact nature of the mechanism remains unknown up to date.[270]

The catalytic cycle of the proposed stepwise mechanism begins with the formation of a copper(I) acetylide **(I)** (Figure 4-48). The next step is a ligand exchange of the azide and one of the ligands at the copper atom **(II)**. The azide binds to the copper *via* the nitrogen which is situated in direct vicinity to the carbon atom. Then the terminal nitrogen of the azide binds to the inner carbon atom of the acetylide which results in a six-membered copper(II) metallacycle **(III)**. This unusual metallacycle contracts then to a triazole-copper species **(IV)**, which subsequently releases the triazole product **(V)**. Due to its gained popularity, more than thousand research articles have been published over the last decade on CuAAC. Therefore, to not go beyond the scope of this work, the following state of the art examples exclusively deal with macrocyclic systems.

The CuAAC reaction offers elegant possibilities to form large macrocycles like cyclic melanocortin **4-39** (Figure 4-49).[271] This was the first reported intramolecular cyclization *via* a triazole formation using CuAAC. Dimer macrocyclization was first proven to be possible in the synthesis of sugar-containing macrocycle **4-40** (Figure 4-49).[272] Beneficially the Cu(I) transitions state is able to coordinate a second alkyne and whenever an intramolecular reaction is favored a macrocycle is formed. In the case of macrocycle **4-40** dimerization was preferred over monomer macrocyclization due to the rigidity of the carbohydrate structure.

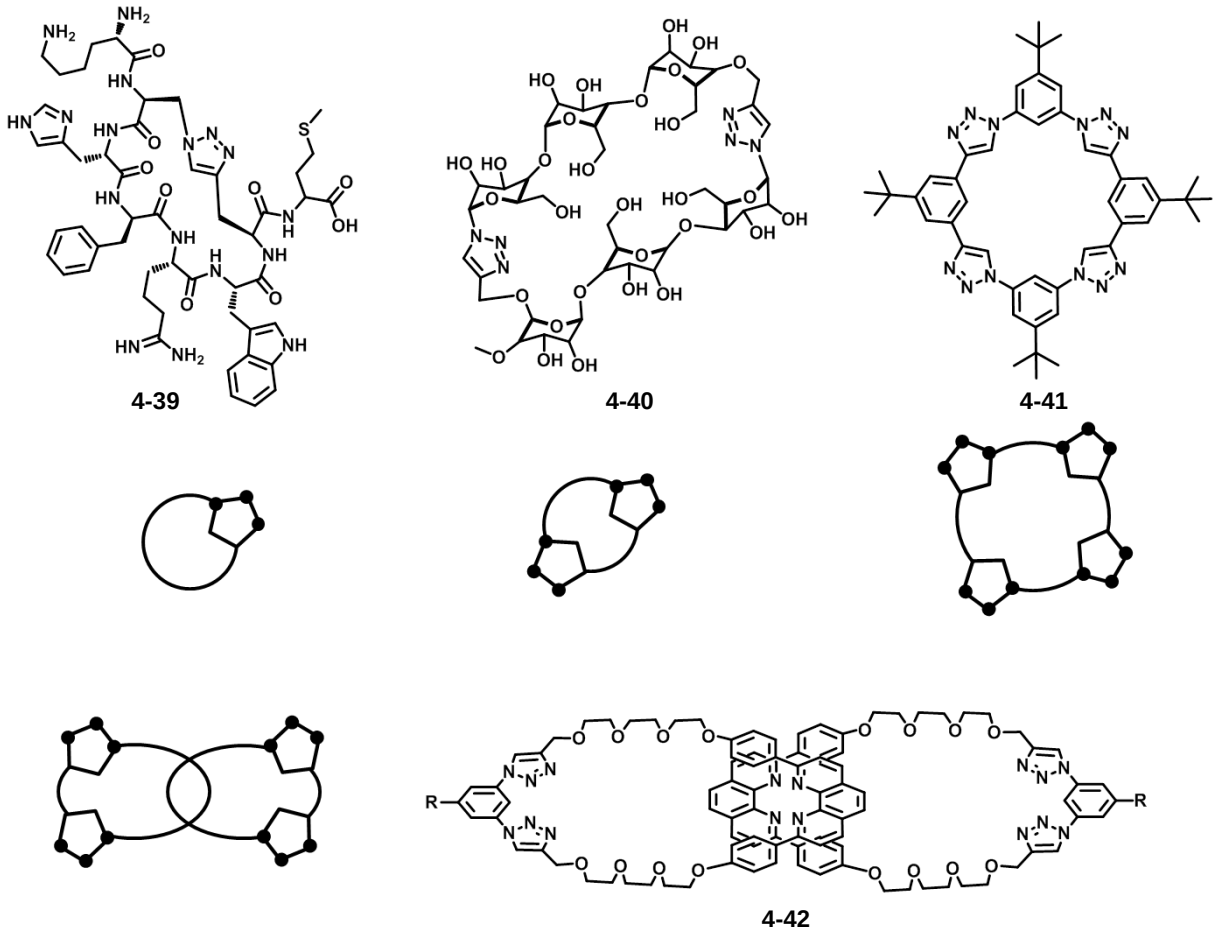

Figure 4-49: Examples of macrocyclic compound synthesized by CuAAC.

The CuAAC has been also applied very successfully in the syntheses of catenanes (**4-42**)[273] and [34]triazolophanes (**4-41**)[274] (Figure 4-49). The high chemoselectivity of the reaction between azides and alkynes, proved to be very effective for the formation of catenanes, even though the formation of large macrocycles is not always the favored one.

4.3.1 Synthesis

Macrocyle **4-48** was synthesized *via* a double CuAAC between diethynyl-carbazole **4-44** and diazido-carbazole **4-46** (Scheme 4-14). Besides the possibility of linear oligomers no larger macrocycles can be formed and dimerization was favored. Dimerization is actually the only feasible ring formation due to the precast of the 1,8-disubsituted building blocks.

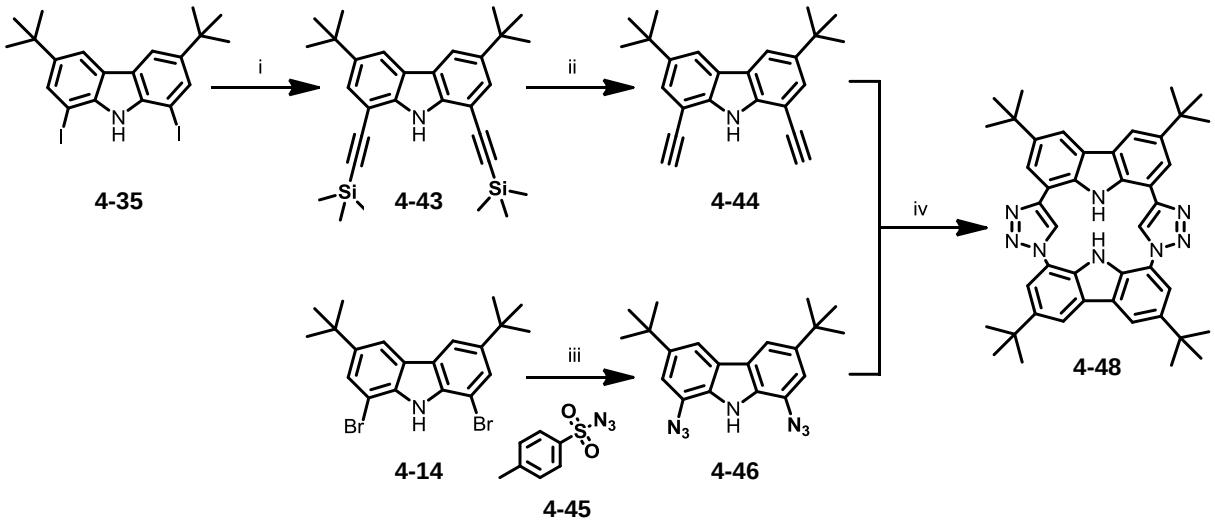

Scheme 4-14: Synthesis of macrocycle **4-48**. Conditions: *i* $Pd(OAc)_2$, CuI, PPh_3, THF, $^{i}Pr_2NH$, TMSA, 60°C, 57%; *ii* TBAF, THF, rt, 94%; *iii* 1. *n*-BuLi, THF, 0°C, 2. CO_2, rt, 3. *t*-BuLi, THF, -78°C, 4. **4-45**, 30%; *iv* sodium ascorbate, TBTA, $CuSO_4$, THF, TEA, 60°C, 17%.

Diethynyl-carbazole **4-44** was prepared in 54% yield over two steps under Sonogashira-Hagihara[275-276] reaction conditions starting from 3,6-di-*tert*-butyl-1,8-diiodo-9*H*-carbazole (**4-35**). The diazido building block **4-46** was synthesized *via* double lithiation of 1,8-dibromo-3,6-di-*tert*-butyl-9*H*-carbazole (**4-14**) using BuLi and subsequent treatment with 4-methylbenzenesulfonyl azide (**4-45**). Prior to this, the free proton at the carbazole's nitrogen needed to be protected and CO_2 as the N-protection group was used during the initial lithiation reaction. The protecting group was easily cleaved during the work-up procedure.

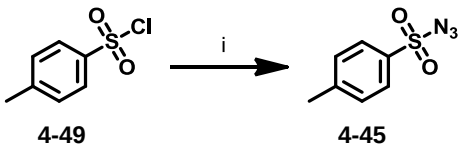

Scheme 4-15: Synthesis of 4-methylbenzenesulfonyl azide (**4-45**). Conditions: *i* NaN_3, aceton, H_2O, 0°C, 94%.

4-Methylbenzenesulfonyl azide (**4-45**) was obtained in 94% by treating 4-methylbenzene-1-sulfonyl chloride (**4-49**) with NaN_3 following the literature procedure (Scheme 4-15).[277] Diazido carbazole **4-46** has never been described in literature, and therefore its structure was fully characterized by NMR and FT-IR spectroscopy, FD-MS spectrometry and X-ray analysis. FT-IR spectroscopy showed characteristic peaks at 2101 cm^{-1} for the azide groups and 3450 cm^{-1} for the NH stretching (Figure 4-50).

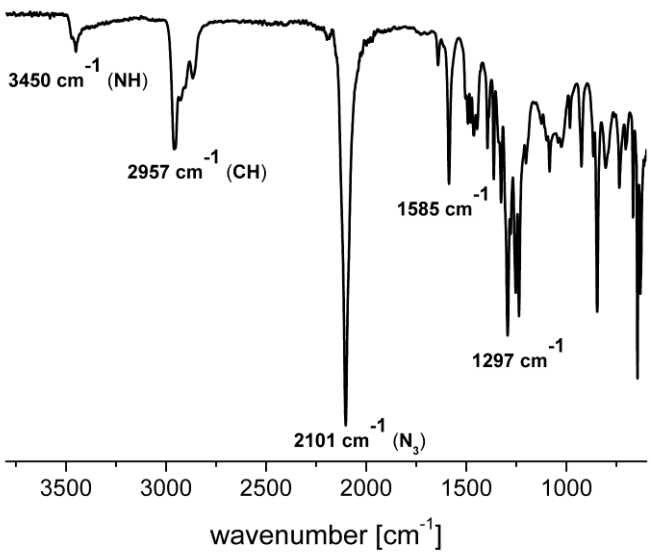

Figure 4-50: FT-IR spectrum of diazido carbazole **4-46**.

Additionally, the structure of compound **4-46** was evidenced by its crystal structure. Crystals suitable for X-ray analysis were grown by slow evaporation from hexane solution. The unit cell consisted of two molecules which were situated with the sterically demanding *tert*-butyl groups opposite to each other ('back to back', Figure 4-51b). The π-systems arranged in a parallel but staircase fashion which was induced by the π–stacking between only one benzene ring of a carbazole to one benzene ring of the lower lying carbazole. With the other benzene ring, the carbazole stacked to one benzene ring of an upper carbazole. The staircase rows were aligned alternately 'face to face' and 'back to back' being generated by the dipole-dipole interaction of the azide units.

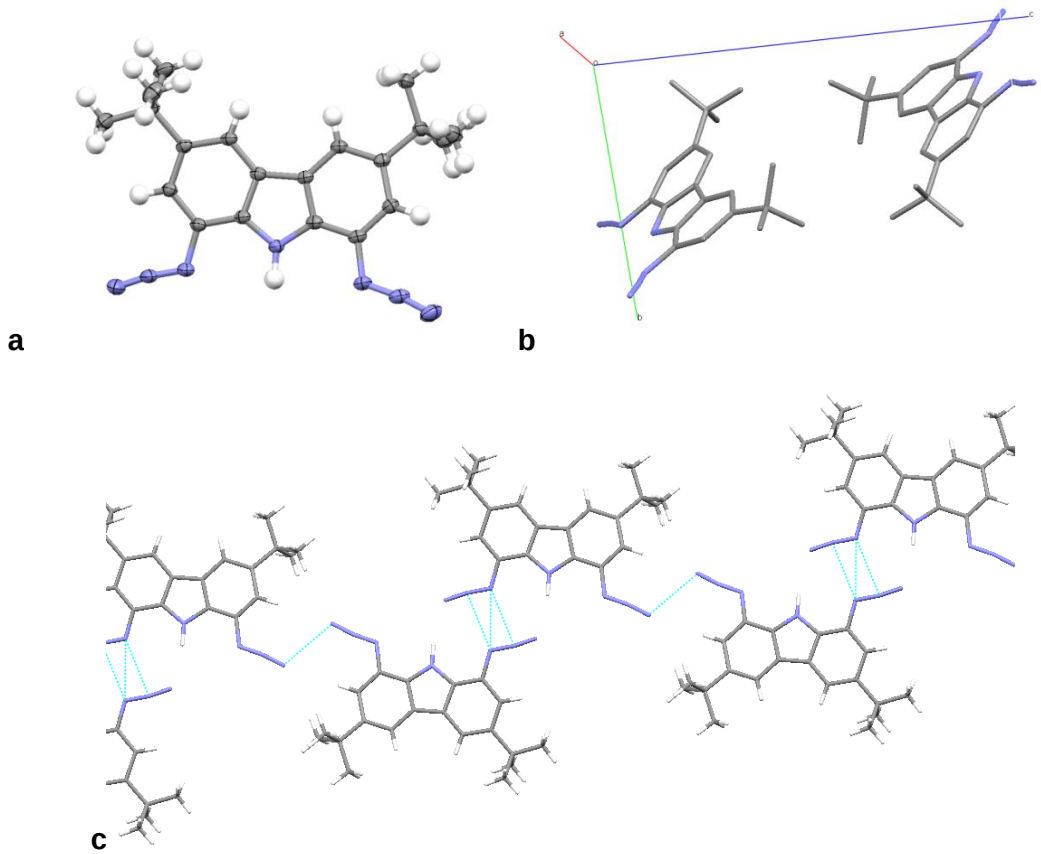

Figure 4-51: Crystal structure of 1,8-diazido-3,6-di-*tert*-butyl-9*H*-carbazole **4-46 a**: single molecule (the ellipsoids correspond to 50% propability); **b**: unit cell (hydrogen atoms are omitted for clarity); **c:** molecular packing.

For the synthesis of macrocycle **4-48** Sharpless' standard reaction conditions[146] for CuAAC were used including the *in situ* generation of copper(II) sulfate by sodium ascorbate and the use of the stabilizing ligand TBTA. The first attempt towards macrocycle **4-48** was accomplished in a diluted system (10^{-4} M), in order to prevent polymerizations as side reactions (Ruggli-Ziegler dilution principle).[171, 182] Unfortunately, the desired compound **4-48** could not be observed but the reaction yielded two compounds, the open cycle **4-50** and a tricarbazole **4-51** (Figure 4-52). Both structures were identified by ^{1}H NMR spectroscopy and mass spectrometry (cf. 7.2.25 and 7.2.26).

At the same time, the reaction was also performed in concentrated solution in order to investigate the formation of oligomers. Surprisingly, this reaction yielded the target macrocycle **4-48**. To better understand the reaction mechanism, firstly, the reaction was repeated in concentrated solution but endcapping was omitted. Astonishingly, again only the open cycle **4-50** and the tricarbazole **4-51** could be isolated. This outcome suggested that an endcapper was needed to promote the second ring closure.

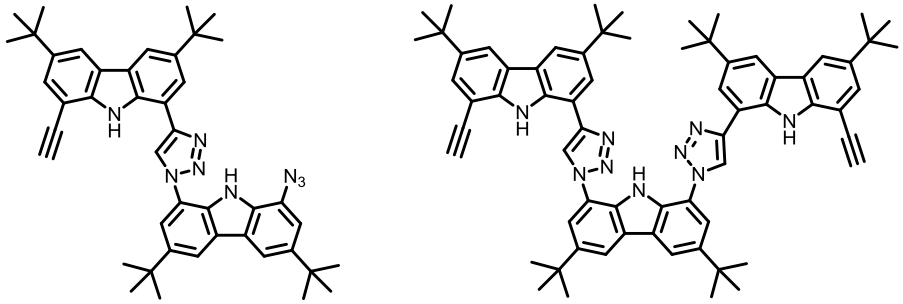

4-50 **4-51**

Figure 4-52: Structures of side products obtained from the Click reaction. Open cycle **4-50** and tricarbazole **4-51**.

A possible reason for the need of the endcapper was that the copper catalyst coordinated between the nitrogen atoms, after the first triazole formation (Figure 4-53b). Therefore, the open cycle **4-50** was twisted in such a way, that the reacting sites were spatially separated and no further reaction was possible (Figure 4-53). If the "endcapper" was added to the reaction mixture the copper was caught away and the open cycle could twist back to form the second triazole without the interaction of the catalysts (Figure 4-53a). As explained before the reaction between azides and terminal alkynes without the presence of a catalyst is possible but rather slow (cf. chapter 4.3).[143]

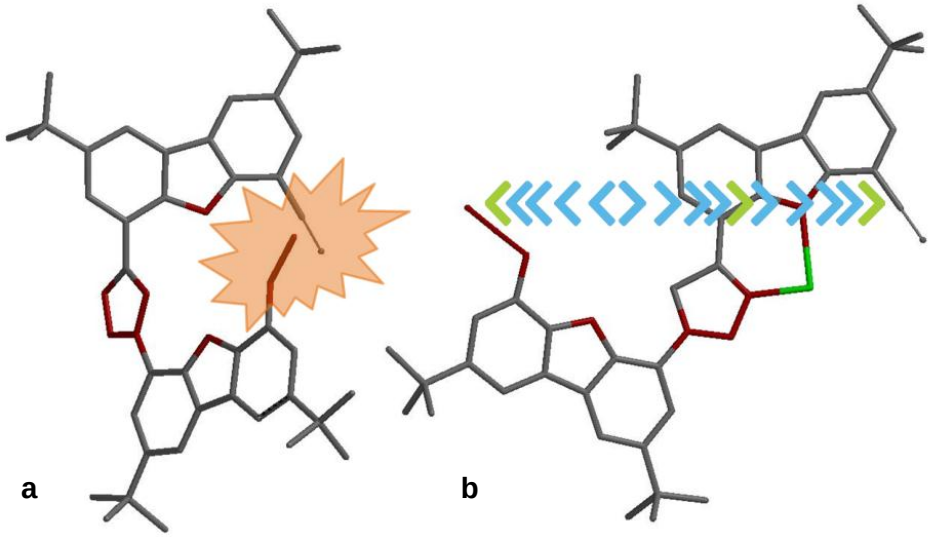

Figure 4-53: Click reaction is **a:** possible; **b:** not possible due to the presence of coordinated copper between the nitrogens.

Based on this results, the reaction was also performed without the use of a copper(I) catalysts but unfortunately, only starting material was recovered.

Consequentely, the catalyst was needed to build the first triazole, whereas the second was formed without the help of copper(I) but favored due to the spatial proximity of the reactive sites in the preformed dicarbazole **4-50**.

A study was made to identify the ideal "endcapper". NaN_3 proved to be the best, because after precipitation in MeOH the pure product could be collected without further purification. When NaCN or ethynylbenzene/azidobenzene were used, the product was formed as well but the formation of side products massively hindered the subsequent purification.

Table 4-4: Study of different endcappers for the reaction towards macrocycle **4-48**.

entry	endcapper	product	notes
# 1	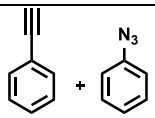	yes	side products which hinder purifications
# 2	NaCN	yes	side product cannot be separated
# 3	NaN_3	yes	pure compound after precipitation

Macrocycle **4-48** was obtained in 17% yield as a colorless solid which was not soluble in polar solvents like MeOH or EtOH, poorly soluble in common solvents like DCM, $CHCl_3$ or EtOAc and better soluble in THF and DMSO. Its structure was proven by NMR spectroscopy and HRESI-MS spectrometry.

Apart from the low yield of this reaction, the applied reaction fulfilled the following criteria of the Click Chemistry approach (cf. chapter 4.3): simple reaction conditions, readily available starting materials and easy purification procedures like filtration whereby time-consuming column chromatography were avoided.

4.3.2 NMR Analysis

The ^1H NMR spectrum evidenced the formation of macrocycle **4-48** (Figure 4-54). Due to the triazole moieties which are connected through nitrogens to one carbazole and through carbon atoms on the other, the symmetry of the macrocycle is reduced to C_{1v} (compared to macrocycle **4-18** with C_{2v} symmetry, chapter 4.1). Therefore, the aromatic carbazole protons exhibited four signals (●) and the protons at the nitrogen two individual signals (●) since

they are also not identical. On the other hand, the protons situated at the triazole carbon atoms (●) are magnetically identical since they have the same chemical environment.

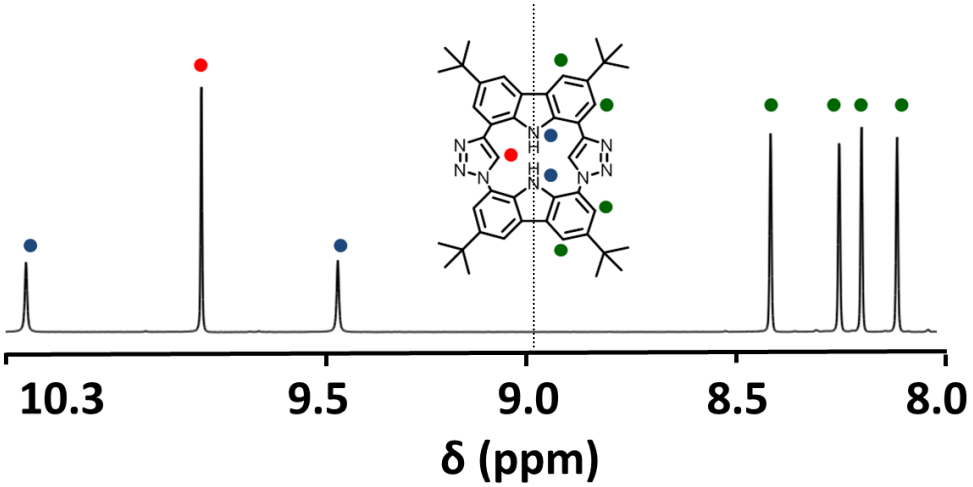

Figure 4-54: Aromatic region of the ^{1}H NMR spectrum of macrocycle **4-48** in THF-d_8, 298 K, 700 MHz.

NOESY (nuclear Overhauser effect spectroscopy) spectroscopy proved that the CH-groups of the triazole moieties point inside the cavity of the ring, since the hydrogens at the triazoles and carbazoles produced cross peaks (Figure 4-55).

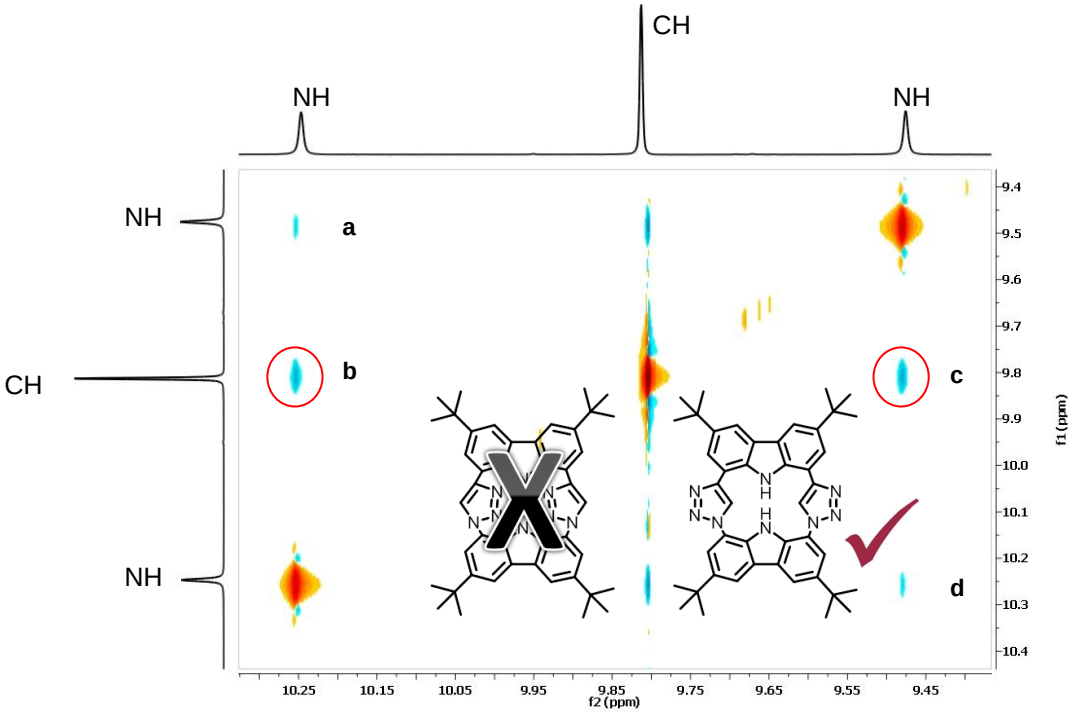

Figure 4-55: NOESY spectrum of macrocycle **4-48** in THF-d_8, 298 K, 700 MHz, τ_m = 500ms.

Generally, the cross peaks arise from nuclei which are in close proximity < 4 Å. This is in agreement with molecular modeling using density functional theory calculations (DFT, B3LYP/6-31G*[184, 278-279]) which revealed a distance of 2.3 Å between the triazole (●) and the carbazole (●) protons. No cross peak for the CH (●) protons of the triazole and the benzene ring of the carbazole (●) was observed which excluded a different arrangement of macrocycle **4-48**.

NOESY NMR spectroscopy also allows conformational analysis of a molecule including structural information.[280-281] Distances can be estimated assuming the linear growth of cross peaks at different mixing times. For this analysis, the observed spins are considered to be close enough that their dipole-dipole interaction is appreciable. Secondly, it is assumed that the molecule including the observed spins is rigid and tumbles only isotropically (only dipole-dipole relaxations are perceptible). If the distances in a molecule are known, the cross peak intensities for a certain mixing time $V(\tau_m)$ in a 2D NOESY spectrum can be recalculated from known diagonal peak intensities V_0 at $\tau_m=0$ by:

$$V(\tau_m) = e^{(-R\tau_m)}V^0 \qquad (4\text{-}2)$$

where R is the relaxation matrix.[281] It is beyond the scope of the present work to explain the meaning of the relaxation matrix R. Besides this, matrix R is not relevant for the assumption which will be taken as follows. Amongst other approaches, isolated spin-pair approximations (ISPA) can be used for distance estimations based on the NOE. Even though the relationship between the NOE-peak intensity and distance is nonlinear, under certain approximations like short mixing times, it can be linearized. With this assumption the calculation of an unknown interproton distance becomes possible using the peak intensity and distance of a proton pair within the molecule with a known distance r_{ref} as reference by:

$$r_{ij} = r_{ref}\left[\frac{V_{ref}}{V_{ij}}\right]^{\frac{1}{6}} \qquad (4\text{-}3)$$

In general, distances smaller than the reference are underestimated and *vice versa*.[281]

In the present case, the interproton distance between the two nitrogen protons r_{ij}(NHNH) of the carbazoles and the spacing between the nitrogen proton to the proton at the triazole r_{ij}(CHNH) were estimated by using the ISPA approach. As a reference the distance between the *tert*-butyl groups and the proton in position 4 of the carbazole has been considered (Figure 4-56). Since the *tert*-butyl groups rotate fast on the NMR timescale, only the

centroid of them was taken as the reference distance r_{ref} = 3.19 Å (DFT, B3LYP/6-31G*; Figure 4-56).

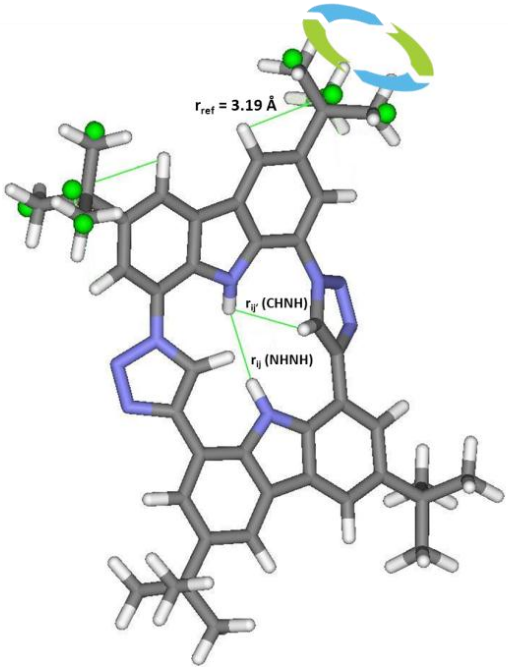

Figure 4-56: Calculated structure of macrocycle **4-48** using DFT, B3LYP/6-31G*.

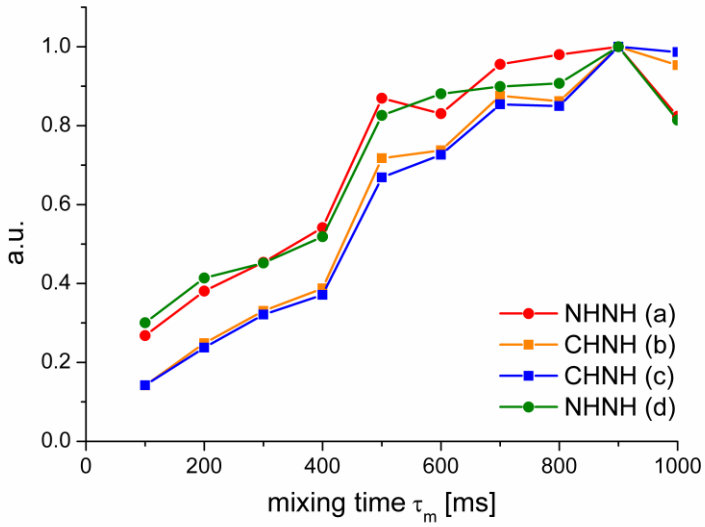

Figure 4-57: NOESY cross peak buildup curves as a function of mixing time τ_m of macrocycle **4-48** in THF-d_8.

For the evaluation of the interproton distances r_{ij}(NHNH) and r_{ij}(CHNH) 2D NOESY spectra with different mixing times τ_m = 100, 200, … 1000 ms were recorded. Each NOESY spectrum provided four cross peaks for the reference proton pair V_{ref}. For each of the examined proton pairs V_{ij}(NHNH) and $V_{ij'}$(CHNH) two cross peaks were observed. The cross

peaks for V_{ij}(NHNH) have been labeled **(a)** and **(d)**, and for $V_{ij'}$(CHNH) **(b)** and **(c)**, respectively (Figure 4-55). The buildup curves of the cross-peaks **(a-d)** were plotted as a function of cross peak intensity *vs.* mixing time τ_m (Figure 4-57). As expected the buildup curves for cross peaks **(a)** and **(d)** show similar growth behavior, as in the case of cross peaks **(b)** and **(c)**. The distances for $r_{ij'}$(CHNH) and r_{ij}(NHNH) were calculated according to equation (4-2) at mixing time τ_m = 100 ms (Table 4-5). The short mixing time was chosen in order to ensure linear dependency.

Table 4-5: Distance approximation calculations for $r_{ij'}$(CHNH) and r_{ij}(NHNH) using r_{ref} = 3.19 Å for all possible combinations of the cross peaks at τ_m = 100 ms.

$V_{ij(')}$ / V_{ref}	V_{ij}(NHNH) (a)	V_{ij}(CHNH) (b)	$V_{ij'}$(NHNH) (c)	$V_{ij'}$(CHNH) (d)
	-1.83E+06	-3.88E+06	-1.24E+06	-2.17E+06
-5.94E+05	2.64	2.33	2.82	2.57
-5.82E+05	2.64	2.32	2.81	2.56
-5.19E+05	2.50	2.20	2.67	2.43
-5.36E+05	2.51	2.21	2.68	2.44
$r_{ij(')}$ (Å)	2.57	2.27	2.75	2.50
	r_{ij}(NHNH)	**2.66 Å**	**2.38 Å**	**$r_{ij'}$(CHNH)**

It is known from literature, that methyl proton peak volumes have to be scaled down by 1/3 to obtain correct cross-relaxation rates.[282] Therefore, all cross peak intensities of the *tert*-butyl groups were corrected by 1/9 since they comprise three methyl groups. The values of $V_{ij'}$(CHNH) have been corrected by 1/2, because of equivalence of the two CH protons in the spectrum. Since four reference intensities V_{ref} and two intensities for each proton pair were recorded, 8 possible combination for the calculation of each nuclei pair can be considered. The values obtained for $r_{ij'}$(CHNH) and r_{ij}(NHNH) were averaged over all possible combinations (Table 4-5).

Taking all the assumptions into account, finally, the distances have been determined to be r_{ij}(NHNH)= 2.66 Å and $r_{ij'}$(CHNH)= 2.38 Å, which is in good agreement with the distances derived from DFT calculations (r^{theo}_{ij}(NHNH)= 2.34 Å and $r^{theo}_{ij'}$(CHNH)= 2.34 Å).

4.3.3 Electronic Structure

The UV-vis absorption and photoluminescence spectra of macrocycle **4-48** were recorded in THF (c = 5*10^{-5} M, Figure 4-58). The electronic absorption spectrum showed two local maxima at λ = 299 and 360 nm. As previously mentioned 3,6-di(*tert*-butyl)carbazoles exhibit a typical band around λ = 230 nm,[152, 185] which originates from carbazole-centered transitions (see also chapter 4.1.3). Therefore, the first absorption maximum of compound **4-48** was assigned to be carbazole-centered. The optical energy gap was derived from the absorption edge and found to be ΔE_{opt} = 3.31 eV. Macrocycle **4-48** exhibited violet emission with a maximum at λ_{em} = 378 nm and a quantum yield of Φ_f = 0.29 (referenced against Coumarin 1, Comparative Method).[186] The emission in various solvents by increasing their polarity resulted in a very small bathochromic shift of the emission maximum. The triazole moiety can theoretically act as an electron donor[283] or as an electron acceptor,[284] resulting in a weak intrinsic polar character of the emitting state.

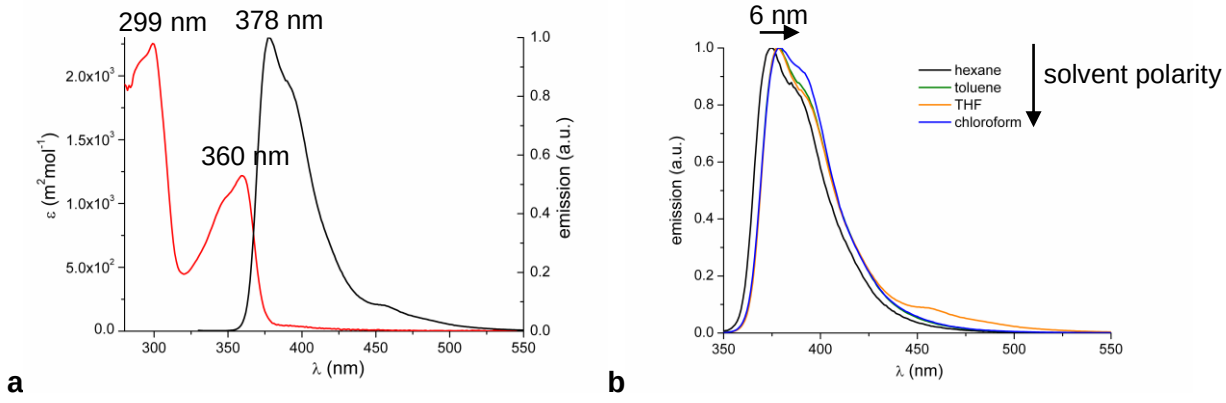

Figure 4-58: **a:** Electronic absorption and emission spectra of macrocycle **4-48** (c = 5*10^{-5} M in THF), **b:** Solvent dependent emission spectra of macrocycle **4-48** (c = 5*10^{-5} M, λ_{ex} = 299 nm).

Cyclic voltammetry was performed on macrocycle **4-48** in order to further investigate the electronic properties.[189] The measurements were conducted under identical conditions as used for macrocycles **4-18** and **4-38** (chapter 4.1.3 and 4.2.2). The cyclic voltammogram showed one quasi-reversible oxidation wave arising from the oxidation of carbazole to its cation radical (Figure 4-59). Macrocycle **4-18** and **4-38** showed two irreversible oxidation waves which indicated the successive oxidation of the carbazole units and therefore electronic communication between them. Compared to this, the single quasi-reversible

oxidation wave resulting from macrocycle **4-48** gave rise to a conjugation barrier between the individual carbazoles which is hindered by the triazole units.[192]

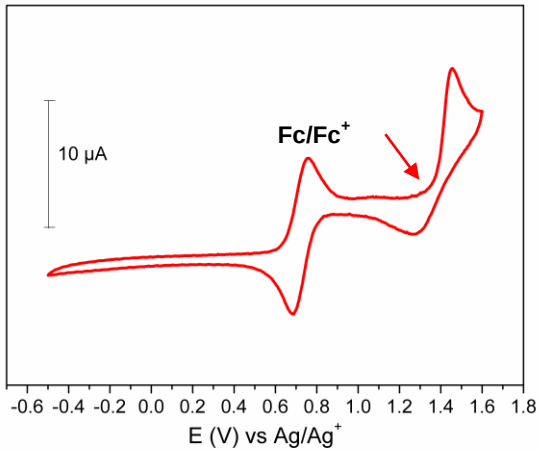

Figure 4-59: Cyclic voltammogram of macrocycle **4-48**; 10^{-3} M sample solution in DMF, 10^{-1} M solution of *n*-Bu_4NPF_6 as electrolyte; working and counter electrode: Pt, reference electrode: Ag; ferrocene reference (Fc/Fc^+), scan rate 100 mVs^{-1}.

The HOMO level was estimated from the oxidation onset potential to E^{HOMO} = -5.46 eV with regard to the internal standard Fc/Fc^+. The LUMO level was calculated empirically to be E^{LUMO} = -2.15 eV using the optical energy gap.

DFT calculations (B3LYP/6-31G*)[184] revealed that the LUMO was exclusively distributed over the carbazole moiety which connects the triazole units by nitrogen atoms (Figure 4-60). In contrast the HOMO orbitals were located only at the opposite carbazole unit which is anchored to the triazole through carbon atoms.

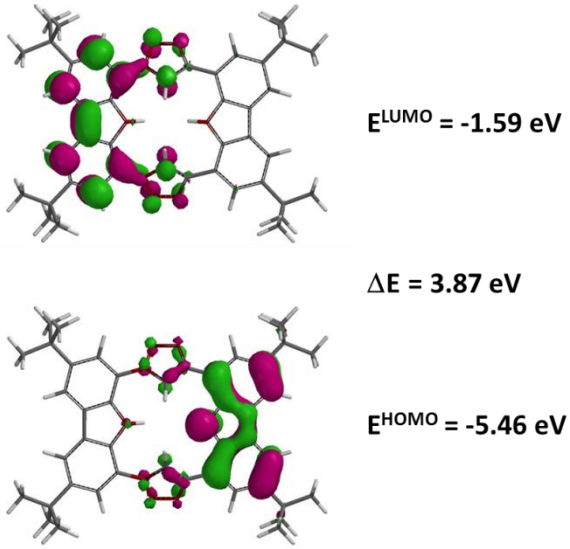

Figure 4-60: Calculated HOMO and LUMO orbital energies of macrocycle **4-48** (DFT, B3LYP/6-31G*).[184]

This finding is in agreement with the observation received from CV measurements, revealing a conjugation barrier between the two carbazole units. The HOMO and LUMO levels were estimated to be E^{HOMO} = -5.46 eV and E^{LUMO} = -1.59 eV. The calculated energy gap (ΔE = 3.87 eV) is in good agreement with the optical energy band derived from the long wavelength absorption band.

To the best of our knowledge, macrocycle **4–48** is the first porphyrinoid comprising valuable NH and CH hydrogen bond donor units for halide binding. Therefore, macrocycle **4–48** was investigated as an anion receptor and proved to be selectively sensing fluoride ions. This will be motivated and described in detail in the following chapter 4.3.4.

4.3.4 Anion recognition

Anions are ubiquitous throughout biological systems since they carry genetic information (DNA is a polyanion) and the majority of enzyme substrates and co-factors are anionic. The research in anion recognition chemistry began in the late 1960s but in contrast to the well-developed cation recognition chemistry it has received little attention. The design of anion receptors is particularly challenging due to the larger size of the anions compared to the isoelectronic cations (Table 4-6).[194] The therefore lower charge to radius ratio results in a less effective electrostatic binding interaction. Besides this, anions may lose their negative charge depending on their sensitivity to pH values. Their binding strength can also be influenced by solvent effects or hydrophobicity (Hofmeister series[285]). The major challenge however, is the need for a variety in receptor design keeping in mind the wide range of geometries of anions. Receptors should be complementary to their *e.g.* spherical (F^-, Cl^-, Br^-, I^-), linear (N_3^-, CN^-, SCN^-, OH^-), trigonal planar (CO_3^{2-}, NO_3^-), tetrahedral (PO_4^{3-}, VO_4^{3-}, SO_4^{2-}, MnO_4^-) or octahedral ($[Fe(CN)_6]^{4-}$, $[Co(CN)_6]^{3-}$ anionic guest.[286] For these and other reasons the development of defined anion receptors is an important field in today's research.

Table 4-6: Comparison of the ionic radii of isoelectronic cations and anions in octahedral environment.[194]

Cation	r [Å]	Anion	r [Å]
Na^+	1.16	F^-	1.19
K^+	1.52	Cl^-	1.67
Rb^+	1.66	Br^-	1.82
Cs^+	1.81	I^-	2.06

Amongst the most popular hydrogen bond donors, the pyrrole ring has been applied in a multitude of anion receptors like calixpyrroles,[248] expanded porphyrins[13] and 2,5-diamidopyrroles.[287] The bond-donating strength of pyrrole can be enhanced by the acidity of the NH which can be tuned through the attachment of electron-withdrawing groups or *via* the annulation with benzene rings. This can be understood by the pK_a value of pyrrole (23.0) compared to that of indole (20.9) and carbazole (19.9, all measured in DMSO[133]). Carbazole is a very rigid molecule which has been shown to be a beneficial attribute in anion recognition.[288] On the other hand, shape persistent macrocyclic anion

receptors have been proven to show stronger guest binding than their acyclic counterparts.[289] Therefore, the host-guest chemistry of the herein presented carbazole-containing macrocycles was investigated. The cyclic preformed cavities of compounds **4-18**, **4-38** and **4-48**, make them perfect host candidates for spherical anions such as F^-, Cl^-, Br^-. Due to the calculated rather small cavity dimensions (**4-18**: d_{NHNH} = 2.05 Å, d_{NN} =4.85 Å; **4-38**: d_{NHNH} = 2.04 Å, d_{NHNH}(pyrrole) = 2.67 Å; **4-48**: d_{NHNH} = 2.34 Å, d_{CHCH} = 2.67 Å) the fluoride anion was expected to show the highest binding affinity. The central cavity dimensions have been determined between the facing pairs of hydrogen atoms. Additionally, the distances between the hydrogens are long enough to support linear NH···F^- (0.66 Å) and CH···F^- (0.85 Å) interactions.[290] The detection of fluoride is applied *e.g.* in dental care[291] and in the treatment of osteoporosis.[292] Additionally fluoride is a common ingredient in anesthetics,[293] psychiatric drugs[294] and rat poisons.[295] One of the biggest concern though is its toxicological concern in drinking water.[296]

The host-guest chemistry between the macrocycles **4-18**, **4-38** and **4-48** and the halide anions fluoride, chloride and bromine was investigated by titration experiments and monitored by UV-vis, photoluminescence and proton NMR spectroscopy. To take advantage of their good solubilities in organic solvents tetrabutylammonium salts (TBAX) were used. All spectroscopic titration experiments were conducted at rt in THF (THF-d_8 for NMR experiments).

For the UV-vis spectroscopic titrations a solution of the corresponding macrocycle ($5*10^{-5}$ M, THF) was prepared, and an initial spectrum was taken. A stock solution of TBAX ($1.0*10^{-3}$ M, THF) containing also the macrocycle ($5*10^{-5}$ M) was prepared, in order to obviate the need to account for dilution effects during the titrations. A 2.0 mL solution of the macrocycle was transferred to a sealed vial, and small portions of the TBAX stock solution (2 µL, then 5–10 µL) were added to the macrocycle solution, and a spectrum was recorded after each addition.

Photoluminescence spectroscopic titration is probably the most popular and sensitive technique for anion recognition.[297] In this case, stock solutions of the halide anions were prepared with three different concentrations c(TBAX-1) = $5*10^{-5}$ M, c(TBAX-2) = $5*10^{-4}$ M and c(TBAX-3) = $5*10^{-3}$ M. Then 10, 20 to 120 µl of each solution was added to 2 ml of the receptor solution (c(M) = $1*10^{-5}$ M).

NMR experiments were performed at rt in THF-d_8 and the receptor solutions of **4-18**, **4-38** and **4-48** (c(M) = $3*10^{-3}$M) were titrated by adding known quantities of a concentrated stock solution comprising the host (c(M) = 3 mM) and the guest (c(TBAX) = $1*10^{-1}$ M).

a **b**

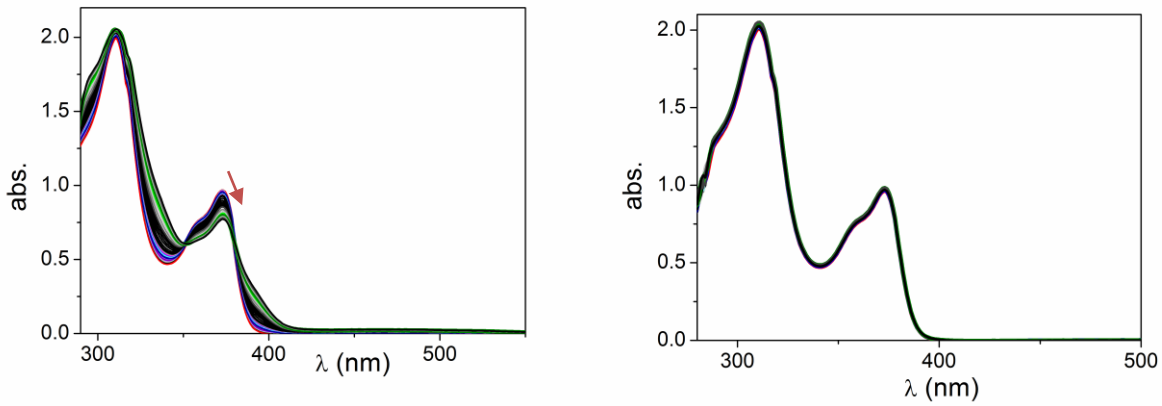

Figure 4-61: Electronic absorption spectra in THF of macrocycle **4-18** ($5*10^{-5}$M) upon titration of **a:** TBAF and **b:** TBACl.

The host-guest chemistry between pyridine-containing macrocycle **4-18** and fluoride and chloride was investigated. Bromide was not titrated due to the little effect already observed for chloride. As expected, the greatest effect occurred in the absorption spectrum when fluoride ions were titrated into a solution of macrocycle **4-18** (Figure 4-61a).

a **b**

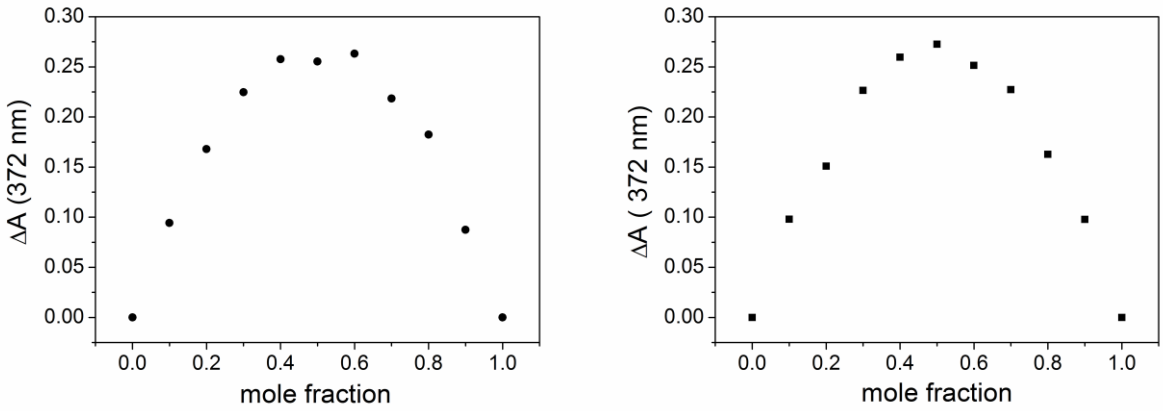

Figure 4-62: Job Plot determination for the binding stoichiometry between macrocycle **4-18** and **a:** fluoride and **b:** chloride.

Job plot[298] determination showed a 1 : 1 binding stoichiometry for both halides with macrocycle **4-18**. The Job's method[298] is based on the idea, that the concentration of the formed host-guest complex $[H_mG_n]$ is at maximum when the concentration ratio $[H]/[G]$ is equal to m/n. Job Plots were generated by varying the mole fraction of the two binding partners whereas their total molar concentration ($[H]_0 + [G]_0 = \text{const.}$) was held constant.[299] In practice, the mole fraction of the guest is varied and the concentration of

the emerging complex is monitored by UV-vis spectrometry. $[H_mG_n]$ is then plotted against the mole fraction x yielding, in the case of a 1 : 1 binding stoichiometry, a curve with a maximum at x = n/(m + n) = 0.5.

Because of the very weak interactions between macrocycle **4-18** and the investigated halides, no further investigations were done on these host-guest systems.

The host-guest interaction between the halide anions and macrocycle **4-38** and **4-48** were also studied. Unlike macrocycle **4-18**, bearing an electron-deficient pyridine moiety, which acts as an acceptor, the binding properties of the triazole ring in **4-48** and the pyrrole unit in **4-38** are expected to be more efficient. Surely, pyrrole-containing macrocycle **4-38** will show strongest guest binding due to strong NH hydrogen bond donor ability of the pyrrole.[138-140, 300] Nevertheless, the CH hydrogen bond properties of triazoles towards halides have been proven for preorganized receptors.[142, 274, 301] Usually, those shape persistent receptors include triazoles and phenyl moieties and create a ring size which is favoring the binding of chloride ions.[141] On the contrary, triazole-containing macrocycle **4-48** offers a perfect fitting cavity for smaller fluoride anions. Furthermore, as already mentioned, it represents the first example of an anion receptor which includes hydrogen bond donor units arising from NH and CH moieties unified in one macrocycle. Hence, the host-guest chemistry of triazole-containing macrocycle **4-48** was of particular interest.

The investigations of the host-guest interactions between triazole-containing macrocycle **4-48** and fluoride, chloride and bromide showed, that the affinity to bind a halide anion in the macrocyclic cavity was highest for fluoride. This was expected, since chlorine and bromine were too large to penetrate inside the cavity. The most apparent indicator for the fluoride selectivity was the visible colorimetric response expressed by a vivid color change from colorless to shiny yellow, which was not the case for chloride and bromide (Figure 4-63).

Figure 4-63: Colorimetric response of macrocycle **4-48** (c = 10^{-5} M in THF) to fluoride (10 eq) anion under ambient light and λ = 366 nm.

The dramatic change in the absorption spectrum is depicted in Figure 4-64a (the absorption spectrum of macrocycle **4-48** is pictured in red). Upon titration up to 1 eq of TBAF (blue), the absorption maximum at 360 nm was bathochromically shifted along with a reduction in intensity. Furthermore, new maxima appear in the region of 400-450 nm. By increasing the equivalents, four intense new local maxima appeared whereby the original bands vanished. The most significant maximum at around 460 nm, causing the color change, could be attributed to a deprotonation of one of the acidic NH at the carbazole.[302] Neutral hydrogen bond donor units are known to show significant color changes as a result of anion induced deprotonation.[303]

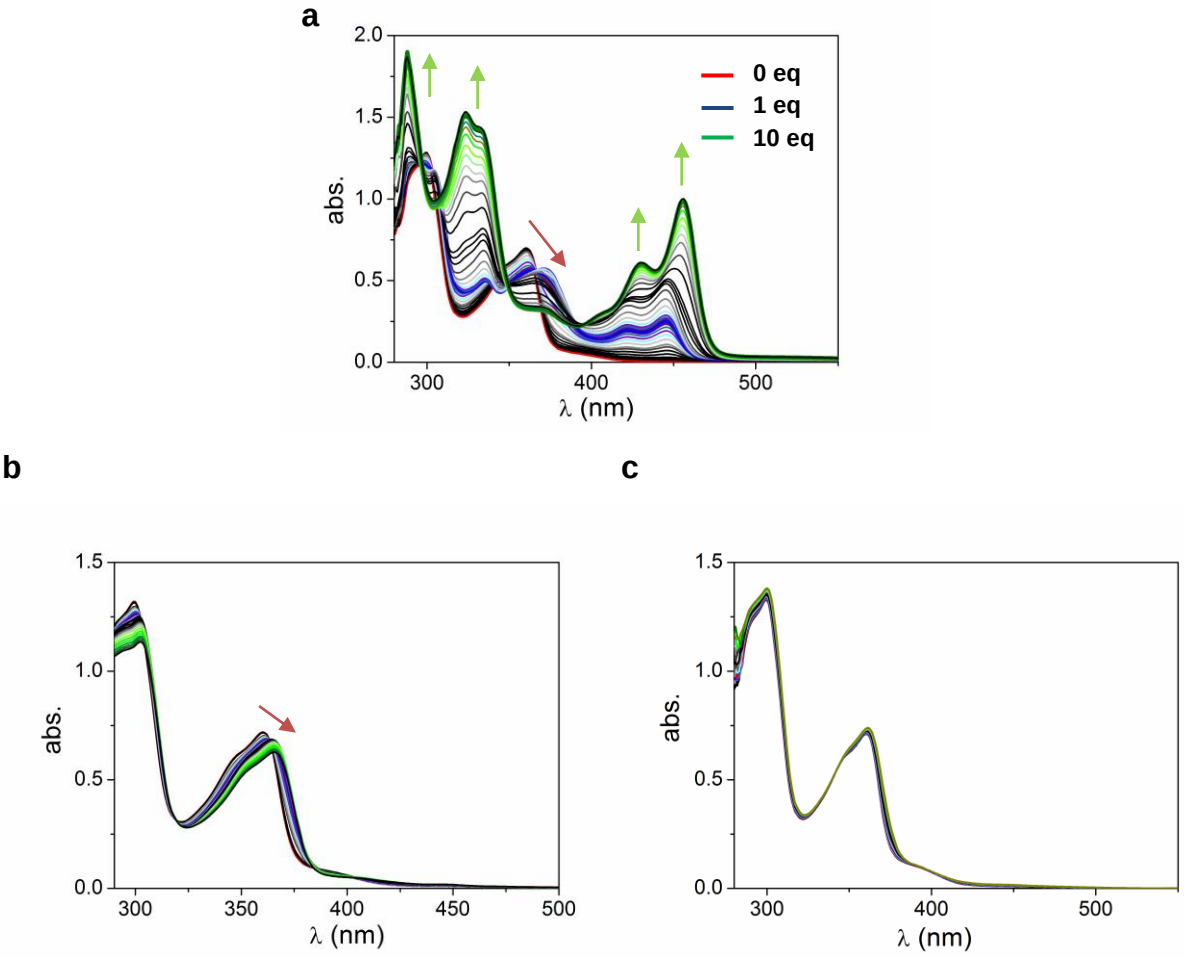

Figure 4-64: Electronic absorption spectra in THF of macrocycle **4-48** ($5*10^{-5}$ M) upon titration of **a:** TBAF, **b:** TBACl and **c:** TBABr.

In the case of the chloride anion the binding affinity of **4-48** was weaker, because this anion was too large to penetrate inside the cavity. A small bathochromic shift in the absorption maximum could be monitored in the UV-vis spectrum upon the titration of **4-48** with TBACl (Figure 4-64b). The binding affinity of the bigger bromide to **4-48** was even weaker

and only a negligible change in the UV-vis absorption spectrum could be observed (Figure 4-64c).

A binding stoichiometry of 1 : 1 was determined for all anions based on Job Plot determinations ($\Delta\lambda$ = 360 nm, Figure 4-65a-c).

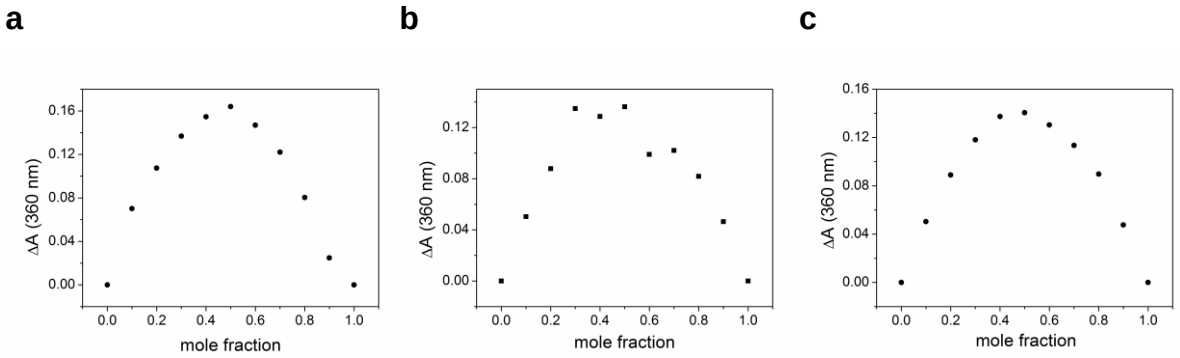

Figure 4-65: Job Plot determination for the binding stoichiometry between macrocycle **4-48** and **a:** fluoride, **b:** chloride and **c:** bromide.

To further understand the halide binding events of macrocycle **4-48**, proton NMR titration experiments were performed (Figure 4-66a-c). Proton NMR spectroscopic titrations do not only give information about the relative shifts of the free host compared to the bound host but also valuable insights about how they interact, *e.g.* changes in symmetry or which proton is more affected.

Equal to the observation based on UV-vis absorption experiments, the NMR titrations proved the highest binding affinity for fluoride. The addition of a small quantity of TBAF to the solution of the host **4-48** caused an immediate decrease of the intensity of the signals for all hydrogens, indicating a strong host-guest interaction (Figure 4-66). If up to 1.0 eq of TBAF were titrated into the solution, the signals for the NHs and CHs became very broad and hardly observable, whereas the signals for the aromatic hydrogens were still sharp. This could be explained by the emerging of an intermediate state, with the fluoride being bonded to the inner hydrogens through hydrogen bonds. Further addition of TBAF caused a second interaction process indicated by the repeated broadening of the aromatic hydrogen signals. This was in agreement with the conclusions drawn from the of UV-vis titration where the formation of an intermediate state at 1 eq had been proposed. Above 4.0 eq the signals of the exocyclic hydrogens and the CHs appeared again and got sharper until no change could be observed anymore. If 10 eq of TBAF were reached the signal of the triazole's CH was shifted downfield to 13.5 ppm ($\Delta\delta$ = 3.8 ppm). On the other hand the signals for the exocyclic aromatic hydrogens of the new species were slightly shifted upfield. It is worth mentioning

that the signals for the exocyclic hydrogens of the new species were symmetric compared to **4-48**, indicating a higher conjugation by planarization of the macrocyclic skeleton caused by the deprotonation.

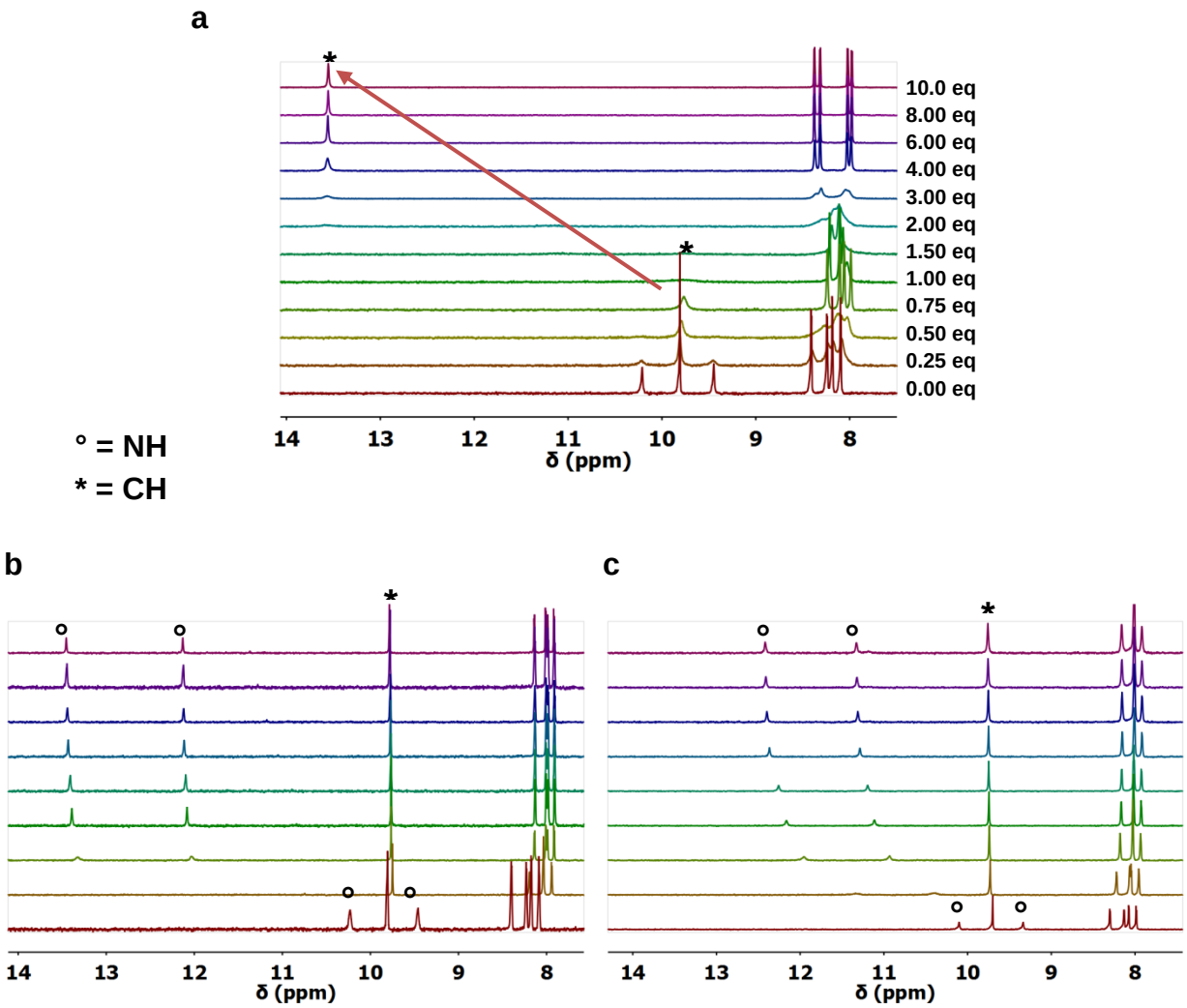

Figure 4-66: ^{1}H NMR spectra of macrocycle **4-48** in THF-d_8, 298 K, 250 MHz upon titration of **a:** TBAF, **b:** TBACl and **c:** TBABr.

The signals of the aromatic protons and the triazole's CH in the proton NMR showed only a small upfield shift upon titration of TBACl to **4-48** (Figure 4-66b). In contrast, a downfield shift of about $\Delta\delta$ = 3.2 ppm was observed for the signals of the NHs at the carbazoles. Therefore, it is suggested, that the chloride anion interacts with the stronger hydrogen-bond donor (NH) from the "outside" of the macrocycle. This is consistent with the observation based on the UV-vis absorption measurements and the statement that the chloride anion is too large to penetrate inside the cavity (Figure 4-67).

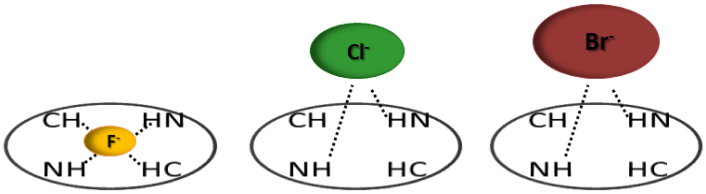

Figure 4-67: Schematic illustration of the host-guest interaction of **4-48** and the halide anions fluoride, chloride and bromide. Fluoride fits perfectly in the cavity whereas the larger halides are too large to penetrate inside the ring.

UV-vis and ^{1}H NMR titration experiments of TBABr to a solution of triazole-containing macrocycle **4-48** showed that the host-guest interaction was very weak. The proton signals of **4-48** in the ^{1}H NMR spectrum suffered only small shifts upon titration with TBABr (Figure 4-66c). However, the signals of the carbazole's NHs were shifted downfield about $\Delta\delta$ = 2.3 ppm, which was due to the interactions of the bromide anion with the NH donor from outside the macrocycle as also assumed for the chloride (Figure 4-67).

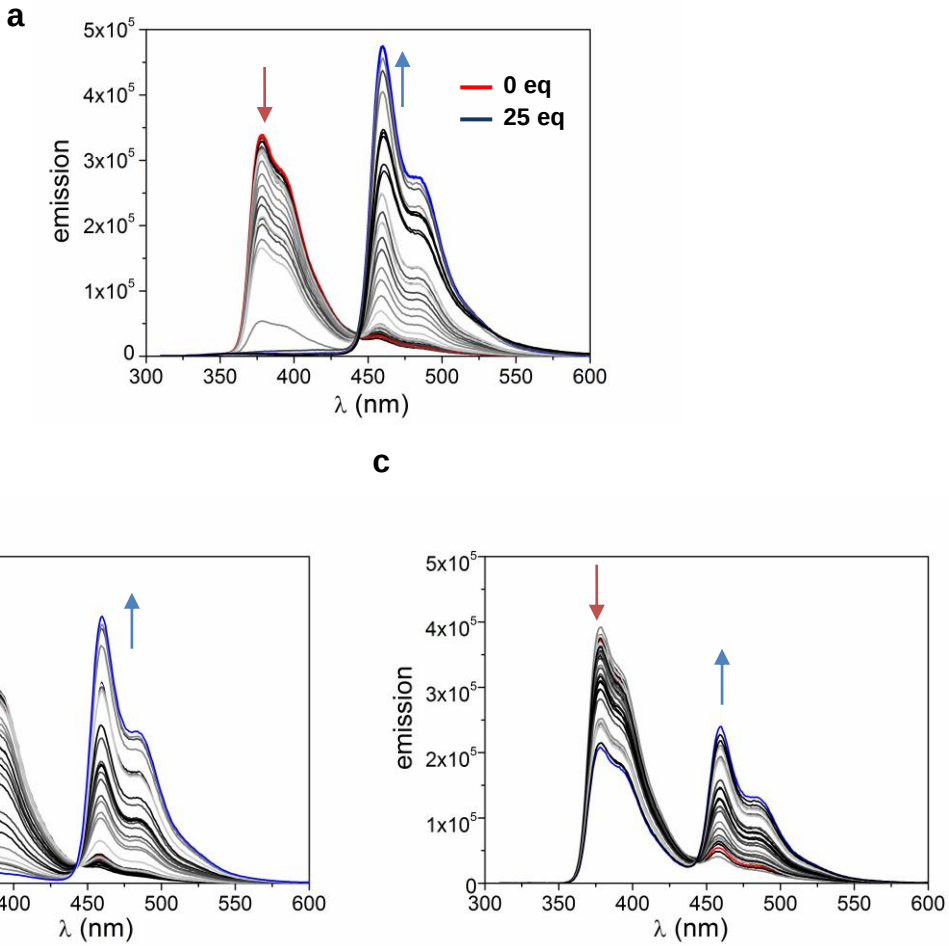

Figure 4-68: Emission spectra in THF of macrocycle **4-48** ($1*10^{-5}$ M) upon titration of **a:** TBAF, **b:** TBACl and **c:** TBABr at rt, λ_{ex} = 300 nm.

Quantitative measurements of anion affinity were performed using fluorescence titration measurements, since the high sensitivity of fluorescence spectroscopy enables the detection of weak host-guest interactions (Figure 4-68).[297]

Fluorescence titration experiments showed, that the emission maximum of macrocycle **4-48** at λ_{em} = 378 nm (red) decreased and a new bathochromically shifted maximum at λ_{em} = 460 nm (blue) aroused upon titration of **4-48** with 0.025 up to 25 equivalents (blue) of all halides (Figure 4-68). For the fluoride anion the original maximum entirely disappeared, whereas for the chloride and bromide anion the maximum was not completely quenched upon titration with 25 equivalents of the halide salts. The quenching effect was lowest for bromide.

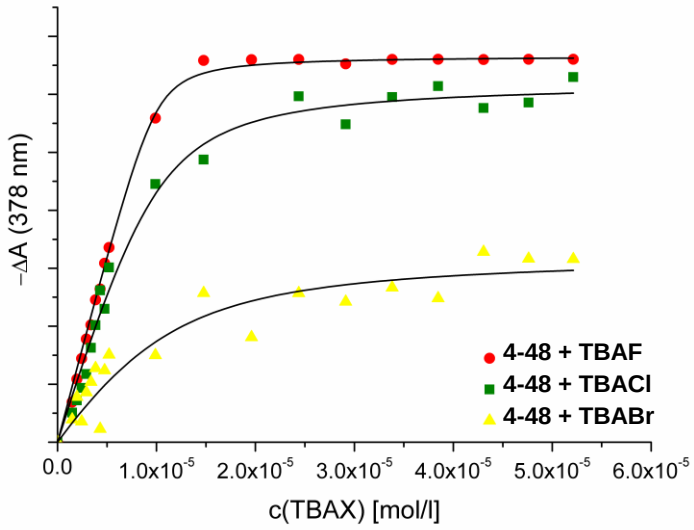

Figure 4-69: Binding isotherms of macrocycle **4-48** and the corresponding halide ions, fluoride (red), chloride (green) and bromine (yellow).

The association constants K_a were estimated from the changes in the emission spectra at λ_{em} = 378 nm as a function of halide added (Figure 4-69). The resulting binding isotherm was then fitted to a mathematical model assuming 1:1 binding stoichiometry based on the Job plot determination derived from UV-vis measurements (Figure 4-65).

The data were fitted to

$$y = A\left(\left([M] + x + \frac{1}{K_a}\right)\right) - \frac{1}{2}\sqrt{\left([M] + x + \frac{1}{K_a}\right)^2 - (4[M]x)} \quad (4\text{-}4)$$

where y corresponds to the change in the emission spectra at $\lambda = 378$ nm, x is the concentration of the corresponding halide, A the extinction coefficient, K_a the association constant and $[M]$ the concentration of the corresponding macrocycle.[299] These calculations provided association constants of $K_a(F^-) = 4.1 \pm 1.1 * 10^6\ M^{-1}$, $K_a(Cl^-) = 7.4 \pm 2.3 * 10^5\ M^{-1}$ and $K_a(Br^-) = 2.5 \pm 1.4 * 10^5\ M^{-1}$. The selectivity for the binding to fluoride was undoubtedly expressed in the value of its association constant which was one order of magnitude higher than for the other halides. The strength of the binding compares well to a variety of receptors.[274, 304-305]

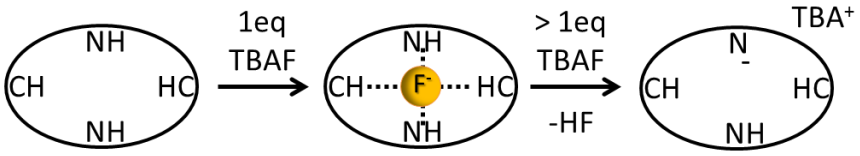

Figure 4-70: Schematic illustration of the suggested two-step interaction mechanism of macrocycle **4-48** with fluoride.

UV-vis and NMR spectroscopic titration experiments gave evidence for a two-step host-guest interaction mechanism between macrocycle **4-48** and TBAF (Figure 4-70). It is suggested, that firstly, macrocycle **4-48** interacts with the fluoride anion by the formation of hydrogen bonds at the donor units, namely triazole (CH···F$^-$) and carbazole (NH···F$^-$). If 1 eq TBAF is added to macrocycle **4-48**, each receptor molecule is saturated with one fluoride anion resulting in an intermediate state. This is reflected by the initial bathochromic shift of the absorption spectrum and the defined signals in the ^{1}H NMR spectrum at this stage. Further addition however causes deprotonation of one of the carbazole's NHs,[302] leading to the formation of an anionic species. The negative charge is distributed over both carbazole units, stabilized by TBA$^+$ as the counter ion. Due to its acidic character, carbazoles are prone of deprotonation.[306] It has been shown earlier that anion induced deprotonation of neutral hydrogen bond donor moiety can lead to significant color changes.[303] The proton exchange at the carbazole units is fast on the NMR timescale explaining the broadened (not observable) signals in the ^{1}H NMR spectra. The emerging deprotonated species is suggested to cause the drastic bathochromic shift in the absorption spectrum (Figure 4-64a) and could be verified by X-ray spectroscopy. Suitable crystals for X ray diffraction analysis were grown from a THF solution containing macrocycle **4-48** and TBAF at a ratio of 1 : 10. The crystal structure determination revealed the deprotonated species with a more flattened

macrocyclic structure than compared to pyridine-containing macrocycle **4-18** (Figure 4-71). As described earlier, macrocycle **4-18** featured a saddle-like conformation with the pyridine units pointing in the same direction (cf. chapter 4.1.2). In contrast, in the case of **4-48-TBA**$^+$ the pyrrole units were parallel with each pyrrolic proton pointing in a different direction (Figure 4-71b). X-ray analysis also showed that each negatively charged macrocycle had one TBA$^+$ counter ion associated. Summarizing, the suggested two-step host-guest interaction mechanism between macrocycle **4-48** and TBAF could yet not fully be verified, but nevertheless, the final deprotonated species could be evidenced. Further investigation to prove the intermediate state, in which the fluoride anion is bonded by hydrogen bonds in the macrocyclic cavity of **4-48**, will be required to verify the assumption.

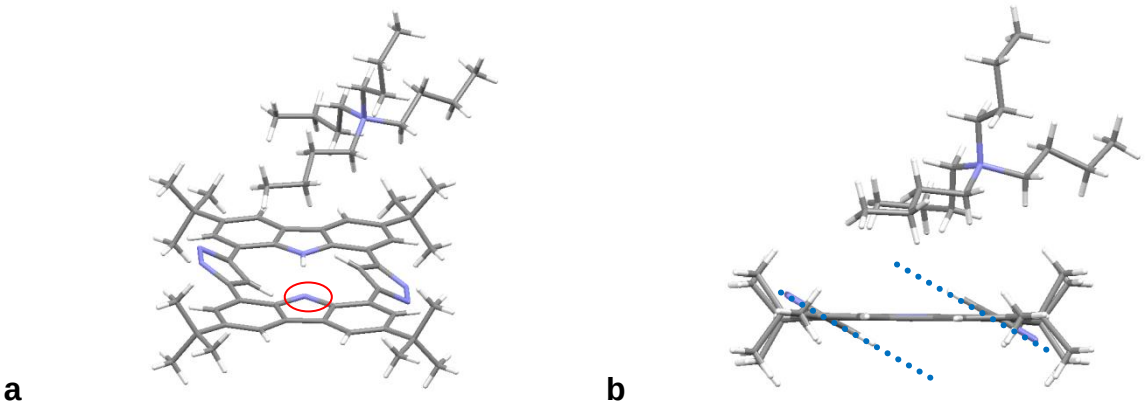

Figure 4-71: Crystal structure of macrocycle **4-48**$^-$ and TBA$^+$ (1:10 in THF, for clarity reason only the major isomer is shown).

Finally, the host-guest interaction of pyrrole-containing macrocycle **4-38** was investigated by UV-vis and fluorescence titration techniques. As expected the strongest affinity was also found for fluoride which was reflected in the strong colorimetric response (Figure 4-72).

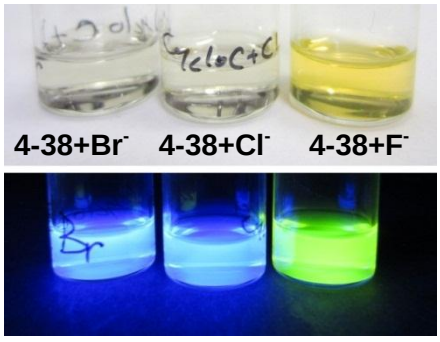

Figure 4-72: Colorimetric response of macrocycle **4-38** (c = 10^{-5} M in THF) to fluoride (10 eq) anion under ambient light and λ = 366 nm.

Again, a color change from colorless to yellow occurred under ambient light. Compared to earlier described triazole-containing macrocycle **4-48** (Figure 4-63, from blue to turquoise), the response at λ = 366 nm for macrocycle pyrrole-containing **4-38** was more pronounced (Figure 4-72, from blue to yellow).

The radical change of the absorption spectrum of compound **4-38** upon titration with TBAF is shown in Figure 4-73. Similar to receptor **4-48** the absorption maximum at λ = 400 nm decreased and new intense bands in the region of 450 to 550 nm appeared. Again, when larger halides like chloride and bromine were titrated to a solution of receptor **4-38** almost no change in the absorption was observed. Likewise as in the previously described case for **4-48**, chlorine and bromine were too large to insert into its cavity.

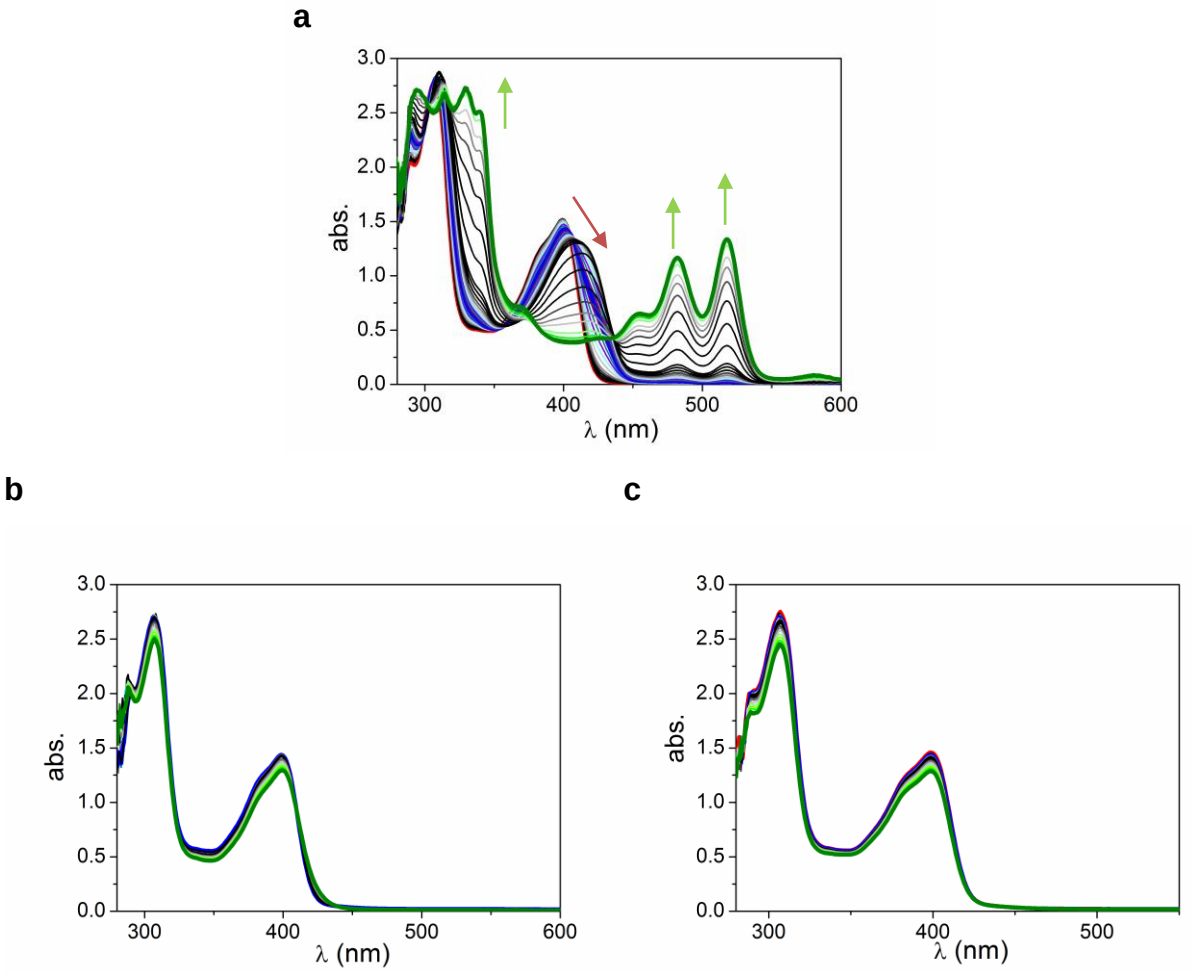

Figure 4-73: Electronic absorption spectra in THF of macrocycle **4-38** ($5*10^{-5}$ M) upon titration of **a:** TBAF, **b:** TBACl and **c:** TBABr.

In equal measure, Job Plot determination showed a binding stoichiometry of 1 : 1 of **4-38** with all three halides (Figure 4-74). Note, that for the data recorded for macrocycle **4-38** and

TBAF, two data points unfortunately deviate from the others which nevertheless adopted the progression for a 1 : 1 stoichiometry.

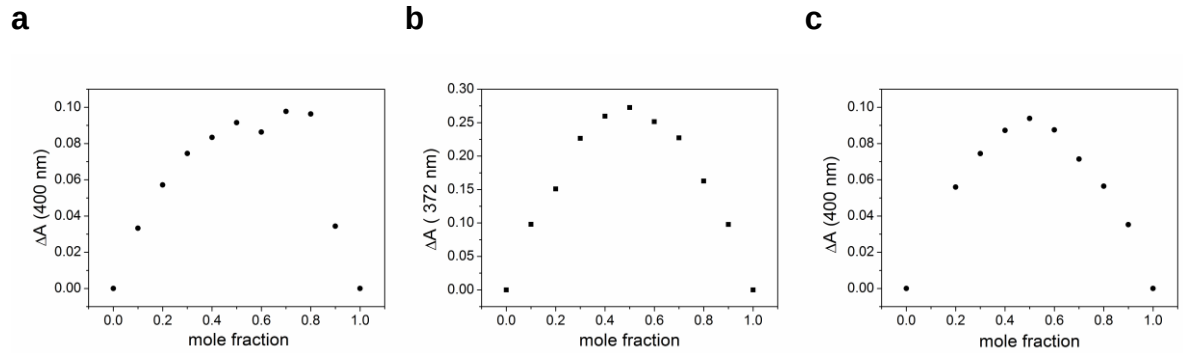

Figure 4-74: Job Plot determination for the binding stoichiometry between macrocycle **4-38** and **a:** fluoride, **b:** chloride and **c:** bromide.

Surprisingly, the rigorous changes in the absorption upon interaction of pyrrole-containing macrocycle **4-38** with the fluoride anion were not reflected in fluorescence (Figure 4-75).

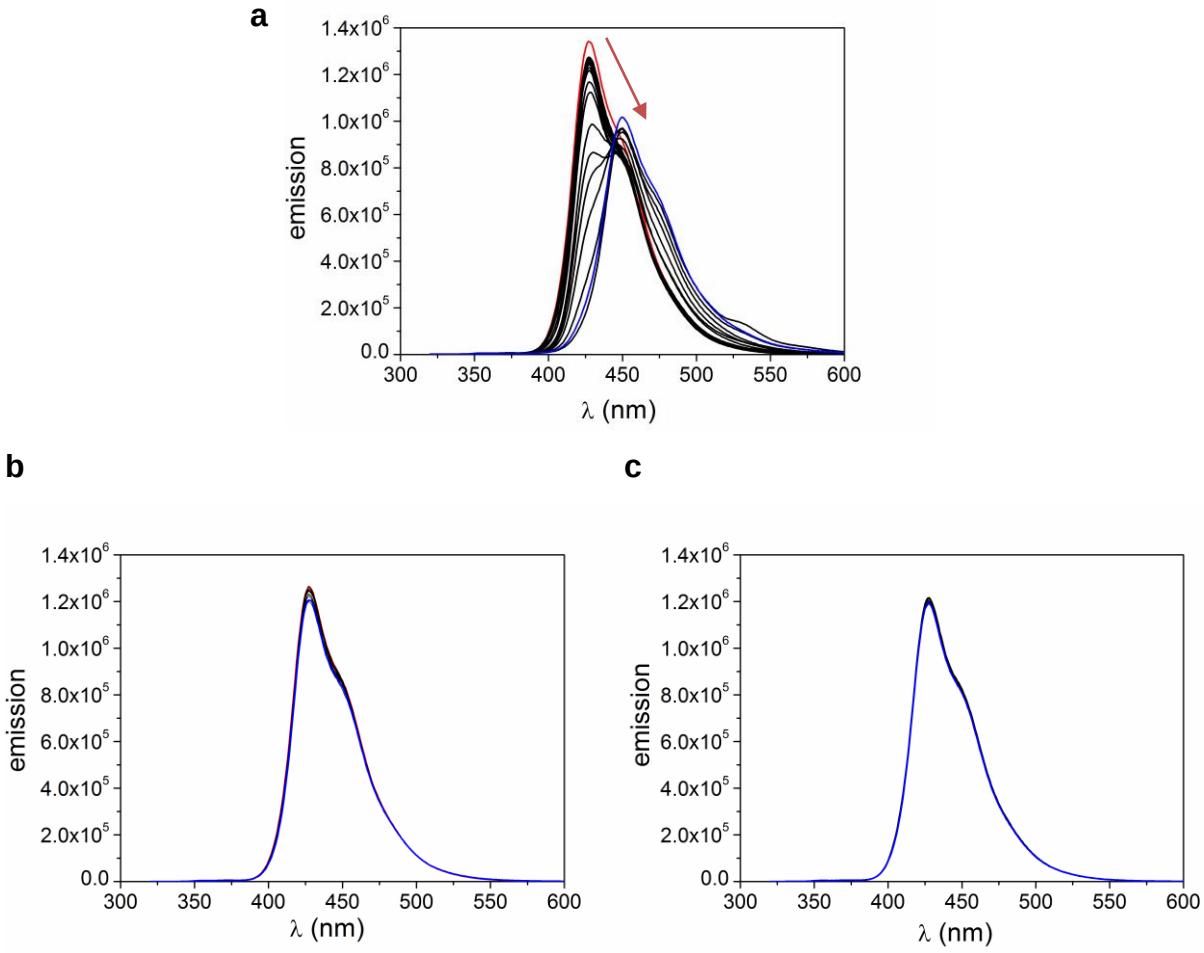

Figure 4-75: Emission spectra in THF of macrocycle **4-38** ($1*10^{-5}$ M) upon titration of **a:** TBAF, **b:** TBACl and **c:** TBABr at rt, λ_{ex} = 310 nm.

Furthermore, the changing profile in fluorescence differed from the ones detected for the host guest interaction of fluoride with triazole-containing macrocycle **4-48** (cf. Figure 4-68), though the changes in the absorption were quite similar. In the case of **4-38**, the emission maximum at λ= 427 nm was bathochromically shifted to 450 nm along with a reduction in the intensity when titrated with fluoride anions (Figure 4-75a).
On the contrary, almost no change in the fluorescence was detected when larger halides like chloride or bromine anions were added to a solution of macrocycle **4-38** (Figure 4-75b-c).

Although, Job plot determination showed a binding stoichiometry, deplorably, the data received from the fluorescence titration experiments could not be fitted to a 1 : 1 isotherm model. Nevertheless, the plotted data nicely showed that the affinity of macrocycle **4-38** to bind a halide was strongest for fluoride and almost negligible for chloride and bromide (Figure 4-76).

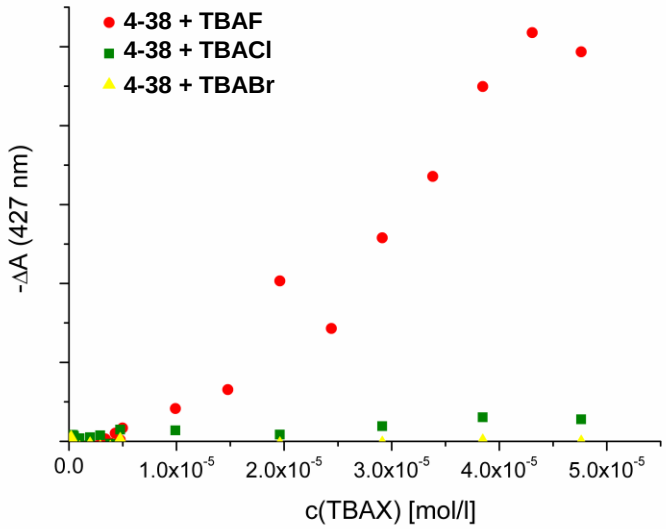

Figure 4-76: Binding isotherms of macrocycle **4-38** and the corresponding halide ions.

Summarizing, the host-guest chemistry of the three related macrocycles **4-18, 4-38** and **4-48** have been investigated for the halide anions fluoride, chloride and bromide. Due to the size of the macrocyclic cavities, the fluoride anion was expected to show the highest binding affinity to all three receptors. This prognosis could be approved for all the macrocyclic receptors **4-18, 4-38** and **4-48**. Pyridine-containing macrocycle **4-18** showed the weakest host-guest interactions, which can be explained by the absence of hydrogen bond donor properties of pyridine.

The most rigorous colorimetric response and change in absorption when titrated with fluoride anions were found for pyrrole-containing macrocycle **4-38**. This can be explained by the presence of the two NH hydrogen bond donor units, namely, carbazole and pyrrole, which are able to bind the fluoride strongly. In contrast, the weaker CH hydrogen bond donors represented by a triazole units in **4-48**, caused the weaker host-guest interaction of **4-48** with fluoride. Although, not the best within the series, macrocycle **4-48** is the first example in literature of an anion receptor containing both, NH and CH hydrogen bond donor units. Therefore, the binding ability of triazole-containing compound **4-48** was investigated in detailed and revealed an association constant for the fluoride anion of $K_a(F^-) = 4.1 \pm 1.1 * 10^6\ M^{-1}$, which compares well to a variety of receptors found in recent literature ($K_a(F^-) = 2.8 \pm 3.0 * 10^5\ M^{-1}$ for [3$_4$]triazolophane derivative,[141] $K_a(F^-) = 2.0 * 10^8\ M^{-1} \pm 6\%$ for indole-based macrocycle,[304] $K_a(F^-) = 1.7 \pm 0.09 * 10^3\ M^{-1}$ for tripodal receptor[305]).

4.4 Summary and Comparison

In summary, three novel porphyrinoids have been successfully synthesized *via* palladium-catalyzed Suzuki cross-coupling reaction or copper(I)-catalyzed azide-alkyne cycloaddition (CuAAC). All of these derivatives incorporated carbazole units that were linked through aryl-aryl bonds to other heterocycles like pyridine (**4-18**), pyrrole (**4-38**) or triazole (**4-48**). Different from porphyrins the individual building blocks were not connected *via* methine bridges and therefore unstable *meso*-carbons could be avoided. The dimensions of their cavities were similar to those of porphyrins which offer the possibility to act as metal-complexing ligand or as an anion receptor. The main motivation for the design of new porphyrinoids is to control and tune electronic properties. Interestingly, none of the herein reported porphyrinoid possessed porphyrin-like aromaticity or a planar geometry and rather behaved as simple carbazole derivatives. If the optical properties were compared the influence of the pyridine (**4-18**), pyrrole (**4-38**) or triazole (**4-48**) to the macrocyclic core could be assessed (Figure 4-77, Table 4-7).

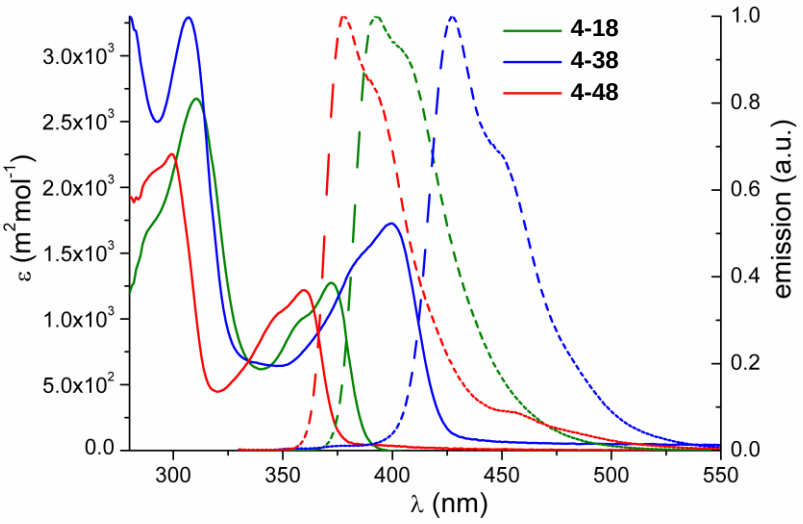

Figure 4-77: Electronic absorption and emission spectra of macrocycles **4-18** (green), **4-38** (blue) and **4-48** (red, c = 5*10^{-5} M in THF),

The higher energy maxima in the region 300-320 nm of the electronic absorption spectra originated for all porphyrinoids from carbazole-centered transitions. These corresponded to the π–π*-electron transitions of the localized conjugated skeleton and were little influenced by the exchanged of different heterocycles in the macrocyclic core. On the contrary, the

absorption bands in the longer-wavelength region (325-435 nm) showed greater differences depending on the heterocycle attached to the carbazoles. The longest wavelength absorption at 400 nm was found for pyrrole-containing macrocycle **4-38**, assuming a good conjugation in the macrocyclic core influenced by the pyrrole units. For the triazole-containing macrocycle **4-48** this band absorbed at 360 nm, which corroborated the assumption that the triazole units hinderd complete delocalization of π-electrons and thus the electronic communication in the macrocycle.

All three compounds featured a broad emission band in the blue region with one peak and one shoulder, which were mirror symmetrical to the absorption spectra. Shoulders in the emission generally are attributed to vibronic bands resulting from the rigidity of the macrocycle.[307-308] Quantum yields Φ_f have been determined using the Comparative Method[186] for all macrocycles (λ_{ex} = 349 nm in THF). This investigation showed that Φ_f was highest for the pyrrole-containing macrocycle **4-38** and lowest for triazole-containing macrocycle **4-48**. In pyrroles and carbazoles the non-bonding orbitals are perpendicular to the plane of ring, which allows the overlap of the π-orbitals on the adjacent carbon atoms. Therefore, both heterocycles usually have high fluorescence quantum yields. In conclusion, pyrrole-containing macrocycle **4-38** featured an extended π–electron system with a higher degree of π-conjugation compared to **4-18** and **4-48**, which was reflected in the shifts to higher wavelength in absorption and emission spectra.

Table 4-7: Summary of the electronic properties of macrocycles **4-18**, **4-38** and **4-48**.

compound	λ_{abs} [nm]	λ_{em} [nm]	Φ_f [a]	$E^{LUMO[b]}$ [eV]	$E^{HOMO[b]}$ [eV]	ΔE_g [b] [ev]
4-18	313, 372	393	0.46	-1.17	-5.14	3.97
4-38	307, 400	427	0.68	-1.18	-4.74	3.56
4-48	299, 360	378	0.29	-1.59	-5.46	3.87

[a] Φf were estimated using the Comparative Method.[186] Samples in THF are referenced against Coumarin 1 in EtOH, λex = 346 nm. [b] received from molecular modeling using DFT, B3LYP/6-31G*.[184]

An overview of the orbital energies of all macrocycles based on theoretical calculation[184] compared with the data received from experimental measurements is given in Figure 4-78. The data evaluated from quantum mechanical calculations were in good agreement with the experimental data, if the different conditions were considered, namely, experimentally determined energy levels were based on solution measurements whereas in theoretical calculations the solvochromic effects were neglected.[309] The most apparent fact which

could be seen by this line-up (Figure 4-78) was the increased HOMO energy level of macrocycle **4-38**. This could be explained by the strong electron donor ability of pyrrole, which resulted in a small energy gap for the resulting macrocycle and was one reason for the reduced stability of **4-38**.

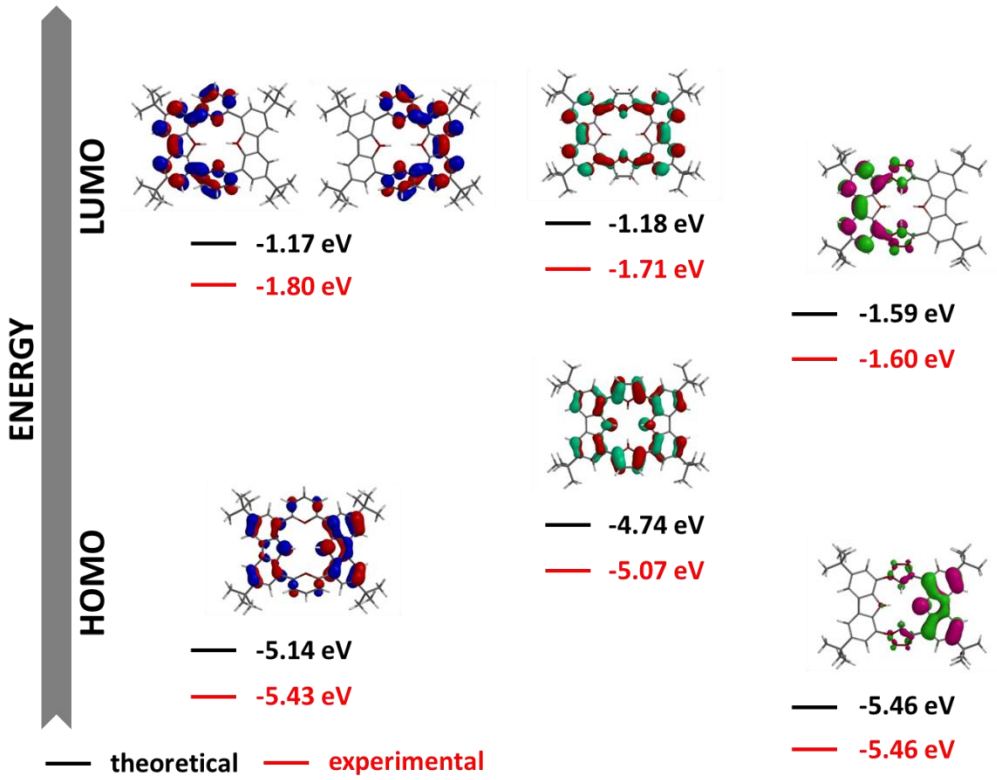

Figure 4-78: Experimental (red) and theoretical (black) orbital energies of macrocycles **4-18** (left), **4-38** (middle) and **4-48** (right, DFT, B3LYP/6-31G*).[184]

By and large, the concept to synthesize small porphyrin-like macrocycles from aromatic building blocks using contemporary chemistry was proven in three different cases. Furthermore, different applications for each of them were investigated as follows. The cobalt complex of pyridine-containing macrocycle **4-18** was tested as an active electrochemical catalyst for the reduction of oxygen and showed a number of electron transferred of n = 3.78 (pyrolyzed at 600°C).

Macrocycle **4-38** on the other hand, is the first reported anion-receptor including CH and NH hydrogen bond donors for halide binding in one macrocyclic core. It showed colorimetric selectivity for fluoride anion with a calculated association constant of $K_a(F^-) = 4.07*10^6\ M^{-1}$ based on fluorescence titration measurements.

Although, pyrrole-containing macrocycle **4-38** was found to be very instable, it showed the ability to be oxidized to its aromatic porphyrin-state featuring highly red-shifted absorption bands.

Moreover, the first synthesis of the key intermediates 3,6-di-*tert*-butyl-1,8-bis(4,4,5,5-tetramethyl-1,3,2-dioxaborolan-2-yl)-9*H*-carbazole **4-16** and 1,8-diazido-3,6-di-*tert*-butyl-9*H*-carbazole **4-46** might be valuable for the design of novel poly-(1,8-carbazoles), which chemistry is still in its childhood.[177] Compared to their related well-established poly-(3,6- and 2,7-carbazoles),[72] conjugated poly-(1,8-carbazoles) have been based so far exclusively on 1,8-diethynyl-carbazole derivatives.[192, 310-311] First and foremost, the new key intermediates open access to a variety of novel porphyrinoids. In theory other heterocycles such as thiophene,[35] furan, tetrazole or simply benzene might be incorporated in the porphyrin core just like puzzle pieces in a jigsaw.

5 Triangular Trinuclear Systems

Two-dimensional π-extended porphyrinoids comprising multi-metal sites are still neglected in the literature but feature unique properties for applications *e.g.* in photodynamic therapy,[24] non-linear optics,[46] or as organic semiconductors[90] and electrochemical catalysts for the reduction of oxygen (ORR = oxygen reduction reaction).[144] Macrocyclic N_4-complexes are known to be promising alternatives to platinum based catalyst for ORR *e.g.* in fuel cells.[110] It has been shown that the direct 4-electron reduction of oxygen to water is favored if the oxygen can interact simultaneously with two metal sites.[98] The current most active catalyst is platinum which reduces oxygen exclusively *via* the direct pathway while the molecular oxygen adopts a bridge-*cis* type configuration on the metal centers (cf. chapter 2.2). In this sense, development of macrocyclic N_4-complexes with multi-metal sites in order to promote the direct 4-electron reduction is an active field. Bimetallic cofacial complexes, where the oxygen atom can simultaneously bind in the "bite" of the Pacman,[124-125] already showed improved catalytic activity.[126] Nevertheless, in the Pacman cleft the oxygen interacts in bridge-*trans* type configuration, whereas on planar bimetal complexes the oxygen can adopt the bridge-*cis* configuration. Those dinuclear systems proved to promote the four-electron reduction of oxygen but are rarely found in literature and not conjugated and therefore suffer from instability.[127]

This pointed us to the development of a planar, π-conjugated ligand with the possibility to coordinate two or more metals in close vicinity to enable interaction with oxygen in the bridge-*cis* configuration. Moreover, it should be producible from readily available building blocks in order to keep the costs low. In this regard, 1,4,5,8,9,12-**h**exa**a**za**t**riphenylene (HAT) derivatives attracted our attention, due to their trigonal symmetrical arrangement of conjugated fused 1,10-phenanthroline-type binding sites (Figure 5-1). A variety of metal complexes have been prepared based on the HAT including ruthenium,[312] chromium,[313] cobalt[314] and copper[315] complexes. Besides the valuable coordination ability, HATs offer interesting properties concerning self-assembly in solution and on surfaces,[316-317]

liquid-crystal-behavior[318-319] and redox-properties.[320-321] Moreover, the pyrazine function induces an electron-deficient character, leading to electron-acceptor properties.[322]

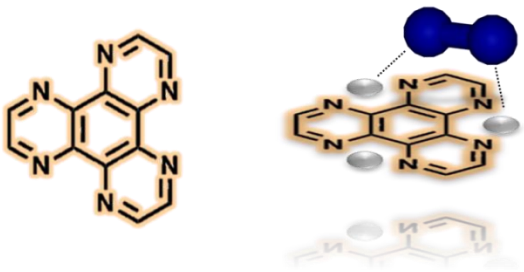

HAT

Figure 5-1: Schematic strucutre of tris-bidentate (triple metal-chelating) hexaazatriphenylenes (HATs) with the ability to bind molecular oxygen in its bridge-*cis* configuration.

Mainly, HATs can be obtained by two different synthetic approaches, more precisely, by the reaction of hexaaminobenzene **5-2** with 1,2-diketone **5-1** or by the threefold condensation of hexaketocyclohexane **5-5** and 1,2-diamino derivatives **5-4** (Scheme 5-1).[323-327] The first route is suitable for a variety of HATs including alkyl, aryl or vinyl derivatives. Nevertheless, this procedure involves the use of triaminotrinitrobenzene, which is an explosive and used in military applications. The second approach is relevant for derivatives with electron-withdrawing groups such as cyano-, carboxyl- and amide-derivatives. Generally, in these derivatives the coordination ability of the aromatic nitrogen atoms is reduced due to the electron-withdrawing groups.

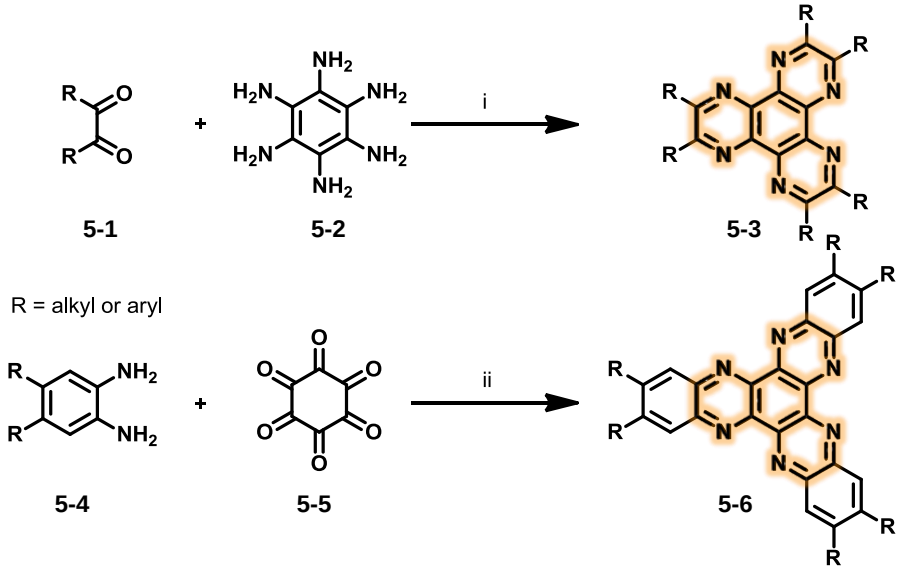

Scheme 5-1: Synthesis of HAT derivatives. Conditions: *i* EtOH, H_2O, 50°C; *ii* AcOH, $CHCl_3$, reflux.

The first HAT was synthesized in 1981 by the condensation of pyrazino[2,3-*f*]quinoxaline-5,6-diamine with aqueous glyoxal, and served as a ligand to coordinate chromium.[324] Although most of the literature concerning HATs refer to their coordination properties and the characteristics of the resulting metal complexes, recently more attention has been devoted to HATs in the absence of metals. HATs can be self-assembled both in solution and in bulk state to form π-stacked one-dimensional aggregates,[328-330] resulting in discotic liquid crystals that may transport charge. Hereby, the crystalline character is promoted by the conjugated core and the liquid character is provided by the long chains in the periphery. This characteristic is responsible for HAT being one of the new candidates as parent of large sized n-type semiconductors.[331] For example, the first HAT derivatives showing charge-carrier mobility (μ = 0.08 $cm^2V^{-1}s^{-1}$) carried amido groups in its periphery (Figure 5-2, HAT **5-7**).[332] By the introduction of sulfur atoms the mobility could be improved (up to μ = 0.9 $cm^2V^{-1}s^{-1}$ for HAT **5-8**, Figure 5-2).[318] If the number of pyrazine units in the HAT core is increased, the molecular orbital levels can be tuned, *e.g.* HAT **5-9** feature an even lower LUMO energy level (-4.02 eV) than the well-known n-type PCBM ([6,6]-**P**henyl **C**61 **B**utyric acid **M**ethyl ester; -3.80 eV).[333-334]

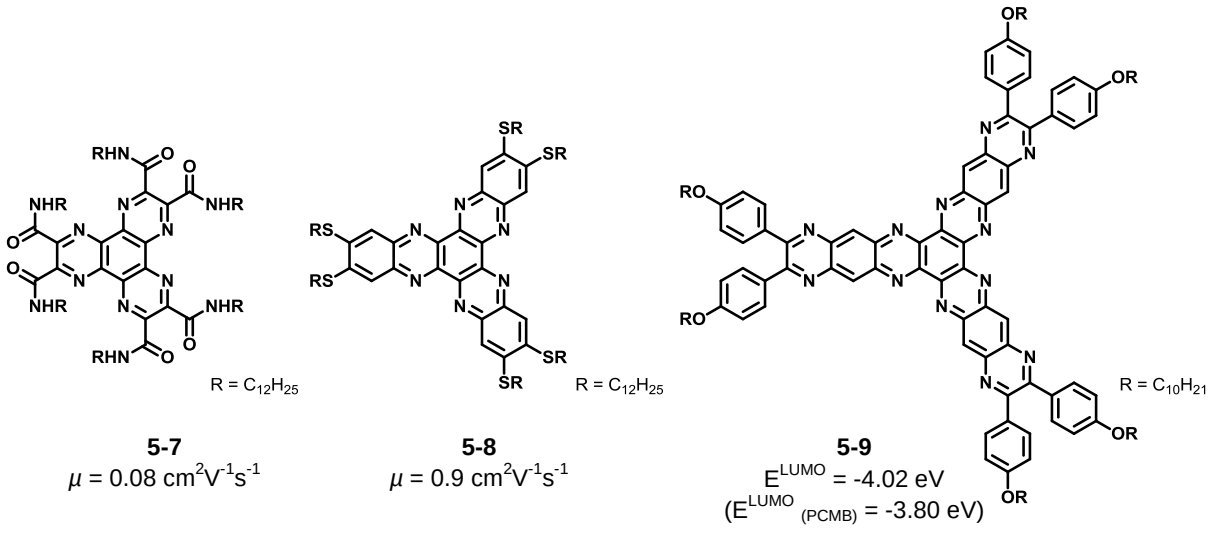

Figure 5-2: Examples of HATs **5-7** and **5-8** with charge-transport properties and **5-9** with low LOMO energy level.

In a nutshell, the ready availability along with the ability to coordinate more than one metal make HAT the ideal candidate for the design of a new macrocyclic N_4-complex with multi-metal sites which is expected to promote the direct 4-electron reduction of oxygen to water (Figure 5-3). In particular, HAT perfectly provides a basic triangular structure for the

fusion of three N_4-macrocyclic porphyrinoids. If theoretically three porphyrins are combined to a HAT molecule, a triangular trinuclear ligand can be created, as shown in Figure 5-3 (middle).

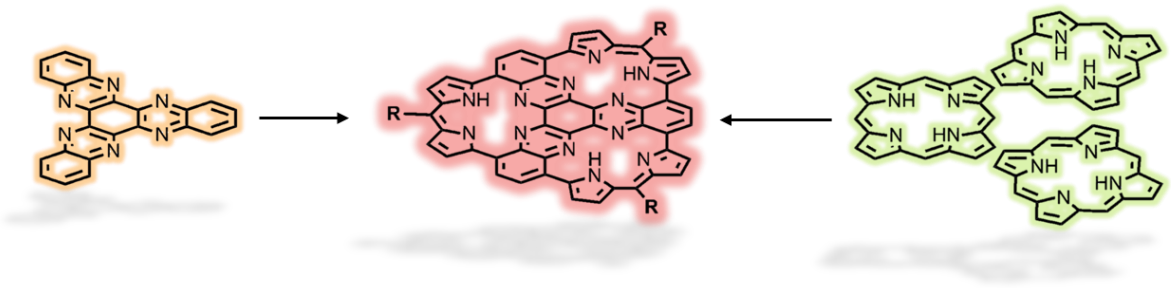

Figure 5-3: Design concept for two-dimensionally triangular porphyrinoid.

For the creation of porphyrin-like centers, two additional nitrogen atoms are required in each of the three corners. In this regard, the attachment of six pyrrole moieties in the periphery of the HAT provides the possibility to create simultaneously three N_4-rings. Two pyrroles can undergo a condensation reaction with an aldehyde at the α-positions,[3] and in this case close the porphyrinoids resulting in a triangular trisnuclear disk. From a design point of view the cavities are as close as possible and well conjugated *via* the central HAT plane. Nevertheless, the three N_4-rings will not be true porphyrins but contain only one pyrrolic and three imine-type nitrogens. Common porphyrins favor the *trans*-NH-tautomers including two pyrrolic and two pyrrolenic nitrogens.[335] In the triangle case, only one nitrogen in each cycle is bearing a free hydrogen atom, consequently, each porphyrin-like ring will act as a monoanion and overall the triangular tricycle as a trianion in coordination chemistry.

Previous work by a former group member, Christian von Malotki, demonstrated the reliability of the design concept by the successful synthesis of the first triangular trisnulcear ligand **5-10** bearing octyl groups in its periphery (Figure 5-4).[144] Nevertheless, until such time, the formation of the structure had only been proven by Maldi-Tof spectrometry and precise structure elucidation was lacking. Nevertheless, it was possible to introduce metal(II) ions such as cobalt(II) and iron(II) into the cavities and to investigate the electrochemical activity towards the ORR. The unique features of the resulting complexes including large planar conjugation and unprecedented high density of active sites proved to be advantageous for the reduction of oxygen *via* the direct four electron pathway. Indeed, the cobalt complex

[CoN$_4$]$_3$ **5-11** showed higher electrocatalytic activity and better long-term operation stability than those of commercially available Pt/C, when tested under the same conditions (Figure 5-4).[144] In detail, for the electrochemical investigations, complex [CoN$_4$]$_3$ **5-11** was supported on carbon black (Vulcan XC-72R) and cyclic voltammetric evaluation in alkaline solution was performed (0.1 M KOH, O_2 saturated, scan rate 100 mVs^{-1}). It has to be emphasized that the catalyst samples were measured without prior heat treatment.

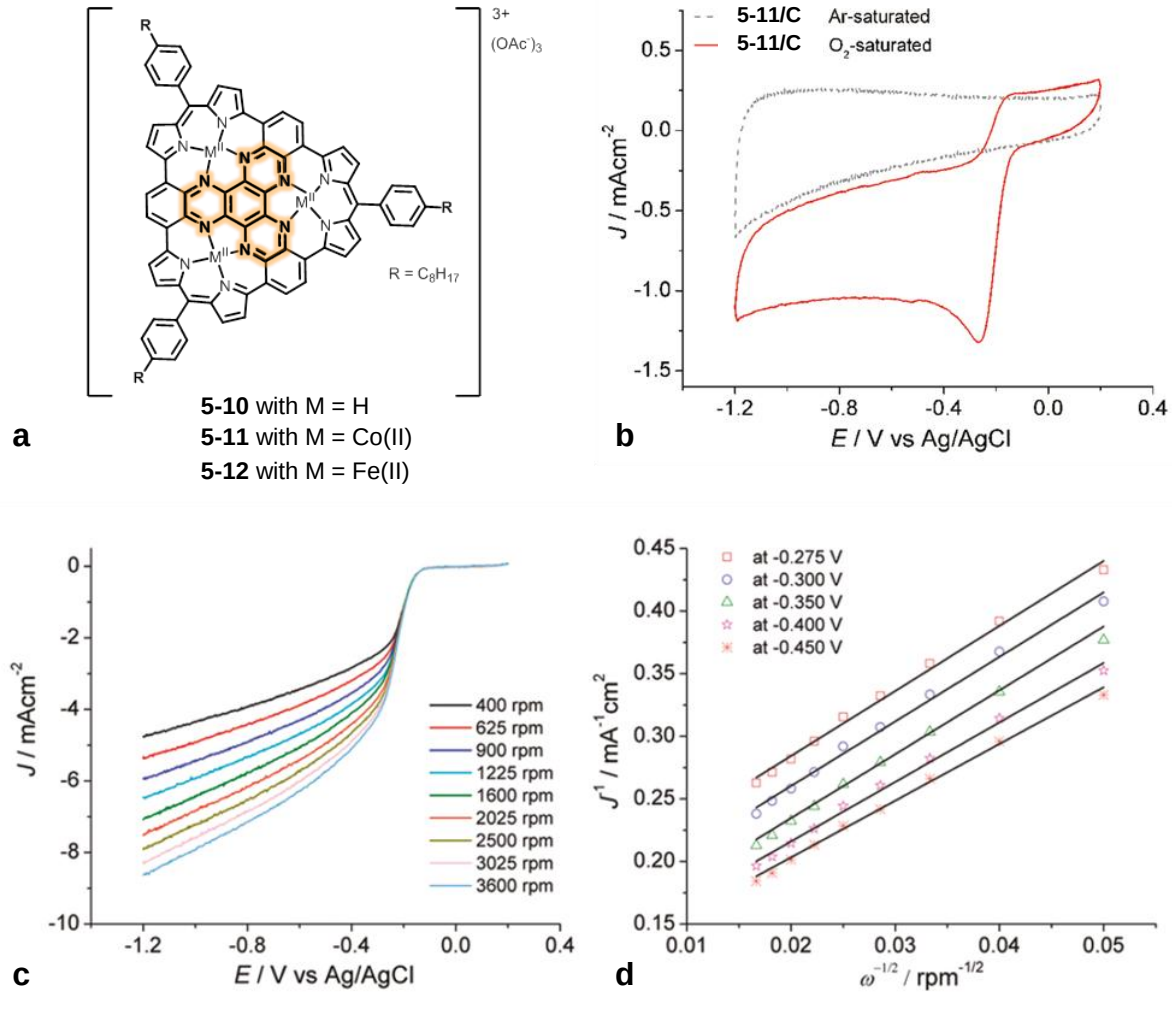

Figure 5-4 : **a:** Triangular trisnuclear ligand **5-10** and its metal complexes **5-11** and **5-12**. **b:** Cyclic voltammograms of **5-11/C** on glassy-carbon RDE electrode (scan rate 100 mVs^{-1}, 0.1 M KOH solution, 25 µgcm^{-2} catalysts loading). **c:** RDE linear sweep voltammograms of **5-11/C** at different rotation speeds. **d:** Koutecky-Levich plot for **5-11/C** at different electrode potentials.[144]

The cyclic voltammogram showed a defined cathodic peak at -0.26 V indicating a pronounced electrochemical activity for the ORR (Figure 5-4b). Further investigation by RDE measurements revealed an onset potential for the ORR at -0.14 V close to that of commercial Pt/C (-0.11 V, Figure 5-4c). A number of electron transferred of n = 3.7 (for

Pt/C n = 3.9) was obtained from the corresponding Koutecky-Levich plots (Figure 5-4d). This proved a high selectivity for the direct four electron oxygen reduction pathway. Furthermore, the well-defined structure of the trinuclear metal-N_4 complexes provided information about the nature of active sites and the relationship between molecular structure and catalytic activity. It could be shown, that the ligand itself exhibited catalytic activity, similar to metal-free nitrogen containing carbon materials,[220, 336-337] and that higher metal content accounted for an increased catalytic activity in the cobalt complex **5-11**. While the fully complexed ligand favored the direct four electron reduction, the partially filled ligand reduced the oxygen *via* the two electron pathway. Only if the ligand was loaded with at least two metal ions, the molecular oxygen could interact in a bridge-*cis* configuration promoting the desired direct four electron reduction. Thus, this complex possesses structurally defined catalytic sites for ORR and therefore provides a platform for new generation of non-precious metal catalysis (NPMC).

Further development of this NPMC firstly and overall required a detailed structure elucidation, including the electronic properties. Secondly, the influence of the substituents in the periphery of the triangular ligand on the catalytic activity is an interesting target, since sufficient contact between catalyst and carbon support might not only improve the conductivity from the carbon support but therewith the catalytic activity.

On the other hand, the direct connection of the individual triangles would further enlarge the conjugation which benefits conductivity and hence the catalytic activity.

Of special interest is the ability to form mesophases depending on the substituents to consider network forming through cross-linking by heat treatment in the liquid crystalline phase. By this even higher density of active sites might be achieved resulting in an improved electrocatalytic activity. Related two-dimensional alkyl substituted graphene disks are known to oligomerize and form carbon nano-particles by pyrolysis in the mesophase.[221] Accessorily, advantage can be taken of the presumably improved stability of the [CoN_4] complex after heat treatment, which was already discovered for metal macrocycles by Jahnke *et al.*[113]

For this reasons, the following will describe the synthesis of a series of planar triangular porphyrinoids with different substituents like phenyl, (phenyl)ethynylbenzene or (phenyl)thiophene moieties with attached alkyl, branched alkyl or alkoxy side chains. Because the synthesis of the **h**exa(**p**yrrol-yl)**h**exa**a**za**t**ri**n**aphthalenes (HPHATNs) deviates from the originally described protocol by von Malokti,[144] it will be specified again. Furthermore, their optical and electrochemical properties, their supramolecular organization

in solid state as well as their metal complexation will be investigated. Finally, some preliminary results of the electrocatalytic experiments are given.

5.1 Results and Discussion

5.1.1 Synthesis

The goal of this part of the present work was to introduce diverse substituents into the periphery of the **h**exa(**p**yrrol-yl)**h**exa**a**za**t**ri**n**aphthalene (HPHATN) core in order to study their influence on the catalytic activity towards the reduction of oxygen. By the variation of the side chains by means of length, number of entities and steric demand the influence on the mesophase formation and electronic properties can be studied. For this purpose, a linear dodecyl-, a branched hexyldecyl- (racemic mixture was used) and a tris-dodecloxy-side chain were chosen (Figure 5-5). The introduction of acetylene spacers might be conducive to enhance contact between catalyst and carbon support and therewith increase the catalytic activity.[145] To ensure solubility and comparability, the dodecyl- and the tris-alkoxy case were contemplated to be enlarged by acetylene spacers (Figure 5-5).

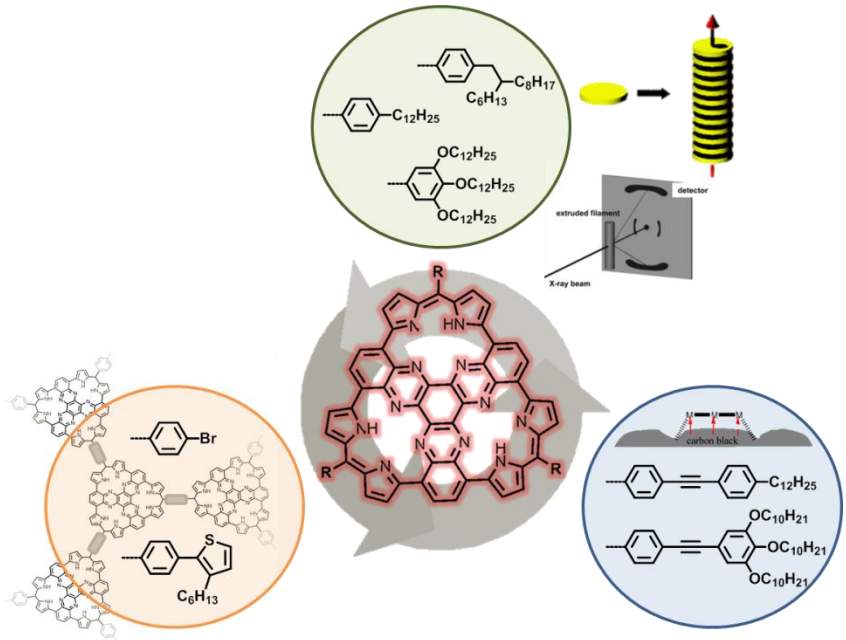

Figure 5-5: Different substituents at the periphery of the hexa(pyrrol-yl)hexaazatrinaphthalene (HPHATN) core.

Network formation might be achieved *e.g.* by the attachment of bromines and subsequent cross-coupling reaction such as the Yamamoto[338] coupling. Also thiophenes are able to undergo oxidative coupling (polymerization) to form a network.[339] Therefore the introduction of bromines and 3-hexyl-2-phenylthiophene into the periphery of the HPHATN core was considered (Figure 5-5).

All HPHATN derivatives (**5-27** to **5-33**) were synthesized by an acid catalyzed condensation of the key intermediate **5-19** and the corresponding arylaldehydes **5-20** to **5-26** (Scheme 5-2). HPHATN **5-19** was synthesized starting from the reductive desulfuration of 4,7-dibromo-2,1,3-benothiodiazole (**5-13**) according to the literature procedures.[340]

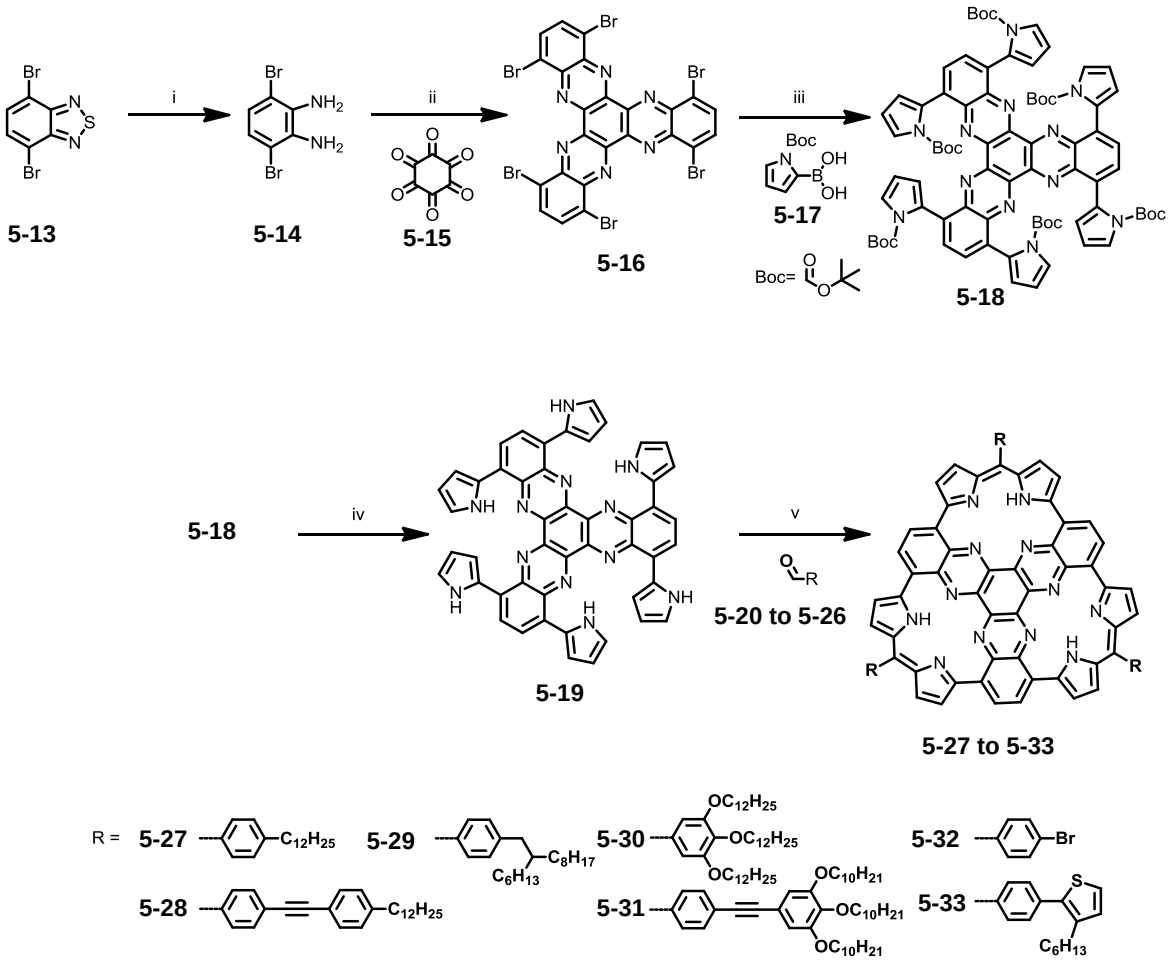

Scheme 5-2: Synthesis of HPHATN disk. Conditions: *i* $NaBH_4$, EtOH, 0°C, 92%. *ii* **5-15**, EtOH, reflux, 85%. *iii* **5-17**, $Pd(PPh_3)_4$, 2M K_2CO_3, EtOH, toluene, 85°C, 62%. *iv* 180°C, 92%. *v* **5-20** to **5-26**, DCM, THF, TFA, microwave, 50 W, 85°C, 32-97%.

The resulting 3,6-dibromobenzene-1,2-diamine (**5-14**) was obtained in 92% and subsequently condensed with hexaketocyclohexane octahydrate (**5-15**) to form the hexabromo-HATN core **5-16**. Compound **5-16** was obtained in 85% as a green insoluble powder, which anyhow reacts smoothly in the subsequent six-fold Suzuki-Miyaura cross-coupling reaction with commercially available boronic acid **5-17** to form soluble HPHATN **5-18** in 62% yield. Although FD mass spectrometry analysis of **5-18** showed a mixture of zero to sixfold Boc-protected species, NMR spectroscopic elucidation revealed solely the signals for compound **5-18** with six Boc-groups attached. The deprotection was assumed to occur due to fragmentation caused by heating during the measurement. HPHATN **5-18** was thermally deprotected to afford HPHATN **5-19** in 92% yield as a black solid which was moderately soluble in common organic solvents like THF, DCM, DMF or DMSO.

The great advantage of the described synthesis procedure was that key intermediate HPHATN **5-19** was the last step before the three porphyrinic cores were closed by simultaneous condensation. In theory every possibly available aldehyde might be condensed to the triangular core (**5-19**). Furthermore, all steps towards compound **5-19** were high yielding with an overall yield of 45% (4 steps) and therefore a gram scale synthesis was straightforward.

For the preparation of the arylaldehydes **5-20** to **5-25**, typical literature methods were applied starting with the corresponding precursors (Table 5-1). 4-Dodecylbenzaldehyde (**5-21**) was obtained by halogen-metal exchange using *n*-BuLi followed by quenching with DMF.[335] 4-((4-Dodecylphenyl)-ethynyl)benzaldehyde (**5-22**) and 4-((3,4,5-tris(decyloxy)phenyl)-ethynyl)benzaldehyde (**5-24**) were synthesized by the reaction of 4-bromobenzaldehyde (**5-26**) and the corresponding acetylenes **5-35** or **5-40**, respectively, under Sonogashira-Hagihara cross-coupling reaction conditions.[341] Williamson ether reaction conditions were used to achieve 3,4,5-tris(dodecyloxy)benzaldehyde (**5-20**).[342] A Kumada coupling towards 4-(2-hexyldecyl)benzaldehyde (**5-23**) was performed by using 2-(4-bromophenyl)-1,3-dioxolane (**5-36**) and a freshly prepared Grignard solution (**5-37**) made from 7-(bromomethyl)pentadecane.[343] 4-(3-Hexylthiophen-2-yl)benzaldehyde (**5-25**) was prepared using standard Suzuki-Miyaura cross-coupoling reaction conditions.[135]

All aldehydes were then reacted with HPHATN **5-19** to give the corresponding triangular trinuclear compound **5-27** to **5-33** (Table 5-1). The substances were collected by precipitation from MeOH and subsequent filtration. Simple Soxhlet extraction with acetone

was used for further purification to afford the corresponding HPHATN in high yields up to 97% (Table 5-1).

Table 5-1: Overview of starting materials, resulting target compounds and corresponding yield.

Starting Materials	Aryl aldehyde	Yield [%]	Condensation with 5-19 results in the target compounds	Yield [%]
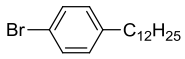 **5-34**	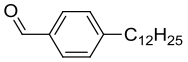 **5-21**	70	**5-27**	32
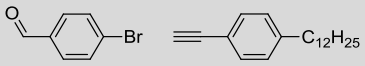 **5-26** **5-35**	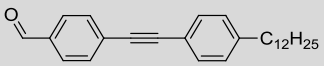 **5-22**	60	**5-28**	82
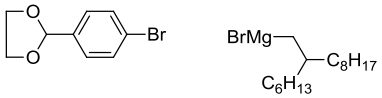 **5-36** **5-37**	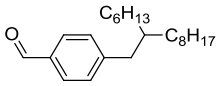 **5-23**	10[a]	**5-29**	52
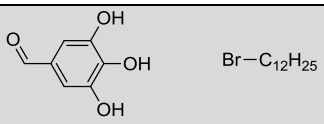 **5-38** **5-39**	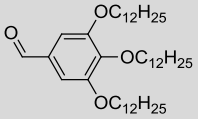 **5-20**	92	**5-30**	92
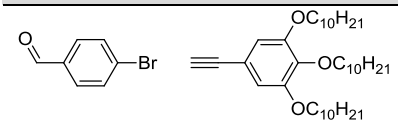 **5-26** **5-40**	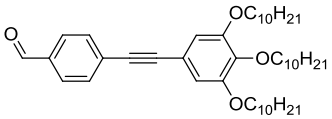 **5-24**	77	**5-31**	97
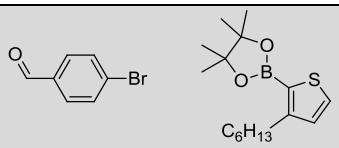 **5-26** **5-41**	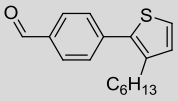 **5-25**	55	**5-33**	65
-	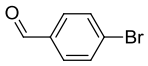 **5-26**	-	**5-32**	87

The resulting tricycles spontaneously dehydrogenated to the conjugated structures as shown in Scheme 5-2 and Figure 5-6 accordingly, which was undoubtedly proven for the first time by HRESI mass spectrometry. Exemplary the HRESI of HPHATN **5-28** is shown in Figure 5-6, with the previously reported structure by von Malotki[144] (Figure 5-6, right-blue) and the herein proposed dehydrogenated form (Figure 5-6, left-red). The results

of the HRESI spectrum could be definitely assigned to the mass of the dehydrogenated species. Therefore, it is suggested that the *meso*-positions were oxidized under work-up conditions, unlike previously reported[144] where DDQ was used as oxidizing agent.

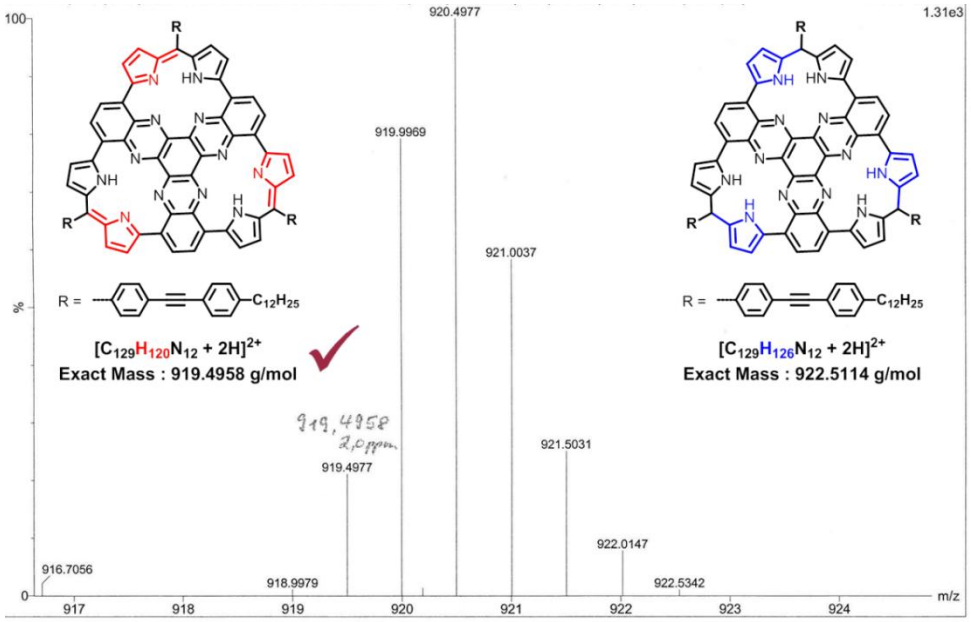

Figure 5-6: HRESI mass spectrum of HPHATN **5-28**. Previously reported structure[144] (right – blue) and the herein proposed dehydrogenated form (left – red).

All triangular HPHATN compounds were moderately soluble in THF, dichloromethane or chloroform. Their structures were characterized by NMR spectroscopy, MALDI-TOF and HRESI mass spectrometry.

NMR analysis of the prepared planar HPHATN derivatives ***5-27*** to ***5-33*** emerged to be hindered by aggregation effects of the compounds. HATs are known to show line-broadening effects in halogenated solvents arising from aggregation.[344] In the case of the herein described HPHATNs, aggregation can occur due to interactions such as hydrogen bonds[345-346] or aromatic π-stacking.[347] To elucidate the triangular structure by NMR spectroscopy, several deuterated solvents were tried but with no success leading only to broad signals. Finally, hexafluoroisopropanol-d_2 (HFIP) with the addition of 0.1% of TFA-d_2 proved to be the best choice to avoid aggregation of the HPHATN derivatives resulting in well-resolved signals in the NMR spectra. Rescindment of aggregation by addition of TFA has also been observed for related HAT derivatives.[344] Nevertheless, it has to be mentioned, that by the use of TFA the nitrogens of the pyrrolenine units are partially protonated.

Unfortunately, by using deuterated alcohols the NH protons are exchanged to deuterium and thus cannot be observed by ^{1}H NMR spectroscopy. Nevertheless, it can be shown by

NMR experiments in non-deuterated HFIP, that the pyrrole proton of the HPHATNs resonates downfield at about 18 ppm.[144] As an example the ^{1}H NMR spectrum of HPHATN **5-30** is shown in Figure 5-7. The resonances of the aromatic protons of the triangular core for the other derivatives are summarized in Table 5-2.

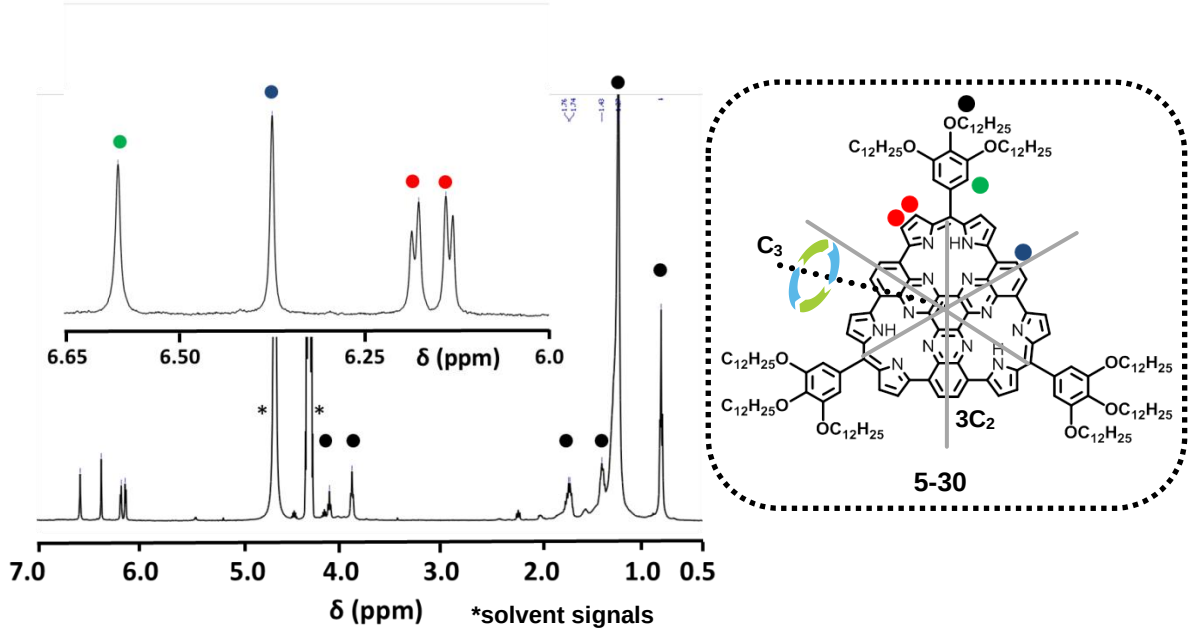

Figure 5-7: ^{1}H NMR spectrum of HPHATN **5-30** in HFIP-d_2 + 0.1% TFA-d_2.

Due to the C_3-symmetry of the molecules the resonances in the spectra were reduced to two doublets for the pyrrolic β-protons (AB-system) and one singlet for the phenylene protons in the aromatic region. In general, the signals of the pyrrolic β-protons were shifted upfield compared to single porphyrins[348] and linear oligoporphyrins[349] which could be attributed to an attenuated diatropic ring current. This finding was also in agreement with the downfield resonance of the NH protons. On the other hand the β-proton signals were in the same region as for Osuka's two-dimensional tetrameric fused porphyrin sheet.[84]

Table 5-2: Summary of the aromatic proton signals for the triangular core of compounds **5-27** to **5-33**. All ^{1}H NMR spectra were recorded in HFIP-d_2 + 0.1% TFA-d_2.

compound	Pyrrolic proton signals ● [ppm]	Phenylene proton signals ● [ppm]
5-27	6.09; 6.15	6.62
5-28	5.92; 5.99	6.40
5-29	6.18; 6.23	6.70
5-30	6.12; 6.18	6.59
5-31	5.99; 6.12	6.50
5-32	5.99; 6.10	6.49

5-33	5.99; 6.12	6.50

By comparison of the spectroscopic data, the weak effect of the substituents on the NMR resonances becomes apparent by the similar signals shifts for the aromatic protons of all HPHATNs.

5.1.2 Electronic structure

The optical absorptions of all HPHATN derivatives ***5-27*** to ***5-31*** and ***5-33*** were first investigated in solution ($CHCl_3$, 10^{-5} M) and thin film (Figure 5-8). Compound ***5-32*** could not be monitored due to its poor solubility.

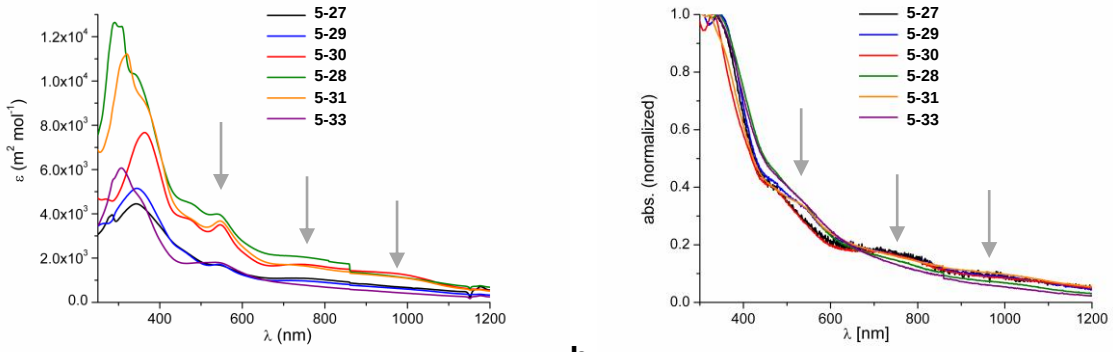

Figure 5-8: Electronic absorption spectra of **5-27** to **5-31** and **5-33** **a:** in $CHCl_3$ (10^{-5} M) and **b:** in film (spincoated on a glass substrate from a 10^{-3} M THF solution, thickness ~50 nm).

Electronic absorption spectra recorded in dilute $CHCl_3$ of the triangular derivatives ***5-27*** to ***5-31*** and ***5-33*** showed similar behavior with considerably broadened absorption bands. The main absorption maximum in the near ultraviolet region of 300-400 nm might probably be attributed to a Soret-like band. The second maxima between 535 and 545 nm could be identified as broad Q-band like absorption (Figure 5-8a; Table 5-3). Usually, porphyrins exhibit defined Q-bands in the visible region of 600-800 nm.[3] In the case of the HPHATN derivatives very broad structureless bands over the whole region of 600-1000 nm were observed. Broad unresolved bands around 300 nm can also be found in the UV-vis spectrum of bare HAT.[350]

The substituents showed only little influence on the electronic structure of the compounds. Almost no change was found by the comparison of linear alkyl side chains (***5-27***) to branched ones (***5-29***). Though, the stronger electron-donating ability of the alkoxy unit in compound ***5-30*** as opposed to linear alkyl-chains (***5-27***) caused a bathochromic shift. The

introduction of ethynyl spacers results in hypsochromic shifts (for ***5-27*-*5-28***: 52 nm and for ***5-30*-*5-31***: 43 nm) which can be explained by the electron-withdrawing properties of the ethynyl groups.[3] In general, along with a shift in the absorption spectra induced by electron-donating groups, the molar absorption coefficients are increased.[246] This finding could also be assessed in the case of compounds ***5-30***, ***5-31*** and ***5-28***. The absorption in thin film featured even more broadened and structureless bands but nevertheless, showed similar trends to those in solutions (Figure 5-8b).

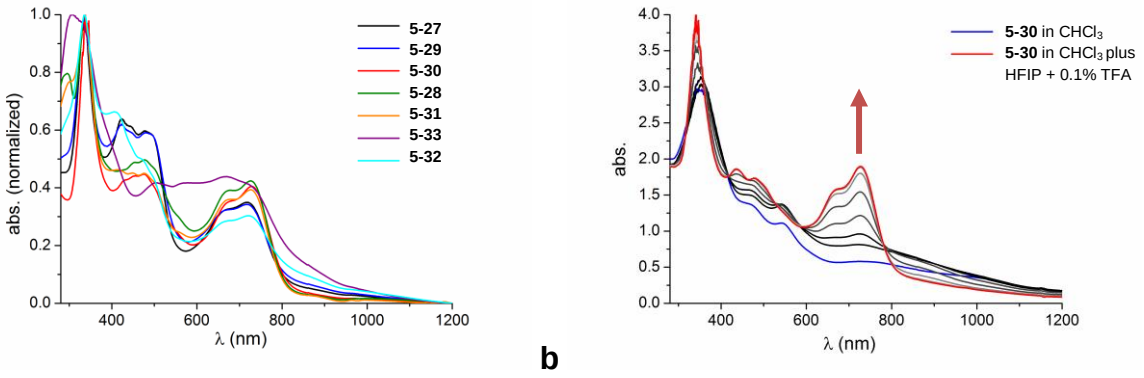

Figure 5-9: **a:** Electronic absorption spectra of **5-27** to **5-33** in HFIP + 0.1% TFA and **b:** titration of HFIP + 0.1% into a $CHCl_3$ solution of **5-30** ($3.4*10^{-5}$ M).

Interestingly, upon addition of small portions of HFIP + 0.1% TFA (10 µl at a time), the very broad absorption bands of ***5-30*** in $CHCl_3$ solution (Figure 5-9b, blue) became defined with pronounced maxima in the region of 600-800 nm (Figure 5-9b, red). This phenomenon could be explained by the rescindment of the aggregation of the HPHATN disks by protonation, and is in agreement with the observations received from previous NMR investigations. Suppression of aggregation by protonation has also been observed for related HAT derivatives,[344] whereby protonation never occurred on the central HAT nitrogens. Therefore it was suggested that in the case of the herein described HPHATNs, protonation happened at the pyrrolenine unit and not at the core nitrogens. The electronic absorption spectra for all HPHATN ***5-27*** to ***5-33*** were recorded in HFIP+0.1% TFA and showed similar absorption profiles with a pronounced local Soret-like maximum at about 340 nm along with defined bands in the region of 600-800 nm (Figure 5-9a, Table 5-3). Generally, for porphyrins absorption maxima in the long-wavelength region of 500-800 nm are assigned as Q-bands.[44] Even less influence of the absorption maxima in dependence of the substituents could be observed compared to prior results. Exception was the thiophene containing derivative ***5-32***, which showed only one broad band in the region of 400-800 nm. Nevertheless, it has to be kept in mind, that the observed species in HFIP + 0.1% TFA are

the protonated ones. The well-resolved absorption profiles with clear vibronic structure was consistent with the rigid structural feature of the triangular HPHATN core.[333] A summary of all absorption maxima along with the results from the following electrochemical measurements is given in Table 5-3.

Table 5-3: Summary of optical and electrochemical properties of the HPHATN derivatives **5-27** to **5-33**.

Compound	λ_{CHCl3} (abs)	$\lambda_{HFIP + TFA}$ (abs)	λ_{film} (abs)	E^{Homo}	E^{Lumo}	E_g^{ec}
5-27	343	335, 668, 720	340	-[a]	-	-
5-28	291	335, 672, 727	309	-4.56	-3.38	1.18
5-29	344	335, 668, 720	343	-4.54	-3.43	1.11
5-30	364	339, 673, 731	334	-4.58	-3.26	1.32
5-31	321	337, 672, 727	322	-4.60	-3.28	1.31
5-32	-[a]	335, 663, 721	-	-[a]	-	-
5-33	307	308, 667	340	-4.54	-3.41	1.12

[a] not soluble at the concentration required for the measurement; [b] DFT quantum mechanical calculations (B3LYP/6-31G*).[184]

Cyclic voltammograms of the HPHATN derivatives ***5-27*** to ***5-33*** were recorded in THF (1 mM, scan rate 25 mVs^{-1}) using *n*-butylammonium-hexaflouorophosphate (*n*-Bu_4NPF_6) as supporting electrolyte and ferrocene (Fc/Fc^+) as an internal reference.

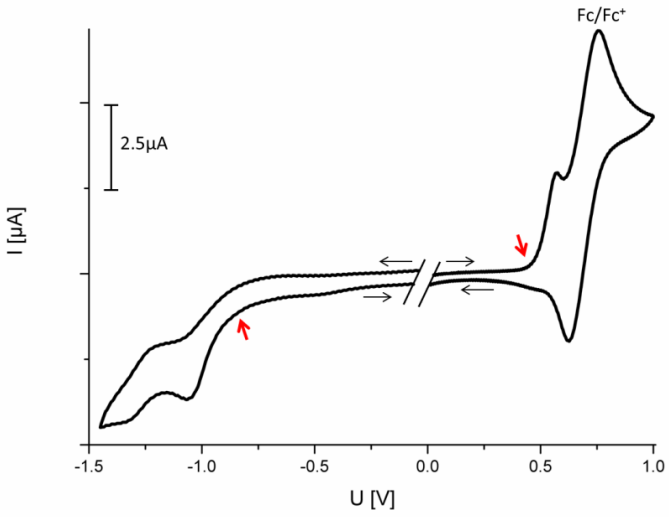

Figure 5-10: Cyclic voltammogram of HPHATN **5-30** in THF (10^{-3} M); the red arrows indicate the first oxidation and reduction onset respectively. 10^{-1} M solution of *n*-Bu_4NPF_6 as electrolyte; working and counter electrode: Pt, reference electrode: Ag; ferrocene (Fc/Fc^+) reference, scan rate 25 mVs^{-1}.

All HPHATNs showed similar redox behavior with quasi-reversible oxidation and reduction waves. As an example, the cyclic voltammogram of compound ***5-30*** is depicted in Figure 5-10. The HOMO and LUMO energy levels were estimated from the first oxidation or reduction onsets, respectively (indicated by the red arrows, Figure 5-10), and determined according to the empirical formula $E^{(HOMO/LUMO)} = -[4.8 - E^{FOC} + E^{(ox/red)}\ (onset)]$.[351] E^{FOC} is the half-wave potential of ferrocene standard. By the replacement of alkyl (***5-29***) with alkoxy side chains (***5-30***) electron affinity was decreased which was reflected in the increased LUMO level of compound ***5-30*** (E^{LUMO} = -3.26 eV), compared to the one of ***5-29*** (E^{LUMO} = -3.43 eV). This could be explained by the stronger electron-donating ability of the alkoxy groups compared to alkyl groups and was also observed for compounds ***5-28*** (E^{LUMO} = -3.38 eV) and ***5-31*** (E^{LUMO} = -3.28 eV). Compared to common HAT derivatives (E^{LUMO} = -3.54 eV)[333] the LUMO energy levels of the HPHATN ***5-27*** to ***5-33*** were slightly higher but they were much lower than those of unsubstituted porphyrins (E^{LUMO} = 2.23 eV).[352] On the contrary, the HOMO levels of compounds ***5-27*** to ***5-33*** were higher than those for HATs (E^{HOMO} = -5.97 eV) and porphyrins (E^{HOMO} = -5.15 eV) resulting in smaller energy gaps. For compounds ***5-28***, ***5-29*** and ***5-33*** the energy gaps were calculated to be in the range of E_g^{ec} = 1.11-1.18 eV. For the alkoxy substituted derivatives ***5-30*** and ***5-31*** the energy gaps were slightly larger between E_g^{ec} =1.31-1.32 eV as a result of their higher LUMO levels. The significant decrease in energy for the triangular disks ***5-27*** to ***5-33*** compared to porphyrins and common HATs could be attributed to the increase of conjugation due to the planarization upon ring closure and the thereof resulting extended π-electron delocalization.

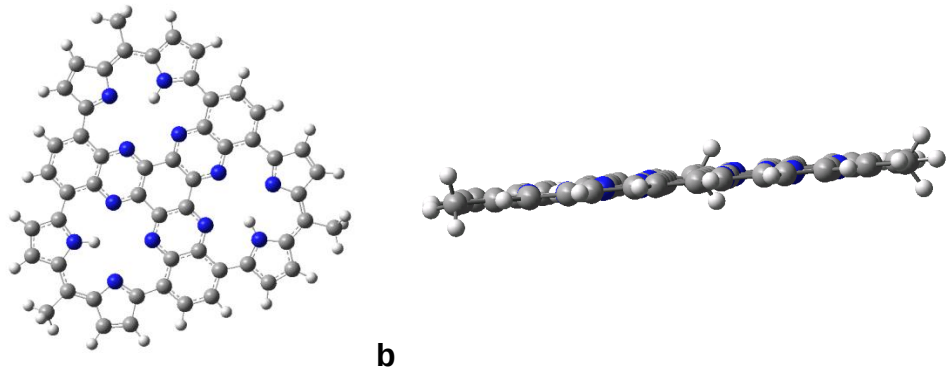

Figure 5-11: Geometric structure of the triangular HPHATN core (DFT, B3LYP/6-31G*); **a:** top view and **b:** side view.

For further investigation of the geometric and electronic structures of the planar HPHATN derivatives, density functional theory calculation (DFT, B3LYP/6-31G*)[278-279, 353] were applied on the triangular core. Substituents were omitted for clarity and calculation time reasons. The fully planar and conjugated structure of the molecule was confirmed by these calculations (Figure 5-11).

The HOMO level was determined to E^{HOMO} = -4.57 eV and was mainly distributed in the outer peripheric ring (Figure 5-12b). On the contrary, the LUMO was distributed in a C_3-symmetric fashion starting from the electron deficient core. The LUMO level was calculated to E^{LUMO} = -3.13 eV which was little higher than the ones of HPHATN derivatives ***5-27*** to ***5-33*** derived from CV measurements, but comparable taking into account, that substituents were not included into the calculations. Thus, the energy gap of ΔE = 1.44 eV was larger compared to the experimental data, but was still in good agreement.

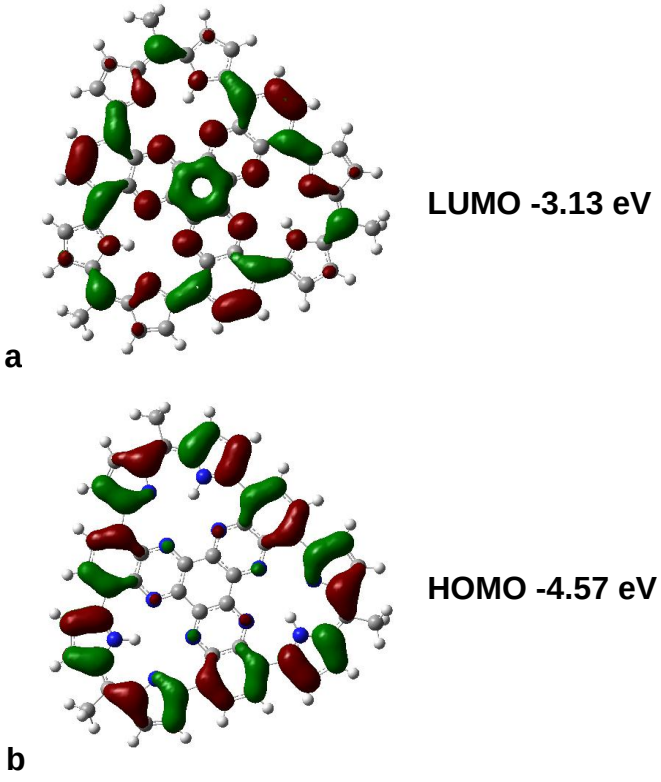

Figure 5-12: **a:** LUMO, **b:** HOMO orbitals of the triangular HPHATN core (DFT, B3LYP/6-31G*).

The thermal properties of the HPHATN derivatives ***5-27*** to ***5-33*** were investigated using thermogravimetric analysis (TGA, Figure 5-13). The temperature of 5 % weight loss based

on the initial weight (T_d) occurred for almost all HPHATN over 350°C, at which point the decomposition of the attached alkyl substituents starts to set in. Exception was HPHATN ***5-33*** bearing thiophenes in its periphery, which started to decompose at T_d = 180°C. A first weight loss of about 30% was observed, which corresponds to the loss of the alkylated thiophene substitutes (Figure 5-13).

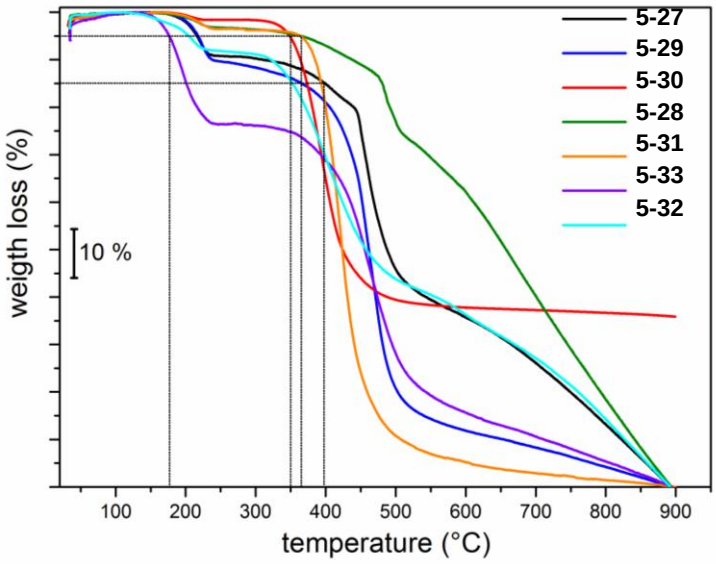

Figure 5-13: Thermogravimetric analysis of the HPHATN derivatives **5-27** to **5-33** under N_2 atmosphere; measured between 25-900°C with a scan rate of 10 $Kmin^{-1}$. For **5-27**, **5-29** and **5-32** the first weight loss is neglected and assigned to the loss of solvent molecules remaining in the sample.

It is worth mentioning, that the HPHATN ***5-30*** showed a defined weight loss of 57% up to 900°C corresponding to the mass of nine alkoxy-chains, but the core seemed to be still consistent. This was not observed for the other HPHATN derivatives which completely decomposed when reaching 900°C.

5.1.3 Metal complexation

Amongst the most promising precursors for NPMCs as alternative to platinum-based catalysts for ORR, cobalt or iron porphyrins have established themselves.[98] Therefore, the insertion of cobalt into the cavities of the HPHATN core was considered.

The cobalt complexes of HPHATN derivatives ***5-30, 5-32*** and ***5-33*** were obtained according to the acetate method[49] used for porphyrins, by treating the ligand with cobalt(II)acetate in DMF (Scheme 5-3). To provide better solubility, THF was added to the dark violet suspensions (DMF/THF = 3:1). After heating, the reaction mixture was poured

into cooled water and the metalcomplexes **5-42** to **5-44** were collected by filtration. The insertion of three metal ions was proven by Maldi-Tof mass spectrometry, and showed no additional peaks for double or single insertion (Figure 5-14). High yields between 89-94% could be achieved for the complexation reaction. Unfortunately, no NMR spectroscopy could be recorded due to the line broadening effect caused by the paramagnetic cobalt atoms.[195]

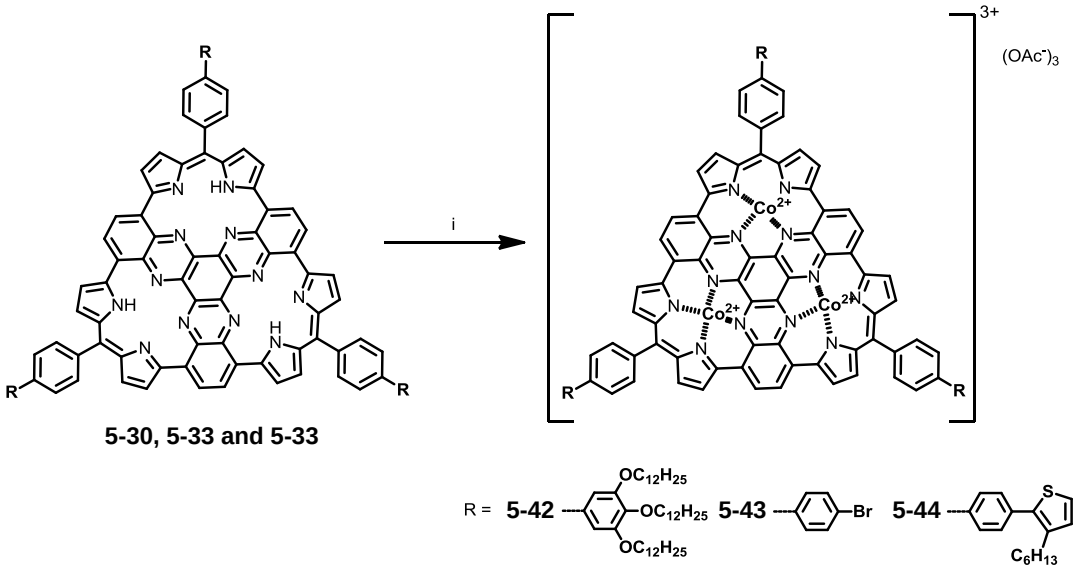

Scheme 5-3: Complexation of the HPHATN ligand with cobalt(II) ion. Conditions: *i* $Co(OAc)_2$, DMF/THF (3 : 1), microwave, 30 W, 180°C or ambient conditions 60°C, 20 h, 89-94%.

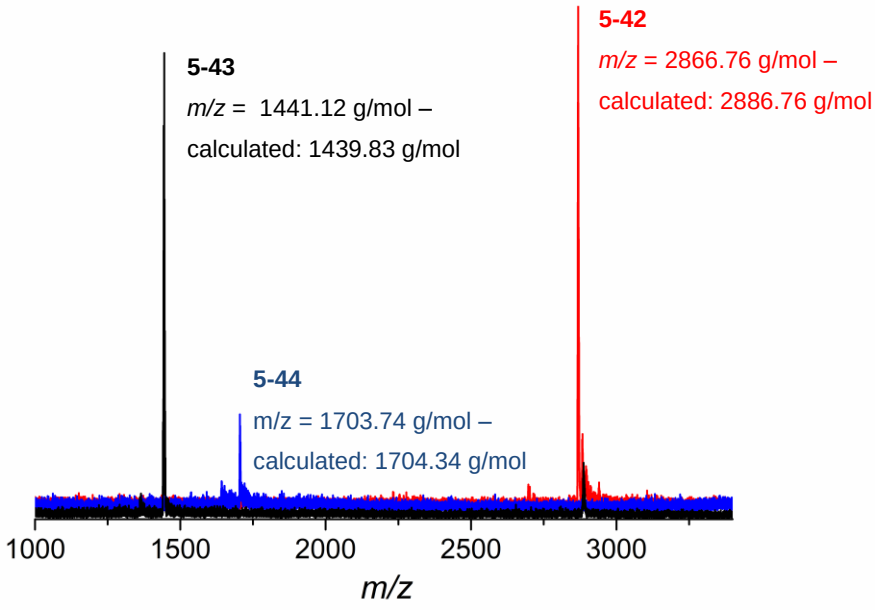

Figure 5-14: Maldi-Tof mass spectra for cobalt(II)complexes **5-42** to **5-44**.

The three Co(II) ions inserted into the cavities under depletion of the three pyrrole protons resulting in a trianionic complex. Most probably acetate ions acted as counterions and coordinated from above and below the plane forming an overall octahedral coordination sphere for each cobalt atom. The geometric structure was calculated (DFT, B3LYP/6-31G*)[278-279, 353] and revealed that the Co(II) ions perfectly fit into the N_4 pockets leading to a flat structure with a distance of 6.6 Å between the Co centers (Figure 5-15). This distance was shorter compared to usual Co_3(HAT) moieties with a Co···Co separation of approximately 7.1 Å,[314] and also to compounds with closed N_4-rings such as in linear oligopohyrins[82] (8.45 Å) and Osukas's tetrameric porphyrin square (8.32 Å).[84] Thus, the request to design a symmetric π-expanded system with incorporated metal-N_4 pockets which are in unprecedented vicinity to each other has been fulfilled with even shorter distances than related systems reported in literature.

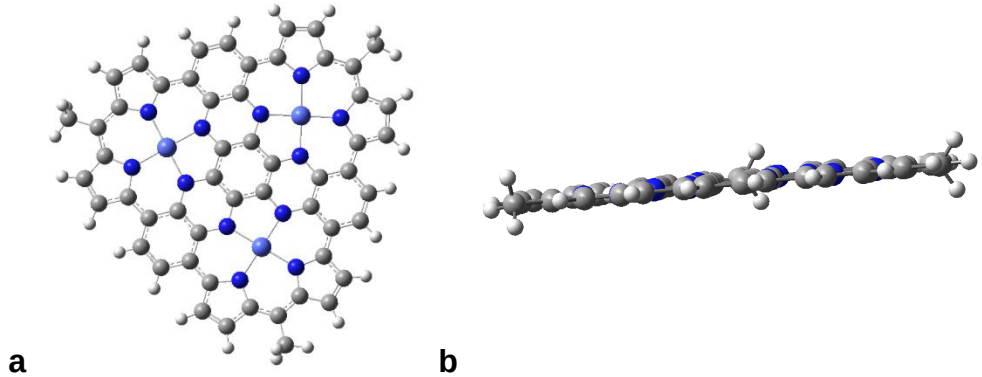

Figure 5-15: Calculated geometric structure of the triangular metal complex core (DFT, B3LYP/6-31G*). **a:** top view and **b:** side view.

The thermal properties of complexes ***5-42*** to ***5-44*** were investigated using thermogravimetric analysis (TGA). Those measurements revealed a stability up to T_d = 330°C for cobalt complex ***5-42*** (T_d corresponds to 5 % weight loss), at which point the decomposition of the alkoxy-chains started (Figure 5-16). The weight loss of 62% corresponded to the mass of nine -$OC_{12}H_{25}$ groups. Consequently, the macrocyclic core is expected to be existent even if heat treatment is considered as a processing step for the application as catalyst in ORR.

Complex ***5-43*** showed stability up to T_d = 144°C, which could be due to the C-Br homolytic bond dissociation.[354] Thus, mild pyrolysis would be sufficient to rupture the C-Br bond in complex ***5-43*** and provide aryl radicals, which could be useful the further application *e.g.* interact with the carbon support used in electrocatalytic ORR measurements. The pyrolysis

of aryl bromides has been used for many years as a classic means of generating aryl radicals in the gas phase.[354]

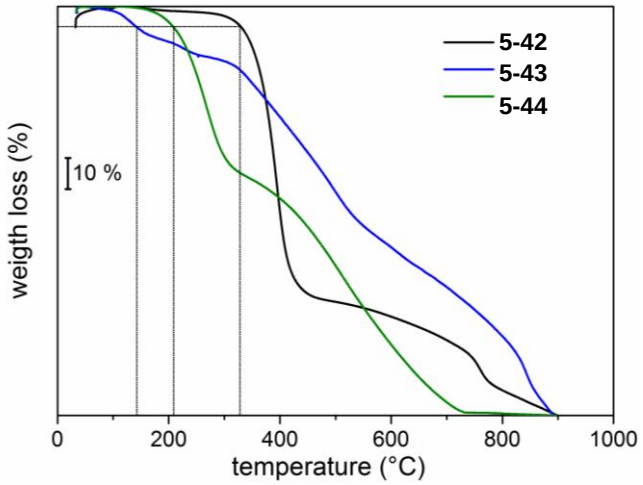

Figure 5-16: Thermogravimetric analysis of complex **5-42** to **5-44** under N_2 atmosphere; measured between 25-900°C with a scan rate of 10 $Kmin^{-1}$.

Thiophene substituted complex ***5-43*** started to decompose at T_d = 220°C which was only slightly higher compared to the decomposition temperature of its ligand ***5-32***. The first weight loss of about 30% corresponded to the loss of the alkylated thiophene substitutes, whereas further weight loss (up to 96%) caused almost complete decomposition of complex ***5-44*** (Figure 5-16). Additionally, none of the complexes showed any obvious thermal transition between 25 and 900°C according to the DSC analysis (not shown herein).

The metal in the complex used as an electrocatalysts for the reduction of oxygen should be in the M(II) state, since the catalytically active site has been proven to be M(II), especially if the metal is cobalt.[98, 355] For the elucidation of the oxidation state in the trinuclear cobalt complexes, the magnetic properties of metal complex ***5-42*** has been investigated exemplarily for all metal complexes using SQUID (Superconducting Quantum Interference Device) measurements. The powdered sample was studied by variable temperature susceptibility measurements in the range of 2-100 K in an applied field of 1 Tesla (Figure 5-17).

The experimental value for $\chi_M T$ at 100 K was 1.058 cm^3Kmol^{-1} followed by a rapid decay reaching a $\chi_M T$ value of 0.388 cm^3Kmol^{-1} at 3 K, indicating an antiferromagnetic coupling between the three cobalt atoms. The theoretical $\chi_M T$ value for an uncoupled spin with S = ½ is 0.375 cm^3Kmol^{-1}. Three cobalt(II) ions in low spin (LS) state are expected to feature a $\chi_M T$ value of 1.125 cm^3Kmol^{-1} which is in good agreement with the observed one at 100 K

(1.058 cm^3Kmol^{-1}). Therefore, the cobalt ions definitely occurred as Co^{2+} in LS state and were in an antiferromagnetic arrangement to each other.

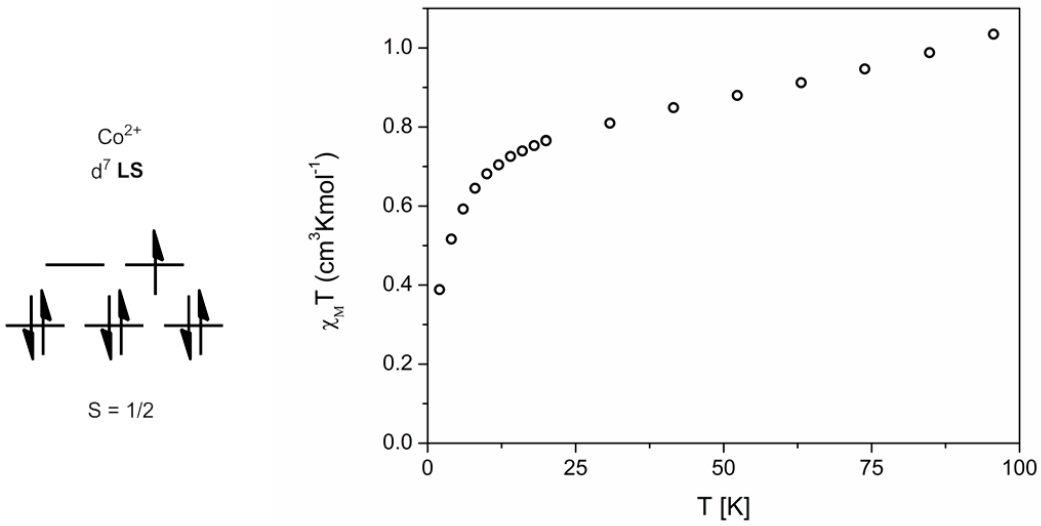

Figure 5-17: Temperature dependence in $\chi_M T$ versus T for cobalt(II)complex **5-42**.

Nevertheless, the three spin centers are unable to satisfy a diamagnetic ground state since spin frustration will always result in at least one unpaired spin leftover.[356] Usually, materials overcome this frustration by the alignment of the unpaired spin to 120° resulting in an overall spin vector equal to zero as it is required for an antiferromagnetic coupling (Figure 5-18).[314]

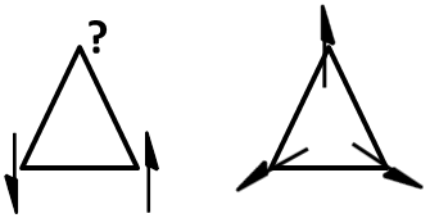

Figure 5-18: Schematic illustration of spin frustration in a triangular array (left) and the compromise spin states (right).

5.1.4 Bulk Properties

Two-dimensional X-ray wide-angle scattering (2D-WAXS) was used to investigate the organization of the triangular trinuclear HPHATN molecules in the solid-state along with the influence of the substituents. Generally, 2D-WAXS measurements give information about the insight into supramolecular organization. Therefore, the samples are prepared by filament extrusion and then positioned perpendicular to the incident X-ray beam (Figure 5-19). The extrusion of the filament forces discotic molecules to align perpendicular to the extrusion direction caused by shear forces. The reflection positions in the 2D-WAXS pattern give information about intra- and intercolumnar supramolecular organization (Figure 5-19). Conjugated macrocycles with flexible alkyl and alkoxy side chains are known to form liquid crystalline columnar phases.[151, 357-359] In cooperation with S. R. Puniredd and Dr. W. Pisula (MPIP, Mainz) the supramolecular organization of HPHATN derivatives **5-27** to **5-31** in the bulk state were studied by 2D-WAXS measurements. It is worth mentioning, that the studied compounds revealed neither a phase transition in the differential scanning calorimetry (DSC) nor a change in organization at different temperatures observed by 2D-WAXS.

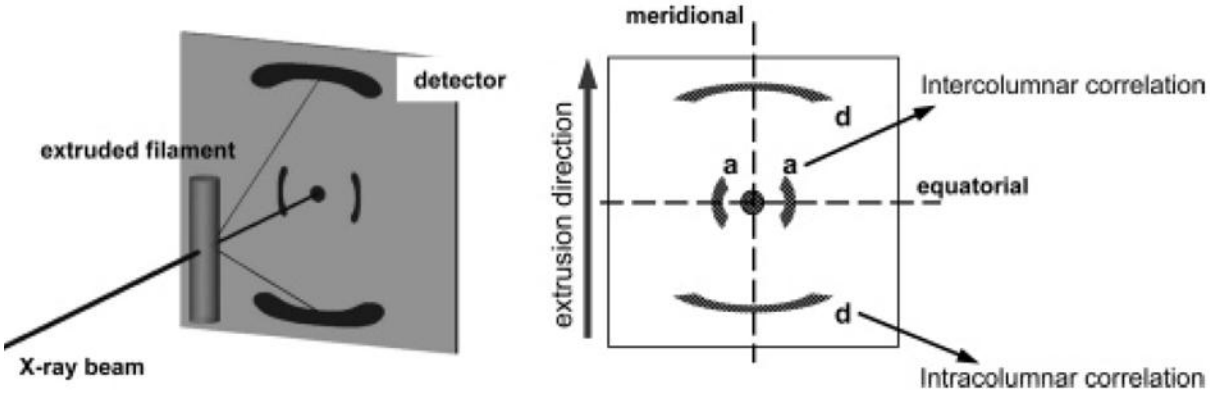

Figure 5-19: Schematic representation of an experimental setup (left) and scheme for the characteristic 2D-WAXS pattern of an extruded filament based on discotic molecules.[360]

Surprisingly, the alkyl substituted compounds **5-27**, **5-28** and **5-29** showed the lowest order (Figure 5-20). All three compounds featured only one isotropic small-angle reflection, which was attributed to the formation of columnar structures.

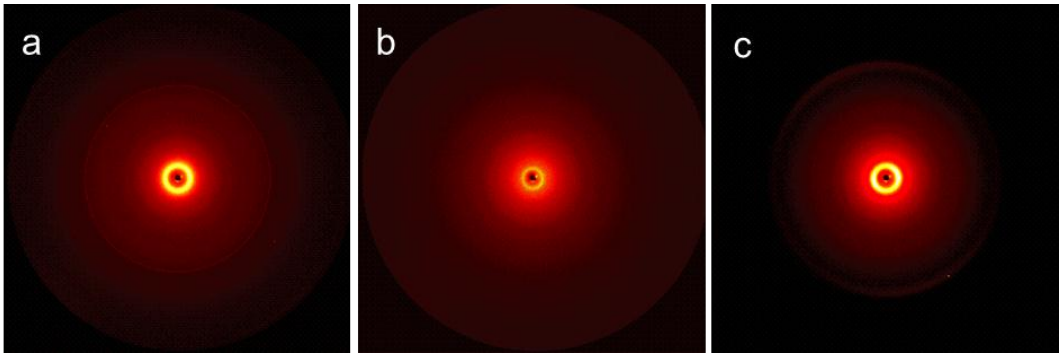

Figure 5-20: 2D-WAXS of **a: 5-27**, **b: 5-28**, and **c: 5-29**.

On the other hand, the alkoxy substituted derivatives ***5-30*** and ***5-31*** possessed significantly higher order in comparison to their alkyl counterparts (Figure 5-21). This was astonishing, since they carry only one side chain on each phenyl in contrast to the alkoxy derivatives which carry three side chains on each phenyl. Moreover, alkyls are generally less sterically demanding and lead to better packing. It is assumed, that the viscous (wax-like) phases of ***5-30*** and ***5-31*** originating from the higher chain flexibility of the alkoxy-chains allowed a better molecular arrangement and columnar alignment in the solid-state.

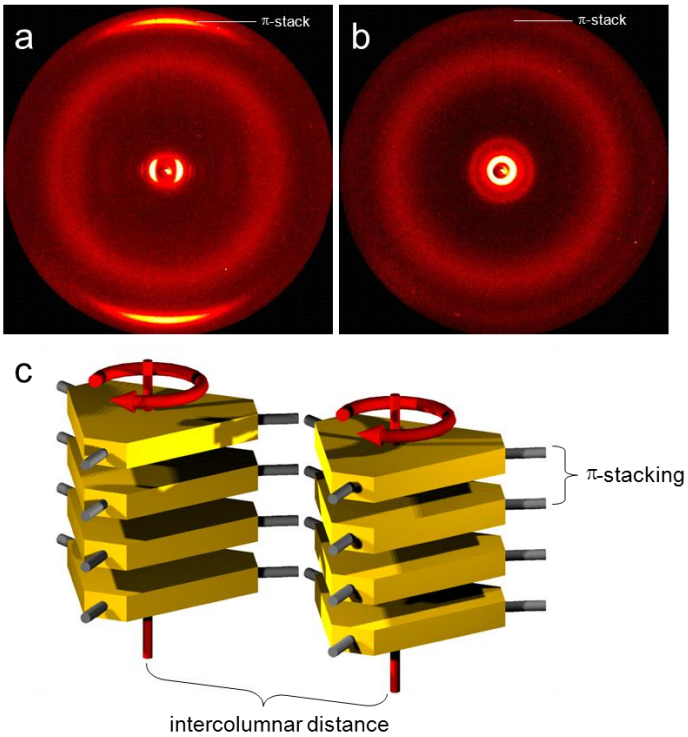

Figure 5-21: 2D-WAXS of **a: 5-30** and **b: 5-31**, **c:** schematic illustration of the molecular organization in the columnar structures. Due to simplicity the side chains are omitted, but the substituent attachment is indicated by the grey sticks. It has to be noted that in the liquid crystalline phase the molecules perform a lateral rotation around the columnar axis (indicated by red arrows) and are not stacked on top of each other as illustrated in c.

The most pronounced X-ray patterns were obtained for HPHATN derivative **5-30** (Figure 5-21a), where the intermolecular correlation could be received from the equatorial reflections and the intramolecular relation was derived from the meridional reflections. The alkoxyl substituted compound (**5-30**) was organized in a characteristic discotic liquid crystalline phase over the whole investigated temperature range. Only few discotics show such broad temperature range for the liquid crystalline state. Typically, phenyls as substituents are known to induce this extended thermotropic behavior. The meridional reflection in the pattern showed, that the molecules were π-stacked with a distance of 0.36 nm within the columns. This is in the same range than the π-π-stacking distances for hexa-peri-**h**exa**b**enzo**c**oronene (HBC) derivatives, which show columnar structures with the distances of 0.35-0.36 nm. HBC are discotic liquid crystal with stable mesophases over a large temperature scale.[361-363] The distinct anisotropic equatorial reflections of the pattern pointed towards a pronounced orientation of these stacks along the fiber axis. A hexagonal unit cell with a_{hex} = 4.20 nm was derived from the positions of the scattering intensities. By the extension of the substituents to phenyl-ethynylbenzene as in HPHATN **5-31** the hexagonal unit cell parameter was enlarged to a_{hex} = 5.28 nm. With the increase of the peripheral steric demand the molecular interactions were decreased which was expressed by the drastic reduction in order as evident from the relative isotropic reflections and the strong amorphous halo in the pattern (Figure 5-21b). Nevertheless, reflections related to the π-stacking distance of 0.36 nm were still obvious in the meridional plane of the pattern, however, significantly weaker than for **5-30**.

In conclusion, for the considered network forming through crosslinking by heat treatment in the liquid crystalline phase the most promising mesophase properties were found for HPHATN **5-30**. For this reason, the supramolecular organization of its cobalt complex **5-42** was investigated as well. The patterns for complex **5-42** also featured pronounced equatorial and meridional reflections (Figure 5-22).

Complex **5-42** showed liquid crystallinity over the whole temperature range, as also observed for its ligand **5-30**. Surprisingly, the incorporation of the cobalt atoms had no influence on the characteristic discotic columnar order with a π-stacked distance of 0.36 nm. Generally, an increase in the π-stacked distance or in the worst case a complete breakup of the π-π-interaction might be possible by the introduction of the cobalt ions. Fortunately, this was not the case and in agreement with the results of molecular modeling (cf. Figure 5-15), revealing that the metal atoms perfectly fit in the pockets and were situated in the plane of the sheet not hindering the π-π-stacking of the aromatic core. Moreover, from positions of

the scattering intensities also an identical hexagonal unit cell with a_{hex} = 4.20 nm was determined.

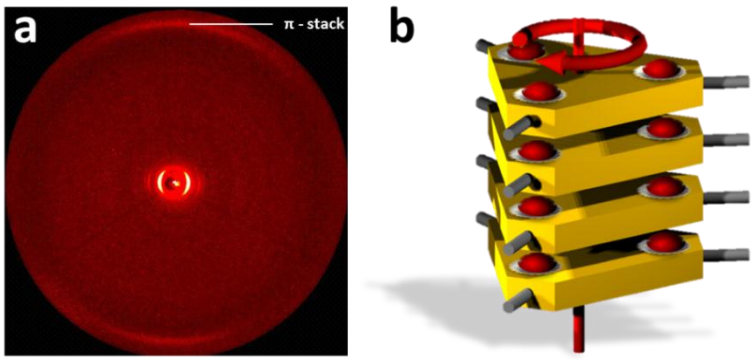

Figure 5-22: **a:** 2D-WAXs of cobalt complex **5-42**, **b:** schematic illustration of the molecular organization in the columnar structures. Due to simplicity the side chains are omitted, but the substituent attachment is indicated by the grey sticks. It has to be noted that in the liquid crystalline phase the molecules perform a lateral rotation around the columnar axis (indicated by the red arrow) and are not stacked on top of each other as illustrated.

By and large, the mesophase formation properties of complex **5-42** show great promise for further investigations of network forming by cross-linking through mild pyrolysis in the liquid crystalline state. Furthermore, the cross-linking is expected to result in a superior catalytic performance for compound **4-42** compared to earlier reported cobalt complex **5-11**,[144] since related alkyl-substituted **4-27** possessed very low order. Therefore, the catalytic activity of **4-42** was evaluated in comparison to complex **5-11** and will be described in the following chapter.

5.1.5 RRDE measurements

Based on very promising electrocatalytic activity of trinuclear cobalt complex **5-11** towards the ORR received by RDE measurements,[144] it was taken as a reference for further investigation by RRDE of the new HPHATN derivatives. Due to the superior mesophase formation into discotic columnar structures, complex **5-42** was expected to show enhanced activity compared to **5-11**. Therefore, the electrochemical activities of both complexes were investigated in collaboration with Sumitomo Chemical Co. in Tsukuba, Japan. Experiments were performed by Dr. Nobuyoshi Koshino under the supervision of Prof. Dr. Hideyuki Higashimura using RRDE techniques. For this reason, a standard three-electrode-electrochemical cell including a platinum wire as counter electrode (ring electrode with

d_{inner} = 7 mm and d_{outer} = 9 mm, 1.4 V *vs.* RHE), a glassy carbon working electrode (disk electrode, d = 6 mm) and Hg/Hg_2SO_4 reference electrode were used. Catalyst inks were prepared from 20wt% of catalyst with carbon black (Ketjen Black 600). The RRDE measurements were performed in O_2 saturated 0.1 M KOH solution at a potential scan rate of 10 mVs^{-1} and a rotation speed of 1600 rpm. Cobalt complex **5-42** was evaluated non-pyrolyzed and pyrolyzed at 400°C and benchmarked against complex **5-11** (non-pyrolyzed) measured under identical conditions. Mild pyrolysis for complex **5-42** at 400°C were considered based on TGA investigation which showed, that the aromatic core remained intact during heat treatment at that temperature and only the gradual loss of alkoxy side chains set in. It is believed that the cleavage of the alkoxy bonds result in the formation of free radicals, which are able to undergo intermolecular cross-linking.[221, 364]

The resulting ring-disk voltammograms and the efficiency of H_2O production are shown in Figure 5-23. It has to be mentioned, that the results of RDE measurements for **5-11** described before, could not be reproduced under the herein applied RRDE conditions. This could be attributed to the diverse catalysts preparation, *e.g.* different carbon support and catalysts loading. Nevertheless, the **5-11** showed good electrocatalytic activity with an efficiency in water production of 64.1% and a number of electrons transferred of n = 3.28. Since **5-11** and **5-42** were measured under identical conditions, their results could be benchmarked directly and evaluated. Although, complex **5-42** featured slightly improved efficiency of water production (%H_2O = 67.0%, n = 3.34) the mass activity was reduced to 3.7 mA/cm^2. Nevertheless, after mild pyrolysis of **5-42**, its activity was increased, as expected but unfortunately not superior than for the **5-11**.

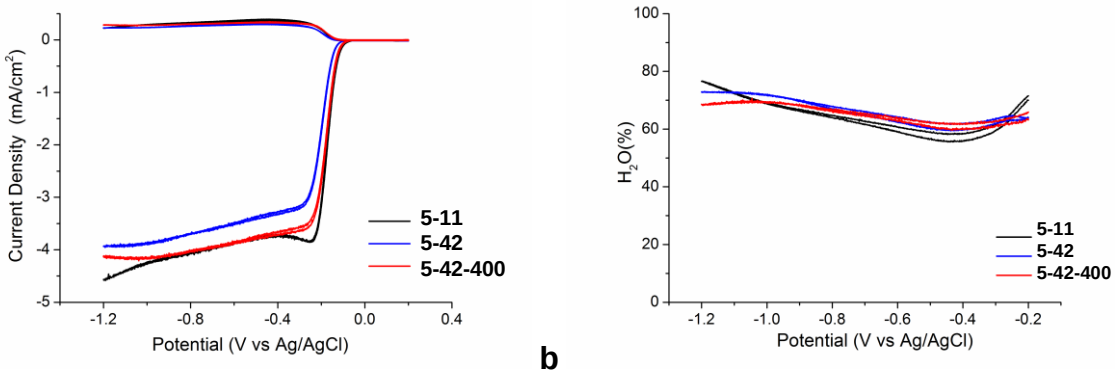

Figure 5-23: **a:** Ring-disk voltammograms and **b:** efficiency of H_2O production (plotted till -0.2 V) of cobalt complex **5-42** (blue), **5-42-400** (red) benchmark against **5-11** (black) in alkaline conditions (0.1 M KOH, 1600 rmp).

As a result, alkoxy substituted complex **5-42** showed good electrocatalytic activity towards the reduction of oxygen which could be improved by mild pyrolysis (**5-42-400**). This was expected, since heat treatment induces cross-linking in the mesophases. Although, the catalytic activity could not be improved, comparable data as for complex **5-11** were received. The catalytic performances of the herein described HPHATN complexes compete well with the values reported in literature for non-precious metal catalysts for ORR.[110-111] Nevertheless, it has to me mentioned, that the results received in the present work are only preliminary results and further optimization of processing techniques such as variation of the carbon support and catalyst loading, will tune the catalytic performance.

Compound	Current density @-0.8V [mA/cm^2]	%H_2O[a]	n[b]
5-11	4.07	64.1	3.28
5-42	3.70	67.0	3.34
5-42-400	4.03	66.0	3.32

[a] efficiency of 4 electron transfer @-0.8 V (%H2O = 100(4-n)/2); [b] number of electrons passed @-0.8 V (n = 4ID/(ID + IR/N), N = 3.7);

Durability tests and further evaluation including different carbon support and catalysts preparation is currently under process at Sumitomo Chemical Co. Additionally, the electrochemical activity of thiophene and bromine substituted complexes **5-43** and **5-44**, respectively, are also under investigations along with further development by network forming through oxidative polymerization or metal mediated cross-coupling reaction.

5.1.6 Summary

In summary, different substituents have been successfully introduced onto a triply fused triangular two-dimensional porphyrinoid. The synthesis of a key intermediate (**5-18**) was established using well-known HAT chemistry and opened a straighforward access to functionalize the periphery by facile condensation procedures. Seven different HPHATNs have been synthesized in high yields and their optical and electrochemical properties have been studied. The inspiration to introduce different substituents was based on previous results of HPHATN **5-11**, which showed excellent electrocatalytic activity towards the reduction of oxygen.[144] To further improve catalytic activity the investigation of the influence of different substituents was considered. In this regards, two basic approaches have

been contemplated, namely, the enhancement of sufficient contact between catalyst and the carbon support, and the increase of density of active sites. The latter might be achieved *e.g.* by network forming either by the direct connection of the triangles or through cross-linking in the mesophases. As a conclusion, systematical functionalization with different substituents fulfilling the requirements was established in the present work. Structure analysis by fiber 2D-WAXS confirmed the formation of a well-arranged discotic columnar liquid crystalline phase for the alkoxy substituted derivative **5-30**, while the compounds with alkyl side chains (**5-27** to **5-29**) showed surprisingly low order. The improvement in organization of the alkoxy carrying compound was attributed to the reduced viscosity of the solid-state which is induced by the side chains. This underlines the importance of a well-tuned liquid crystalline state for the self-assembly of the HPHATNs into highly ordered pathways for charge carriers. Therefore, the alkoxy substituted complex **5-42** was expected to show superior results in catalytic tests compared to **5-11**. Unfortunately, these expectations could not be fulfilled, and further studies for the understanding are currently under process.

6 Conclusion and Outlook

Within the scope of the first part of the present work, three different core-modified porphyrinoids constructed by aryl-aryl bond-formation have been successfully synthesized and characterized in terms of their structural and electronic properties (Figure 6-1). Two distinct macrocyclization protocols, namely, the metal catalyzed Suzuki-Miyaura cross-coupling and the CuAAC reactions have been successfully applied for the built-up of the porphyrinoids.

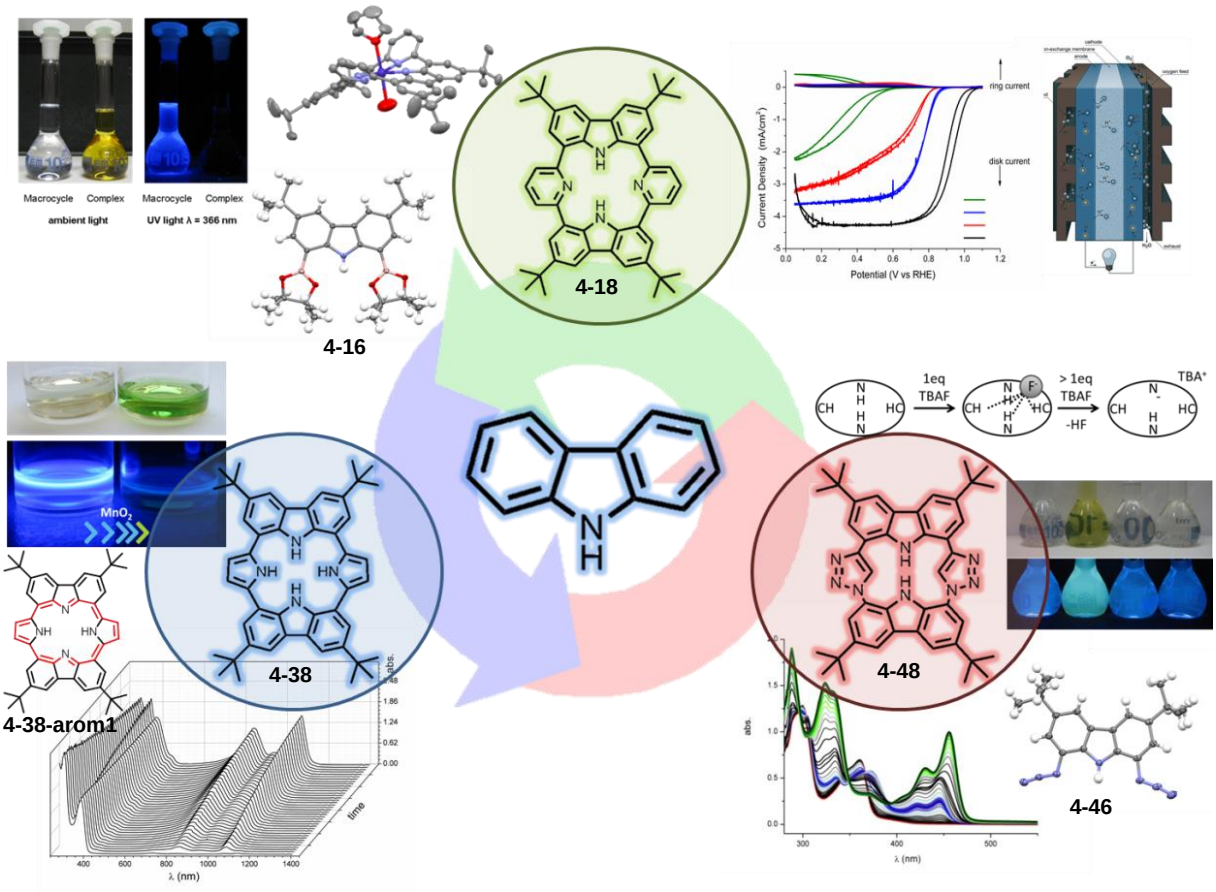

Figure 6-1: Overview of the achieved carbazole-containing macrocycles and their most striking features.

The challenge to create similar cavity sizes to that of porphyrins, was achieved by the development of purpose-made 1,8-disubsituted carbazole derivatives for the applied synthetic procedures. Therefore, 1,8-diboronic- (**4-16**) and 1,8-diaza- (**4-46**) carbazole derivatives have been successfully synthesized and enabled the formation of the porphyrinoids. These novel derivatives could also serve as intermediates to enrich the class of 1,8-carbazole polymers.[177, 276]

The synthesis of carbazole-containing macrocycle **4-18** was established by the macrocyclization of 1,8-diboronic-carabzole derivative **4-16** and 2,6-dibromopyridine (**4-17**, chapter 4.1). Porphyrinoid **4-18** features identical nitrogen substitution pattern (pyrrole and pyyrolenine units) in the inner cavity to porphyrins. Thus, it serves for a comprehensive comparison of the electronic properties to the unique ones of porphyrins. Nevertheless, the novel porphyrinoid proved to be different from regular porphyrins, which was reflected in the non-planar structure and the thereof resulting electronic properties (chapter 4.1.2 and 4.1.3). Consequently, the question of metal insertion into the non-porphyrin-like macrocycle was ambiguous but substantial. It could be shown, that, despite the saddle-like configuration, macrocycle **4-18** was able to bind metals such as cobalt, iron, copper and nickel (chapter 4.1.4).

Cobalt complex **4-32** was subjected to electrocatalytic evaluation towards the reduction of oxygen. It showed good results, with a number of electrons transferred of n = 3.78 and efficiency in H_2O production of 89.3% (heat treated at 600°C, in 0.5 M H_2SO_4, chapter 4.1.5) when compared to a catalyst of 20wt% Pt (n = 3.99 and 99.7 % efficient water conversion). Compared to the literature, the catalytic performance of cobalt complex **4-32** is superior to related monocyclic Co(II)porphyrins and Co(II)phthalocyanines,[219] and compares well with other non-precious metal catalysts for ORR.[110-111]

To further tune the catalytic performance and prevent pyrolysis, accumulation of the active sites was considered by means of oligomerization of macrocycle **4-18** (chapter 4.1.8). This could be achieved by the introduction of chlorine at the pyridine building block before macrocyclization, which ensured further transformation steps. The resulting oligomeric cobalt complex **4-32** did not show the expected improvement in the catalytic performance (chapter 4.1.10). This was explained by the lack of π-conjugation between the individual macrocycles due to the free rotation around the connecting single bonds. Nevertheless, the introduction of the chlorine substituent will guide the way for further substitution and extension of porphyrinoid **4-18**.

The Suzuki-Miyaura cross-coupling has been successfully applied as well in the synthesis of porphyrinoid **4-38** (chapter 4.2). Macrocycle **4-38** provides the unique feature of a $(NH)_4$ motif in its cavity as also found in calix[4]pyrroles.[136] Therefore, macrocycle **4-38** can be described as a benzo-fused calix[4]pyrrole. Contrary to calixpyrroles, which are not susceptible to oxidation, macrocycle **4-38** could be oxidized to its porphyrin state (chapter 4.2.3). The porphyrin-like aromaticity was reflected by a pronounced bathochromic shift in the UV-vis absorption spectrum upon oxidation of **4-38**. Nevertheless, compound **4-38** is sensitive to heat and air due to the electron rich character and tends to decompose easily denying further studies. Improvements in terms of stability should focus on additional substituents *e.g.* at the pyrrole units, which withdraw electron density from the inner ring.

The last target, to introduce CH bond donor units additionally to the NH bond donor units of the carbazole into the macrocyclic core, was achieved by the creation of triazoles at the pyrrolenine moieties by using the CuAAC[143] reaction. Therefore, the 1,8-diaza-carbazole derivative **4-46** was reacted with 1,8-diethynyl-carbazole **4-44** under copper-catalyzed conditions (chapter 4.3). Compared to the latter described porphyrinoids **4-18** and **4-38**, the symmetry of macrocycle **4-48** is reduced due to the triazole moieties. To the best of our knowledge, **4-48** is the first example of a macrocycle unifying NH- and CH-bond donor units for anion binding. The host-guest interaction between **4-48** and fluoride, chloride and bromide was investigated by UV-vis and fluorescence titration experiments and showed selectivity towards fluoride (chapter 4.3.4). A binding constant for fluoride of $K_a = 4.1 \pm 1.1 * 10^6\ M^{-1}$ was determined, which is one order of magnitude higher than for the herein investigated larger halides and compares well to a variety of receptors.[274, 304-305] Porphyrinoid **4-46** represents the smallest triazole-carbazole-containing anion receptor and will guide future developments for new macrocyclic receptors containing simultaneously CH and NH halide binding moieties.

In conclusion, new approaches to generate porphyrin-like macrocycles by contemporary, catalyst mediated synthetic protocols have been introduced. This strategy can be applied in the development of further porphyrinoids by using different building blocks, *e.g.* on the one hand fluorenes and dibenzothiphenes or on the other hand benzenes, thiophenes and furans.

The second part of the present work was devoted to the modification of the recently developed triangular trinuclear HPHATN **5-11** (Figure 6-2). This unique structure was established in our group and showed promising electrocatalytic activity towards the reduction of oxygen to water. As soon as a chemical compound is no longer simply a new

substance the tuning of its material characteristics relevant for applications becomes essential. On account of the synthetic design, which encloses the ring closure in the last step, functionality can be easily introduced into the existing structure to fine-tune material properties. On that basis, seven new derivatives (**5-27** to **5-33**) were effectively synthesized and characterized (Figure 6-2, chapter 5.1.1 and 5.1.2). Bearing in mind future application issues, firstly the synthesis was optimized to be as easy as possible, including simple work-up processes such as Soxhlet extraction. Furthermore, the structure could be elucidated by HRESI spectrometry and NMR spectroscopy, after the rescindment of the strong aggregation of the HPHATN core. Different substituents were chosen for the attachment to the triangular core, all with the common goal to further improve the catalytic performance of earlier described HPHATN **5-11**. Hereby two strategies were followed, firstly, accumulation of active sites either by network forming through synthetic transformations or by cross-linking through pyrolysis in the mesophases. Secondly, the improvement of the contact between the catalyst and the carbon support.

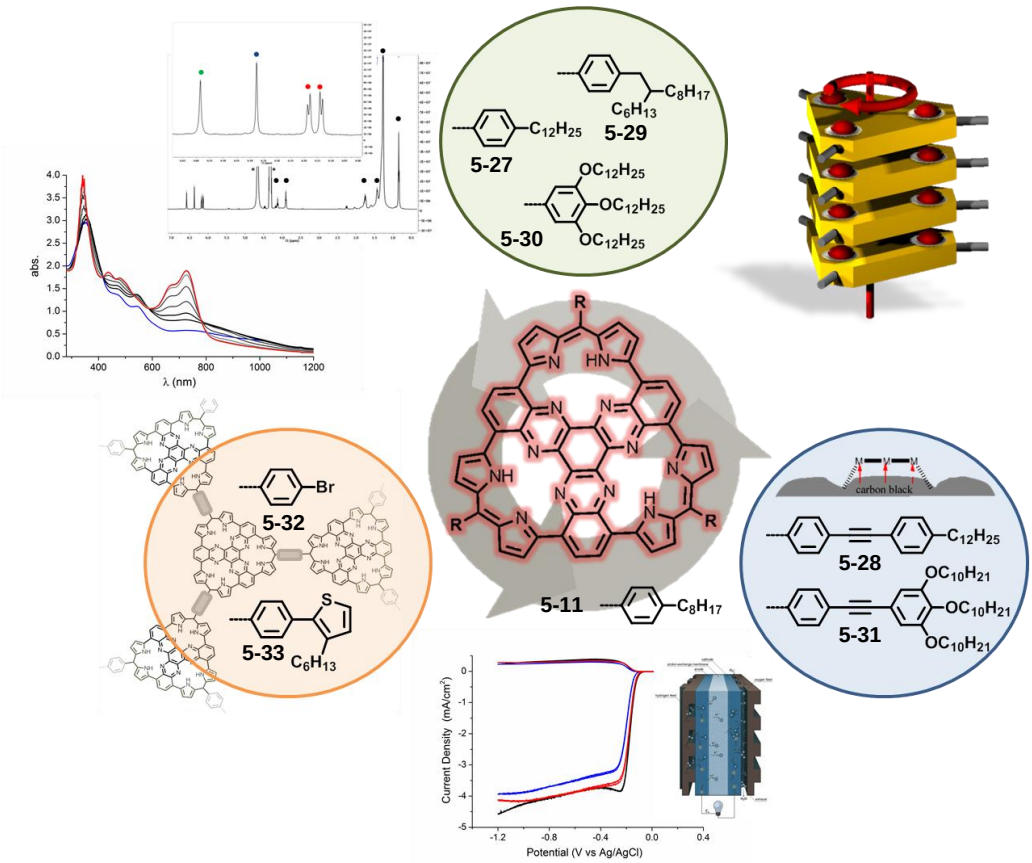

Figure 6-2: Overview of the successfully introduced side chains on the periphery of the triangular HPHATN core.

Within the scope of this work, the syntheses of all targeted structures were covered. Unfortunately, due to time reasons, only molecular self-assembly properties could be studied along with evaluation of the catalytic activity influence by cross-linking in the mesophase. Therefore, further investigation of network formation by protocols such as oxidative polymerization of the thiophene substituents in ***5-33*** or Yamamoto coupling of the bromines attached in ***5-32*** will be the target of future work. Additionally, electrocatalytic evaluation of the acetylene π-spacer containing HPHATN ***5-31*** and ***5-28*** together with the variation of carbon support shall be investigated in the near future.

The structure analysis by fiber 2D-WAXS confirmed the formation of a well-arranged discotic columnar liquid crystalline phase for alkoxy substituted HPHATN ***5-30***, while the compounds with alkyl side chains (***5-27*** and ***5-28***) show surprisingly low order (chapter 5.1.5). This was attributed to the reduced viscosity of the solid state supramolecular induced by the alkyl-chains. Therefore, the resulting cobalt complex ***5-42*** was also submitted to self-assembly investigation, and showed the desired molecular organization in the columnar structures. The electrocatalytic activity of complex ***5-42*** was investigated using RRDE techniques and showed good activity with a current density of 3.70 mA/cm², efficiency in water production of 67% and a number of electrons transferred of n = 3.34 (measured in 0.1 M KOH). The beneficial effect of cross-linking in the mesophases could be proven, by the enhancement of the current density up to 4.03 mA/cm². However, compared to HPHATN ***5-11*** no major improvement in activity could be observed. Nevertheless, the catalytic performances of the herein described HPHATN complexes compete well with values reported in literature for non-precious metal catalysts for ORR.[110-111]

In summary, next to the synthesis of new HPHATNs holding promise for cathode catalysis materials in fuel cells, novel concepts have been developed to further improve the catalysts performance of HPHATN ***5-11***.

7 Experimental Part

7.1 General Methods and Analytical Techniques

7.1.1 Chemicals and solvents

Commercially available reagents and solvents were obtained from the companies Acros, Aldrich, Alpha-Aesar, Fluka and Strem and used without further purification unless otherwise stated.

7.1.2 Chromatography

Analytical thin layer chromatograpy (TLC) were prepared using silica gel coated substrates "60 F254" from Merck. For preparative column chromatography silica gel with grain size 0.063 – 0.200 mm (silica gel, Merck) or 0.04 – 0.063 mm (flash silica gel, Gedruan Si 60, Merck) was used.

7.1.3 Inert atmosphere

Standard Schlenck technique was used for oxygen or moisture sensitive reactions.

7.1.4 Microwave assisted synthesis

The microwave assisted syntheses were carried out in a CEM Discover™ system equipped with a temperature and pressure sensor using 10 ml or 35 ml vials.

7.1.5 NMR Spectroscopy

^{1}H-NMR and ^{13}C-NMR spectra were recorded on a Bruker AVANCE 300 or Bruker AVANCE III 500 or AVANCE III 700 using a 5 mm broadband probe with z-Gradient. The experiments were conducted between 298 K and the temperature was regulated by standard ^{1}H methanol or glycol NMR samples using the topspin 2.1 software (Bruker). The deuterated solvent was used as an internal standard, CD_2Cl_2 was set to δ_H = 5.32 ppm and

δ_C = 54.00 ppm, THF-d_8 to δ_H = 3.58 ppm and δ_C = 67.57 ppm, DMSO-d_6 to δ_H = 2.50 ppm and δ_C = 39.51 ppm, $C_2D_2Cl_4$ to δ_H = 5.91 ppm and δ_C = 74.20 ppm,[365] hexafluoroisopropanol-d_2 (HFIP-d_2) plus 0.1% TFA-d_2 to δ_H = 4.32 ppm and δ_C = 67.15 ppm.

7.1.6 Melting Points

Melting points were determined on a Büchi hot stage apparatus and were uncorrected.

7.1.7 Infrared Spectroscopy

Infrared spectroscopy was measured on a Nicolet 730 FT-IR spectrometer in the evanescence field of diamond.

7.1.8 Mass Spectrometry

Mass spectra were obtained using FD on a VG Instruments ZAB 2 SE-FPD. MALDI-TOF spectrometry was conducted on a Bruker Reflex IITOF spectrometer, utilizing a 337 nm nitrogen laser. Tetracyanoquinodimethane (TCNQ) was used as the matrix substance for solid state prepared samples. HRESI mass spectrometry was measured on a QTof Ultima 3 Fa. Micromass/Waters.

7.1.9 Elemental Analysis

Elemental analysis was performed on a Foss Heraeus-Vario EL.

7.1.10 UV-vis Spectroscopy

Solution UV-vis spectra were recorded at 298 K on a Perkin-Elmer Lambda 100 spectrophotometer. Solution photoluminescence spectra were recorded on a SPEX-Fluorolog II(212) spectrometer.

7.1.11 Cyclic Voltammetry

Cyclic voltammetry was measured on a Princeton Applied Research Parstat 2273 instrument with anhydrous solvents under argon atmosphere. Tetrabutylammonium hexafluorophosphate was used as conductive salt at a concentration of 0.1 mol/l. A platinum working electrode (0.5 mm diameter), a platinum wire as counter electrode, and a silver wire as quasi-reference electrode were used. The peaks were calibrated versus the half-wave oxidation peak of the internal standard ferrocene (1 mM).

7.1.12 Two-dimensional X-ray Wide Angle Scattering (2D-WAXs)

The 2D-WAXS experiments were performed by using a copper anode X-ray tube, operated at 35 kV/20 mA, and Osmic confocal Max-Flux with pinhole collimation and a two-dimensional MAR345 image plate detector. A double-graphite monochromator for the CrKα radiation (λ = 0.154) was used. The samples were prepared as thin filaments of 0.7 mm diameter by filament extrusion using a home-made miniextruder and were positioned perpendicular to the incident X-ray beam and vertical to the 2D detector for the X-ray experiments.

7.1.13 Thermogravimetic analysis (TGA) and Differential Scanning Calorimetry (DSC)

Thermogravimetric analysis (TGA) was performed on a Mettler TGA-851 Analyszer at a heating rate of 10 $Kmin^{-1}$ under N_2 flow. Differential scanning calorimetry (DSC) was measured on a Mettler DSC 30 with heating and cooling rates of 10 K/min.

7.1.14 Superconducting Quantum Interference Device (SQUID) measurements

Magnetic susceptibility data for solvent free samples were collected in the temperature range of 2.300 K in an applied magnetic field of 1 T with a SQUID magnetometer (MPMS-7, Quantum Design). The data were corrected for the underlying diamagnetism using Pascal's constants. Temperature dependent magnetic contributions of the sample holder was experimentally determined and subtracted from the measured data.

7.1.15 RDE measurements (MPI)

The catalysts ink were prepared as follows. Typically, 20 mg of the compound (cobalt complex **4-19**) was mixed with 80 mg carbon black (KB 600) in 4 ml DCM at rt under stirring in an open crucible. Additionally, the samples were treated 10 min in an ultra-sonic bath. After evaporation of DCM, the obtained composites are dried overnight at 60°C in an oven and subsequently calcined at 470, 600 and 800 °C for 2 h, respectively. 1 mg of the catalysts composite was dissolved in 1 mL solvent mixture of Nafion (5mol% in H_2O) and EtOH (ratio = 1:9) by sonication. For comparison, a commercially available catalyst of 20wt% Pt supported on black carbon (from Sigma, fuel cell grade) is used and 1 mg/ml Pt-C suspension is also prepared as the same procedure described above.

The used glass carbon rotating disk electrode (3 mm in diameter, from Autolab) was polished mechanically with 0.5 µm diamond down to 0.05 µm alumina slurry to obtain a mirror-like surface and then washed with Mill-Q water and acetone and allowed to dry. 1.8 µL catalysts suspension was pipetted on the glassy carbon electrode surface and was allowed to dry at rt and then heated at 50 °C for 30 min before measurement. This results in a catalyst loading of 25.5 µg/cm^2.

Electrochemical experiments are conducted using PARSTAT 2273 advanced electrochemical system. A conventional three-electrode cell was employed incorporating a working glass carbon RDE (Autolab), an Ag/AgCl, KCl (3 M) electrode as reference electrode, and a Pt electrode as counter electrode. All potentials were measured and reported *vs.* the Ag/AgCl, KCl (3 M) reference electrode. The experiments are carried out in O_2 saturated 0.1 M KOH solution for the oxygen reduction reaction. The potential range is cyclically scanned between -1.2 and +0.2 V at different scan rate of 100 mV/s at the ambient temperature after purging O_2 or Ar gas for 15 min. RDE measurements are conducted at different rotating speeds from 400 to 3600 rpm by using an Autolab Model.

7.1.16 RDDE measurements (Sumitomo)

RRDE measurements were performed using a standard three-electrode-electrochemical cell including a platinum ring as counter electrode (ring electrode with d_{inner} = 7 mm and d_{outer} = 9 mm, 1.4 V *vs.* RHE), a glassy carbon working electrode (disk electrode, d = 6 mm) and an Ag/AgCl (sat. KCl) reference electrode. Catalyst inks have been prepared by suspending 5 mg of catalyst and 40 mg carbon black (Ketjen Black KB600) in 15 ml MeOH and subsequent ultrasonic treatment. The inks were then dried and/or pyrolyzed for 2h at the corresponding temperature. The RRDE measurements were performed in O_2 saturated 0.5 M H_2SO_4 solution at a potential scan rate of 5 mVs^{-1} and a rotation speed of 900 rmp.

7.2 Synthetic Procedures

7.2.1 3,6-Di-*tert*-butyl-9*H*-carbazole (4-13)

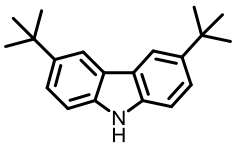

4-13

3,6-Di-*tert*-butyl-9-carbazole (**4-13**) was synthesized following the literature procedures.[153] 5 g (30 mmol, 1 eq) of 9*H*-carbazole (**4-1**) and 12 g (90 mmol, 3 eq) $ZnCl_2$ (dried at high vacuum) were suspended in 75 ml nitromethane. Then 10 ml (8.51 g, 90 mmol, ρ = 0.851 g/ml, 3 eq) *t*-BuCl were added slowly. The reaction mixture was stirred at rt for 16 h. The reaction was quenched with H_2O and the aqueous layer extracted with DCM. The organic layer was washed with H_2O, dried over $MgSO_4$, filtered and the solvent removed *in vauo*. After recrystalliszation from hot hexane 5.8 g (20.8 mmol, 69 %) of 3,6-di-*tert*-butyl-9-carbazole (**4-13**) were obtained as colorless crystals.

^{1}H-NMR (CD_2Cl_2, 300 MHz, 298 K): δ = 1.47 (s, 18H), 7.37 (dd, ^3J=8.5 Hz, ^4J=0.6 Hz, 2H), 7.50 (dd, ^3J=8.5 Hz, ^4J=1.9 Hz, 2H), 7.91 (s, 1H), 8.11 (d, ^4J=1.9 Hz, 2H) ppm. ^{13}C-NMR (CD_2Cl_2, 75 MHz, 298 K): δ = 32.2, 34.9, 110.4, 116.5, 123.6, 123.9, 138.5, 142.6 ppm. MS (FD, 8 kV) m/z = 279.4 g/mol - calculated for $C_{20}H_{25}N$: 279.2 g/mol. Mp 230°C (from hexane).

The analytic data are in agreement with the literature.[153]

7.2.2 1,8-Dibromo-3,6-di-*tert*-butyl-9*H*-carbazole (4-14)

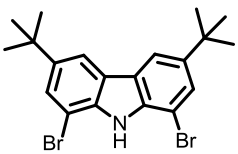

4-14

1,8-Dibromo-3,6-di-*tert*-butyl-9H-carbazole (**4-14**) was synthesized following the literature procedures.[152] 2.5 g (9 mmol, 1 eq) of 3,6-di-*tert*-butyl-9-carbazole (**4-13**) was suspended in 300 ml AcOH and heated to 90°C. The flask was covered with aluminum foil. To this solution 0.95 ml (2.96 g, 18.9 mmol, δ = 3.119 g/mol, 2.1 eq) Br_2 was slowly added. The reaction was completed after 30 min and the reaction was stopped by the addition of 1 ml saturated Na_2SO_3-solution and then cooled to rt. To the solution 400 ml EtOAc was added

and the organic layer was washed twice with H_2O, dried over $MgSO_4$, filtered and the solvent removed *in vauo*. The crude product was purified by column chromatography using DCM as eluent. 3.93 g (quant., 9 mmol) of 1,8-dibromo-3,6-di-*tert*-butyl-9*H*-carbazole (**4-14**) were obtained as colorless crystals.

^{1}H-NMR (CD_2Cl_2, 300 MHz, 298 K): δ = 1.44 (s, 18H), 7.68 (d, ^4J=*1.6 Hz*, 2H), 8.05 (dd, ^4J=*0.5, 1.6 Hz*, 2H), 8.23 (s, 1H) ppm. ^{13}C-NMR (CD_2Cl_2, 75 MHz, 298 K): δ = 32.0, 35.2, 104.2, 116.5, 125.2 , 127.1, 136.7, 145.3 ppm. MS (FD, 8 kV) m/z = 435.6 g/mol - calculated for $C_{20}H_{25}Br_2N$: 435.0 g/mol. Mp 173°C.

The analytic data are in agreement with the literature.[152]

7.2.3 3,6-Di-*tert*-butyl-1,8-bis(4,4,5,5-tetramethyl-1,3,2-dioxaborolan-2-yl)-9*H*-carbazole (4-16)

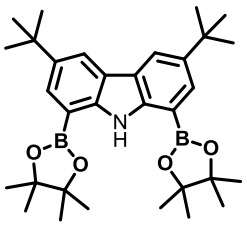

4-16

7.8 ml *n*-BuLi (1.6 M in hexane, 12.5 mmol, 1.1 eq) was added at 0°C to a solution of 1,8-dibromo-3,6-di-*tert*-butyl-9H-carbazole (**4-14**, 5 g, 11.5 mmol, 1 eq) in degassed THF (250 ml). After stirring at this temperature for 1 h, the reaction mixture was allowed to warm to room temperature (rt) while CO_2 gas was bubbled through the solution for 30 min. The solvent was then removed *in vacuo* and the residue was redissolved in degassed THF (250 ml). 29.4 ml *t*-BuLi (1.7 M in pentane, 49.9 mmol, 4.3 eq) was slowly added at -78°C and the reaction mixture was then stirred at 0°C for 3 h. Freshly distilled 2-isopropoxy-tetramethyl-dioxaborolane (**4-15**, 11.6 ml, 43.5 g, 57.5 mmol, ρ = 0.92 g/mol, 5 eq) was added at -78°C and the reaction mixture was allowed to warm to rt overnight. The mixture was hydrolyzed at 0°C by addition of 1M aqueous HCl and then diluted with EtOAc. The organic phase was washed twice with 1M aqueous NaOH and once with 1M $NaHCO_3$ solutions, dried over $MgSO_4$, filtered, and the solvent removed *in vacuo*. The crude product was purified by recrystallisation from hot hexane to afford 2.7 g (5.1 mmol, 50%) of compound **4-16** as a colorless solid.

^{1}H-NMR (CD_2Cl_2, 300 MHz, 298 K): δ = 1.47 (s, 42H), 7.85 (d, 2H), 8.24 (d, 2H), 9.99 (s, 1H) ppm. ^{13}C-NMR (CD_2Cl_2, 75 MHz, 298 K): δ = 24.9, 31.8, 34.5, 83.76, 119.9, 121.7, 129.8, 140.9, 143.6 ppm. Anal. Found: C, 71.92; H, 8.94; N, 2.63. Calcd for $C_{32}H_{47}B_2NO_4$: C, 72.13; H, 8.92; N, 2.64. MS (FD, 8 kV) m/z = 531.4 g/mol - calculated for for $C_{32}H_{47}B_2NO_4$: 531.7 g/mol. Mp 387°C (from hexane).

7.2.4 Cyclo[bis-(3,6-di-*tert*-butyl-1,8-di(pyridin-2,6-yl)-9*H*-carbazole)] (4-18) (Porphyrinoid 4-18)

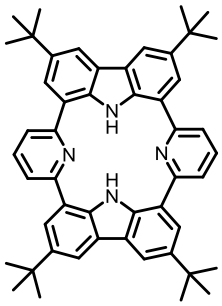

4-18

132.8 mg (0.25 mmol, 1 eq) of 3,6-di-*tert*-butyl-1,8-bis(4,4,5,5-tetramethyl-1,3,2-dioxaborolan-2-yl)-9H-carbazole (**4-16**), 58.7 mg (0.25 mmol, 1 eq) of 2,6-dibromopyridine (**4-17**) and 6 mg (5 µmol, 0.01 eq) of $Pd(PPh_3)_4$ were dissolved in toluene (500 ml). EtOH (200 ml) and 2M K_2CO_3 (30 ml, excess) were added to the solution and the reaction mixture was degassed 3 times. The reaction mixture was stirred at 85°C for 17 h. The solvents were removed *in vacuo*, the crude was redissolved in DCM and filtered over 1 cm silica. Crude impurities were removed by GPC chromatography in DCM. The product was purified by column chromatography hexane : DCM (1:1) to yield 30 mg (0.04 mmol, 15%) of macrocycle **4-18** as a colorless solid.

^{1}H-NMR (CD_2Cl_2, 300 MHz, 298 K): δ = 1.52 (s, 36H), 7.61 (d, ^{4}J=1.85 Hz, 4H), 7.68 (d, ^{3}J=7.83 Hz, 4H), 8.22 (t, ^{3}J=7.57 Hz, 2H), 8.24 (d, ^{4}J=1.69 Hz, 4H), 9.66 (s, 2H) ppm. ^{13}C-NMR (CD_2Cl_2, 75 MHz, 298 K): δ = 32.1, 35.0, 117.2, 122.6, 124.1, 124.7, 125.9, 136.1, 138.8, 143.4, 159.7 ppm. MALDI TOF (TCNQ as matrix) m/z = 708.42 g/mol - calculated: 708.42 g/mol for $C_{50}H_{52}N_4$. EA found: 84.42 % C; 7.77 % H; 7.77 % N – calculated: 84.70 % C; 7.39 % H; 7.90 % N. HRESI MS (THF 1:1 MeCN): $[C_{50}H_{52}N_4+H]^+$ m/z = 709.4265 g/mol – calculated: 709.4270 g/mol. Mp > 400°C.

7.2.5 Cobalt(II)-cyclo[bis-(3,6-di-*tert*-butyl-1,8-di(pyridin-2,6-yl)-9*H*-carbazole)] (4-19)

(Cobalt complex 4-19)

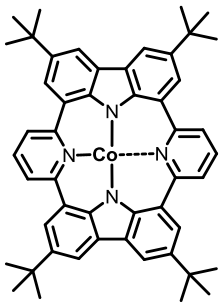

4-19

25 mg (0.035 mmol, 1 eq) of macrocycle **4-18** and 8 mg (0.046 mmol, 1.3 eq) of $Co(OAc)_2$ were put in a microwave-tube and dissolved in 2 ml of dry DMF. The reaction mixture was stirred for 4 h in the microwave at 170°C and 300 W. It was cooled to rt and poured into ice-cold water. The precipitate was filtered off and dried under vacuum to afford 23 mg (0.030 mmol, 86 %) of cobalt complex **4-19** as a yellow solid.

^{1}H-NMR (DMF-d_7, 500 MHz, 403 K): δ = -8.47 (s), 5.44 (s), 8.52 (s), 11.63 (s), 45.42 (s) ppm. MALDI TOF (TCNQ as matrix) m/z = 765.80 g/mol - calculated: 765.34 g/mol for $C_{50}H_{50}CoN_4$.

7.2.6 2,6-Dibromo-4-chloropyridine (4-29)

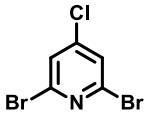

4-29

According to the literature procedure[241] 250 mg (1.1 mmol, 1 eq) 2,6-dibromopyridine (**4-17**) was dissolved in 1.5 ml dry THF and cooled to -30°C. To this solution 1.6 ml (1.6 mmol, 1M in THF, 1.5 eq) TMPMgCl·LiCl were added and the reaction mixture as stirred for 30 min at this temperature. Then 254 mg (1.2 mmol, 1.1 eq) hexachloroethane dissolved in 2 ml dry THF were added dropwise and the reaction was allowed to warm to rt overnight. The reaction was quenched with aqueous NH_4Cl solution and extracted with EtOAc. The organic phase was with H_2O and brine, dried over $MgSO_4$, filtered, and the solvent removed *in vacuo*. The crude product was purified by column chromatography using

hexane : DCM (1 : 1) and additional crystallization from hot EtOH to give 125 mg (0.5 mmol, 44%) of 2,6-dibromo-4-chloropyridine (**4-29**) as colorless crystals.

^{1}H-NMR (CD_2Cl_2, 300 MHz, 298 K): δ = 7.53 (s, 2H) ppm. ^{13}C-NMR (CD_2Cl_2, 75 MHz, 298 K): δ = 127.6, 141.2, 146.8 ppm. Mp 53°C (from EtOH).

The analytic data are in agreement with the literature.[241]

7.2.7 Cyclo[bis-(3,6-di-*tert*-butyl-1-(4-chloropyridin-2,6-yl)-8-(pyridin-2,6-yl)-9*H*-carbazole)] (4-33)

(Porphyrinoid 4-*33*)

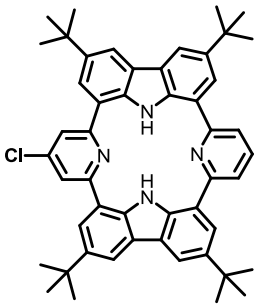

4-*33*

590.43 mg (1.12 mmol, 1 eq) of 3,6-di-*tert*-butyl-1,8-bis(4,4,5,5-tetramethyl-1,3,2-dioxaborolan-2-yl)-9*H*-carbazole (**4-16**), 130.48 mg (0.56 mmol, 0.5 eq) of 2,6-dibromopyridine (**4-17**), 149.35 mg (0.56 mmol, 0.5 eq) 2,6-dibromo-4-chloropyridine (**4-29**) and 13 mg (11.2 µmol, 0.01 eq) of $Pd(PPh_3)_4$ were dissolved in toluene (1000 ml). EtOH (400 ml) and 2M K_2CO_3 (60 ml, excess) were added to the solution and the reaction mixture was degassed 3 times. The reaction mixture was stirred at 85°C for 3 d. The solvents were removed *in vacuo*, the crude was redissolved in DCM and filtered over 1 cm silica. The crude product was purified by column chromatography using hexane : DCM (1:1) to yield 60 mg (0.08 mmol, 7%) of macrocycle **4-*33*** as a colorless solid.

^{1}H-NMR (CD_2Cl_2, 700 MHz, 298 K): δ = 1.50 (s, 18H), 1.51 (s, 18H), 7.59 (d, ^{4}J=*1.8 Hz*, 2H), 7.61 (d, ^{4}J=*1.8 Hz*, 2H), 7.69 (d, ^{3}J=*7.8 Hz*, 2H), 7.70 (s, 2H), 8.02 (t, ^{3}J=*7.6 Hz*, 1H), 8.23 (d, ^{4}J=*1.7 Hz*, 2H), 8.26 (d, ^{4}J=*1.7 Hz*, 2H), 9.66 (s, 2H) ppm. ^{13}C-NMR (CD_2Cl_2, 176 MHz, 298 K): δ = 31.2, 31.3, 34.1, 34.2, 116.4, 117.0, 121.5, 121.8, 122.0, 123.3, 123.8, 124.1, 125.0, 125.3, 135.2, 135.3, 137.9, 142.6, 142.7, 145.3, 158.9, 160.4 ppm. MALDI TOF (TCNQ as matrix) m/z = 742.98 g/mol - calculated: 742.38 g/mol for $C_{50}H_{51}ClN_4$. HRESI MS (THF 1:1 MeCN): $[C_{50}H_{51}ClN_4+H]^+$ m/z = 743.3852 g/mol – calculated: 743.3881 g/mol. Mp > 400°C.

7.2.8 Biscyclo[bis-(3,6-di-*tert*-butyl-1,1'-di(pyridin-2,6-yl)-yl)-8,8'-[4,4'-bipyridine]-2,2',6,6'-diyl)-9*H*-carbazole)] (4-34)

(Dimer 4-34)

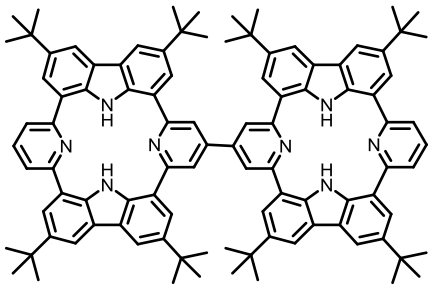

4-34

In a glovebox 78 mg (0.28 mmol, 2 eq) $Ni(COD)_2$, 30 mg (0.28 mmol, 2eq) COD and 43 mg (0.28 mg, 2 eq) 2,2-bipyridine were put into a dry flask and dissolved in 2.25 ml toluene and 1.5 ml DMF. The flask was closed and transferred to the fume hood, heated to 60°C and stirred for 30 min. To this solution 106 mg (0.14 mmol, 1 eq) of macrocycle **4-33** dissolved in 2 ml DMF were added to the reaction and the reaction was stirred for 3 d at this temperature. To reaction was allowed to cool to rt and precipitated into a solution mixture of MeOH : 1M HCl (1 : 1). The solid was filtered off and further purified by column chromatography using hexane : DCM (1 : 1) to yield 30 mg (0.02 mmol, 30%) of dimer **4-34** as a yellow solid.

^{1}H-NMR (CD_2Cl_2, 500 MHz, 298 K): δ = 1.51 (s, 36H), 1.52 (s, 36H), 7.64 (d, ^4J=*1.7 Hz*, 4H), 7.71 (d, ^3J=*7.8 Hz*, 4H), 7.74 (d, ^4J=*1.6 Hz*, 4H), 8.04 (t, ^3J=*7.8 Hz*, 2H), 8.14 (s, 4H), 8.25 (d, ^4J=*1.4 Hz*, 4H), 8.28 (d, ^4J=*1.4 Hz*, 4H), 9.74 (s, 4H) ppm. ^{13}C-NMR (CD_2Cl_2, 125 MHz, 298 K): δ = 32.0, 32.1, 3.1, 117.3, 117.7, 120.4, 122.7, 123.8, 124.2, 124.7, 125.0, 126.0, 126.1, 136.2, 136.3, 138.8, 143.5, 143.6, 148.4, 159.8, 161.0 ppm. MALDI TOF (TCNQ as matrix) m/z = 1416.22 g/mol - calculated: 1414.82 g/mol for $C_{100}H_{102}N_8$. HRESI MS (THF 1:1 MeCN): $[C_{100}H_{102}N_8+2H]^{2+}$ m/z = 708.4188 g/mol – calculated: 708.4192 g/mol. Mp > 400°C.

7.2.9 Cyclo[bis-3,6-di-*tert*-butyl-1,8-bis(4-chloropyridin-2,6-yl)-9*H*-carbazole)] (4-30)

(Porphyrinoid 4-30)

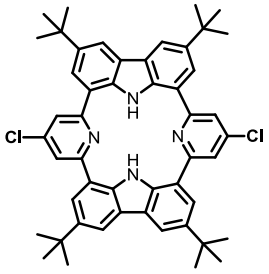

4-30

595.26 mg (1.12 mmol, 1 eq) of 3,6-di-*tert*-butyl-1,8-bis(4,4,5,5-tetramethyl-1,3,2-dioxaborolan-2-yl)-9H-carbazole (**4-16**), 301.14 mg (1.12 mmol, 1 eq) 2,6-dibromo-4-chloropyridine (**4-29**) and 13 mg (11.2 µmol, 0.01 eq) of $Pd(PPh_3)_4$ were dissolved in toluene (850 ml). EtOH (340 ml) and 2M K_2CO_3 (50 ml, excess) were added to the solution and the reaction mixture was degassed 3 times. The reaction mixture was stirred at 85°C for 3 d. The solvents were removed *in vacuo*, the crude was redissolved in DCM and filtered over 1 cm silica. The crude product was purified by column chromatography using hexane : DCM (1:1) to yield 113 mg (0.15 mmol, 13%) of macrocycle **4-33** as a colorless solid.

^{1}H-NMR (CD_2Cl_2, 300 MHz, 298K): δ = 1.53 (s, 36H), 7.61 (d, ^4J=*1.8 Hz*, 4H), 7.72 (s, 4H), 8.27 (d, ^4J=*1.7 Hz*, 4H), 9.59 (s, 2H) ppm. ^{13}C-NMR (CD_2Cl_2, 75 MHz, 298K): δ = 32.1, 35.1, 117.9, 122.5, 123.0, 124.9, 126.0, 136.1, 143.7, 146.3, 161.2 ppm. MALDI TOF (TCNQ as matrix) m/z = 775.86 g/mol - calculated: 776.34 g/mol for $C_{50}H_{50}Cl_2N_4$. HRESI MS (THF 1:1 MeCN): $[C_{50}H_{50}Cl_2N_4+H]^+$ m/z = 777.3488 g/mol – calculated: 777.3491 g/mol. Mp > 400°C.

7.2.10 Oligomer 4-31

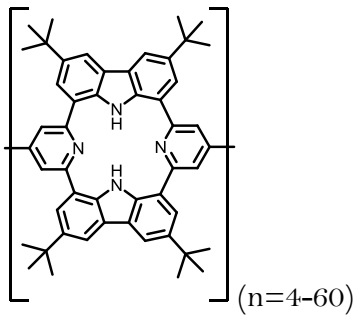

4-31

In a glovebox 110 mg (0.40 mmol, 2 eq) $Ni(COD)_2$, 44 mg (0.40 mmol, 2eq) COD and 60 mg (0.40 mg, 2 eq) 2,2-bipyridine were put into a dry flask and dissolved in 2.25 ml toluene and 1.5 ml DMF. The flask was closed and transferred to the fume hood, heated to 60°C and stirred for 30 min. To this solution 166 mg (0.20 mmol, 1 eq) of macrocycle **4-30** dissolved in 2 ml toluene were added to the reaction and the reaction was stirred for 3 d at this temperature. The reaction was allowed to cool to rt, the solvents concentrated *in vacuo* and precipitated into a solution mixture of MeOH : 1M HCl (1 : 1). The solid was filtered and this procedure was repeated twice to yield 130 mg oligomer **4-31** as an oligomeric mixture. ^{1}H-NMR (THF-d_8, 500 MHz, 298 K): δ = 1.521 (s, br, 36H), 7.72-7.90 (m, br, 4H), 8.21-8.39 (m, br, 6H), 10.54 (s, br, 2H) ppm. GPC (THF *vs* PS, 303 K, UV detector λ = 254 nm): M_n = 3749 g/mol, M_w = 20993 g/mol, PDI = 5.60; MALDI TOF (TCNQ as matrix) m/z (max) = 2828.17 g/mol - calculated: 2833.68 g/mol for n= 4.

7.2.11 Cobalt complex 4-32

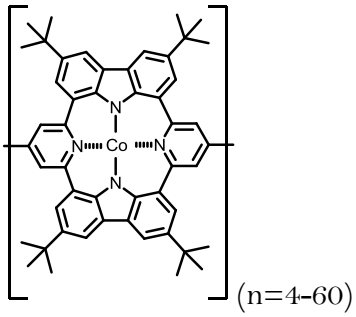

(n=4-60)

4-32

33 mg of oligomer **4-31** and 40 mg (excess) of $Co(OAc)_2$ were put in a microwave-tube and dissolved in 4 ml of dry DMF. The reaction mixture was stirred for 4 h in the microwave at 170°C and 300 W. It was cooled to rt and poured into ice-cold water. The precipitate was filtered off and dried under vacuum to afford 23 mg of cobalt complex **4-19** as a yellow solid. MALDI TOF (TCNQ as matrix) m/z (max) = 3063.80 g/mol - calculated: 3069.68 g/mol for n= 4.

7.2.12 3,6-Didodecyl-9-carbazole (4-24)

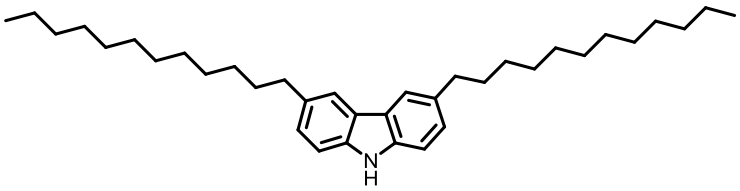

4-24

5 g (15.4 mmol, 1 eq) of 3,6-dibromo-9*H*-carbazole (**4-23**) and 640 mg (0.77 mmol, 0.05 eq) of $Pd(dppf)Cl_2$ were dissolved in 160 ml THF (dry). To this solution 77.5 ml (77.4 mmol, 5 eq) of a 1M solution of dodecylmagnesium bromide in Et_2O were added slowly at rt. After the addition was completed the reaction mixture was heated to 75°C and stirred at this temperature for 16 h. The reaction was cooled to rt and quenched with MeOH. The solvent was removed *in vacuo* and the crude product was purified by column chromatography using hexane : ethyl acetate (9:1) as eluent. 4.34 g (56%, 8.62 mmol) of 3,6-didodecyl-9*H*-carbazole (**4-24**) was obtained as a yellowish liquid.

^{1}H-NMR (CD_2Cl_2, 300 MHz, 298 K): δ = 0.89 (t, ^3J=6.8 Hz, 6H), 1.24 (m, 32H), 1.35 (m, 4H), 1.70 (m, 4H), 2.76 (t, ^3J=7.9 Hz, 4H), 7.21 (dd, ^3J=8.2 Hz, ^4J=1.6 Hz, 2H), 7.32 (d, ^3J=8.2 Hz, 2H), 7.85 (s, 2H), 7.98 (s, 1H) ppm. ^{13}C-NMR (CD_2Cl_2, 75 MHz, 298 K): δ = 14.3, 23.1, 29.7, 29.8, 30.0, 30.1, 30.1, 32.3, 32.8, 36.4, 110.6, 119.8, 123.6, 126.8, 134.3, 138.7 ppm. MS (FD, 8 kV) m/z = 502.9 g/mol - calculated for $C_{36}H_{57}N$: 503.4 g/mol. Mp 67°C.

The analytic data are in agreement with the literature.[236]

7.2.13 1,8-Dibromo-3,6-didodecyl-9*H*-carbazole (4-25)

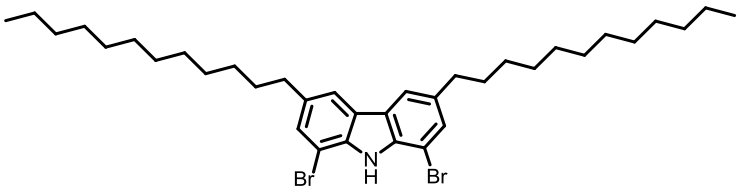

4-25

1 g (2.0 mmol, 1 eq) of 3,6-didodecyl-9*H*-carbazole **4-24** was dissolved in 8 ml DCM and 8 ml AcOH. To this solution 777 mg (4.4 mmol, 2.1 eq) NBS were added successively and the resulting reaction mixture was stirred for 1 h at rt. The reaction was quenched with water and extracted with DCM. The organic layer was washed with brine, dried over $MgSO_4$, filtered and the solvent removed *in vacuo*. The crude product was purified by

column chromatography (hexane) to give 1.2 g (90%, 1.8 mmol) of 1,8-dibromo-3,6-didodecyl-9*H*-carbazole (**4-25**) as a colorless solid.

^{1}H-NMR (CD_2Cl_2, 500 MHz, 298 K): δ = 0.87 (t, ^3J=7.1 Hz, 6H), 1.26 (m, 32H), 1.35 (m, 4H), 1.69 (m, 4H), 2.76 (t, ^3J=7.8 Hz, 4H), 7.45 (d, ^4J=1.3 Hz, 2H), 7.78 (d, ^4J=1.3 Hz, 2H), 8.21 (s, 1H) ppm. ^{13}C-NMR (CD_2Cl_2, 125 MHz, 298 K): δ = 14.3, 23.1, 29.6, 29.7, 29.8, 29.9, 30.0, 30.0, 30.0, 32.3, 32.4, 36.0, 104.2, 119.6, 125.2, 129.6, 136.8, 136.9 ppm. MS (FD, 8 kV) m/z = 660.6 g/mol - calculated for $C_{36}H_{55}Br_2N$: 659.3 g/mol.

7.2.14 3,6-Didodecyl-1,8-bis(4,4,5,5-tetramethyl-1,3,2-dioxaborolan-2-yl)-9*H*-carbazole (4-26)

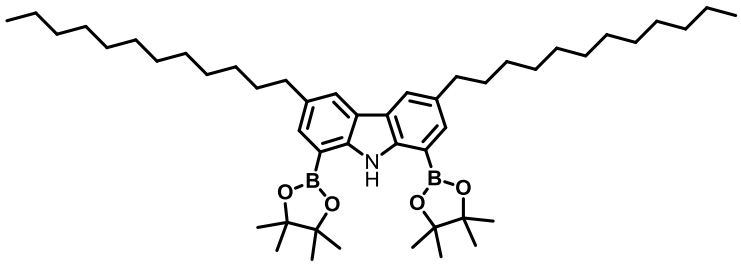

4-26

0.9 ml *n*-BuLi (1.6 M in hexane, 1.5 mmol, 1.1 eq) was added at 0°C to a solution of 1,8-dibromo-3,6-didodecyl-9*H*-carbazole (**4-25**, 884 mg, 1.4 mmol, 1 eq) in degassed THF (20 ml). After stirring at this temperature for 1 h, the reaction mixture was allowed to warm to rt while CO_2 gas was bubbled through the solution for 30 min. The solvent was then removed *in vacuo* and the residue was redissolved in degassed THF (20 ml). 3.6 ml *t*-BuLi (1.7 M in pentane, 5.8 mmol, 4.3 eq) was slowly added at -78°C and the reaction mixture was then stirred at 0°C for 3 h. Freshly distilled 2-isopropoxy-tetramethyl-dioxaborolane (**4-15**, 2.7 ml, 2.5 g, 13.4 mmol, ρ = 0.92 g/mol, 10 eq) was added at -78°C and the reaction mixture was allowed to warm to rt overnight. The mixture was hydrolyzed at 0°C by addition of 1M aqueous HCl and then diluted with EtOAc. The organic phase was washed twice with 1M aqueous NaOH and once with 1M $NaHCO_3$ solutions, dried over $MgSO_4$, filtered, and the solvent removed *in vacuo*. The crude product was purified by recrystallisation from EtOH to afford 211 g (0.3 mmol, 21%) of compound **4-26** as a colorless solid.

^{1}H-NMR (CD_2Cl_2, 500 MHz, 298 K): δ = 0.88 (t, ^3J=7.1 Hz, 12H), 1.27 (m, 32H), 1.36 (m, 4H), 1.45 (m, 24H), 1.70 (m, 4H), 2.77 (t, ^3J=7.9 Hz, 4H), 7.61 (d, ^4J=1.4 Hz, 2H), 7.96 (d, ^4J=1.3 Hz, 2H), 9.97 (s, 1H) ppm. ^{13}C-NMR (CD_2Cl_2, 125 MHz, 298 K): δ = 14.3, 23.1, 25.3,

29.7, 29.8, 29.9, 30.0, 30.1, 32.3, 32.9, 36.4, 84.2, 122.2, 123.4, 133.2, 133.2, 144.1 ppm. MS (FD, 8 kV) m/z = 755.2 g/mol - calculated for for $C_{48}H_{79}B_2NO_4$: 755.6 g/mol.

7.2.15 Cyclo[bis-(3,6-didodecyl-1,8-di(pyridin-2,6-yl)-9*H*-carbazole)] (4-27)

Porphyrinoid 4-27

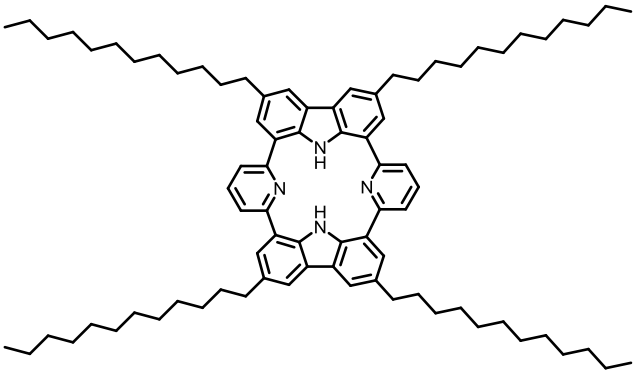

4-27

134.9 mg (0.18 mmol, 1 eq) of 3,6-didodecyl-1,8-bis(4,4,5,5-tetramethyl-1,3,2-dioxaborolan-2-yl)-9*H*-carbazole (**4-26**), 41.8 mg (0.18 mmol, 1 eq) of 2,6-dibromopyridine (**4-17**) and 2 mg (1.8 µmol, 0.01 eq) of $Pd(PPh_3)_4$ were dissolved in toluene (500 ml). EtOH (200 ml) and 2M K_2CO_3 (30 ml, excess) were added to the solution and the reaction mixture was degassed 3 times. The reaction mixture was stirred at 85°C for 15 h. The solvents were removed *in vacuo* and the crude was redissolved in DCM and filtered over 1 cm silica. The crude product was purified by column chromatography hexane : DCM (1:1) to yield 20 mg (17.3 µmol, 10%) of macrocycle **4-27** as a colorless solid.

^{1}H-NMR (CD_2Cl_2, 700 MHz, 298 K): δ = 0.87 (t, ^3J=7.1 Hz, 12H), 1.27 (m, 72H), 1.77 (m, 8H), 2.86 (t, ^3J=7.7 Hz, 8H), 7.39 (d, ^4J=1.7 Hz, 4H), 7.65 (d, ^4J=7.1 Hz, 4H), 7.99 (d, ^4J=1.3 Hz, 4H), 8.00 (t, ^4J=7.8 Hz, 2H), 9.66 (s, 2H) ppm. ^{13}C-NMR (CD_2Cl_2, 176 MHz, 298 K): δ = 14.2, 23.1, 29.7, 29.9, 30.0, 30.1, 32.3, 32.6, 36.3, 120.3, 122.6, 124.4, 124.8, 128.7, 135.0, 136.3, 138.7, 159.5 ppm. MALDI TOF (TCNQ as matrix) m/z = 1157.33 g/mol - calculated: 1156.92 g/mol for $C_{82}H_{116}N_4$. HRESI MS (THF 1:1 MeCN): $[C_{50}H_{52}N_4+H]^+$ m/z = 1157.9232 g/mol – calculated: 1157.9278 g/mol.

7.2.16 Cobalt(II)-cyclo[bis-(3,6-didodecyl-1,8-di(pyridin-2,6-yl)-9*H*-carbazole)] (4-28)

(Cobalt complex 4-28)

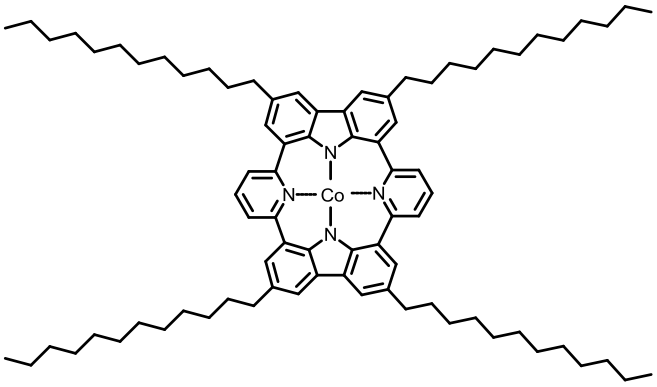

4-28

15 mg (0.013 mmol, 1 eq) of macrocycle **4-27** and 3 mg (0.017 mmol, 1.3 eq) of $Co(OAc)_2$ were put in a microwave-tube and dissolved in 2 ml of dry DMF. The reaction mixture was stirred for 4h in the microwave at 170°C and 300 W. It was cooled to rt and poured into ice-cold water. The precipitate was filtered of and dried under vacuum to afford 10 mg (8.2 µmol, 63 %) of cobalt complex **4-28** as a yellow solid.

MALDI TOF (TCNQ as matrix) m/z = 1213.79 g/mol - calculated: 1213.85 g/mol for $C_{82}H_{114}CoN_4$.

7.2.17 3,6-Di-*tert*-butyl-1,8-diiodo-9*H*-carbazole (4-35)

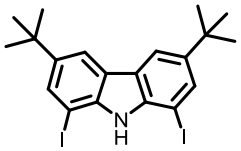

4-35

According literature procedure[155] 100 mg (0.23 mmol, 1 eq) 3,6-di-*tert*-butyl-9-carbazole (**4-13**) was dissolved in 3.5 ml acetic acid. 1 ml H_2O, 0.1 ml H_2SO_4, 26.1 mg (0.115 mmol, 0.5 eq) HIO_4*$2H_2O$ and 58.4 mg (0.23 mmol, 1 eq) I_2 were added and the reaction was heated to 80°C for 18.5 h. The reaction mixture was allowed to cool down to rt and was poured into H_2O. The aqueous layer was extracted three times with ethyl acetate. The organic layer was washed with $NaHCO_3$ (sat.), $Na_2S_3O_3$ (sat.) and brine, it was dried over $MgSO_4$, filtered and the solvent was evaporated. The crude product was recrystallized from hot EtOH to yield 62 mg (0.12 mmol, 50%) of 3,6-di-*tert*-butyl-1,8-diiodo-9*H*-carbazole (**4-**

35) as a yellow solid. ^{1}H-NMR (CD_2Cl_2, 300 MHz, 298 K): δ = 1.44 (s, 18H), 7.86 (d, ^{3}J=*7.9 Hz*, 2H), 7.89 (s, 1H), 8.06 (d, ^{3}J=*8.0 Hz*, 2H) ppm. ^{13}C-NMR (CD_2Cl_2, 75 MHz, 298 K): δ = 32.0, 35.1, 76.0, 117.6, 124.5, 33.21, 139.7, 145.6 ppm. MS (FD, 8 kV) m/z = 531.4 g/mol – calculated: 530.9 g/mol for $C_{20}H_{23}I_2N$. Mp 166°C (from EtOH).
The analytic data are in agreement with the literature.[155]

7.2.18 2,5-Bis(4,4,5,5-tetramethyl-1,3,2-dioxaborolan-2-yl)-1*H*-pyrrole (4-37)

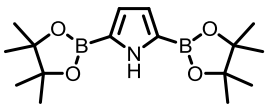

4-37

According to the literature[257] 2.01 g (8 mmol, 1.1 eq) bispinacolatodiboronate and 10 mg (0.023 mmol, 0.003 eq) of 4,4′-di-*tert*-butylbipyridine (dtbpy) were put into a flask and were transferred into a glovebox. In here 10 mg (0.012 mmol, 0.0015 eq) of the catalyst $[IrCl(COD)]_2$ and 15 ml octane were added. The flask was then transferred outside the glovebox and 500 mg (7.5 mmol, 1 eq) of freshly distilled pyrrole was added under argon. The reaction mixture was heated to 80°C for 16.5 h. The solvent was removed *in vacuo* and the crude product was dissolved in hot heptane. The hot solution was filtered and was allowed to crystallize at 4°C. 2,5-Bis(4,4,5,5-tetramethyl-1,3,2-dioxaborolan-2-yl)-1*H*-pyrrole (**4-37**) was recrystallized again from hot heptane to yield 1.37 g (4.3 mmol, 60%) of as colorless crystals. ^{1}H-NMR (CD_2Cl_2, 300 MHz, 298 K): δ = 1.30 (s, 24H), 6.70 (d, ^{3}J=*2.3 Hz*, 2H), 9.27 (s, 1H,-NH) ppm. ^{13}C-NMR (CD_2Cl_2, 75 MHz, 298 K): δ = 24.9, 84.1, 120.4 ppm. Mp 194°C.The analytic data are in agreement with the literature.[257]

7.2.19 Cyclo[bis-(3,6-di-*tert*-butyl-1,8-di(1*H*-pyrrol-2,5-yl)-9*H*-carbazole)] (4-38)

(Porphyrinoid 4-38)

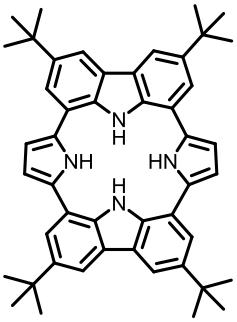

4-38

396.4 mg (0.74 mmol, 1 eq) of 3,6-di-*tert*-butyl-1,8-diiodo-9*H*-carbazole (**4-35**), 239.3 mg (0.81 mmol, 1 eq) of 2,5-bis(4,4,5,5-tetramethyl-1,3,2-dioxaborolan-2-yl)-1*H*-pyrrole (**4-37**) and 9 mg (5 µmol, 0.01 eq) of $Pd(PPh_3)_4$ were dissolved in toluene (1000 ml). EtOH (400 ml) and 2M K_2CO_3 (60 ml, excess) were added to the solution and the reaction mixture was degassed 3 times. The reaction mixture was stirred at 85°C for 17h. The solvents were removed *in vacuo*, the crude was redissolved in EtOAc and filtered over 1 cm silica. The crude product was purified by column chromatography using hexane : EtOAc (3:1) as eluent. Additionally, the crude was suspended in hexane and the precipitated was filtered off to yield 46 mg (0.04 mmol, 10%) of macrocycle **4-18** as a greenish solid.

^{1}H-NMR (THF-d_8, 700 MHz, 298 K): δ = 1.53 (s, 36H), 6.73 (d, ^3J=2.22 Hz, 4H), 7.72 (d, ^4J=1.80 Hz, 4H), 8.07 (t, ^4J=1.80 Hz, 4H), 10.53 (s, 2H), 11.13 (s, 2H) ppm. ^{13}C-NMR (THF-d_8, 176 MHz, 298 K): δ = 32.4, 35.4, 109.1, 115.4, 118.6, 122.8, 126.3, 133.8, 136.9, 143.7 ppm. ^{1}H^{15}N-NMR (THF-d_8, 700MHz, 298K): δ = -231.35 (pyrrole), -271.68 (carbazole) ppm. MALDI TOF (TCNQ as matrix) m/z = 684.36 g/mol - calculated: 684.42 g/mol for $C_{48}H_{52}N_4$. HRESI MS (THF 1:1 MeCN): $[C_{50}H_{52}N_4+H]^+$ m/z = 685.4290 g/mol - calculated 685.4270 g/mol.

7.2.20 3,6-Di-*tert*-butyl-1,8-bis((trimethylsilyl)ethynyl)-9*H*-carbazole (4-43)

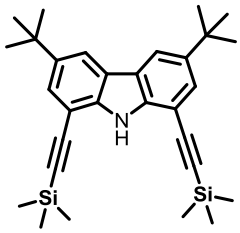

4-43

According to the literature procedure[276] 100 mg (0.19 mmol, 1 eq) of 3,6-di-*tert*-butyl-1,8-diiodo-9*H*-carbazole (**4-35**), 2 mg (9.5 µmol, 0.05 eq) $Pd(OAc)_2$, 2 mg (9.5 µmol, 0.05 eq) CuI and 7.5 mg (28.5 µmol, 0.15 eq) PPh_3 were dissolved in 2 ml dry THF under argon atmosphere. To this solution 8 ml diisopropylamine were added and the reaction mixture was heated to 60°C. Then 60 µl (46 mg, 0.47 mmol, 2.5 eq) TMSA were added and the reaction was stirred for 1.5 h at this temperature. The reaction was stopped and the solvent removed *in vacuo*. The crude product was purified by column chromatography using hexane : DCM (9 : 1) to afford 51 mg (0.11 mmol, 57 %) of 3,6-di-*tert*-butyl-1,8-bis((trimethylsilyl)ethynyl)-9*H*-carbazole (**4-43**) as a yellowish solid.

^{1}H-NMR (CD_2Cl_2, 300 MHz, 298 K): δ = 0.34 (s, 18H), 1.43 (s, 18H), 7.60 (d, ^4J=1.8 Hz, 2H), 8.09 (d, ^4J=1.8 Hz, 2H), 8.39 (s, 1H) ppm. ^{13}C-NMR (CD_2Cl_2, 75 MHz, 298 K): δ = 0.5, 32.2, 35.3, 99.4, 101.9, 105.9, 118.4, 123.9, 127.4, 139.8, 143.7 ppm. MS (FD, 8 kV) m/z = 470.9 g/mol - calculated for $C_{30}H_{41}NSi_2$: 471.3 g/mol.

The analytic data are in agreement with the literature.[276]

7.2.21 3,6-Di-*tert*-butyl-1,8-diethynyl-9*H*-carbazole (4-44)

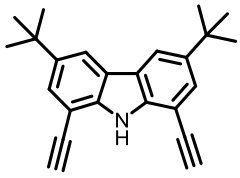

4-44

27.1 mg (57.5 µmol, 1 eq) of 3,6-di-*tert*-butyl-1,8-bis((trimethylsilyl)ethynyl)-9*H*-carbazole (**4-43**) was dissolved in 5 ml dry THF at rt under argon atmosphere. To this solution 0.2 ml (0.20 mmol, 3.4 eq) of a 1M TBAF solution (in THF) were added. The deprotection was followed by TLC chromatography and was completed after 10 min. The reaction was stopped and EtOAc was added and extracted with water. The organic layer was washed

with brine, dried over $MgSO_4$, filtered and the solvent removed *in vacuo*. The crude product was purified by column chromatography using hexane : DCM (4 : 1) to afford 16 mg (48.8 µmol, 85 %) of 3,6-di-*tert*-butyl-1,8-diethynyl-9*H*-carbazole (**4-44**) as a yellowish solid.

^{1}H-NMR (CD_2Cl_2, 300 MHz, 298K): δ = 1.44 (s, 18H), 3.52 (d, 2H), 7.65 (d, ^4J=*1.8 Hz*, 2H), 8.13 (d, ^4J=*1.8 Hz*, 2H), 8.54 (s, 1H) ppm. ^{13}C-NMR (CD_2Cl_2, 75 MHz, 298K): δ = 32.0, 35.0, 80.5, 81.7, 104.3, 118.5, 123.6, 127.9, 139.5, 143.3. MS (FD, 8 kV) m/z = 328.4 g/mol - calculated for $C_{24}H_{25}N$: 327.2 g/mol. Mp 87°C.

The analytic data are in agreement with the literature.[276]

7.2.22 4-Methylbenzenesulfonyl azide (4-45)

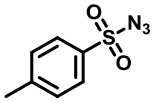

4-45

According to the literature procedure[277] 1 g (5.3 mmol, 1 eq) of 4-methylbenzene-1-sulfonyl chloride (**4-49**) was dissolved in 16 ml acetone. To this solution 16 ml H_2O were added and the reaction mixture was cooled to 0°C. Then 342 mg (5.3 mmol, 1 eq) NaN_3 were added and the reaction was stirred for 2 h at this temperature. Acetone was removed *in vacuo* and the aqueous layer was extracted with EtOAc which was again removed *in vacuo*. 975 mg (4.9 mmol, 94%) of 4-methylbenzenesulfonyl azide (**4-45**) was obtained as a colorless liquid which was stored at -30°C.

^{1}H-NMR (CD_2Cl_2, 300 MHz, 298 K): δ = 1.44 (s, 18H), 3.52 (d, 2H), 7.65 (d, ^4J=*1.8 Hz*, 2H), 8.13 (d, ^4J=*1.8 Hz*, 2H), 8.54 (s, 1H) ppm. ^{13}C-NMR (CD_2Cl_2, 75 MHz, 298 K): δ = 21.9, 127.8, 130.7, 135.8, 146.9 ppm.

The analytic data are in agreement with the literature.[277]

7.2.23 1,8-Diazido-3,6-di-*tert*-butyl-9*H*-carbazole (4-46)

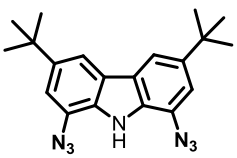

4-46

4.9 ml *n*-BuLi (1.6 M in hexane, 7.9 mmol, 1.1 eq) was added at 0°C to a solution of 1,8-dibromo-3,6-di-*tert*-butyl-9*H*-carbazole (**4-14**, 3.1 g, 7.2 mmol, 1 eq) in degassed THF (100 ml). After stirring at this temperature for 1 h, the reaction mixture was allowed to warm to rt while CO_2 gas was bubbled through the solution for 20 min. The solvent was then removed *in vacuo* and the residue was redissolved in degassed THF (100 ml). 19.2 ml *t*-BuLi (1.7 M in pentane, 30.8 mmol, 4.3 eq) was slowly added at -78°C and the reaction mixture was then stirred at 0°C for 30 min. 11.3 g (57.3 mmol, 8 eq) 4-methylbenzenesulfonyl azide (**4-45**) was added at -78°C and the reaction mixture cooled at this temperature for 16 h. An aqueous solution of NH_4Cl was added and the reaction was allowed to warm to rt. The mixture was extracted with EtOAc and the organic layer washed with water and brine, dried over $MgSO_4$, filtered, and the solvent removed *in vacuo*. The crude product was purified by column chromatography hexane : DCM (3 : 1) and subsequent crystallisation from hot hexane afforded 743 mg (2.1 mmol, 30%) of 1,8-diazido-3,6-di-*tert*-butyl-9*H*-carbazole (**4-46**) as a yellow solid.

^{1}H-NMR (CD_2Cl_2, 300 MHz, 298 K): δ = 1.46 (s, 18H), 7.29 (d, ^4J=*1.5 Hz*, 2H), 7.87 (d, ^4J=*1.5 Hz*, 2H), 8.17 (s, 1H) ppm. ^{13}C-NMR (CD_2Cl_2, 75 MHz, 298 K): δ = 32.0, 35.3, 113.1, 113.7, 123.7, 124.9, 130.0, 144.6 ppm. MS (FD, 8 kV) m/z = 360.7 g/mol - calculated for $C_{20}H_{23}N_7$: 361.2 g/mol. Mp 140°C (decomposition).

7.2.24 Cyclo[bis-(3,6-di-*tert*-butyl-1,8-di(1,2,3-triazol-1,4-yl)-9*H*-carbazole)] (4-38)

(Porphyrinoid 4-48)

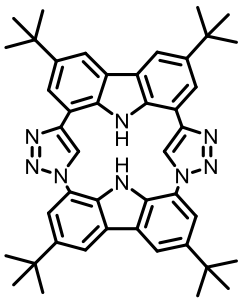

4-48

154.88 (0.43 mmol, 1 eq) 1,8-diazido-3,6-di-*tert*-butyl-9*H*-carbazole (**4-46**), 140.31 (0.43 mmol, 1 eq) 3,6-di-tert-butyl-1,8-diethynyl-9*H*-carbazole (**4-44**), 85 mg (0.43 mmol, 1eq) sodium ascorbate, 57 mg (0.11 mmol, 025 eq) TBTA and (0.11, 0.25 eq) copper(II) sulfate pentahydrate were dissolved in 9 ml dry THF under argon atmosphere. To this solution

0.9 ml triethylamine were added and the reaction was heated to 60°C and stirred for 3 d. Then 5 ml aqueous saturated NaN_3 solution was added and the reaction mixture was stirred additionally for 2 h at 60°C. The reaction was finally quenched with 5 ml aqueous saturated NH_4Cl solution. The aqueous and organic phases were separated and the organic layer concentrated *in vacuo*. The resulting suspension was precipitated in MeOH and filtered to afford 50 mg (0.07 mmol, 17%) of macrocycle **4-48** as a colorless solid.

^{1}H-NMR (THF-d_8, 700 MHz, 298 K): δ = 1.54 (s, 18H), 1.56, (s, 18H), 8.10 (d, ^4J =*1.8 Hz*, 2H), 8.18 (d, ^4J =*1.7 Hz*, 2H), 8.24 (d, ^4J =*1.8 Hz*, 2H), 8.41 (d, ^4J =*1.7 Hz*, 2H), 9.48 (s, 1H), 9.82 (s, 2H), 10.25 (s, 1H) ppm. ^{13}C-NMR (THF-d_8, 176 MHz, 298K): δ = 32.4, 32.6, 35.8, 36.1, 116.1, 118.2, 118.5, 118.8, 122.7, 124.4, 126.8, 128.6, 133.5, 139.4, 144.8, 146.5, 146.6 ppm. HRESI MS (THF 1:1 MeCN): $[C_{44}H_{48}N_8+H]^+$ m/z = 689.4099 g/mol - calculated 689.4080 g/mol. Mp > 400°C.

7.2.25 1-Azido-3,6-di-*tert*-butyl-8-(4-(3,6-di-*tert*-butyl-8-ethynyl-9-carbazol-1-yl)-1,2,3-triazol-1-yl)-9-carbazole (4-50)

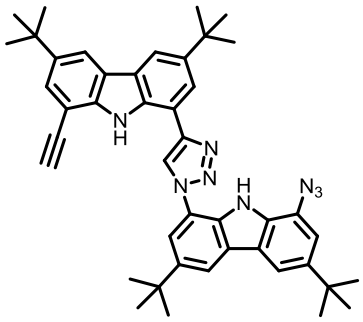

4-50

^{1}H-NMR (CD_2Cl_2, 250 MHz, 298 K): δ = 1.48 (s, 9H), 1.50 (s, 9H), 1.55 (s, 9H), 1.57 (s, 9H), 7.37 (d, ^4J=*1.5 Hz*, 1H), 7.71 (d, ^4J=*1.8 Hz*, 1H), 7.81 (d, ^4J=*1.5 Hz*, 1H), 7.91 (d, ^4J=*1.8 Hz*, 1H), 7.98 (d, ^4J=*1.3 Hz*, 1H), 8.19 (d, ^4J=*1.5 Hz*, 1H), 8.20 (d, ^4J=*1.8 Hz*, 1H), 8.22 (d, ^4J=*1.4 Hz*, 1H), 8.78 (s, 1H), 9.94 (s, 1H), 10.62 (s, 1H) ppm. MS (FD, 8 kV) m/z = 689.2 g/mol - calculated for $C_{44}H_{48}N_8$: 688.4 g/mol.

7.2.26 8,8'-(1,1'-(3,6-Di-*tert*-butyl-9*H*-carbazole-1,8-diyl)bis(1,2,3-triazole-4,1-diyl))bis(3,6-di-*tert*-butyl-1-ethynyl-9*H*-carbazole) (4-51)

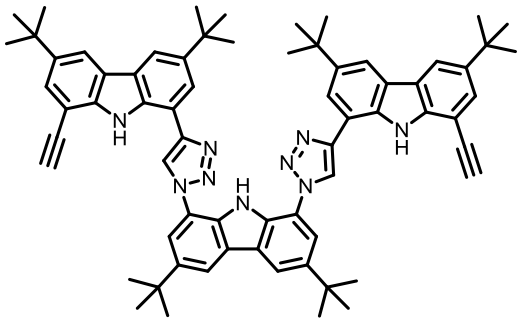

4-51

^{1}H-NMR (CD_2Cl_2, 250 MHz, 298 K): δ = 1.48 (s, 18H), 1.55 (s, 18H), 1.60 (s, 18H), 3.48 (s, 2H), 7.68 (d, ^4J=*1.8 Hz*, 2H), 7.87 (d, ^4J=*1.5 Hz*, 2H), 7.92 (d, ^4J=*1.8 Hz*, 2H), 8.20 (m, 4H), 8.36 (d, ^4J=*1.5 Hz*, 2H), 8.78 (s, 1H), 10.56 (s, 2H), 10.89 (s, 1H) ppm. MS (FD, 8 kV) m/z = 1017.3 g/mol - calculated for $C_{68}H_{73}N_9$: 1015.6 g/mol.

7.2.27 3,6-Dibromobenzene-1,2-diamine (5-14)

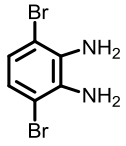

5-14

According to the literature procedure[340] 5 g (17 mmol, 1eq) of 4,7-dibromo-2,1,3-benzothiadiazole (**5-13**) were suspended in 170 ml EtOH and cooled to 0°C. To this suspension 11.4 g (300 mmol, 17.6 eq) $NaBH_4$ were added portionwise and the reaction mixture was stirred 16h at rt. EtOH was removed *in vacuo*, to the resulting slurry 100 ml H_2O were added and the crude product was extracted wit Et_2O. The organic layer was washed with brine, dried over MgSO4, filtered and the solvent removed *in vacuo*. The resulting solid was dried in HV to give 4.1 g (15.6 mmol, 92%) of 3,6-dibromobenzene-1,2-diamine (**5-14**).

^{1}H-NMR (CD_2Cl_2, 300 MHz, 298 K): δ = 3.94 (s, 4H), 6.84 (s, 2H) ppm. ^{13}C-NMR (CD_2Cl_2, 75 MHz, 298 K): δ = 109.7, 123.3, 134.1 ppm. Mp 91°C.

The analytic data are in agreement with the literature.[340]

7.2.28 1,4,7,10,13,16-Hexabromodiquinoxalino[2,3-*a*:2',3'-c]phenazine (5-16)

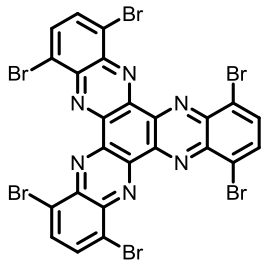

5-16

4.5 g (17 mmol, 3 eq) 3,6-dibromobenzene-1,2-diamine ***5-14*** and 1.8 g 85.6 mmol, 1 eq) hexaketocyclohexane octahydrate ***5-15*** were dissolved in 60 ml EtOH and heated to reflux for 15 h. The reaction mixture was cooled to rt and filtered over a silica frit. The green solid was suspended in 30% HNO_3 and heated to reflux for 3 h. The solid was again filtered off and dried at HV to give 4.1 g (4.8 mmol, 85%) of compound ***5-16***.

^{1}H-NMR (D_2SO_4, 250 MHz, 298 K): δ = 8.84 (s, 6H). Maldi-TOF (TCNQ): m/z = 854.77 g/mol – calculated: 851.58 g/mol for $C_{24}H_6Br_6N_6$. Mp > 400°C.

The analytic data are in agreement with the literature.[144]

7.2.29 Hexa-*tert*-butyl 2,2',2'',2''',2'''',2'''''-(diquinoxalino[2,3-:2',3'-c]phenazine-1,4,7,10,13,16-hexayl)hexakis(1-pyrrole-1-carboxylate) (5-18)

(HPHATPN 5-18)

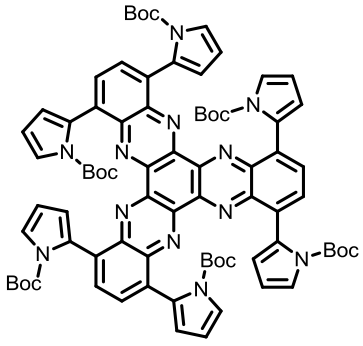

5-18

1.12 g (1.32 mmol, 1 eq) of 1,4,7,10,13,16-hexabromodiquinoxalino[2,3-a:2',3'-c]phenazine (***5-16***) 2.78 g (13.19 mmol, 10 eq) (1-(*tert*-butoxycarbonyl)-1*H*-pyrrol-2-yl)boronic acid (***5-17***) and 152 mg (0.13 mmol, 0.1 eq) $Pd(PPh_3)_4$ were dissolved in 50 ml toluene under an argon atmosphere. To this solution 20 ml of EtOH and 20 ml of a 2M K_2CO_3 solution were added and the reaction mixture was heated to 85°C for 20 h. The

solvents were concentrated *in vacuo* and the aqueous layer was extracted with DCM. The organic layer was washed with H_2O and brine, dried over $MgSO_4$, filtered and the solvents removed *in vacuo*. The crude product was purified by column chromatography using hexane : DCM : ethyl acetate (1 : 1 : 0.1) to give 1.13 g (0.82 mmol, 62 %) of compound ***5-18*** as a purple solid.

^{1}H-NMR (CD_2Cl_2, 300 MHz, 298 K): δ = 0.91 (s, 54H), 6.46 (t, ^3J=*3.3 Hz*, 6H), 6.67 (dd, ^3J=*3.3 Hz*, 6H), 7.45 (dd, ^3J=*3.3 Hz*, 6H), 7.89 (s, 6H) ppm. ^{13}C-NMR (CD_2Cl_2, 75 MHz, 298 K): δ = 27.5, 83.0, 110.7, 116.9, 124.6, 131.0, 131.5, 134.3, 142.3, 143.1, 149.4 ppm. Mp 200°C (decomposition). The analytic data are in agreement with the literature.[144]

7.2.30 1,4,7,10,13,16-Hexa(1*H*-pyrrol-2-yl)diquinoxalino[2,3-*a*:2',3'-c]phenazine (5-19)

(HPHATN *5*-19)

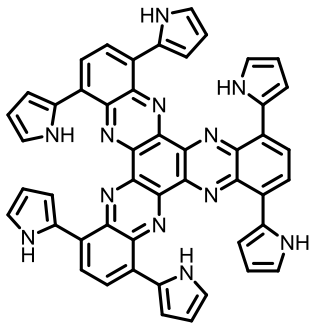

***5*-19**

A thin layer of 2.570 g (1.87 mmol) of HPHATN ***5*-18** dissolved in THF was prepared into a flask. Then the flask was heated to 180°C under vacuum in an oil bath for 60 min. The purple color of compound ***5*-18** turned to dark lavender and 1.331 g (1.72 mmol; 92%) of HPHATN ***5*-19** was obtained.

^{1}H-NMR (DMSO-d_6, 500 MHz, 298 K): δ = 6.33 (s, 6H), 6.85 (s, 6H), 7.19 (s, 6H), 8.36 (s, 6H), 11.74 (s, 6H) ppm. ^{13}C-NMR (DMSO-d_6, 125 MHz, 298 K): δ = 108.6, 109.7, 120.7, 126.7, 126.8, 128.7, 131.1, 138.9 ppm. Maldi-TOF (TCNQ): m/z = 772.33 g/mol – calculated: 774.27 g/mol for $C_{48}H_{30}N_{12}$.[144]

The analytic data are in agreement with the literature.[144]

7.2.31 3,4,5-Tris(dodecyloxy)benzaldehyde (5-20)

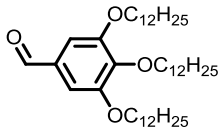

5-20

According to the literature procedure[342] 1.0 g (5.8 mmol, 1 eq) 3,4,5-trihydroxybenzaldehyde (***5-38***) and 8.7 g (8.5 ml, 35 mmol, 6 eq) 1-bromododecane (***5-39***) were dissolved in 35 ml DMF. To this solution 2.4 g K_2CO_3 (17.4 mmol, 3 eq) and 60 mg KI (0.4 mmol, 0.06 eq) were added. The reaction mixture was heated to 70°C and stirred for 18 h. After cooling to rt the reaction was quenched with water and extracted with DCM. The organic layer was dried over $MgSO_4$, filtered and the solvent removed *in vacuo*. The resulting crude product was purified by column chromatography using hexane : DCM (3 : 1) as eluent, to obtain 3.5 g (5.3 mmol, 92%) of 3,4,5-tris(dodecyloxy)benzaldehyde (***5-20***) as a colorless solid.

^{1}H-NMR (CD_2Cl_2, 300 MHz, 298 K): δ = 0.88 (m, 9H), 1.28 (m, 48H), 1.38 (m, 6H), 1.72 (m, 6H), 4.03 (m, 6H), 7.08 (s, 2H), 9.82 (s, 1H) ppm. ^{13}C-NMR (CD_2Cl_2, 75 MHz, 298 K): δ = 14.3, 23.1, 26.4, 26.5, 29.7, 29.8, 29.8, 29.9, 30.0, 30.1, 30.1, 30.1, 30.2, 30.8, 32.3, 69.6, 73.9, 107.9, 132.0, 144.3, 154.3, 191.4 ppm. HRESI MS (THF 1:1 MeCN): $[C_{43}H_{78}O_4+Na]^+$ m/z = 681.5811 g/mol – calculated: 681.5798 g/mol. Mp 52°C.

7.2.32 4-Dodecylbenzaldehyde (5-21)

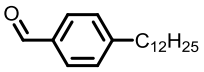

5-21

According to the literature procedure[335] 1.8 g (5.4 mmol, 1 eq) 1-bromo-4-dodecylbenzene (***5-34***) was dissolved in 10 ml dry THF under argon atmosphere and was cooled to -78°C. To this solution 8.5 ml (13.5 mmol, 1.6 M in hexane, 2.5 eq) *n*-BuLi was added slowly and stirred for 1 h at this temperature. Finally, 1 ml (13.5 mmol, 2.5 eq) DMF (dry) was added and the reaction mixture was allowed to warm to rt overnight. The reaction mixture was hydrolyzed at 0°C by the addition of 1M aqueous HCl and then diluted with EtOAc. The organic phase was washed twice with 1M aqueous NaOH and once with 1M $NaHCO_3$ solutions, dried over $MgSO_4$, filtered, and the solvent removed *in vacuo*. The crude

product was purified by column chromatography using hexane : EtOAc (100 : 2) as eluent to give 1.0 g (3.65 mmol, 70%) of 4-dodecylbenzaldehyde (***5-21***) as a colorless liquid.

^{1}H-NMR (CD_2Cl_2, 300 MHz, 298 K): δ = 0.87 (m, 3H), 1.29 (m, 18H), 1.63 (m, 2H), 2.69 (t, ^{3}J=*7.6 Hz*, 2H), 7.34 (d, ^{3}J=*8.0 Hz*, 2H), 7.77 (d, ^{3}J=*8.0 Hz*, 2H), 9.65 (s, 1H) ppm. ^{13}C-NMR (CD_2Cl_2, 75 MHz, 298 K): δ = 14.3, 23.1, 29.6, 29.7, 29.8, 29.9, 30.0, 30.1, 31.5, 32.3, 36.5, 129.4, 130.0, 134.9, 150.9, 193.2 ppm. HRESI MS (THF 1:1 MeCN): $[C_{19}H_{20}O]^+$ m/z = 275.2375 g/mol – calculated: 275.2375 g/mol.

7.2.33 4-(2-Hexyldecyl)benzaldehyde (5-23)

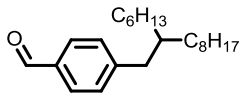

5-23

5 g (22 mmol, 1 eq) 2-(4-Bromophenyl)-1,3-dioxolane (***5-36***) and 200 mg (0.29 mmol, 10%mol) 1,1'-bis(diphenylphosphino)ferrocene]dichloronickel(II) were suspended in 200 ml anhydrous THF. A freshly prepared Grignard solution, made from 0.8 g magnesium (33 mmol, 1.5 eq) and 10 g (33 mmol, 1.5 eq) 7-(bromomethyl)pentadecane in 200 mL anhydrous THF, were transferred *via* cannula into the suspension. The mixture was stirred at 45 °C for 12 h. The solvent was removed *in vacuo* and the crude product was purified by column chromatography using hexane as eluent to give 0.8 g (2.4 mmol, 10% over two steps) of 4-(2-hexyldecyl)benzaldehyde (***5-23***) as a colorless liquid.

^{1}H-NMR (CD_2Cl_2, 300 MHz, 298 K): δ = 0.89 (m, 6H), 1.26 (m, 24H), 1.68 (m, 1H), 2.64 (d, ^{3}J=*7.2 Hz*, 2H), 7.35 (d, ^{3}J=*8.1 Hz*, 2H), 7.80 (d, ^{3}J=*8.1 Hz*, 2H), 9.96 (s, 1H) ppm. ^{13}C-NMR (CD_2Cl_2, 75 MHz, 298 K): δ = 14.2, 14.3, 23.0, 23, 1, 26.9, 29.7, 29.9, 30.3, 32.2, 32.3, 33.5, 33.6, 40.0, 41.2, 129.9, 130.2, 134.8, 150.1, 192.2 ppm. MS (FD, 8 kV) m/z = 330.5 g/mol - calculated for $C_{23}H_{38}O$: 330.3 g/mol.

7.2.34 1-Dodecyl-4-ethynylbenzene (5-35)

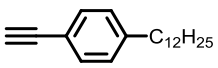

5-35

1.6 g (4.9 mmol, 1 eq) 1-Bromo-4-dodecylbenzene (***5-34***) was dissolved in 14 ml anhydrous THF under argon atmosphere. To this solution 16 ml diisopropylamine, 30 mg (25 µmol,

5%mol) $Pd(PPh_3)_4$ and 10 mg (52 µmol, 10%mol) CuI were added. The reaction mixture was heated to 60°C and 1.4 ml ethynyltrimethylsilane was added through a septum. The reaction was strirred for 12 h at this temperature. The reaction mixture was filtered over a silica frit and the solvent removed *in vacuo*. The crude product was redissolved in THF and 6 ml of a 1M TBAF solution was added and stirred for 1 h at rt. The solvent was again removed *in vacuo* and the crude product was purified by column chromatography (hexane) affording 330 mg (1.22 mmol, 25%) of 1-dodecyl-4-ethynylbenzene (***5-35***) as a colorless liquid.

^{1}H-NMR (CD_2Cl_2, 300 MHz, 298 K): δ = 0.88 (t, ^3J=*6.4 Hz*, 3H), 1.26 (m, 18H), 1.59 (m, 2H), 2.60 (t, ^3J=*8.0 Hz*, 2H), 3.08 (s, 1H), 7.16 (d, ^3J=*8.2 Hz*, 2H), 7.37 (d, ^3J=*8.2 Hz*, 2H) ppm. ^{13}C-NMR (CD_2Cl_2, 75 MHz, 298 K): δ = 14.3, 23, 1, 29.6, 29.7, 29.8, 29.9, 30.0, 30.1, 31.6, 32.3, 36.2, 76.7, 84.1, 119.5, 128.8, 132.3, 144.6 ppm. MS (FD, 8 kV) m/z = 270.2 g/mol - calculated for $C_{20}H_{30}$: 270.5 g/mol.

7.2.35 4-((4-Dodecylphenyl)ethynyl)benzaldehyde (5-22)

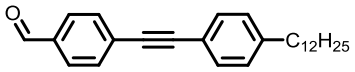

5-22

307.5 mg (1.14 mmol, 1 eq) 1-Dodecyl-4-ethynylbenzene (***5-35***) and 209.3 mg (1.14 mmol, 1 eq) 4-bromobenzaldehyde (***5-26***) were dissolved in 4 ml anhydrous THF under argon atmosphere. To this solution 16 ml diisopropylamine, 15 mg (13 µmol, 10%mol) $Pd(PPh_3)_4$ and 5 mg (26 µmol, 20%mol) CuI were added. The reaction mixture was heated to 60°C and stirred for 3 h at this temperature. The reaction mixture was filtered over a frit and the solvent removed *in vacuo*. The crude product was purified by column chromatography using hexane : DCM (2 : 1) as eluent, affording 255 mg (0.68 mmol, 60%) of 4-((4-dodecylphenyl)ethynyl)benzaldehyde (***5-22***) as a colorless liquid.

^{1}H-NMR (CD_2Cl_2, 300 MHz, 298 K): δ = 0.88 (t, ^3J=*7.0 Hz*, 3H), 1.27 (m, 18H), 1.61 (m, 2H), 2.63 (t, ^3J=*8.0 Hz*, 2H), 7.20 (d, ^3J=*8.2 Hz*, 2H), 7.47 (d, ^3J=*8.2 Hz*, 2H), 7.67 (d, ^3J=*8.2 Hz*, 2H), 7.85 (d, ^3J=*8.2 Hz*, 2H), 10.00 (s, 1H) ppm. ^{13}C-NMR (CD_2Cl_2, 75 MHz, 298 K): δ = 14.3, 23.1, 29.6, 29.7, 29.8, 29.9, 30.0, 30.1, 31.6, 32.3, 36.2, 88.3, 93.9, 119.9, 129.0, 129.8, 130.0, 132.0, 132.3, 135.8, 144.9, 191.6 ppm. MS (FD, 8 kV) m/z = 374.6 g/mol - calculated for $C_{27}H_{34}O$: 374.6 g/mol.

7.2.36 4-((3,4,5-Tris(decyloxy)phenyl)ethynyl)benzaldehyde (5-24)

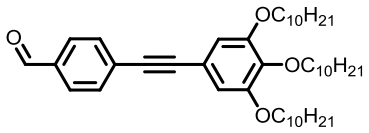

5-24

382 mg (0.67 mmol, 0.98 eq) 1,2,3-Tris(decyloxy)-5-ethynylbenzene (***5-40***), 126 mg (0.68 mmol, 1 eq) 4-bromobenzaldehyde (***5-26***), 60 mg (51 µmol, 10%mol) $Pd(PPh_3)_4$ and 30 mg (158 µmol, 20%mol) CuI were dissolved in 5 ml anhydrous THF and 20 ml diisopropylamine. The reaction mixture was heated to 60°C and stirred for 2 h at this temperature. The reaction mixture was filtered over a frit and the solvent removed *in vacuo*. The crude product was purified by column chromatography using hexane : EtOAc (6 : 1) as eluent, affording 355 mg (77%, 0.53 mmol) of compound ***5-24*** as a colorless liquid.

^{1}H-NMR (CD_2Cl_2, 300 MHz, 298 K): δ = 0.88 (t, ^3J=*6.6 Hz*, 9H), 1.29 (m, 42H), 1.79 (m, 6H), 3.93 (dt, ^3J=*6.5 Hz*, 6H), 6.77 (s, 2H), 7.66 (d, ^3J=*8.3 Hz*, 2H), 7.85 (d, ^3J=*8.3 Hz*, 2H), 10.00 (s, 1H) ppm. ^{13}C-NMR (CD_2Cl_2, 75 MHz, 298 K): δ = 14.3, 23.1, 26.5, 29.7, 29.8, 30.0, 30.1, 30.1, 30.2, 30.7, 32.3, 32.4, 69.5, 73.9, 89.6, 94.2, 110.5, 117.1, 129.8, 129.9, 132.3, 135.9, 136.0, 153.5, 191.6 ppm. HRESI MS (THF 1:1 MeCN): $[C_{45}H_{70}O_4+Na]^+$ m/z = 697.5192 g/mol – calculated 697.5172 g/mol.

7.2.37 4-(3-Hexylthiophen-2-yl)benzaldehyde (5-25)

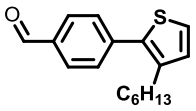

5-25

1.4 g (8.15 mmol, 1.5 eq) 2-(3-Hexylthiophen-2-yl)-4,4,5,5-tetramethyl-1,3,2-dioxaborolane (***5-41***), 1 g (5.43 mmol, 1 eq) 4-bromobenzaldehyde (***5-26***), 300 mg (26 µmol, 5%mol) $Pd(PPh_3)_4$ were dissolved in 10 ml toluene under argon atmosphere. To this solution 5 ml EtOH and 5 ml 2M K_2CO_3 solution were added and the reaction was heated to 85°C for 16 h. The solvents were reduced *in vacuo* and DCM was added to the residue. The organic layer was extracted with water and washed with brine, dried over $MgSO_4$, filtered and the solvent removed *in vacuo*. The crude product was purified by column chromatography using hexane : DCM (3 : 1) as eluent to afford 817 mg (3.00 mmol, 55%) of 4-(3-hexylthiophen-2-yl)benzaldehyde (***5-25***) as a yellow liquid.

^{1}H-NMR (CD_2Cl_2, 300 MHz, 298 K): δ = 0.89 (m, 3H), 1.34 (m, 6H), 1.65 (m, 2H), 2.643 (t, ^3J=7.8 Hz, 2H), 7.02 (s, 1H), 7.35 (s, 1H), 7.75 (d, ^3J=8.3 Hz, 2H), 7.85 (d, ^3J=8.4 Hz, 2H), 9.97 (s, 1H) ppm. ^{13}C-NMR (CD_2Cl_2, 75 MHz, 298 K): δ = 14.2, 23.0, 29.4, 30.8, 30.9, 32.1, 121.1, 126.1, 126.9, 130.7, 135.5, 140.6, 142.5, 145.4, 191.6 ppm. HRESI MS (THF 1:1 MeCN): $[C_{17}H_{20}OS+H]^+$ m/z = 273.1319 g/mol – calculated 273.1313 g/mol.

7.2.38 General procedure for the preparation of HPHATN 5-27 to 5-33

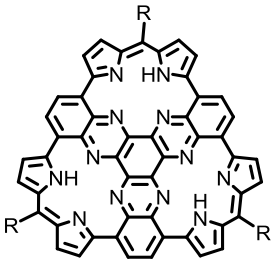

HPHATN **5-19** and the corresponding aldehydes **5-20** to **5-26** (4.5 eq) were suspended in 4 ml DCM and 2 ml THF. To this solution 0.5 ml TFA were added and the reaction mixture was degassed. The compounds were reacted under microwave irradiation (3 x 6 h, 85°C, 50 W). The reaction mixture was concentrated *in vacuo* and the crude product was precipitated from MeOH. The solid was filtered off and purified by Soxhlet extraction with acetone affording the corresponding trinuclear compound **5-27** to **5-33**. Note that all melting points were Mp > 400°C.

7.2.39 HPHATN 5-27

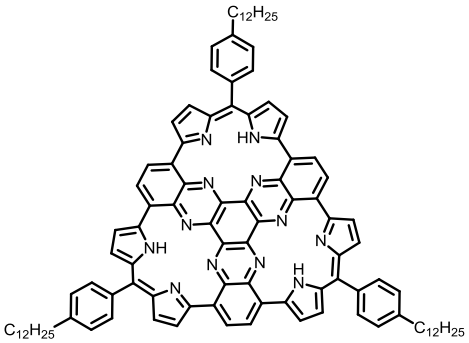

5-27

Prepared from 119 mg (0.15 mmol, 1 eq) HPHATN **5-19** and 190 mg (0.70 mmol, 4.5 eq) 4-dodecylbenzaldehyde (**5-21**). Yield: 75 mg (0.05 mmol, 32%) of compound **5-27** as a black

solid. ^{1}H NMR ($C_3D_2F_6O$ plus 0.1% $C_2DF_3O_2$, 700 MHz, 298 K): δ = 0.74 (m, 9H), 1.14 (m, 54H), 1.50 (m, 6H), 2.54 (m, 6H), 6.09 (d, 6H), 6.15 (d, 6H), 6.62 (s, 6H), 6.92 (d, ^{3}J=7.3 Hz, 6H), 7.11 (d, ^{3}J=7.3 Hz, 6H) ppm. ^{13}C NMR ($C_3D_2F_6O$ plus 0.1% $C_2DF_3O_2$, 176 MHz, 298 K): δ = 10.6, 20.3, 26.9, 27.0, 27.1, 27.2, 27.3, 27.4, 27.5, 28.8, 29.8, 33.0, 126.8, 129.4, 129.7, 130.1, 133.7, 135.0, 135.5, 143.2, 143.8, 148.6, 149.1, 149.5 ppm. Maldi-TOF (TCNQ): m/z = 1538.78 g/mol – calculated: 1536.88 g/mol for $C_{105}H_{108}N_{12}$. HRESI MS (THF 1:1 MeCN): $[C_{105}H_{108}N_{12}+2H]^{2+}$ m/z = 769.4471 g/mol – calculated: 769.4488 g/mol.

7.2.40 HPHATN 5-28

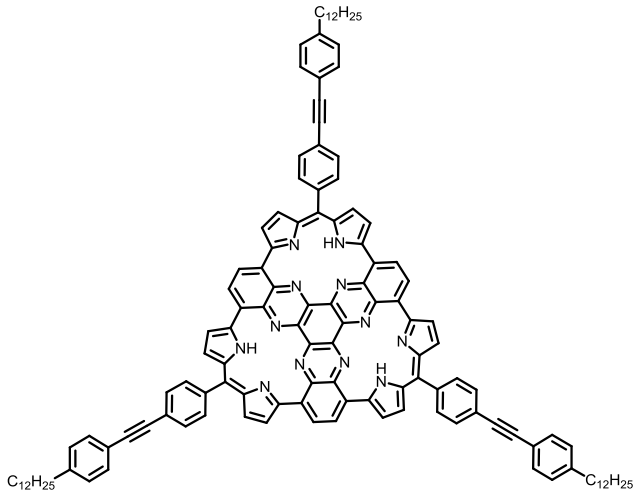

5-28

Prepared from 69 mg (0.09 mmol, 1 eq) HPHATN ***5-19*** and 150 mg (0.40 mmol, 4.5 eq) 4-((4-dodecylphenyl)ethynyl)benzaldehyde (***5-22***). Yield: 137 mg (0.07 mmol, 82%) of compound ***5-28*** as a black solid. ^{1}H NMR ($C_3D_2F_6O$ plus 0.1% $C_2DF_3O_2$, 500 MHz, 298 K): δ = 0.65 (m, 9H), 1.07 (m, 54H), 1.51 (m, 6H), 2.42 (m, 6H), 5.92 (d, ^{3}J=4.7 Hz, 6H), 5.99 (d, ^{3}J=4.7 Hz, 6H), 6.40 (s, 6H), 6.88 (d, ^{3}J=8.2 Hz, 6H), 7.02 (d, ^{3}J=8.2 Hz, 6H), 7.24 (d, ^{3}J=8.2 Hz, 6H), 7.30 (d, ^{3}J=8.2 Hz, 6H) ppm. ^{13}C NMR (C_3D_2F6O plus 0.1% $C_2DF_3O_2$, 176 MHz, 298 K): δ = 10.6, 20.3, 26.9, 27.1, 27.2, 27.3, 27.3, 27.4, 27.4, 29.0, 29.8, 33.7, 91.5, 96.4, 127.1, 129.0, 129.6, 129.7, 130.3, 131.9, 135.1, 135.2, 143.5, 144.1, 144.5, 144.8, 149.8 l ppm. Maldi-TOF (TCNQ): m/z = 1842.36 g/mol – calculated: 1843.02 g/mol for $C_{129}H_{120}N_{12}$. HRESI MS (THF 1:1 MeCN): $[C_{129}H_{120}N_{12}+2H]^{2+}$ m/z = 919.4977 g/mol – calculated: 919.4958 g/mol.

7.2.41 HPHATN 5-29

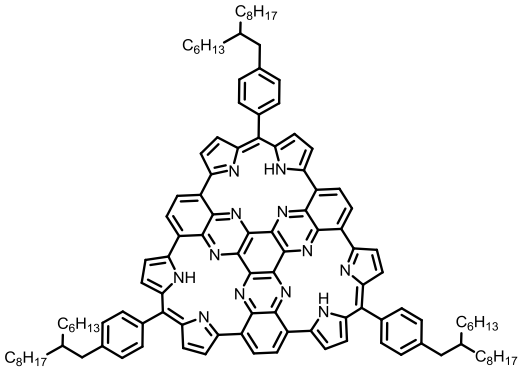

5-29

Prepared from 100 mg (0.13 mmol, 1 eq) HPHATN ***5-19*** and 191 mg (0.58 mmol, 4.5 eq) 4-(2-hexyldecyl)benzaldehyde (***5-23***). Yield: 117 mg (0.06 mmol, 52%) of compound ***5-29*** as a black solid. ^{1}H NMR ($C_3D_2F_6O$ plus 0.1% $C_2DF_3O_2$, 700 MHz, 298 K): δ = 0.81 (m, 18H), 1.22 (m, 72H), 1.63 (m, 3H), 2.58 (d, ^3J=6.6 Hz, 6H), 6.18 (d, ^3J=4.5 Hz, 6H), 6.23 (d, ^3J=4.5 Hz, 6H), 6.70 (s, 6H), 7.01 (d, ^3J=7.7 Hz, 6H), 7.20 (d, ^3J= 7.7 Hz, 6H) ppm. Maldi-TOF (TCNQ): m/z = 1707.27 g/mol – calculated: 1705.07 g/mol for $C_{117}H_{132}N_{12}$. HRESI MS (THF 1:1 MeCN): $[C_{117}H_{132}N_{12}+2H]^{2+}$ m/z = 853.5408 g/mol – calculated: 853.5427 g/mol.

7.2.42 HPHATN 5-30

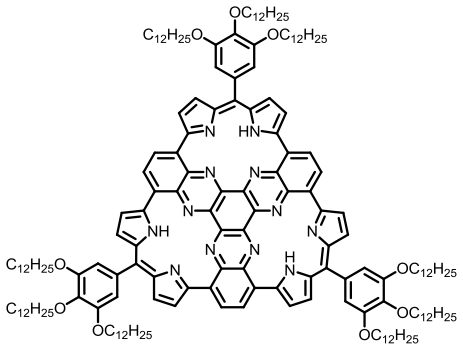

5-30

Prepared from 100 mg (0.13 mmol, 1 eq) HPHATN ***5-19*** and 383 mg (0.56 mmol, 4.5 eq) 3,4,5-tris(dodecyloxy)benzaldehyde (***5-20***). Yield: 250 mg (0.09 mmol, 71%) of compound ***5-30*** as a black solid. ^{1}H-NMR ($C_3D_2F_6O$ plus 0.1% $C_2DF_3O_2$, 500 MHz, 298 K): δ = 0.84 (t, 27H, ^3J= 6.8 Hz), 1.24 (m, 144H), 1.43 (m, 18H), 1.75 (m, 18H), 3.89 (t, 12H, ^3J= 6.1 Hz), 4.12 (t, 6H, ^3J= 6.8 Hz), 6.12 (d, 6H, ^3J=4.7 Hz), 6.18 (d, 6H, ^3J=4.7 Hz), 6.37 (s, 6H), 6.59 (s,

6H) ppm. ^{13}C NMR ($C_3D_2F_6O$ plus 0.1% $C_2DF_3O_2$, 176 MHz, 298 K): δ = 10.7, 20.4, 23.8, 23.9, 26.9, 27.1, 27.3 27.4, 27.6, 27.9, 29.9, 74.0, 107.7, 128.9, 130.3, 133.8, 135.0, 135.1, 138.7, 143.6, 144.1, 146.8, 149.8, 151.0 ppm. Maldi-TOF (TCNQ): m/z = 2693.08 g/mol – calculated: 2696.01 g/mol for $C_{177}H_{252}N_{12}O_9$. HRESI MS (THF 1:1 MeCN): $[C_{177}H_{252}N_{12}O_9+2H]^{2+}$ m/z = 1345.9829 g/mol – calculated: 1345.9893 g/mol.

7.2.43 HPHATN 5-31

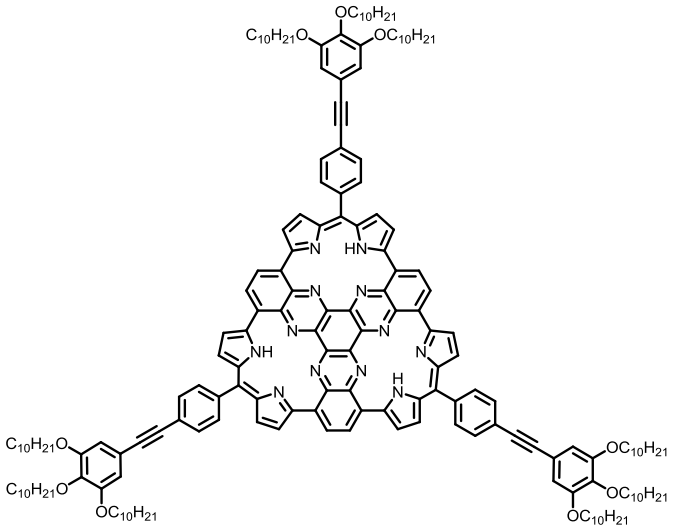

5-31

Prepared from 66 mg (0.08mmol, 1 eq) HPHATN **5-19** and 260 mg (0.39 mmol, 4.9 eq) 4-((3,4,5-tris(decyloxy)phenyl)ethynyl)benzaldehyde (**5-24**). Yield: 213 mg (0.077 mmol, 97%) of compound **5-31** as a black solid. ^{1}H NMR ($C_3D_2F_6O$ plus 0.1% $C_2DF_3O_2$, 700 MHz, 298 K): δ = 0.76 (m, 27H), 1.34 (m, 126H), 1.78 (m, 18H), 3.95 (m, 18H), 5.99 (d, 6H), 6.12 (d, 6H), 6.50 (s, 6H), 6.97 (d, ^3J= *7.8 Hz*, 6H), 7.34 (d, ^3J= *8.5 Hz*, 6H) ppm. Maldi-TOF (TCNQ): m/z = 2741.44 g/mol – calculated: 2743.84 g/mol for $C_{183}H_{228}N_{12}O_9$. HRESI MS (THF 1:1 MeCN): $[C_{183}H_{228}N_{12}O_9]^{2+}$ m/z = 1369.8903 g/mol – calculated: 1369.8954 g/mol.

7.2.44 HPHATN 5-32

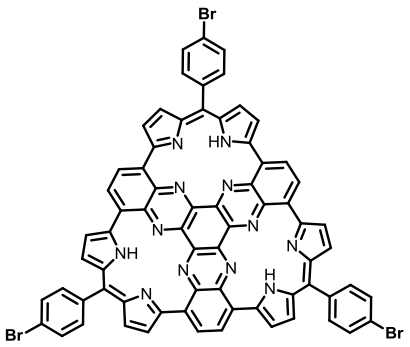

5-32

Prepared from 120 mg (0.15 mmol, 1 eq) HPHATN ***5-19*** and 172 mg (0.92 mmol, 6 eq) 4-bromobenzaldehyde (***5-26***). Yield: 165 mg (0.13 mmol, 87%) of compound ***5-32*** as a black solid. ^{1}H NMR ($C_3D_2F_6O$ plus 0.1% $C_2DF_3O_2$, 700 MHz, 298 K): δ = 5.99 (d, ^3J= *3.5Hz*, 6H), 6.10 (d, ^3J= *3.5Hz*, 6H), 6.49 (s, 6H), 6.90 (d, ^3J= *7.5Hz*, 6H), 7.49 (d, ^3J= *7.6Hz*, 6H) ppm. Maldi-TOF (TCNQ): m/z = 1271.10 g/mol – calculated: 1266.05 g/mol for $C_{69}H_{33}Br_3N_{12}$. HRESI MS (THF 1:1 MeCN): $[C_{99}H_{78}N_{12}S_3+H]^+$ m/z = 1267.0586 g/mol – calculated: 1267.0579 g/mol.

7.2.45 HPHATN 5-33

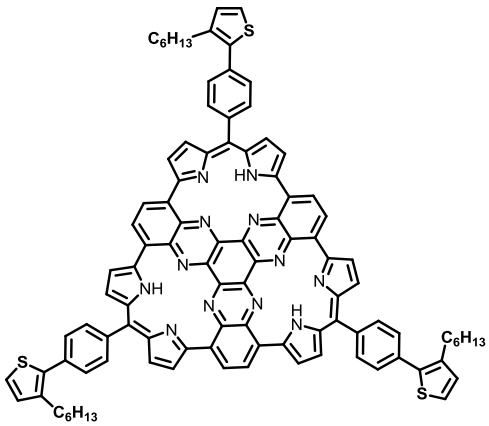

5-33

Prepared from 120 mg (0.15 mmol, 1 eq) HPHATN ***5-19*** and 230 mg (0.85 mmol, 5.6 eq) 4-(3-hexylthiophen-2-yl)benzaldehyde (***5-25***). Yield: 150 mg (0.10 mmol, 65%) of compound ***5-33*** as a black solid. ^{1}H NMR ($C_3D_2F_6O$ plus 0.1% $C_2DF_3O_2$, 700 MHz, 298 K): δ = 0.76 (m, 27H), 1.34 (m, 126H), 1.78 (m, 18H), 3.95 (m, 18H), 5.99 (d, 6H), 6.12 (d, 6H), 6.50 (s, 6H), 6.97 (d, ^3J= *7.8Hz*, 6H), 7.34 (d, ^3J= *8.5Hz*, 6H) ppm. Maldi-TOF (TCNQ):

m/z = 1707.27 g/mol – calculated: 1705.07 g/mol for $C_{183}H_{228}N_{12}O_9$. HRESI MS (THF 1:1 MeCN): $[C_{99}H_{78}N_{12}S_3+2H]^{2+}$ m/z = 766.2870 g/mol – calculated: 766.2896 g/mol.

7.2.46 General procedure for the preparation of cobalt complexes 5-42 to 5-44

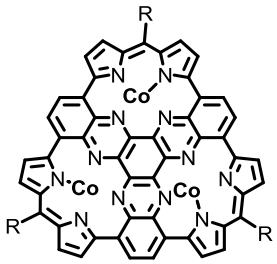

Procedure A: The corresponding HPHATN derivative (1 eq) was dispersed in DMF/THF (3 : 1) while argon was bubbled through the suspension. Then $Co(OAc)_2$ (6 eq) were added to the reaction mixture and the reaction was placed into a microwave for 3 x 2 h at 180°C (300 W). The reaction was allowed to cool to rt and poured into water. The precipitate was filtered off and dried under high vacuum.

Procedure B: Different from *procedure A*, the reaction was performed in a round bottom flask at 60°C for 20 h.

7.2.47 Cobalt complex 5-42

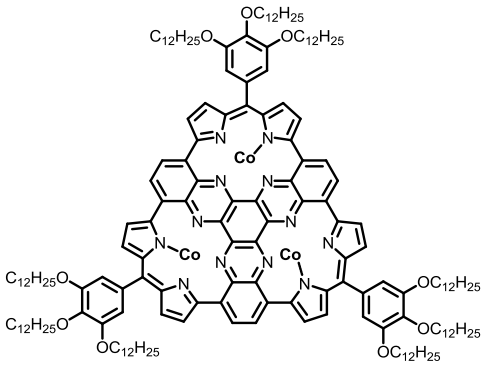

5-42

Prepared by *procedure A* from 55 mg (20 µmol, 1 eq) HPHATN **5-30** and 22 mg (124 µmol, 6 eq) $Co(OAc)_2$ in 2 ml DMF and 1 ml THF. Yield: 52 mg (18 µmol, 89%) of complex **5-42** as a black solid. Maldi-TOF (TCNQ): m/z = 2862.47 g/mol – calculated: 2866.76 g/mol for $C_{177}H_{252}Co_3N_{12}O_9$.

7.2.48 Cobalt complex 5-43

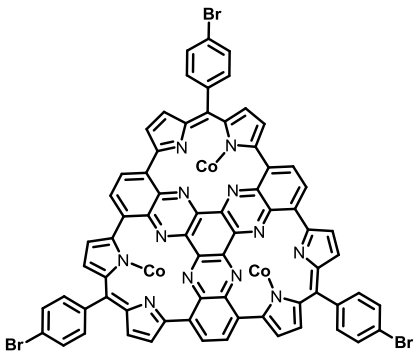

5-43

Prepared by *procedure B* from 330 mg (0.26 mmol, 1 eq) HPHATN ***5-32*** and 280 mg (1.58 mmol, 6 eq) $Co(OAc)_2$ in 15 ml DMF and 5 ml THF. Yield: 353 mg (0.24 mmol, 94%) of complex ***5-43*** as a black solid. Maldi-TOF (TCNQ): m/z = 1441.12 g/mol – calculated: 1439.83 g/mol for $C_{69}H_{30}Br_3Co_3N_{12}$.

7.2.49 Cobalt complex 5-44

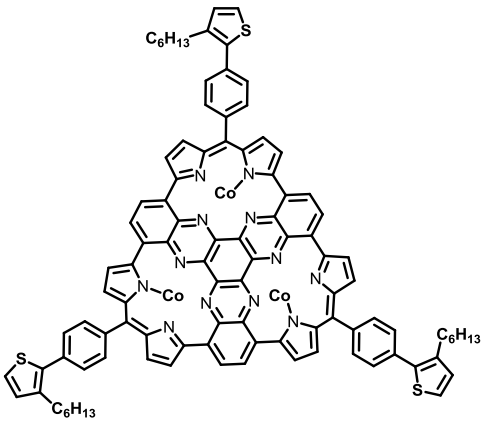

5-44

Prepared by *procedure B* from 203 mg (0.13 mmol, 1 eq) HPHATN ***5-33*** and 138 mg (0.78 mmol, 6 eq) $Co(OAc)_2$ in 10 ml DMF and 3 ml THF. Yield: 220 mg (0.12 mmol, 92%) of complex ***5-44*** as a black solid. Maldi-TOF (TCNQ): m/z = 1703.74 g/mol – calculated: 1704.34 g/mol for $C_{99}H_{75}Co_3N_{12}S_3$.

8 Appendix

8.1 Crystal Strucutres

8.1.1 3,6-Di-*tert*-butyl-1,8-bis(4,4,5,5-tetramethyl-1,3,2-dioxaborolan-2-yl)-9*H*-carbazole (4-16)

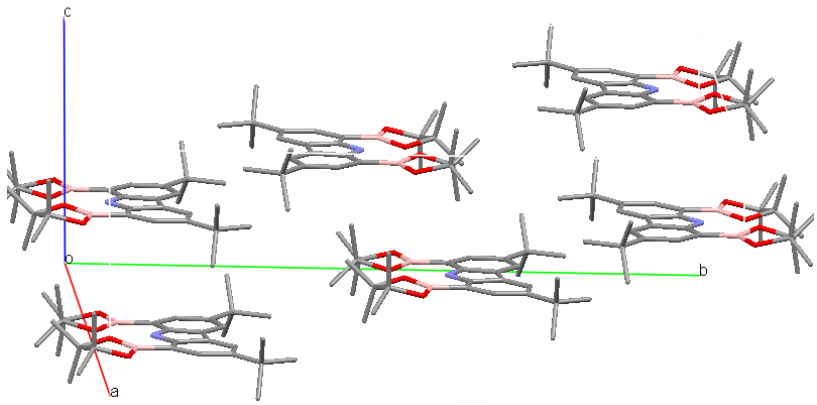

$C_{32}H_{47}B_2NO_4$, M = 531.35, monoclinic, space group P C2/c, a = 13.9158(6) Å, b = 25.9695(9) Å, c = 10.1072(3) Å, β = 121.2687(19)°, V = 3122.04 (4) A^3, T = 120 K, Z = 4, D_x = 1.130 gcm^{-3}, 16718 reflections measured, 4966 unique reflections, R_{int} = 0.0008, 2692 reflections observed (I > 3σ (I)). Refinement on F, R = 0.045, Rw = 0.054.

Cambridge Crystallographic Data Centre identifier: CCDC-859758.

8.1.2 Porphyrinoid 4-18

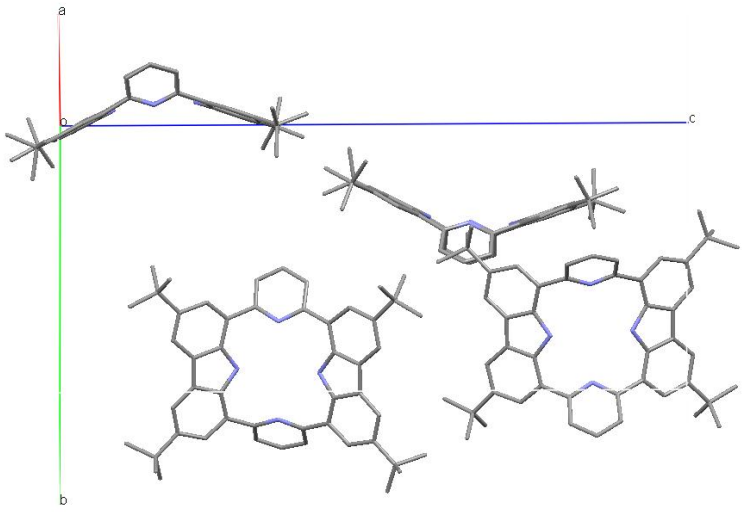

$C_{50}H_{52}N_4$*4.5THF ($C_{68}H_{88}N_4O_{4.5}$), M = 1032.46, orthorhombic, space group $P22_12_1$, a = 8.9009(3) Å, b = 22.2751(9) Å, c = 29.7836(9) Å, V = 5905.3(4) A^3, T = 120 K, Z = 4, D_x = 1.161 gcm^{-3}, 27036 reflections measured, 11884 unique reflections, R_{int} = 0.046, 8509 reflections observed ($I > 2\sigma(I)$). Refinement on F, R = 0.053, Rw = 0.058.

Cambridge Crystallographic Data Centre identifier: CCDC-787489.

8.1.3 Cobalt complex 4-19

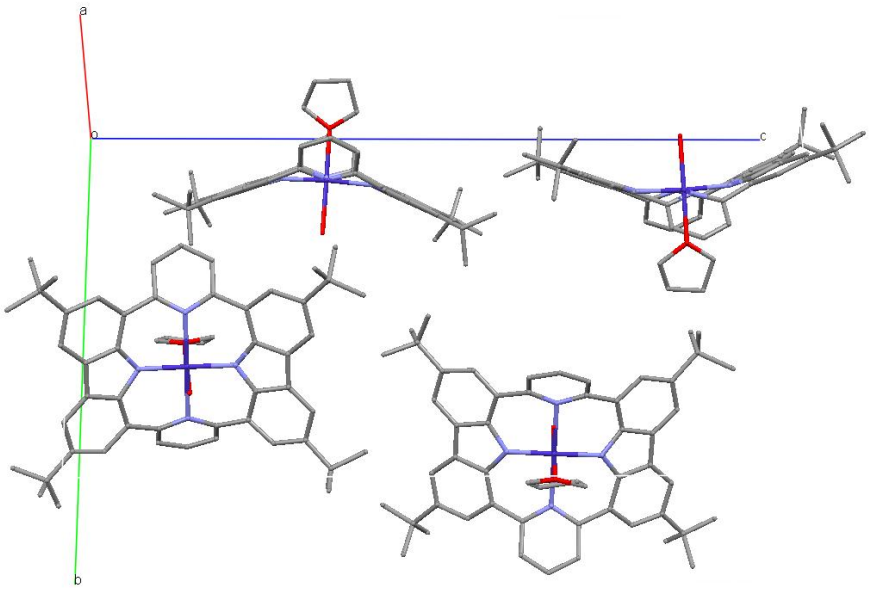

$C_{50}H_{50}N_4Co*H_2O*4.5THF$ ($C_{68}H_{88}N_4CoO_{5.5}$), M = 1108.40, orthorhombic, space group $P22_12_1$, a = 9.1483(4) Å, b = 21.8882(9) Å, c = 29.7527(9) Å, V = 5957.7(4) A^3, T = 120 K, Z = 4, D_x = 1.236 gcm^{-3}. 29056 reflections measured, 10964 unique reflections, 9174 reflections observed ($I > 2\sigma(I)$). Refinement on F, R = 0.063, Rw = 0.063.

Cambridge Crystallographic Data Centre identifier: CCDC - 787490

8.1.4 1,8-Diazido-3,6-di-*tert*-butyl-9*H*-carbazole (4-46)

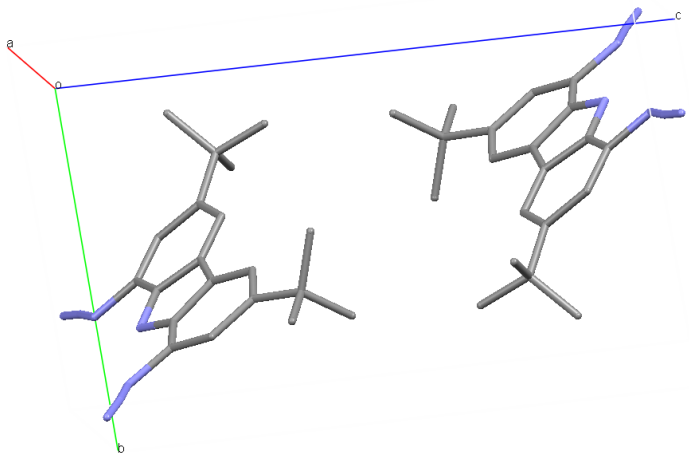

$C_{20}H_{23}N_7$, M = 361.45, triclinic, space group P-1, a = 6.0820(2) Å, b = 10.2880(5) Å, c = 15.9610(9) Å, V = 940.79(8) A^3, α = 79.545(3)°, β = 84.492(3)°, γ = 73.533(3), T = 120 K, Z = 2, D_x = 1.27 gcm^{-3}, 8865 reflections measured, 4235 unique reflections, R_{int} = 0.0004, 2934 reflections observed (I > 3σ (I)). Refinement on F, R = 0.048, Rw = 0.058. Cambridge Crystallographic Data Centre identifier: CCDC-859757.

8.1.5 Porphyrinoid 4-48 and TBAF

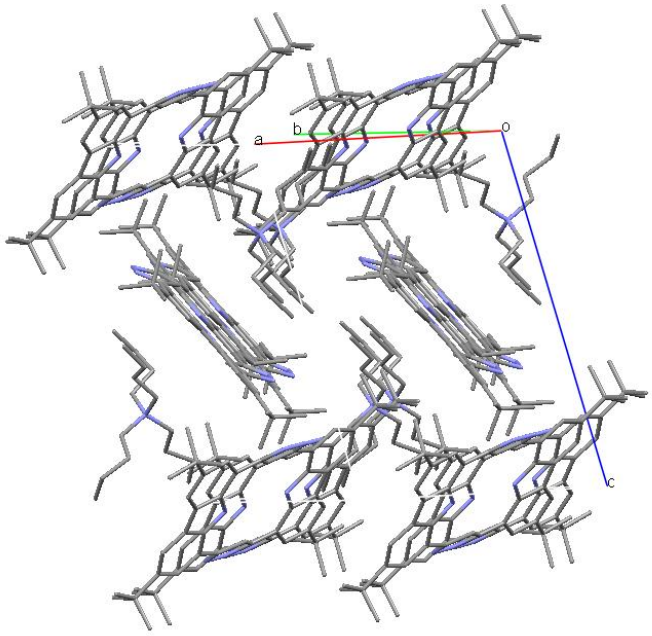

$C_{60}H_{83}N_9$, M = 465.69, monoclinic, space group P C2/c, a = 32.0463(9) Å, b = 10.1050(3) Å, c = 20.7437(9) Å, β = 127.7510(14)°, V = 5311.3(3) A^3, T = 120 K, Z = 8, D_x = 1.16 gcm^{-3}, 18905 reflections measured, 6002 unique reflections, R_{int} = 0.0003, 4846 reflections observed (I > 2σ (I)). Refinement on F, R = 0.043, Rw = 0.045. For clarity reasons only the major isomer is shown.

Cambridge Crystallographic Data Centre identifier: CCDC-859756.

8.2 Literature

[1] J. L. W. Thudichum, *Rep. Med. Off. Privy Counc* **1867**, *10*, 152.
[2] D. L. Drabkin, Philadelphia Oxford Press, London, England, **1958**.
[3] K. M. Kadish, K. M. Smith, R. Guilard, Academic Press, San Diego, **2000**.
[4] L. Teichmann, *Z. Ration. Med.* **1852**, *3*, 375.
[5] R. Willstätter, A. Stoll, Springer, Berlin, **1913**.
[6] R. B. Woodward, *Angew. Chem. Int. Ed.* **1960**, *72*, 650-662.
[7] R. B. Woodward, W. A. Ayer, J. M. Beaton, F. Bickelhaupt, R. Bonnett, P. Buchschacher, G. L. Closs, H. Dutler, J. Hannah, F. P. Hauck, S. Ito, A. Langemann, E. Legoff, W. Leimgruber, W. Lwowski, J. Sauer, Z. Valenta, H. Volz, *J. Am. Chem. Soc.* **1960**, *82*, 3800-3802.
[8] R. B. Woodward, W. A. Ayer, J. M. Beaton, F. Bickelhaupt, R. Bonnett, P. Buchschacher, G. L. Closs, H. Dutler, J. Hannah, F. P. Hauck, S. Ito, A. Langemann, E. Legoff, W. Leimgruber, W. Lwowski, J. Sauer, Z. Valenta, H. Volz, *Tetrahedron* **1990**, *46*, 7599-7659.
[9] R. B. Woodward, *Angew. Chem.* **1973**, *33*, 145.
[10] E. Vogel, M. Köcher, H. Schmickler, J. Lex, *Angew. Chem. Int. Ed.* **1986**, *25*, 257-259.
[11] V. K. Jain, H. C. Mandalia, *Heterocycles* **2007**, *71*, 1261.
[12] A. Jasat, D. Dolphin, *Chem. Rev.* **1997**, *97*, 2267-2340.
[13] J. L. Sessler, S. Camiolo, P. A. Gale, *Coord. Chem. Rev.* **2003**, *240*, 17-55.
[14] S. Saito, A. Osuka, *Angew. Chem. Int. Ed.* **2011**, *50*, 4342-4373.
[15] I. Gupta, M. Ravikanth, *Coord. Chem. Rev.* **2006**, *250*, 468-518.
[16] P. J. Chmielewski, L. Latos-Grazynski, *Coord. Chem. Rev.* **2005**, *249*, 2510-2533.
[17] P. J. Chmielewski, L. Latos-Grażyński, K. Rachlewicz, T. Glowiak, *Angew. Chem. Int. Ed.* **1994**, *33*, 779-781.
[18] H. Furuta, T. Asano, T. Ogawa, *J. Am. Chem. Soc.* **1994**, *116*, 767-768.
[19] S. Ito, N. Ochi, H. Uno, T. Murashima, N. Ono, *Chem. Commun.* **2000**, 893-894.
[20] N. Ono, H. Hironaga, K. Ono, S. Kaneko, T. Murashima, T. Ueda, C. Tsukamura, T. Ogawa, *J. Chem. Soc., Perkin Trans. 1* **1996**, 417-423.
[21] T. D. Lash, P. Chandrasekar, A. T. Osuma, S. T. Chaney, J. D. Spence, *J. Org. Chem.* **1998**, *63*, 8455-8469.
[22] P. L. Chen, I. V. Tomov, A. S. Dvornikov, M. Nakashima, J. F. Roach, D. M. Alabran, P. M. Rentzepis, *J. Phys. Chem.* **1996**, *100*, 17507-17512.
[23] S. A. Vinogradov, D. F. Wilson, *J. Chem. Soc., Perk. Trans. 2* **1995**, 103-111.
[24] R. Bonnett, *Chem. Soc. Rev.* **1995**, *24*, 19-33.
[25] K. Sendt, L. A. Johnston, W. A. Hough, M. J. Crossley, N. S. Hush, J. R. Reimers, *J. Am. Chem. Soc.* **2002**, *124*, 9299-9309.
[26] J. R. Reimers, L. E. Hall, M. J. Crossley, N. S. Hush, *J. Phys. Chem. A* **1999**, *103*, 4385-4397.
[27] Z. L. Cai, M. J. Crossley, J. R. Reimers, R. Kobayashi, R. D. Amos, *J. Phys. Chem. B* **2006**, *110*, 15624-15632.
[28] M. J. Crossley, P. L. Burn, *Chem. Commun.* **1991**, 1569-1571.
[29] M. Stepien, L. L. Grazynski, *Acc. Chem. Res.* **2005**, *38*, 88-98.
[30] T. D. Lash, *Eur. J. Org. Chem.* **2007**, *2007*, 5461-5481.
[31] T. D. Lash, *Synlett* **1999**, *3*, 279-295.
[32] K. M. Smith, Academic Press, San Diego, **1999**.
[33] L. Arnold, K. Müllen, *J. Porphyrins Phthalocyanines* **2011**, *15*, 757-779.

[34] L. Arnold, H. Norouzi-Arasi, M. Wagner, V. Enkelmann, K. Müllen, *Chem. Commun.* **2011**, *47*, 970-972.
[35] C. Maeda, T. Yoneda, N. Aratani, M. C. Yoon, J. M. Lim, D. Kim, N. Yoshioka, A. Osuka, *Angew. Chem. Int. Ed.* **2011**, *50*, 5690-5693.
[36] H. Norouzi-Arasi, W. Pisula, A. Mavrinskiy, X. Feng, K. Müllen, *Chem. Asian J.* **2011**, *6*, 367-371.
[37] W. Küster, *Hoppe-Seyler's Z. Physiol. Chem.* **1912**, *82*, 463.
[38] E. Hückel, *Z. Phys.* **1931**, *72*, 310-337.
[39] E. Hückel, *Z. Phys.* **1931**, *70*, 204-286.
[40] E. B. Fleischer, *Acc. Chem. Res.* **1970**, *3*, 105-112.
[41] F. Sondheimer, R. Wolovsky, Y. Amiel, *J. Am. Chem. Soc.* **1962**, *84*, 274-284.
[42] J. L. Soret, *C.R. Acad. Sci., Ser. IIc: Chim.* **1883**, *97*, 1269.
[43] M. Gouterman, G. H. Wagnière, L. C. Snyder, *J. Mol. Spectrosc.* **1963**, *11*, 108-127.
[44] M. Gouterman, *J. Mol. Spectrosc.* **1961**, *6*, 138.
[45] K. S. Suslick, R. A. Watson, *New J. Chem.* **1992**, *16*, 633-642.
[46] M. O. Senge, *Angew. Chem. Int. Ed.* **1996**, *35*, 1923-1925.
[47] D. F. Marsh, L. M. Mink, *J. Chem. Educ.* **1996**, *73*, 1188-1190.
[48] J. W. Buchler, L. Puppe, *Liebigs Ann Chem* **1970**, *740*, 142-&.
[49] A. D. Adler, F. R. Longo, F. Kampas, J. Kim, *J. Inorg. Nucl. Chem.* **1970**, *32*, 2443-&.
[50] P. Rothemund, *J. Am. Chem. Soc.* **1935**, *57*, 2010-2011.
[51] P. Rothemund, A. R. Menotti, *J. Am. Chem. Soc.* **1941**, *63*, 267-270.
[52] J. S. Lindsey, I. C. Schreiman, H. C. Hsu, P. C. Kearney, A. M. Marguerettaz, *J. Org. Chem.* **1987**, *52*, 827-836.
[53] J. S. Lindsey, I. C. Schreiman, H. C. Hsu, P. C. Kearney, A. M. Marguerettaz, *J. Org. Chem.* **1987**, *52*, 827-836.
[54] G. P. Arsenault, E. Bullock, S. F. MacDonald, *J. Am. Chem. Soc.* **1960**, *82*, 4384-4389.
[55] M. J. Broadhurst, R. Grigg, A. W. Johnson, *J. Chem. Soc., C* **1971**, 3681-3690.
[56] K. M. Smith, J. A. S. Cavaleiro, *Heterocycles* **1987**, *26*, 1947-1963.
[57] J. L. Sessler, D. Seidel, *Angew. Chem. Int. Ed.* **2003**, *42*, 5134-5175.
[58] B. Siridevi, S. J. Narayanan, A. Srinivasan, M. V. Reddy, T. K. Chandrashekar, *J. Porphyrins Phthalocyanines* **1998**, *2*, 69.
[59] M. J. Broadhurst, R. Grigg, A. W. Johnson, *J. Chem. Soc., Chem. Commun.* **1969**, 1480-1482.
[60] D. A. Colby, T. D. Lash, *Chem. Eur. J.* **2002**, *8*, 5397-5402.
[61] T. D. Lash, M. J. Hayes, *Angew. Chem. Int. Ed.* **1997**, *36*, 840-842.
[62] T. D. Lash, S. T. Chaney, *Angew. Chem. Int. Ed.* **1997**, *36*, 839-840.
[63] K. Berlin, E. Breitmaier, *Angew. Chem. Int. Ed.* **1994**, *33*, 1246-1247.
[64] T. D. Lash, *Angew. Chem. Int. Ed.* **1995**, *34*, 2533-2535.
[65] R. Myśliborski, L. Latos-Grażyński, *Eur. J. Org. Chem.* **2005**, *2005*, 5039-5048.
[66] D. Liu, T. D. Lash, *Chem. Commun.* **2002**, 2426-2427.
[67] D. Liu, G. M. Ferrence, T. D. Lash, *J. Org. Chem.* **2004**, *69*, 6079-6093.
[68] T. D. Lash, S. T. Chaney, *Chem. Eur. J.* **1996**, *2*, 944-948.
[69] R. Myśliborski, L. Latos-Grażyński, L. Szterenberg, *Eur. J. Org. Chem.* **2006**, *2006*, 3064-3068.
[70] T. D. Lash, K. Pokharel, J. M. Serling, V. R. Yant, G. M. Ferrence, *Org. Lett.* **2007**, *9*, 2863-2866.
[71] J. V. Grazulevicius, P. Strohriegl, J. Pielichowski, K. Pielichowski, *Prog. Polym. Sci.* **2003**, *28*, 1297-1353.
[72] J.-F. Morin, M. Leclerc, D. Adès, A. Siove, *Macromol. Rapid Commun.* **2005**, *26*, 761-778.

[73] N. Blouin, M. Leclerc, *Acc. Chem. Res.* **2008**, *41*, 1110-1119.
[74] H. Aihara, L. Jaquinod, D. J. Nurco, K. M. Smith, *Angew. Chem. Int. Ed.* **2001**, *40*, 3439-3441.
[75] M. Nath, J. C. Huffman, J. M. Zaleski, *J. Am. Chem. Soc.* **2003**, *125*, 11484-11485.
[76] M. Nath, M. Pink, J. M. Zaleski, *J. Am. Chem. Soc.* **2005**, *127*, 478-479.
[77] P. Piatek, V. M. Lynch, J. L. Sessler, *J. Am. Chem. Soc.* **2004**, *126*, 16073-16076.
[78] R. G. Bergman, *Acc. Chem. Res.* **1973**, *6*, 25-31.
[79] F. B. Mallory, K. E. Butler, A. C. Evans, C. W. Mallory, *Tetrahedron Lett.* **1996**, *37*, 7173-7176.
[80] J. K. Stille, *Angew. Chem. Int. Ed.* **1986**, *25*, 508-524.
[81] C. Maeda, N. Yoshioka, *Org. Lett.* **2012**, *14*, 2122-2125.
[82] F. Cheng, S. Zhang, A. Adronov, L. Echegoyen, F. Diederich, *Chem. Eur. J.* **2006**, *12*, 6062-6070.
[83] L.-A. Fendt, H. Fang, M. E. Plonska-Brzezinska, S. Zhang, F. Cheng, C. Braun, L. Echegoyen, F. Diederich, *Eur. J. Org. Chem.* **2007**, *2007*, 4659-4673.
[84] Y. Nakamura, N. Aratani, H. Shinokubo, A. Takagi, T. Kawai, T. Matsumoto, Z. S. Yoon, D. Y. Kim, T. K. Ahn, D. Kim, A. Muranaka, N. Kobayashi, A. Osuka, *J. Am. Chem. Soc.* **2006**, *128*, 4119-4127.
[85] V. S. Y. Lin, S. G. Dimagno, M. J. Therien, *Science* **1994**, *264*, 1105-1111.
[86] H. L. Anderson, *Chem. Commun.* **1999**, 2323-2330.
[87] M. Graca, H. Vicente, L. Jaquinod, K. M. Smith, *Chem. Commun.* **1999**, 1771-1782.
[88] M. J. Crossley, P. L. Burn, S. J. Langford, J. K. Prashar, *Chem. Commun.* **1995**, 1921-1923.
[89] N. Kobayashi, M. Numao, R. Kondo, S. Nakajima, T. Osa, *Inorg. Chem.* **1991**, *30*, 2241-2244.
[90] M. Sayyad, M. Saleem, K. Karimov, M. Yaseen, M. Ali, K. Cheong, A. Mohd Noor, *Appl. Phys. A* **2010**, *98*, 103-109.
[91] A. Osuka, H. Shimidzu, *Angew. Chem. Int. Ed.* **1997**, *36*, 135-137.
[92] N. Aratani, D. Kim, A. Osuka, *Chem. Asian J.* **2009**, *4*, 1172-1182.
[93] A. Tsuda, A. Osuka, *Adv. Mater.* **2002**, *14*, 75-79.
[94] A. Tsuda, A. Osuka, *Science* **2001**, *293*, 79-82.
[95] N. Aratani, A. Osuka, Y. H. Kim, D. H. Jeong, D. Kim, *Angew. Chem. Int. Ed.* **2000**, *39*, 1458.
[96] H. S. Cho, D. H. Jeong, S. Cho, D. Kim, Y. Matsuzaki, K. Tanaka, A. Tsuda, A. Osuka, *J. Am. Chem. Soc.* **2002**, *124*, 14642-14654.
[97] Y. Nakamura, S. Y. Jang, T. Tanaka, N. Aratani, J. M. Lim, K. S. Kim, D. Kim, A. Osuka, *Chem. Eur. J.* **2008**, *14*, 8279-8289.
[98] J. Zagal, F. Bedioui, J.-P. Dodelet, Springer, New York, USA, **2006**.
[99] W. R. Grove, *Phil. Mag. Ser* **1839**, *3*, 127-130.
[100] J. Rosenthal, D. G. Nocera, *Acc. Chem. Res.* **2007**, *40*, 543-553.
[101] B. C. H. Steele, A. Heinzel, *Nature* **2001**, *414*, 345-352.
[102] G. Brumfiel, *Nature* **2003**, *422*, 104-104.
[103] A. Bauen, D. Hart, *J. Power Sources* **2000**, *86*, 482-494.
[104] C. W. B. Bezerra, *Electrochim. Acta* **2008**, *53*, 4937-4951.
[105] R. Bashyam, P. Zelenay, *Nature* **2006**, *443*, 7.
[106] L. Zhang, *Power Sources* **2006**, *156*, 171.
[107] K. A. Starz, E. Auer, T. Lehmann, R. Zuber, *J. Power Sources* **1999**, *84*, 167-172.
[108] M. S. Wilson, J. A. Valerio, S. Gottesfeld, *Electrochim. Acta* **1995**, *40*, 355-363.
[109] M. Uchida, Y. Fukuoka, Y. Sugawara, H. Ohara, A. Ohta, *J. Electrochem. Soc.* **1998**, *145*, 3708-3713.

[110] R. Othman, A. L. Dicks, Z. H. Zhu, *Int. J. Hydrogen Energy* **2012**, *37*, 357-372.
[111] Z. W. Chen, D. Higgins, A. P. Yu, L. Zhang, J. J. Zhang, *Energ. Environ. Sci.* **2011**, *4*, 3167-3192.
[112] R. Jasinski, *Nature* **1964**, *201*, 1212.
[113] H. Jahnke, *Top. Curr. Chem.* **1976**, *61*, 133.
[114] G. Faubert, G. Lalande, R. Cote, D. Guay, J. P. Dodelet, L. T. Weng, P. Bertrand, G. Denes, *Electrochim. Acta* **1996**, *41*, 1689-1701.
[115] C. Medard, M. Lefevre, J. P. Dodelet, F. Jaouen, G. Lindbergh, *Electrochim. Acta* **2006**, *51*, 3202-3213.
[116] D. Villers, X. Jacques-Bedard, J. P. Dodelet, *J. Electrochem. Soc.* **2004**, *151*, A1507-A1515.
[117] B. Wang, *J. Power Sources* **2005**, *152*, 1-15.
[118] J. Zagal, M. Paez, A. A. Tanaka, J. R. Dossantos, C. A. Linkous, *J. Electroanal. Chem.* **1992**, *339*, 13-30.
[119] C. Shi, F. C. Anson, *J. Am. Chem. Soc.* **1991**, *113*, 9564-9570.
[120] T. Kuwana, M. Fujihira, K. Sunakawa, T. Osa, *J. Electroanal. Chem.* **1978**, *88*, 299-303.
[121] N. Kobayashi, T. Matsue, M. Fujihira, T. Osa, *J. Electroanal. Chem.* **1979**, *103*, 427-431.
[122] B. Steiger, F. C. Anson, *Inorg. Chem.* **1995**, *34*, 3355-3357.
[123] R. Adzic, Wiley-VCH, New York, **1998**, pp. 197-242.
[124] C. K. Chang, H. Y. Liu, I. Abdalmuhdi, *J. Am. Chem. Soc.* **1984**, *106*, 2725-2726.
[125] J. P. Collman, P. S. Wagenknecht, J. E. Hutchison, *Angew. Chem. Int. Ed.* **1994**, *33*, 1537-1554.
[126] R. R. Durand, C. S. Bencosme, J. P. Collman, F. C. Anson, *J. Am. Chem. Soc.* **1983**, *105*, 2710-2718.
[127] A. Vanderputten, A. Elzing, W. Visscher, E. Barendrecht, *Chem. Commun.* **1986**, 477-479.
[128] F. C. Anson, C. N. Shi, B. Steiger, *Acc. Chem. Res.* **1997**, *30*, 437-444.
[129] A. J. Bard, L. R. Faulkner, John Wiley & Sons, New York, **2001**.
[130] H. Qin, Z. Liu, S. Lao, J. Zhu, Z. Li, *J. Power Sources* **2010**, *195*, 3124-3129.
[131] K. C. Nicolaou, P. G. Bulger, D. Sarlah, *Angew. Chem. Int. Ed.* **2005**, *44*, 4442-4489.
[132] H. Nandivada, X. Jiang, J. Lahann, *Adv. Mater.* **2007**, *19*, 2197-2208.
[133] F. G. Bordwell, X. Zhang, J. P. Cheng, *J. Org. Chem.* **1991**, *56*, 3216-3219.
[134] M. J. Chmielewski, M. Charon, J. Jurczak, *Org. Lett.* **2004**, *6*, 3501-3504.
[135] N. Miyaura, T. Yanagi, A. Suzuki, *Synth. Commun.* **1981**, *11*, 513-519.
[136] A. Baeyer, *Ber. Dtsch. Chem. Ges.* **1886**, *19*, 2184.
[137] J. Bachmann, D. G. Nocera, *J. Am. Chem. Soc.* **2005**, *127*, 4730-4743.
[138] K. A. Nielsen, W. S. Cho, J. Lyskawa, E. Levillain, V. M. Lynch, J. L. Sessler, J. O. Jeppesen, *J. Am. Chem. Soc.* **2006**, *128*, 2444-2451.
[139] T. Mizuno, W. H. Wei, L. R. Eller, J. L. Sessler, *J. Am. Chem. Soc.* **2002**, *124*, 1134-1135.
[140] M. Cametti, K. Rissanen, *Chem. Commun.* **2009**, 2809-2829.
[141] Y. L. Li, A. H. Flood, *J. Am. Chem. Soc.* **2008**, *130*, 12111-12122.
[142] Y. R. Hua, A. H. Flood, *Chem. Soc. Rev.* **2010**, *39*, 1262-1271.
[143] R. Huisgen, *Proc. Chem. Soc.* **1961**, 357-396.
[144] R. Liu, C. von Malotki, L. Arnold, N. Koshino, H. Higashimura, M. Baumgarten, K. Müllen, *J. Am. Chem. Soc.* **2011**, *133*, 10372-10375.
[145] A. M. Dolgonosov, *J. Phys. Chem. B* **1998**, *102*, 4715-4730.

[146] V. V. Rostovtsev, L. G. Green, V. V. Fokin, K. B. Sharpless, *Angew. Chem. Int. Ed.* **2002**, *41*, 2596-2599.
[147] C. Graebe, C. Glaser, *Ber. Dtsch. Chem. Ges.* **1872**, *5*, 12.
[148] C. Graebe, C. Glaser, *Ann. Chem. Pharm.* **1872**, *163*, 343.
[149] **http://www.sigmaaldrich.com**.
[150] W.-Y. Wong, *Coord. Chem. Rev.* **2005**, *249*, 971-997.
[151] B. Schmaltz, A. Rouhanipour, H. J. Rader, W. Pisula, K. Müllen, *Angew. Chem. Int. Ed.* **2009**, *48*, 720-724.
[152] M. S. Mudadu, A. N. Singh, R. P. Thummel, *J. Org. Chem.* **2008**, *73*, 6513-6520.
[153] Y. Liu, M. Nishiura, Y. Wang, Z. Hou, *J. Am. Chem. Soc.* **2006**, *128*, 5592-5593.
[154] C. C. Price, *Org. React.* **1946**, *3*, 1-82.
[155] M. Inoue, T. Suzuki, M. Nakada, *J. Am. Chem. Soc.* **2003**, *125*, 1140-1141.
[156] J. I. G. Cadogan, *Synthesis* **1969**, 11-17.
[157] J. I. G. Cadogan, M. Cameron-Wood, R. K. Mackie, R. J. G. Searle, *J. Chem. Soc.* **1965**.
[158] J. I. G. Cadogan, M. J. Todd, *J. Chem. Soc., C* **1969**.
[159] J.-F. Morin, M. Leclerc, *Macromolecules* **2001**, *34*, 4680-4682.
[160] K. Tamao, K. Sumitani, M. Kumada, *J. Am. Chem. Soc.* **1972**, *94*, 4374-4376.
[161] R. J. P. Corriu, J. P. Masse, *J. Chem. Soc., Chem. Commun.* **1972**.
[162] F. Diederich, A. d. Meijere, Wiley-VCH, New York, **2004**.
[163] N. Miyaura, *Top. Curr. Chem.* **2002**, 1-241.
[164] T. Noel, S. L. Buchwald, *Chem. Soc. Rev.* **2011**, *40*, 5010.
[165] J. Sakamoto, M. Rehahn, G. Wegner, A. D. Schlüter, *Macromol. Rapid Commun.* **2009**, *30*, 653-687.
[166] B. Rieger, L. S. BAugh, S. Kracker, S. Striegler, Wiley-VCH, Weinheim, **2006**.
[167] N. Miyaura, K. Yamada, A. Suzuki, *Tetrahedron Lett.* **1979**, *20*, 3437-3440.
[168] N. Miyaura, A. Suzuki, *J. Chem. Soc., Chem. Commun.* **1979**, 866.
[169] **http://www.nobelprize.org/**.
[170] C. Grave, A. D. Schlüter, *Eur. J. Org. Chem.* **2002**, *2002*, 3075-3098.
[171] V. Hensel, K. Lützow, A.-D. Schlüter, J. Jacob, K. Gessler, W. Saenger, *Angew. Chem. Int. Ed.* **1997**, *36*, 2654-2656.
[172] K. Memminger, T. Oeser, T. J. J. Müller, *Org. Lett.* **2008**, *10*, 2797-2800.
[173] W. Huang, M. Wang, C. Du, Y. Chen, R. Qin, L. Su, C. Zhang, Z. Liu, C. Li, Z. Bo, *Chem. Eur. J.* **2011**, *17*, 440-444.
[174] U. Lehmann, A. D. Schlüter, *Eur. J. Org. Chem.* **2000**, *2000*, 3483-3487.
[175] U. Velten, M. Rehahn, *Macromol. Chem. Phys.* **1998**, *199*, 127-140.
[176] R. Miyakoshi, A. Yokoyama, T. Yokozawa, *J. Polym. Sci., Part A: Polym. Chem.* **2008**, *46*, 753-765.
[177] T. Michinobu, H. Osako, K. Shigehara, *Macromolecules* **2009**, *42*, 8172-8180.
[178] V. C. Gibson, S. K. Spitzmesser, A. J. P. White, D. J. Williams, *Dalton Trans.* **2003**, 2718-2727.
[179] B. Ederer, N. Metzler, H. Nöth, *Chem. Ber.* **1993**, *126*, 2003-2010.
[180] J. Bernstein, R. E. Davis, L. Shimoni, N.-L. Chang, *Angew. Chem. Int. Ed.* **1995**, *34*, 1555-1573.
[181] S. Kotha, K. Lahiri, D. Kashinath, *Tetrahedron* **2002**, *58*, 9633-9695.
[182] G. Wilke, *Angew. Chem. Int. Ed.* **2003**, *42*, 5000-5008.
[183] S. Neya, H. Yodo, N. Funasaki, *J. Heterocyclic Chem.* **1993**, *30*, 549.
[184] Spartan version 4.0, Wavefunction, Inc., 18401 ed., Karman Ave. Suite 370, Irvine, CA 92612 USA.

[185] N. D. McClenaghan, R. Passalacqua, F. Loiseau, S. Campagna, B. Verheyde, A. Hameurlaine, W. Dehaen, *J. Am. Chem. Soc.* **2003**, *125*, 5356-5365.
[186] G. A. Crosby, J. N. Demas, *J. Phys. Chem.* **1971**, *75*, 991-1024.
[187] T. D. Lash, S. T. Chaney, D. T. Richter, *J. Org. Chem.* **1998**, *63*, 9076-9088.
[188] N. S. Golubev, I. G. Shenderovich, S. N. Smirnov, G. S. Denisov, H.-H. Limbach, *Chem. Eur. J.* **1999**, *5*, 492-497.
[189] J. Heinze, *Angew. Chem. Int. Ed.* **1984**, *23*, 831-847.
[190] B. Seiwert, U. Karst, *Anal. Bioanal. Chem.* **2008**, *390*, 181-200.
[191] J. F. Ambrose, L. L. Carpenter, R. F. Nelson, *J. Electrochem. Soc.* **1975**, *122*, 876-894.
[192] H. Fujita, T. Michinobu, *Macromol. Chem. Phys.* **2012**, *213*, 447-457.
[193] L. Cuesta, J. L. Sessler, *Chem. Soc. Rev.* **2009**, *38*, 2716-2729.
[194] R. D. Shannon, *Acta Crystallographica Section A* **1976**, *32*, 751-767.
[195] K. E. Schwarzhans, *Angew. Chem.* **1970**, *82*, 975-982.
[196] A. Nanthakumar, S. Fox, N. N. Murthy, K. D. Karlin, *J. Am. Chem. Soc.* **1997**, *119*, 3898-3906.
[197] C. Luchiant, S. Ciurli, New York, **1993**, pp. 357-420.
[198] R. W. Kluiber, W. D. Horrocks, *Inorg. Chem.* **1967**, *6*, 1427-1429.
[199] W. Q. Zheng, N. Shan, L. X. Yu, X. Q. Wang, *Dyes and Pigments* **2008**, *77*, 153-157.
[200] L. Ruhlmann, M. Gross, A. Giraudeau, *Chem. Eur. J.* **2003**, *9*, 5085-5096.
[201] D. D. Bao, B. Millare, W. Xia, B. G. Steyer, A. A. Gerasimenko, A. Ferreira, A. Contreras, V. I. Vullev, *J. Phys. Chem. A* **2009**, *113*, 1259-1267.
[202] C. Bernard, J. P. Gisselbrecht, M. Gross, E. Vogel, M. Lausmann, *Inorg. Chem.* **1994**, *33*, 2393-2401.
[203] K. Aoki, T. Goshima, Y. Kozuka, Y. Kawamori, N. Ono, Y. Hisaeda, H. D. Takagi, M. Inamo, *Dalton Trans.* **2009**, 119-125.
[204] K. M. Kadish, M. M. Morrison, *Bioinorg. Chem.* **1977**, *7*, 107-115.
[205] A. Wahab, M. Bhattacharya, S. Ghosh, A. G. Samuelson, P. K. Das, *J. Phys. Chem. B* **2008**, *112*, 2842-2847.
[206] A. Wolberg, J. Manassen, *J. Am. Chem. Soc.* **1970**, *92*, 2982-2991.
[207] R. H. Felton, H. Linschitz, *J. Am. Chem. Soc.* **1966**, *88*, 1113-1116.
[208] F. A. Chavez, C. V. Nguyen, M. M. Olmstead, P. K. Mascharak, *Inorg. Chem.* **1996**, *35*, 6282-6291.
[209] **www.csiro.au**.
[210] L. H. Gade, WILEY-VCH Verlag GmbH, Weinheim, **1998**.
[211] O. Kahn, WILEY-VCH, New York, **1993**.
[212] L. M. Carrella, D. Schollmeyer, E. Rentschler, *Z. Anorg. Allg. Chem.* **2011**, *637*, 1756-1760.
[213] M. S. Liao, S. Scheiner, *J. Chem. Phys.* **2002**, *117*, 205-219.
[214] P. Madura, W. R. Scheidt, *Inorg. Chem.* **1976**, *15*, 3182-3184.
[215] A. Bencini, I. Bertini, G. Canti, D. Gatteschi, C. Luchinat, *J. Inorg. Biochem.* **1981**, *14*, 81-93.
[216] T. Lukasczyk, K. Flechtner, L. R. Merte, N. Jux, *J. Phys. Chem. C* **2007**, *111*, 3090-3098.
[217] J. H. Burness, J. G. Dillard, L. T. Taylor, *J. Am. Chem. Soc.* **1975**, *97*, 6080-6088.
[218] T. Ivanova, A. Naumkin, A. Sidorov, I. Eremenko, M. Kiskin, *J. Electron. Spectrosc. Relat. Phenom.* **2007**, *156-158*, 200-203.
[219] C. W. B. Bezerra, L. Zhang, K. C. Lee, H. S. Liu, J. L. Zhang, Z. Shi, A. L. B. Marques, E. P. Marques, S. H. Wu, J. J. Zhang, *Electrochim. Acta* **2008**, *53*, 7703-7710.

[220] R. L. Liu, D. Q. Wu, X. L. Feng, K. Müllen, *Angew. Chem. Int. Ed.* **2010**, *49*, 2565-2569.
[221] L. Gherghel, C. Kübel, G. Lieser, H.-J. Räder, K. Müllen, *J. Am. Chem. Soc.* **2002**, *124*, 13130-13138.
[222] J. Frommer, *Angew. Chem. Int. Ed.* **1992**, *31*, 1298-1328.
[223] S. Weigelt, C. Bombis, C. Busse, M. M. Knudsen, K. V. Gothelf, E. Laegsgaard, F. Besenbacher, T. R. Linderoth, *Acs Nano* **2008**, *2*, 651-660.
[224] K. Weiss, G. Beernink, F. Dotz, A. Birkner, K. Müllen, C. H. Woll, *Angew. Chem. Int. Ed.* **1999**, *38*, 3748-3752.
[225] B. Hulsken, R. Van Hameren, J. W. Gerritsen, T. Khoury, P. Thordarson, M. J. Crossley, A. E. Rowan, R. J. M. Nolte, J. A. A. W. Elemans, S. Speller, *Nat. Nanotechnol.* **2007**, *2*, 285-289.
[226] N. Reitzel, T. Hassenkam, K. Balashev, T. R. Jensen, P. B. Howes, K. Kjaer, A. Fechtenkotter, N. Tchebotareva, S. Ito, K. Müllen, T. Bjornholm, *Chem. Eur. J.* **2001**, *7*, 4894-4901.
[227] S. Kubowicz, U. Pietsch, M. D. Watson, N. Tchebotareva, K. Müllen, A. F. Thunemann, *Langmuir* **2003**, *19*, 5036-5041.
[228] P. Ruffieux, O. Groning, M. Bielmann, C. Simpson, K. Müllen, L. Schlapbach, P. Groning, *Phys. Rev. B* **2002**, *66*.
[229] C. Gunther, N. Karl, J. Pflaum, R. Strohmaier, B. Gompf, W. Eisenmenger, M. Müller, K. Müllen, *Langmuir* **2005**, *21*, 656-665.
[230] F. Jackel, M. Ai, J. S. Wu, K. Müllen, J. P. Rabe, *J. Am. Chem. Soc.* **2005**, *127*, 14580-14581.
[231] L. Piot, A. Marchenko, J. S. Wu, K. Müllen, D. Fichou, *J. Am. Chem. Soc.* **2005**, *127*, 16245-16250.
[232] M. D. Watson, F. Jackel, N. Severin, J. P. Rabe, K. Müllen, *J. Am. Chem. Soc.* **2004**, *126*, 1402-1407.
[233] E. Delamarche, B. Michel, *Thin Solid Films* **1996**, *273*, 54-60.
[234] E. Delamarche, B. Michel, H. A. Biebuyck, C. Gerber, *Adv. Mater.* **1996**, *8*, 719-&.
[235] J. P. Rabe, S. Buchholz, *Science* **1991**, *253*, 424-427.
[236] T. Yasuda, T. Shimizu, F. Liu, G. Ungar, T. Kato, *J. Am. Chem. Soc.* **2011**, *133*, 13437-13444.
[237] N. Katsonis, J. Vicario, T. Kudernac, J. Visser, M. M. Pollard, B. L. Feringa, *J. Am. Chem. Soc.* **2006**, *128*, 15537-15541.
[238] Y. Takakazu, *Prog. Polym. Sci.* **1992**, *17*, 1153-1205.
[239] C. Coperet, H. Adolfsson, T.-A. Khuong, A. K. Yudin, K. B. Sharpless, *J. Org. Chem.* **1998**, *63*, 1740-1741.
[240] M. Schlosser, T. Rausis, *Eur. J. Org. Chem.* **2004**, 1018-1024.
[241] A. Krasovskiy, V. Krasovskaya, P. Knochel, *Angew. Chem. Int. Ed.* **2006**, *45*, 2958-2961.
[242] J. S. Wu, M. D. Watson, N. Tchebotareva, Z. H. Wang, K. Müllen, *J. Org. Chem.* **2004**, *69*, 8194-8204.
[243] M. Baumgarten, U. Müller, A. Bohnen, K. Müllen, *Angew. Chem. Int. Ed.* **1992**, *31*, 448-451.
[244] A. Bohnen, K. H. Koch, W. Luttke, K. Müllen, *Angew. Chem. Int. Ed.* **1990**, *29*, 525-527.
[245] M. Kreyenschmidt, M. Baumgarten, N. Tyutyulkov, K. Müllen, *Angew. Chem. Int. Ed.* **1994**, *33*, 1957-1959.
[246] B. Valeur, Wiley-VCH Verlag GmbH, **2001**.

[247] R. G. Sun, Y. Z. Wang, D. K. Wang, Q. B. Zheng, E. M. Kyllo, T. L. Gustafson, F. S. Wang, A. J. Epstein, *Synth. Met.* **2000**, *111*, 595-602.
[248] P. A. Gale, P. Anzenbacher Jr, J. L. Sessler, *Coord. Chem. Rev.* **2001**, *222*, 57-102.
[249] P. A. Gale, J. L. Sessler, V. Kral, *Chem. Commun.* **1998**, 1-8.
[250] K. A. Nielsen, W. S. Cho, J. O. Jeppesen, V. M. Lynch, J. Becher, J. L. Sessler, *J. Am. Chem. Soc.* **2004**, *126*, 16296-16297.
[251] J. L. Sessler, E. Katayev, G. D. Pantos, P. Scherbakov, M. D. Reshetova, V. N. Khrustalev, V. M. Lynch, Y. A. Ustynyuk, *J. Am. Chem. Soc.* **2005**, *127*, 11442-11446.
[252] C. Floriani, *Chem. Commun.* **1996**, 1257-1263.
[253] D. Jacoby, C. Floriani, A. Chiesivilla, C. Rizzoli, *Chem. Commun.* **1991**, 790-792.
[254] D. Jacoby, C. Floriani, A. Chiesivilla, C. Rizzoli, *J. Am. Chem. Soc.* **1993**, *115*, 3595-3602.
[255] A. Matsumoto, T. Kitajima, K. Tsutsumi, *Langmuir* **1999**, *15*, 7626-7631.
[256] W. H. Carothers, *Trans. Faraday Soc.* **1936**, *32*, 0039-0053.
[257] J. Takagi, K. Sato, J. F. Hartwig, T. Ishiyama, N. Miyaura, *Tetrahedron Lett.* **2002**, *43*, 5649-5651.
[258] E. M. Beck, M. J. Gaunt, *Top Curr Chem* **2010**, *292*, 85-121.
[259] K. T. Wong, T. H. Hung, T. C. Chao, T. I. Ho, *Tetrahedron Lett.* **2005**, *46*, 855-858.
[260] T. E. Wood, B. Berno, C. S. Beshara, A. Thompson, *J. Org. Chem.* **2006**, *71*, 2964-2971.
[261] H. Knicker, P. G. Hatcher, A. W. Scaroni, *Energy Fuels* **1995**, *9*, 999-1002.
[262] B. F. O. Nascimento, A. M. D. R. Gonsalves, M. Pineiro, *Inorg. Chem. Commun.* **2010**, *13*, 395-398.
[263] H. C. Kolb, M. G. Finn, K. B. Sharpless, *Angew. Chem. Int. Ed.* **2001**, *40*, 2004-2021.
[264] R. Huisgen, *Angew. Chem. Int. Ed.* **1963**, *2*, 565-598.
[265] R. Huisgen, *Angew. Chem. Int. Ed.* **1963**, *2*, 633-645.
[266] R. Hoffmann, R. B. Woodward, *J. Am. Chem. Soc.* **1965**, *87*, 2046-2048.
[267] I. Fleming, (Ed.: L. John Wiley Sons), Chichester, West Sussex, United Kingdom, **2010**.
[268] C. W. Tornoe, C. Christensen, M. Meldal, *J. Org. Chem.* **2002**, *67*, 3057-3064.
[269] F. Himo, T. Lovell, R. Hilgraf, V. V. Rostovtsev, L. Noodleman, K. B. Sharpless, V. V. Fokin, *J. Am. Chem. Soc.* **2004**, *127*, 210-216.
[270] V. D. Bock, H. Hiemstra, J. H. van Maarseveen, *Eur. J. Org. Chem.* **2006**, 51-68.
[271] M. Roice, I. Johannsen, M. Meldal, *QSAR Comb. Sci* **2004**, *23*, 662-673.
[272] K. D. Bodine, D. Y. Gin, M. S. Gin, *J. Am. Chem. Soc.* **2004**, *126*, 1638-1639.
[273] J. D. Megiatto, D. I. Schuster, *J. Am. Chem. Soc.* **2008**, *130*, 12872-12873.
[274] Y. Li, A. H. Flood, *Angew. Chem. Int. Ed.* **2008**, *47*, 2649-2652.
[275] K. Sonogashira, Y. Tohda, N. Hagihara, *Tetrahedron Lett.* **1975**, *16*, 4467-4470.
[276] T. Michinobu, H. Osako, K. Shigehara, *Macromol. Rapid Commun.* **2008**, *29*, 111-116.
[277] A. Pollex, M. Hiersemann, *Org. Lett.* **2005**, *7*, 5705-5708.
[278] C. Lee, W. Yang, R. G. Parr, *Phys. Rev. B* **1988**, *37*, 785-789.
[279] A. D. Becke, *J. Chem. Phys.* **1993**, 5648-5652.
[280] N. H. Andersen, H. L. Eaton, X. Lai, *Magn. Reson. Chem.* **1989**, *27*, 515-528.
[281] D. Neuhaus, P. P. Williamson, VCH Publischers, INC., New York, **1989**.
[282] Y. Ping F, *J. Magn. Reson.* **1990**, *90*, 382-383.
[283] Z. Zhou, C. J. Fahrni, *J. Am. Chem. Soc.* **2004**, *126*, 8862-8863.
[284] M. Parent, O. Mongin, K. Kamada, C. Katan, M. Blanchard-Desce, *Chem. Commun.* **2005**, 2029-2031.
[285] F. Hofmeister, *Arch. Exp. Pathol. Pharmakol.* **1888**, *32*, 247.
[286] P. D. Beer, P. A. Gale, *Angew. Chem. Int. Ed.* **2001**, *40*, 486-516.

[287] P. A. Gale, S. Camiolo, G. J. Tizzard, C. P. Chapman, M. E. Light, S. J. Coles, M. B. Hursthouse, *J. Org. Chem.* **2001**, *66*, 7849-7853.
[288] P. Bühlmann, S. Nishizawa, K. P. Xiao, Y. Umezawa, *Tetrahedron* **1997**, *53*, 1647-1654.
[289] D. J. Cram, *Angew. Chem. Int. Ed.* **1988**, *27*, 1009-1020.
[290] L. Brammer, E. A. Bruton, P. Sherwood, *Cryst. Growth Des.* **2001**, *1*, 277-290.
[291] S. Matsuo, K. Kiyomiya, M. Kurebe, *Arch. Toxicol.* **1998**, *72*, 798-806.
[292] D. Briancon, *Rev. Rheum.* **1997**, *64*, 78-81.
[293] M. Laisalmi, H. Kokki, A. Soikkeli, H. Markkanen, A. Yli-Hankala, P. Rosenberg, L. Lindgren, *Acta Aneasthesiol. Scand.* **2006**, *50*, 982-987.
[294] C. I. Lin, S. Selvi, J. M. Fang, P. T. Chou, C. H. Lai, Y. M. Cheng, *J. Org. Chem.* **2007**, *72*, 5465-5465.
[295] S. W. Zhang, T. M. Swager, *J. Am. Chem. Soc.* **2003**, *125*, 3420-3421.
[296] G. L. Waldbott, *Clin. Toxicol.* **1981**, *18*, 531-541.
[297] P. Thordarson, *Chem. Soc. Rev.* **2011**, *40*, 1305-1323.
[298] P. Job, *Annales De Chimie France* **1928**, *9*, 113-203.
[299] K. A. Connors, in *Binding Constants*, Wiley & Sons, New York, **1987**.
[300] S. D. Jeong, A. Nowak-Krol, Y. Kim, S. J. Kim, D. T. Gryko, C. H. Lee, *Chem. Commun.* **2010**, *46*, 8737-8739.
[301] W. Zhang, J. S. Moore, *Angew. Chem. Int. Ed.* **2006**, *45*, 4416-4439.
[302] F. M. Pfeffer, K. F. Lim, K. J. Sedgwick, *Org. Biomol. Chem.* **2007**, *5*, 1795-1799.
[303] P. A. Gale, *Chem. Commun.* **2008**, 4525-4540.
[304] K. J. Chang, D. Moon, M. S. Lah, K. S. Jeong, *Angew. Chem. Int. Ed.* **2005**, *44*, 7926-7929.
[305] I. Hisaki, S. I. Sasaki, K. Hirose, Y. Tobe, *Eur. J. Org. Chem.* **2007**, 607-615.
[306] F. G. Bordwell, G. E. Drucker, H. E. Fried, *J. Org. Chem.* **1981**, *46*, 632-635.
[307] M. Ranger, D. Rondeau, M. Leclerc, *Macromolecules* **1997**, *30*, 7686-7691.
[308] D. Braun, A. J. Heeger, *Appl. Phys. Lett.* **1991**, *58*, 1982-1984.
[309] H. Langhals, *New J. Chem.* **1981**, *5*, 97-99.
[310] T. Michinobu, H. Osako, K. Murata, K. Shigehara, *Chem. Lett.* **2010**, *39*, 168-169.
[311] T. Michinobu, H. Osako, C. Seo, K. Murata, T. Mori, K. Shigehara, *Polymer* **2011**, *52*, 5756-5763.
[312] B. D. Yeomans, L. S. Kelso, P. A. Tregloan, F. R. Keene, *Eur. J. Inorg. Chem.* **2001**, 239-246.
[313] N. Defay, D. Maetens, R. Nasielskihinkens, *J. Organomet. Chem.* **1983**, *251*, 317-320.
[314] S. R. Marshall, A. L. Rheingold, L. N. Dawe, W. W. Shum, C. Kitamura, J. S. Miller, *Inorg. Chem.* **2002**, *41*, 3599-3601.
[315] H. Grove, J. Sletten, M. Julve, F. Lloret, *J. Chem. Soc. Dalton* **2001**, 1029-1034.
[316] S. D. Ha, Q. Zhang, S. Barlow, S. R. Marder, A. Kahn, *Phys. Rev. B* **2008**, *77*.
[317] H. Glowatzki, B. Broker, R. P. Blum, O. T. Hofmann, A. Vollmer, R. Rieger, K. Mullen, E. Zojer, J. P. Rabe, N. Koch, *Nano Lett.* **2008**, *8*, 3825-3829.
[318] M. Lehmann, G. Kestemont, R. G. Aspe, C. Buess-Herman, M. H. J. Koch, M. G. Debije, J. Piris, M. P. de Haas, J. M. Warman, M. D. Watson, V. Lemaur, J. Cornil, Y. H. Geerts, R. Gearba, D. A. Ivanov, *Chem. Eur. J.* **2005**, *11*, 3349-3362.
[319] K. Pieterse, P. A. van Hal, R. Kleppinger, J. A. J. M. Vekemans, R. A. J. Janssen, E. W. Meijer, *Chem. Mater.* **2001**, *13*, 2675-2679.
[320] R. Wang, T. Okajima, F. Kitamura, N. Matsumoto, T. Thiemann, S. Mataka, T. Ohsaka, *J. Phys. Chem. B* **2003**, *107*, 9452-9458.
[321] S. Furukawa, T. Okubo, S. Masaoka, D. Tanaka, H. C. Chang, S. Kitagawa, *Angew. Chem. Int. Ed.* **2005**, *44*, 2700-2704.

[322] B. X. Gao, Y. L. Liu, Y. H. Geng, Y. X. Cheng, L. X. Wang, X. B. Jing, F. S. Wang, *Tetrahedron Lett.* **2009**, *50*, 1649-1652.
[323] D. Z. Rogers, *J. Org. Chem.* **1986**, *51*, 3904-3905.
[324] R. Nasielskihinkens, M. Benedekvamos, D. Maetens, J. Nasielski, *J. Organomet. Chem.* **1981**, *217*, 179-182.
[325] B. Kohne, K. Praefcke, *Liebigs Ann. Chem.* **1985**, 522-528.
[326] J. T. Rademacher, K. Kanakarajan, A. W. Czarnik, *Synthesis-Stuttgart* **1994**, 378-380.
[327] M. S. P. Sarma, A. W. Czarnik, *Synthesis-Stuttgart* **1988**, 72-73.
[328] T. Ishi-i, K. Murakami, Y. Imai, S. Mataka, *Org. Lett.* **2005**, *7*, 3175-3178.
[329] T. Ishi-I, K. I. Murakami, Y. Imai, S. Mataka, *J. Org. Chem.* **2006**, *71*, 5752-5760.
[330] T. Ishi-i, H. Tashiro, R. Kuwahara, S. Mataka, T. Yoshihara, S. Tobita, *Chem. Lett.* **2006**, *35*, 158-159.
[331] T. Ishi-i, K. Yaguma, R. Kuwahara, Y. Taguri, S. Mataka, *Org. Lett.* **2006**, *8*, 585-588.
[332] R. I. Gearba, M. Lehmann, J. Levin, D. A. Ivanov, M. H. J. Koch, J. Barbera, M. G. Debije, J. Piris, Y. H. Geerts, *Adv. Mater.* **2003**, *15*, 1614-1618.
[333] M. Wang, Y. Li, H. Tong, Y. Cheng, L. Wang, X. Jing, F. Wang, *Org. Lett.* **2011**, *13*, 4378-4381.
[334] H. Y. Zhao, X. Y. Guo, H. K. Tian, C. Y. Li, Z. Y. Xie, Y. H. Geng, F. S. Wang, *J. Mater. Chem.* **2010**, *20*, 3092-3097.
[335] O. Ongayi, M. G. H. Vicente, B. Ghosh, F. R. Fronczek, K. M. Smith, *Tetrahedron*, *66*, 63-67.
[336] K. A. Kurak, A. B. Anderson, *J. Phys. Chem. C* **2009**, *113*, 6730-6734.
[337] K. P. Gong, F. Du, Z. H. Xia, M. Durstock, L. M. Dai, *Science* **2009**, *323*, 760-764.
[338] T. Yamamoto, A. Morita, Y. Miyazaki, T. Maruyama, H. Wakayama, Z. Zhou, Y. Nakamura, T. Kanbara, S. Sasaki, K. Kubota, *Macromolecules* **1992**, *25*, 1214-1223.
[339] S. K. Ritter, R. E. Noftle, A. E. Ward, *Chem. Mater.* **1993**, *5*, 752-754.
[340] M. J. Edelmann, J.-M. Raimundo, N. F. Utesch, F. Diederich, C. Boudon, J.-P. Gisselbrecht, M. Gross, *Helv. Chim. Acta* **2002**, *85*, 2195-2213.
[341] L. Hu, M. L. Kully, D. W. Boykin, N. Abood, *Bioorg. Med. Chem. Lett.* **2009**, *19*, 3374-3377.
[342] A. Nowak-Król, D. Gryko, D. T. Gryko, *Chem. Asian J.* **2010**, *5*, 904-909.
[343] M. Kastler, W. Pisula, D. Wasserfallen, T. Pakula, K. Müllen, *J. Am. Chem. Soc.* **2005**, *127*, 4286-4296.
[344] T. Ishi-i, R. Hirashima, N. Tsutsumi, S. Amemori, S. Matsuki, Y. Teshima, R. Kuwahara, S. Mataka, *J. Org. Chem.* **2010**, *75*, 6858-6868.
[345] L. Brunsveld, B. J. B. Folmer, E. W. Meijer, R. P. Sijbesma, *Chem. Rev.* **2001**, *101*, 4071-4097.
[346] C. Pak, H. M. Lee, J. C. Kim, D. Kim, K. S. Kim, *Struct. Chem.* **2005**, *16*, 187-202.
[347] F. J. M. Hoeben, P. Jonkheijm, E. W. Meijer, A. P. H. J. Schenning, *Chem. Rev.* **2005**, *105*, 1491-1546.
[348] R. Kachadourian, I. Batinić-Haberle, I. Fridovich, *Inorg. Chem.* **1998**, *38*, 391-396.
[349] T. Ikeue, N. Aratani, A. Osuka, *Isr. J. Chem.* **2005**, *45*, 293-302.
[350] R. Juárez, M. M. Oliva, M. Ramos, J. L. Segura, C. Alemán, F. Rodríguez-Ropero, D. Curcó, F. Montilla, V. Coropceanu, J. L. Brédas, Y. Qi, A. Kahn, M. C. Ruiz Delgado, J. Casado, J. T. López Navarrete, *Chem. Eur. J.* **2011**, *17*, 10312-10322.
[351] Z. Jiang, W. Zhang, H. Yao, C. Yang, Y. Cao, J. Qin, G. Yu, Y. Liu, *J. Polym. Sci., Part A: Polym. Chem.* **2009**, *47*, 3651-3661.
[352] Y. Zhang, P. Yao, X. Cai, H. Xu, X. Zhang, J. Jiang, *J. Mol. Graphics Modell.* **2007**, *26*, 319-326.

[353] M. J. Frisch, G. W. Trucks, H. B. Schlegel, G. E. Scuseria, M. A. Rob, J. R. Cheeseman, J. A. Montgomery Jr., T. Vreven, K. N. Kudin, J. C. Burant, J. M. Millam, S. S. Iyengar, J. Tomasi, V. Barone, B. Mennucci, M. Cossi, G. Scalmani, N. Rega, G. A. Petersson, H. Nakatsuji, M. Hada, M. Ehara, K. Toyota, R. Fukuda, J. Hasegawa, M. Ishida, T. Nakajima, Y. Honda, O. Kitao, H. Nakai, M. Klene, X. Li, J. E. Knox, H. P. Hratchian, J. B. Cross, V. Bakken, C. Adamo, J. Jaramillo, R. Gomperts, R. E. Stratmann, O. Yazyev, A. J. Austin, R. Cammi, C. Pomelli, J. W. Ochterski, P. Y. Ayala, K. Morokuma, P. S. G. A. Voth, J. J. Dannenberg, V. G. Zakrzewski, S. Dapprich, A. D. Daniels, M. C. Strain, O. Farkas, D. K. Malick, A. D. Rabuck, K. Raghavachari, J. B. Foresman, J. V. Ortiz, Q. Cui, A. G. Baboul, S. Clifford, J. Cioslowski, B. B. Stefanov, G. Liu, A. Liashenko, P. Piskorz, I. Komaromi, R. L. Martin, D. J. Fox, T. Keith, M. A. Al-Laham, C. Y. Peng, A. Nanayakkara, M. Challacombe, P. M. W. Gill, B. Johnson, W. Chen, M. W. Wong, C. Gonzalez, J. A. Pople, Gaussian, Inc., Pittsburgh PA, **2003**.
[354] M. Ladacki, M. Szwarc, *J. Chem. Phys.* **1952**, *20*, 1814-1816.
[355] J. H. Zagal, *Coord. Chem. Rev.* **1992**, *119*, 89-136.
[356] J. E. Greedan, *J. Mater. Chem.* **2001**, *11*, 37-53.
[357] W. Pisula, M. Kastler, C. Yang, V. Enkelmann, K. Müllen, *Chem. Asian J.* **2007**, *2*, 51-56.
[358] M. Fischer, G. Lieser, A. Rapp, I. Schnell, W. Mamdouh, S. De Feyter, F. C. De Schryver, S. Höger, *J. Am. Chem. Soc.* **2003**, *126*, 214-222.
[359] D. Zhao, J. S. Moore, *J. Org. Chem.* **2001**, *67*, 3548-3554.
[360] W. Pisula, Z. Tomovic, C. Simpson, M. Kastler, T. Pakula, K. Mullen, *Chem. Mater.* **2005**, *17*, 4296-4303.
[361] S. Chandrasekhar, G. S. Ranganath, *Rep. Prog. Phys.* **1990**, *53*, 57-84.
[362] S. Laschat, A. Baro, N. Steinke, F. Giesselmann, C. Hagele, G. Scalia, R. Judele, E. Kapatsina, S. Sauer, A. Schreivogel, M. Tosoni, *Angew. Chem. Int. Ed.* **2007**, *46*, 4832-4887.
[363] C. D. Simpson, J. S. Wu, M. D. Watson, K. Müllen, *J. Mater. Chem.* **2004**, *14*, 494-504.
[364] I. C. Lewis, C. A. Kovac, *Carbon* **1978**, *16*, 425-429.
[365] H. E. Gottlieb, V. Kotlyar, A. Nudelman, *J. Org. Chem.* **1997**, *62*, 7512-7515.

LEBENSLAUF *Dipl.-Ing. Lena Arnold*

[redacted]

[redacted] [redacted]

[redacted]

[redacted] [redacted]

[redacted] [redacted]

[redacted] [redacted]

[redacted] [redacted]

[redacted] [redacted]

[redacted] [redacted]

[redacted] [redacted]

[redacted]

[redacted] [redacted]

[redacted] [redacted]

[redacted] [redacted]

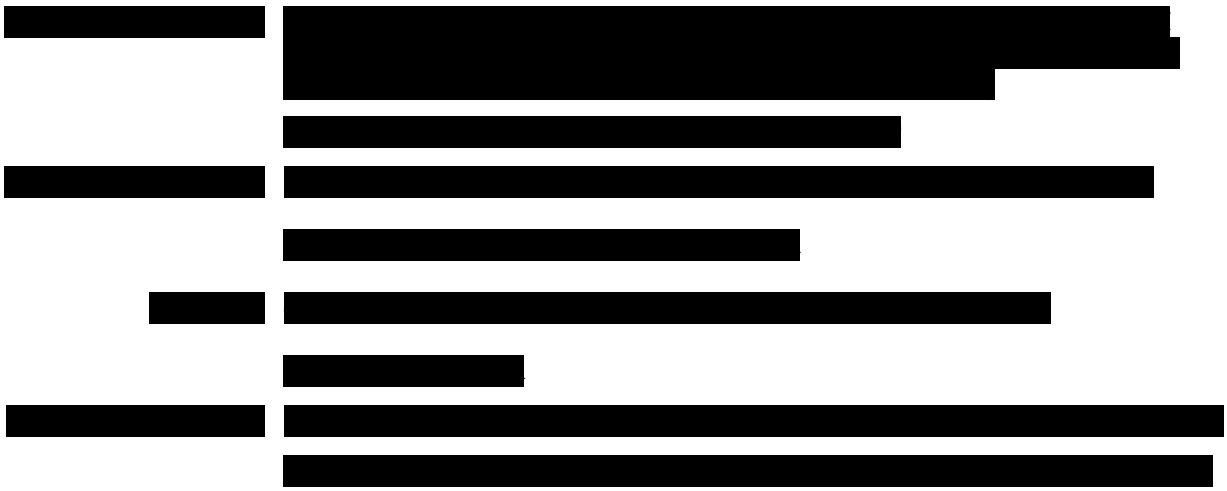

VERÖFFENTLICHUNGEN

[1] L. Arnold, M. Baumgarten, K. Müllen, *Chem. Commun.* **2012**, 48, 9640-9642. *A carbazole-containing porphyrinoid: synthesis and oxidation to the porphyrin-state*

[2] L. Arnold, S. R. Puniredd, C. von Malotki, W. Pisula, N. Koshino, H. Higashimura, M. Baumgarten, M. Wagner and K. Müllen *J. Porphyrins Phthalocycanines*, **2012**, 16, *5-6,* 564-575. *Fused π-Extended Discotic Triangular Porphyrinoids*

[3] N. Koshino, H. Higashimura, K. Müllen, C. von Malotki, Q. Su, M. Baumgarten, H. Norouzi-Arasi, L. Arnold and R. Liu *PCT Int. Appl.*, **2011**, *WO 2011052805 A1 20110505. Nitrogen-containing aromatic compounds and metal complexes for fuel cell electrodes*

[4] R. Liu, C. von Malotki, L. Arnold, N. Koshino, H. Higashimura, M. Baumgarten, and K. Müllen *J. Am. Chem. Soc.*, **2011**, *133*, 27, 10372-10375. *Triangular Trinuclear Metal-N_4 Complexes with High Electrocatalytic Activity for Oxygen Reduction*

[5] L. Arnold and K. Müllen *J. Porphyrins Phthalocycanines,* **2011**, 15, *9-10*, 757-779. *Modifying the porphyrin core - a chemist's jigsaw*

[6] L. Arnold, H. Norouzi-Arasi, M. Wagner, V. Enkelmann and K. Müllen *Chem. Commun.*, **2011**, *47*, 970-972. *A Porphyrin-related Macrocycle from Carbazole and Pyridine Building Blocks: Synthesis and Metal Coordination*

[7] L. Arnold, A. Marx, C. M. Thiele and M. Reggelin *Chem. Eur. J.*, **2010**, *16*, 10342-10346. *Polyguanidines as Chiral Orienting Media for Organic Compounds*

[8] G. Quintanilla, M. Liebeck, C. Bengtsson, L. Arnold and F. Barba *Electrochimica Acta,* **2008***, 53, 2674. Cathodic Reduction of Benzil in Acetone and in Dichloromethane*